Integration of protein containers into microgel systems for potential drug release and delivery

Von der Fakultät für Mathematik, Informatik und Naturwissenschaften der RWTH Aachen University
zur Erlangung des akademischen Grades eines Doktors der Naturwissenschaften
genehmigte Dissertation

vorgelegt von

Made Budiarta M. Sc.

aus

Mataram, Indonesien

Berichter*:* Prof. Dr. Tobias Beck
Prof. Dr. Andrij Pich
Prof. Dr. Ulrich Simon

Tag der mündlichen Prüfung*:* 15.01.2021

To all my kind teachers and mentors

Abstract

The application of ferritin containers as a promising drug delivery vehicle is hampered by proteolytic degradation in systemic circulation. Here, a novel strategy to improve the stability of ferritin containers against protease is presented: Ferritin containers were integrated into the polymeric network of polyelectrolyte microgels. First, ferritin was labeled with fluorophores and nanoparticles (NPs) to enable tracking their integration and release from microgels by fluorescence microscopy and transmission electron microscopy (TEM), respectively. To obtain a high fluorophore loading and yield, a new encapsulation strategy based on the cysteine-maleimide coupling reactions was developed.

The integration of ferritin into microgel systems was performed by the electrostatic interactions between the charged co-monomers of microgels and the surface charges of ferritin. Initially, ferritin was integrated into microgels with randomly distributed ionizable groups. However, the integration was characterized by precipitation, and the resulting microgels could not be purified from the excess ferritin. Therefore, next, ferritin was integrated into a charged core-neutral shell microgel. Although the neutral shell prevented precipitation, ferritin could leak out from the microgels and ferritin was inhomogeneously distributed among the microgels. All these problems were solved when ferritin was integrated during the microgel synthesis. The integration was very effective because about 80% of the applied ferritin containers were integrated into the microgels. To enable ferritin release from microgels, an acid-degradable crosslinker was applied in the synthesis. It is shown that about 85% and 50% of the integrated ferritin can be released rapidly in buffer with pH 2.5 and 4.0, respectively. However, total degradation of the microgels was not observed due to the self-crosslinking of N-isopropylacrylamide (NIPAM). Finally, proteolytic degradation by chymotrypsin proved that the microgels could protect ferritin against protease.

For drug delivery purposes, the anti-cancer drug doxorubicin (DOX) was encapsulated into various ferritin variants. The resulting DOX-ferritin variants then were integrated into the microgel system. However, the cell experiments show that the cytotoxicity of DOX-ferritin variants is lower than the free-DOX. One possible reason is the attachment of DOX molecules on the surface of ferritin cages, which obstructs the ferritin uptake into the cells. Further investigations are needed to confirm and overcome this problem.

In this work, a protein containers-microgel system is developed for the first time. Interestingly, the same synthesis could be applied to integrate ferritin containers containing different cargos into the microgels. This approach describes an innovative, previously not considered strategy for integrating various materials into the microgels. Thereby, this work expands the areas for the applications of colloidal microgel systems.

Zusammenfassung

Die Anwendung von Ferritincontainern als vielversprechender Wirkstoffträger wird durch proteolytischen Abbau im systemischen Kreislauf behindert. Hier wird eine neuartige Strategie zur Verbesserung der Stabilität von Ferritincontainern gegen Protease vorgestellt: Ferritincontainern wurden in das polymere Netzwerk von Polyelektrolyt-Mikrogelen integriert. Zunächst wurde Ferritin mit Fluorophoren und Nanopartikeln (NPs) markiert, um ihre Integration und Freisetzung aus Mikrogelen mittels Fluoreszenzmikroskopie bzw. Transmissionselektronenmikroskopie (TEM) verfolgen zu können. Um eine hohe Fluorophorbeladung und -ausbeute zu erzielen, wurde eine neue Einkapselungsstrategie entwickelt, die auf den Cystein-Maleimid-Kupplungsreaktionen basiert.

Die Integration von Ferritin in Mikrogelsysteme erfolgte durch die elektrostatischen Wechselwirkungen zwischen den geladenen Comonomeren der Mikrogele und den Oberflächenladungen des Ferritins. Zunächst wurde Ferritin in Mikrogele mit zufällig verteilten ionisierbaren Gruppen integriert. Jedoch führte die Integration zur Ausfällung, und die resultierenden Mikrogele konnten nicht von dem überschüssigen Ferritin getrennt werden. Daher wurde als nächstes Ferritin in ein geladenes Kern-Neutral-Schale-Mikrogel integriert. Obwohl die neutrale Schale eine Ausfällung verhinderte, konnte Ferritin aus den Mikrogelen austreten, sodass das Ferritin zwischen den Mikrogelen inhomogen verteilt war. All diese Probleme wurden gelöst, als Ferritin während der Mikrogel-Synthese integriert wurde. Die Integration war sehr effektiv, da etwa 80% der verwendeten Ferritincontainern in die Mikrogele integriert wurden. Um die Freisetzung von Ferritin aus den Mikrogelen zu ermöglichen, wurde bei der Synthese ein säureabbaubarer Vernetzer eingesetzt. Es wird gezeigt, dass etwa 85% bzw. 50% des integrierten Ferritins in Puffer mit pH 2.5 bzw. 4.0 schnell freigesetzt werden können. Ein vollständiger Abbau der Mikrogele wurde jedoch aufgrund der Selbstvernetzung von N-Isopropylacrylamid (NIPAM) nicht beobachtet. Schließlich bewies ein proteolytischer Abbau durch Chymotrypsin, dass die Mikrogele Ferritin vor proteolytischem Abbau schützen konnten.

Für die Anwendung zum Wirkstofftransport wurde das Krebsmedikament Doxorubicin (DOX) in verschiedene Ferritin-Varianten eingekapselt. Die resultierenden DOX-Ferritin-Varianten wurden dann in das Mikrogel-System integriert. Die Zellexperimente zeigen jedoch, dass die Zytotoxizität von DOX-Ferritin-Varianten geringer als die von freiem DOX ist. Ein möglicher Grund ist die Anheftung von DOX-Molekülen auf der Oberfläche von Ferritin-Käfigen, die die Ferritinaufnahme in die Zellen behindern. Weitere Untersuchungen sind notwendig, um dieses Problem zu bestätigen und zu überwinden.

In dieser Arbeit wird zum ersten Mal ein Ferritincontainer-Mikrogel-System entwickelt. Interessanterweise konnte die gleiche Synthese angewandt werden, um Ferritincontainer mit unterschiedlichen Inhalten in die Mikrogele zu integrieren. Dieser Ansatz beschreibt eine innovative, bisher nicht in Betracht gezogene Strategie zur Integration verschiedener Materialien in die Mikrogele. Damit erweitert diese Arbeit die Anwendungsbereiche für kolloidale Mikrogelsystem.

The work presented in this thesis was carried out at the Institute of Inorganic Chemistry of the RWTH Aachen University between December 2017 and December 2020 under the supervision of Prof. Dr. Tobias Beck. The funding for this project was received from SFB 985 Functional Microgels and Microgel systems.

Publications

Parts of this thesis have been published or are in the process of being published:

I. Budiarta, M.; Xu, W.; Schubert, L.; Meledina, M.; Meledin, A.; Wöll, D.; Pich, A.; Beck, T. Protecting Redesigned Supercharged Ferritin Containers against Protease by Integration into Acid-cleavable Polyelectrolyte Microgels, *JCIS* **2021**, *591*, 451-462, DOI: 10.1016/j.jcis.2021.01.072.

II. Budiarta, M.; Boesveld, S.; Strnad, P.; Beck, T. The application of ferritin-microgel systems for drug release and delivery, *in preparation*.

The author has also contributed to the following related publications:

III. Künzle, M.; Lach, M.; Budiarta, M.; Beck, T. Highly-order structures based on molecular interactions for the formation of natural and artificial biomaterials. *ChemBioChem* **2019**, *20*, 1637-1641.

Conference contributions:

- Talk: "Interaction of protein containers and polyelectrolyte microgels – uptake and release study." *Nanotage*, Köln, Germany, **2018**.
- Talk: "Integration of protein containers into polyelectrolyte microgels for drug release and delivery." *Nanotage*, Aachen, Germany, **2019**.
- Poster: "Integration of protein containers into polyelectrolyte microgels for drug release and delivery." *The 30th Annual conference of the European Society for Biomaterials*, Dresden, Germany, **2019**.

Acknowledgment

This PhD thesis is the fruit of great efforts and supports from many people who have been very helpful to me. First and foremost, I would like to thank Prof. Tobias Beck for the supervision of my doctoral study and for the opportunity to work on this exciting and challenging project. In particular, I would like to thank him for the continuous support, numerous discussions, encouragement, and the opportunities to challenge and develop myself. He is a great team leader and a role model for scientists. I am very grateful to have him as my supervisor; it is literally a blessing for me.

I would like to thank the SFB 985 Functional Microgels and Microgel Systems for the funding and the opportunity to perform my doctoral study.

I would like to thank Prof. Ulrich Simon for his great support and generosity during my doctoral study. He provided all the environmental conditions necessary for conducting my research. I am also very thankful that he allowed me to become a part of his group.

I would like to thank Prof. Ulrich Schwaneberg for the continuous access to his laboratory and equipment for conducting molecular biology-related experiments.

I would like to thank Prof. Andrij Pich, Prof. Dominik Wöll, Dr. Pavel Strnad for the fruitful discussions and their invaluable feedback.

I would like to thank Prof. Tobias Beck, Prof. Andrij Pich, Prof. Ulrich Simon, and Prof. Dominik Wöll as the members of the doctoral examination committee.

I would like to thank all the people who have contributed to this work: Wenjing Xu, for the microgels and for introducing me to the semi-batch synthesis of microgels; Sarah Wypysek, for the microgels, discussions, and for introducing me to the batch synthesis of microgels; Sarah Boesveld, for the conducting the cell experiments; Lukas Schubert, for the fluorescence microscopy experiments; Dr. Maria Meledina, for conducting the electron tomography; Dr. Alexander Meledin, for the post-processing of electron tomography; Volkan Besirlioglu, for the two-steps PCR reactions; Hendrik Böhler, for the optimization of cysteine position; Dr. Marcel Lach, for the numerous TEM measurements; Johannes von Campenhausen, for the encapsulation of DOX in $Ftn^{(pos)}$; Simon Schog, for the synthesis of microgels with locking-shells.

I am greatly indebted to Dr. Matthias Künzle and Dr. Marcel Lach, who trained me a lot at the beginning of my doctoral study, also for the numerous discussions and supports. I learned a lot from you!

I would like to thank Dr. Michael Noyong and Dr. Melanie Homberger for their general support and suggestions for my research.

I would like to thank Sabine Eisold and Rebecca Hengsbach for the discussions, suggestions, and help concerning microgel-related problems.

I would like to thank all the members of AK Beck: Dr. Matthias Künzle, Dr. Marcel Lach, Dr. Brandon Seychell, Michael Rütten, Hendrik Böhler, and Laurin Lang for the supports, and friendly working atmosphere. It has been a great time to work with you!

I would like to thank all the members of AK Simon and AK Schwaneberg who have accompanied me during the last three years. Thank you for all the good times and the friendly atmosphere.

Many thanks to all the people from Lab 002. Thank you for your cooperation and friendly supports.

I would like to express my special gratitude to my wife Erni Lim, who has always been a great support for me. Without her, I would not be able to put great effort into my research.

Finally, I would like to thank my parents and family. Thank you for all your kindness and great supports.

Table of contents

1 Introduction

Rapid progress in nanotechnology has brought remarkable advances in the development of drug delivery systems (DDS) to overcome problems related to conventional therapeutics.[1,2] Various nanomaterials have been designed to precisely deliver drugs to the target site or to improve their bioavailability and release properties, therefore enhancing their efficacy while alleviating their adverse effects.[3,4] Some examples for these nanomaterials are polymeric micelles,[5] liposomes,[6] dendrimers,[7,8] quantum dots,[9] metallic NPs,[10] and protein NPs.[11,12]

Recently, the ferritin nanocage has attracted considerable interest due to its unique characteristics as DDS.[13,14] Ferritin is an iron-storage protein with an inner cavity that can be used as a reaction vessel or for cargo loading. It is biocompatible and robust to extreme conditions. Ferritin was shown to withstand a broad range of pH values, from 3 to 10, or can be heated up to 80 °C.[15,16] The cages can be opened and closed to load a broad range of materials, such as small drugs,[17–20] therapeutic protein,[13] photosensitizers,[21] fluorophores,[22,23] and NPs[24] among others. Ferritin cages are also amenable for further chemical or genetic engineering modifications.[25,26] More interestingly, human heavy-chain ferritin (HF) has been known to bind with transferrin receptor 1 (TfR-1) and internalized into the cells. As TfR-1 is overexpressed in many cancer cells, HF offers an easy way to deliver drugs to cancer cells.[22,27,28]

Despite these interesting properties, the application of HF as DDS is limited by its low bioavailability. The plasma half-life of HF is rather too short (∼1 h)[29] for its sufficient accumulation in the targeted sites. Two problems are responsible for this low bioavailability. The first is degradation by protease, which is a common problem shared by therapeutic peptides or proteins in general.[30,31] Secondly, HF also has been known to be rapidly removed from the systemic circulation by liver clearance.[32,33]

Several attempts have been made to increase the plasma half-life of ferritin. For example, Vannucci et al. attached polyethylene glycol (PEG) along with α-melanocyte-stimulating hormone as the targeting peptide on the surface of ferritin, thereby increasing the half-life of ferritin up to 24 h.[29] Similarly, Falvo et al. improved both DOX encapsulation and ferritin circulation time by the genetic fusion of ferritin with stabilizing polypeptides rich in proline, serine, and alanine.[34] Recently, Wang et al. performed the genetic fusion of ferritin and albumin-binding domain to reach the same objective.[35]

In this work, a novel strategy to improve the stability of ferritin against proteolytic degradation is presented. Here, ferritin was integrated into the microgel systems. Microgels are colloidal systems that consist of crosslinked polymer networks.[36] It is presumed that the polymer chains may protect ferritin against protease. Microgels also have other interesting properties.[37,38] They are hydrophilic,

biocompatible, and have an open structure enabling a large uptake capacity. They can be easily produced with controllable size and high monodispersity. A wide variety of monomers is also available to provide microgels multifunctionality. More interestingly, microgels are stimuli-responsive materials. Guest-molecule release can be triggered by various stimuli: pH,[39,40] temperature,[41,42] ionic strength,[43,44] chemicals,[45,46] light,[47] ultrasound,[48] and magnetic field.[49,50]

The integration of ferritin into microgels carries great potential. The ferritin containers can be used as a cargo vessel in a modular approach. Once the integration has been established, the containers can be loaded with different drugs, or used to combine multiple drugs, or to couple drugs with imaging agents. Furthermore, the integration of protein containers into microgels also has the potential to protect ferritin from liver clearance. With all these properties and potential applications, an interesting stimuli-responsive ferritin DDS is expected from the integration of ferritin containers and microgels.

2 Concept of the work

The integration of ferritin containers into microgel systems will be based on the electrostatic interactions between the containers and the microgel polymer. For this, ferritin containers with a redesigned outer surface, named supercharged ferritin will be used. Previously, my group has successfully developed two variants of supercharged ferritin for the self-assembly of binary protein crystals: Ferritin$^{(neg)}$ and Ferritin$^{(pos)}$, designated as Ftn$^{(neg)}$ and Ftn$^{(pos)}$, respectively.[24] Both variants were obtained by substituting the amino acids on the surface of HF with a negatively charged amino acid (glutamic acid) or positively charged amino acids (arginine or lysine, Figure 2.1). These two ferritin variants are suitable for the integration of ferritin containers into the polyelectrolyte microgel system because the charged co-monomers of the microgels can favorably interact with the charged ferritin surface.

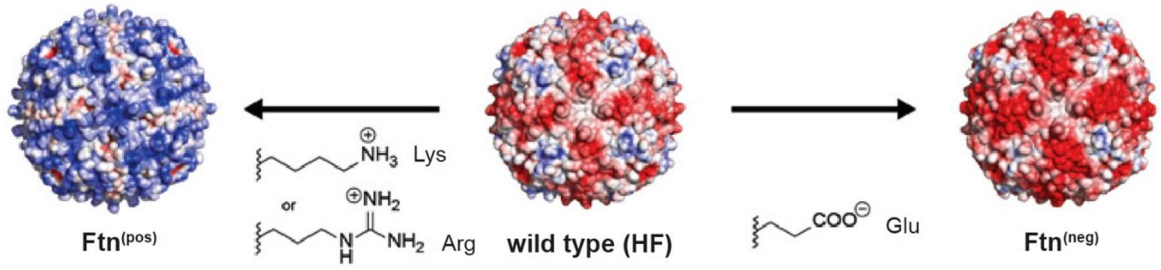

Figure 2.1 Two variants of supercharged ferritin generated by the surface-charging of wild-type ferritin. These are the electrostatic surface potential of the three ferritin variants (red: -5 kT/e, blue: +5 kT/e). The surface charging was performed by the mutation of amino acids on the outer surface of wild-type ferritin.

This work has two main parts. In the first part, it is planned to establish the integration of ferritin into microgel systems, while in the second part the ferritin-microgel system obtained in the first part will be investigated for a potential application in drug delivery. The strategies for the first part are illustrated in Figure 2.2. To be able to monitor the integration and the release of ferritin from the microgels, ferritin needs to be labeled. This can be done by encapsulating fluorophores or nanoparticles inside ferritin. In this way, ferritin can be tracked by fluorescence microscopy and TEM, respectively. Therefore, I will start by encapsulating fluorophores and NPs in both supercharged ferritin variants. Subsequently, the labeled ferritin will be integrated into readily synthesized microgels: (i) microgels with randomly distributed ionic groups and (ii) the core-shell microgels. Alternatively, ferritin will be integrated during the microgel synthesis. After establishing the integration of ferritin into microgels, the ferritin release will be studied in acidic conditions by TEM, UV/Vis, and fluorescence microscopy. Finally, it will be investigated if the microgels can protect the encapsulated ferritin from proteolytic degradation.

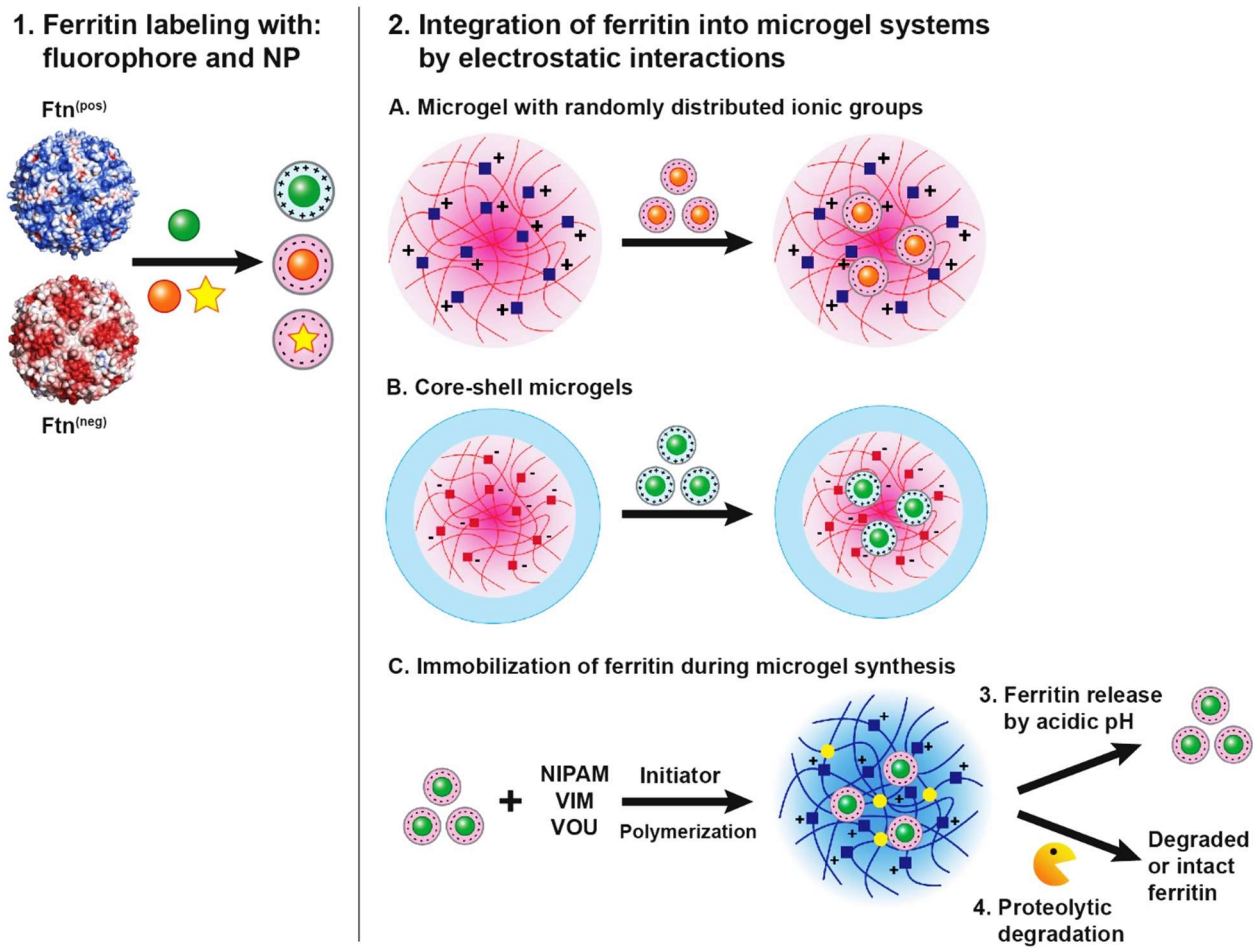

Figure 2.2 Overview of the strategies for establishing the integration of ferritin into microgels.

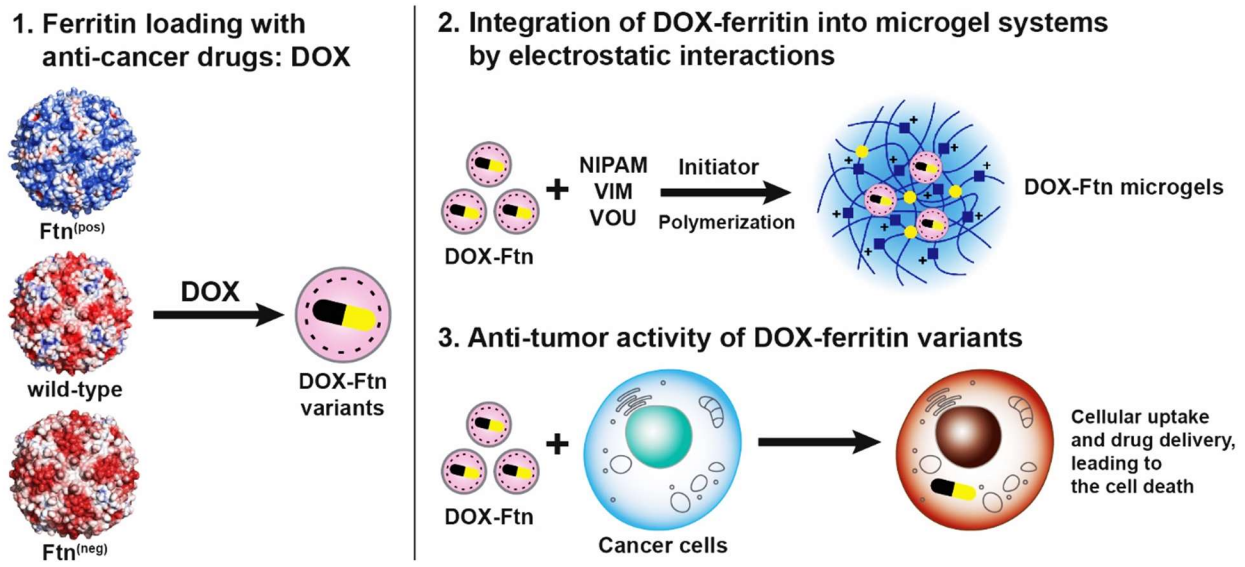

Figure 2.3 Overview of strategies for the application of ferritin-microgels as drug delivery vehicles.

The strategies for the second part of the work are illustrated in Figure 2.3. First, DOX will be encapsulated in both of the supercharged ferritin variants, as well as in the wild-type ferritin. This is because the microgels can be prepared with the positively charged or the negatively charged co-monomers. Furthermore, there is a concern that the surface modifications in supercharged ferritin variants may alter the binding property of ferritin with the TfR-1. Subsequently, the DOX ferritin variants will be integrated into microgels using the same protocol as established in the first part of the work. Finally, the anti-tumor activities of DOX-ferritin variants will be studied against cancer cells.

3 Scientific background

3.1 Drug delivery systems

Conventional drug molecules are very effective for treating illnesses, and they comprise most of the medicines available in the market.[51,52] However, they are also characterized by several problems. A large number of small organic molecule drugs have a low aqueous solubility which limits their applications.[53,54] Although their small sizes enable rapid diffusion through biological barriers, such as cell membranes, to reach their site of actions,[55,56] the small sizes also lead to rapid clearance from the body.[57,58] As a result, only a small fraction of the applied drugs reaches the target site, thereby delivering insufficient therapeutic effect. Moreover, small drug molecules also have a non-specific distribution in the body. They are taken up by both the healthy and the diseased cells, therefore causing severe side effects.[59] This is obvious in many cases of chemotherapeutic treatments. Furthermore, due to the low bioavailability, the drugs need to be administered repeatedly, which is not only ineffective by cost but also uncomfortable for the patients. Drug delivery systems (DDS) are developed to overcome these limitations.

DDS are defined as formulations or technologies that are designed to selectively deliver drugs to the required site[59] or to improve the drug's bioavailability and release properties, therefore enhancing efficacy while alleviating the adverse effects.

Rapid progress in nanotechnology has brought remarkable advances in the development of DDS.[1,2] Nanomaterials can be defined as materials with sizes between 1 and 100 nm.[60] With this range of sizes, nanomaterials can move more freely in the body as compared to larger materials. Furthermore, nanoscale materials show interesting physical, chemical, and biological properties that can be utilized in DDS. For example, they can be used for encapsulating drugs to protect drugs from enzymatic degradation[61] or as carriers to precisely deliver drugs to the target site.[62] Some nanomaterials are stimuli-responsive, and various stimuli can be used to trigger the release of drugs in a controlled manner.[63] Nanomaterials also enable the development of theranostic DDS which combines both therapy and diagnostic (imaging).[64] All these properties make DDS suitable applications for nanomaterials.

In the context of cancer treatments, there are two main strategies to deliver drugs to the tumor sites: passive targeting and active targeting.[57,59] The inner cellular lining of blood vessels in tumor tissues is known to be more permeable than in normal tissues.[65] These leaky blood vessels come about due to the rapid and defective formation of new blood vessels to feed the growing tumor with nutrients and oxygen. Nanomaterials with the size of 10 – 100 nm can escape these leaky blood vessels and enter

into the interstitial space of tumor tissues. Furthermore, tumor tissues have poor lymphatic drainage, which prevents the nanomaterials to be cleared rapidly. Therefore, by longer circulation in the bloodstream, nanomaterials accumulate more and more in the tumor tissue. This is called enhanced permeability and retention (EPR) effect or passive targeting (Figure 3.1).[65] To exploit this EPR effect, the size of the nanomaterials is crucial. They must be larger than 10 nm to avoid removal by filtration in the kidney. However, the upper size limit is less defined because the tumor permeability is not constant. It varies between the tumor type and microenvironment, and may even vary in the same tumor. Some studies comment that the size must be under 100 nm,[66] while others mention 100-400 nm as a size range that is still possible to show the EPR effect.[67]

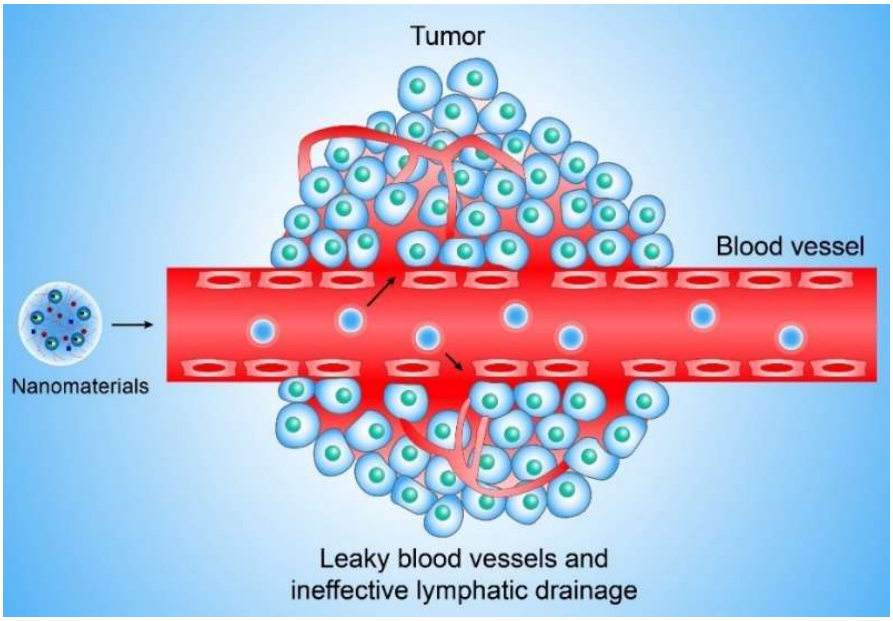

Figure 3.1 Enhanced permeability and retention (EPR) effect. Nanomaterials with sizes of 10-100 nm can escape through the leaky blood vessels into the interstitial space of tumor tissues. Due to the ineffective lymphatic drainage and prolonged circulation in the bloodstream nanomaterials accumulate inside the tumor tissue.

In active targeting, targeting ligands are attached to the surface of nanomaterials, for example by various types of conjugation chemistry. These targeting ligands will actively recognize cancer cells and bind specifically to the over-expressed receptors on the surface of cancer cells.[68] If the nanomaterials bind to the internalizing receptors, they will be taken into the cells via small vesicles called endosomes. These early endosomes rapidly mature into late endosomes and then fuse with lysosomes. In the lysosome, acidic pH and enzymatic digestion can be used to trigger the release of drugs from nanomaterials.[69] Next, the drugs molecule are released from the lysosome to the cytosol to deliver their actions on specific organelles. For example, binding to the DNA inside the nucleus to cause programmed cell death. Various molecules can be applied as targeting ligands: small molecules,[69] aptamers,[70] short peptides,[71] proteins,[72] or antibodies.[73] In principle, these ligands must bind specifically to the cancer cells and leave out the normal and healthy cells.

In short, passive targeting promotes the accumulation of nanomaterials in the tumor tissue environment, while active targeting improves the selectivity and the internalization of nanomaterials into cancer cells. Both strategies can also be combined to increase the efficacy of DDS.

Some examples for nanomaterial-based DDS are polymeric micelles,[74,75] liposomes,[6,76] dendrimers,[7,8] quantum dots,[9] metallic NPs,[10] protein-based DDS,[11,12] among others (Figure 3.2). Polymeric micelles are nanostructures formed by the spontaneous self-assembly of amphiphilic block copolymers in an aqueous solution when their concentration is above critical micelle concentration. The formation of a core-shell structure in polymeric micelles is driven by the solubility difference between the hydrophilic-block and the hydrophobic-block of amphiphilic copolymers in aqueous media. The hydrophobic core can be filled with lipophilic drugs, while the hydrophilic shell solubilizes the polymeric micelles and stabilized the cores.

Polymeric micelles are very useful for the delivery of poorly water-soluble drugs. The drug encapsulation is rather simple: it does not need chemical conjugation between the cargo and the polymer as the drug will bind to the hydrophobic core. Moreover, polymeric micelles have a narrow distribution with sizes between 10 nm to 100 nm, which is suitable for exploiting the EPR effect and for avoiding clearance by macrophages. Despite these benefits, polymeric micelles also have a disadvantage. They are increasingly unstable when diluted in the bloodstream after the injection.[63,75]

Liposomes are small vesicles composed of a spherical double layer of amphiphilic phospholipids surrounding an aqueous core region. The lipid double layer can be loaded with hydrophobic drugs, while the aqueous phase can be filled with hydrophilic drugs. Liposomes have the size of 50 – 450 nm and they are among the most clinically established nanomaterial-based DDS.[76] However, liposomes also have some drawbacks: low drug loading, abrupt drug release profile, poor stability during storage, lack of tunable stimuli to trigger drug release. Furthermore, they usually do not penetrate the cell membrane, therefore drugs are released in the extracellular environment.[69]

Dendrimers are synthetic and hyperbranched polymeric macromolecules that form a tree-like structure. They are synthesized either starting from the core to the outside (divergent approach) or by connecting prepared building blocks. Drugs are loaded into the dendrimer's open structure by encapsulation, electrostatic interactions, or covalent conjugation. Dendrimers are highly monodisperse and small in size: 1 – 10 nm.[77] Therefore, they have a limited drug loading and are subject to renal clearance by the kidney. Furthermore, the presence of the positively charged amine groups from the polymeric materials makes dendrimers toxic to the cells.[7]

Quantum dots (QDs) are semiconductor nanocrystals with size-dependent optical properties which are very useful for bioimaging. QDs can be integrated with the other DDS to provide real-time monitoring of the DDS transport and drug release. Alternatively, QDs can also be used as direct DDS through

surface functionalization chemistry. However, the latter approach remains questionable due to the potential long-term toxicity of the QDs.[9] Similar to QDs, the surface of noble metal like Au NPs can be functionalized and used as a scaffold for drugs and other targeting ligands. Au NPs can also be used for bioimaging and photodynamic therapy.[10] The main challenge for AuNPs DDS lies in the engineering of the particle surface for better bioavailability and non-immunogenicity.[77]

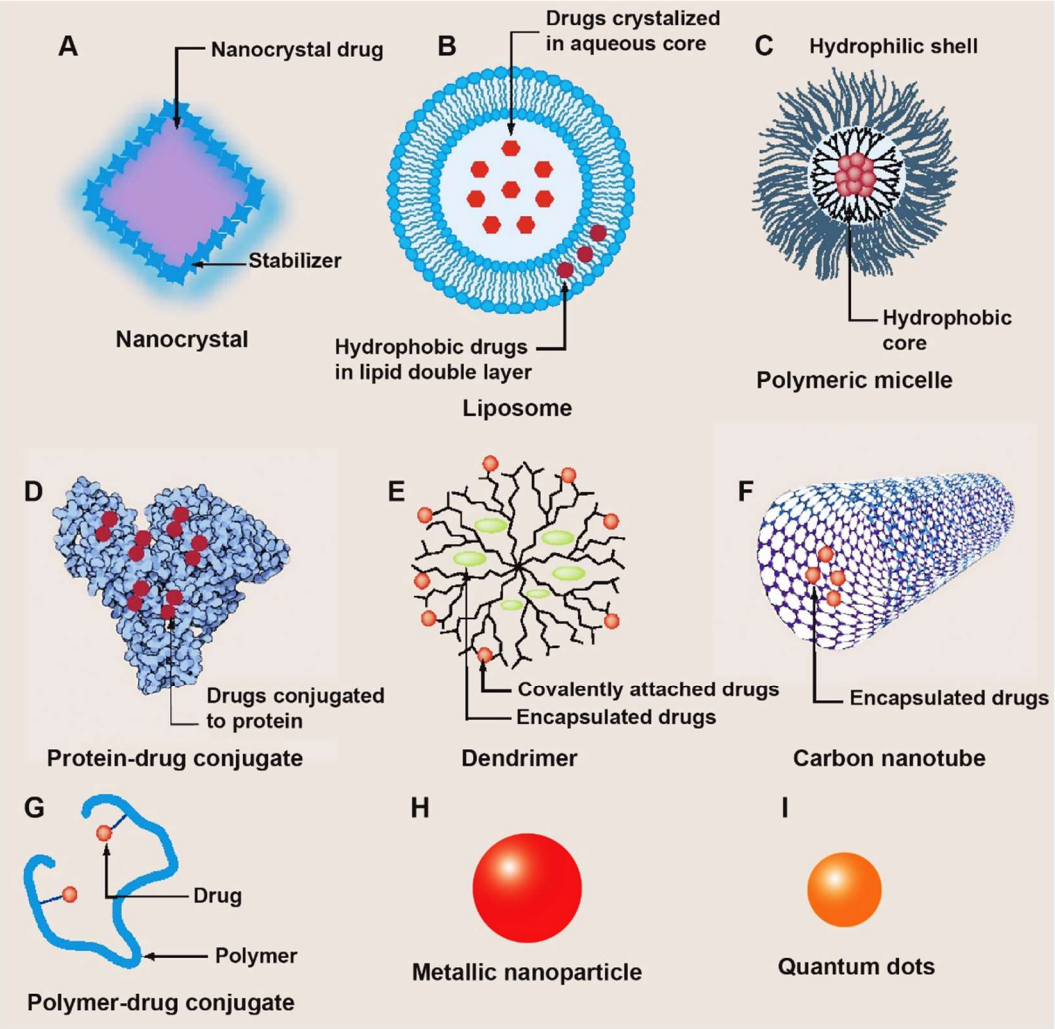

Figure 3.2 Nanomaterial-based DDS. A) Nanocrystal. B) Liposome. C) Polymeric micelle. D) Protein-based NPs. E) Dendrimer F) Carbon nanotube G) Polymer-drug conjugate H) Metallic NP I) Quantum dots. Adapted from Ref. [77].

Protein-based DDS offer several benefits compared to the other DDS: biocompatibility, biodegradability, abundant resources, as well as identical and uniform sizes (in certain types of protein DDS). In general, protein-based DDS can be divided into three classes. The first one, crosslinked protein NPs, are prepared from natural polymers such as gelatin, albumin, casein, collagen, zein (corn protein), and whey protein. There are various methods to synthesize this type of DDS, but the main one is coacervation.[78] The protein is first dissolved along with drugs in an aqueous solution and then added dropwise to a solution of desolvating agent. Protein and the drugs co-precipitates due to the decrease

in solubility. After sonication, glutaraldehyde is added to crosslink the protein. As a result, the drugs are encapsulated inside the protein NPs. The crosslinked protein particles are in the size range from nm to several μm.

The second class is protein-drug conjugates. Here, the drugs are directly conjugated to the protein either by chemical conjugation, physical attractions, or genetic fusion. A famous example of this type of DDS is Abraxane, the first albumin DDS approved in oncology, developed by American Biosciences, Inc. In Abraxane, the hydrophobic drug paclitaxel and albumin are passed through a high-pressure jet. As a result, paclitaxel binds physically to the surface of albumin; subsequently, these paclitaxel-albumin conjugates assemble to form NPs with the size of 130 nm.[79] This DDS removes the inherent problem related to the insolubility of paclitaxel. Previously, paclitaxel had to be dissolved in polyethoxylated castor oil which causes hypersensitivity and neurotoxicity.[80]

The third class is protein containers, which are a special category of hollow proteins formed by the precise self-assembly of individual protein building blocks (subunits).[81,82] Based on their origin, protein containers can be classified as viral containers and non-viral containers.[83] Viral containers, also referred to as capsids, are the protein shell of viruses without the genetic material of the virus. In nature, viral containers function to transport and protect the DNA of the virus from the harsh environment and release the DNA in the appropriate cell environment. Examples for these viral containers are tobacco mosaic virus (TMV),[83] M13 bacteriophage,[84] MS2 bacteriophage,[85] cowpea mosaic virus (CPMV),[86] and cowpea chlorotic mottle virus (CCMV).[87] Non-viral containers are protein cages from sources other than viruses. One example is ferritin,[88] a universal protein cage that is common in nature and used for iron sequestration and mineralization. There are various shapes of protein containers (Figure 3.3). The most common one is spherical, but rods, rings, and other complex structures are also possible.[89–92] Nevertheless, all these protein containers share the same features: their robust nanostructures are formed by the assembly of protein subunits.

Protein containers can be assembled from multiple copies of identical subunits or from a limited number of different subunits.[93–95] As a hollow cage, protein containers have three distinct surfaces: the outer surface, which determines the interactions with the environment; the inner surface, which is responsible for the properties of the cavity; and the interface between subunits, which is important for the self-assembly.[89] Moreover, protein containers also have small pores/channels that are formed at the intersections of the subunits. These channels function as selective gates, which control the access to the internal cavity. Only small molecules and ions can pass through the channels.[96-98] Furthermore, some channels are hydrophobic or have high electrostatic potentials that allow only molecules with certain polarity or charges to diffuse into the cavity.[99,100] Interestingly, the protein container structure can be reversibly disassembled and reassembled by pH change[101] or using

chaotropic agents.[27] Different materials, including drug molecules, can be loaded into the protein containers either by opening the cages or via diffusion through channels.

As DDS, protein containers offer several advantages: they are highly biocompatible, robust, amenable to both chemical and bioengineering modifications, and have precisely defined structures and uniform sizes.[12]

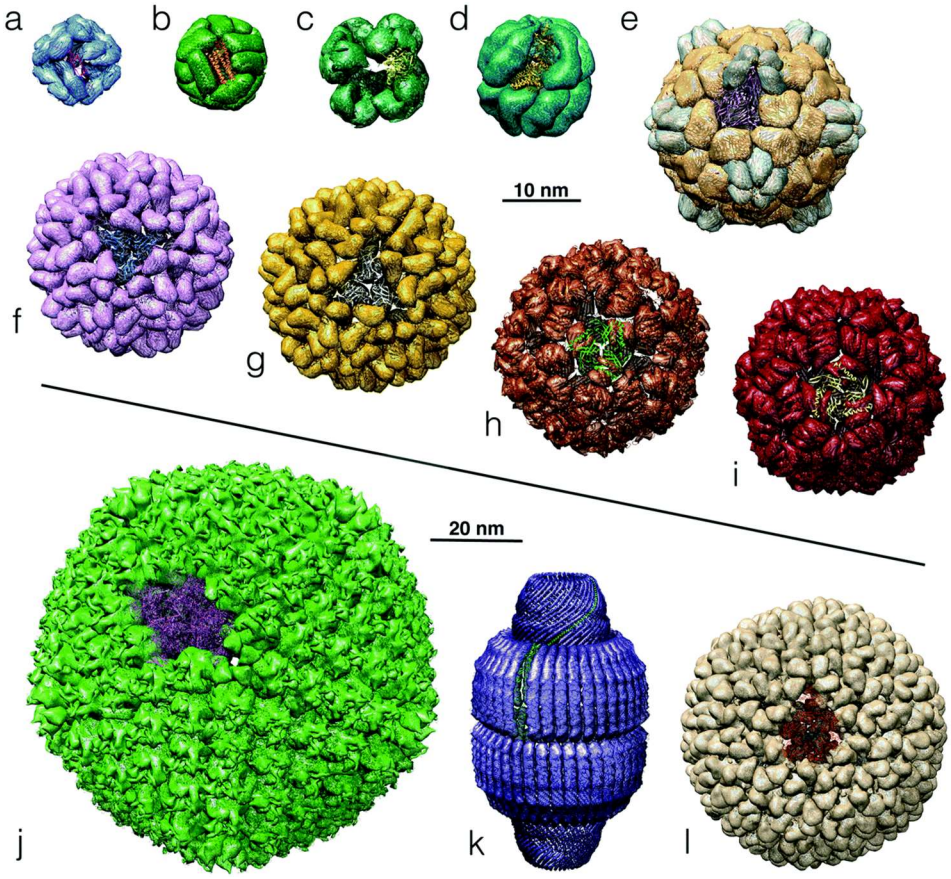

Figure 3.3 Structures of commonly used natural protein containers. A) Small heat-shock protein (HSP) (PDB: 1SHS). B) Apoferritin (PDB: 1DAT). C) Pyruvate dehydrogenase multienzyme complex (PDB: 1EAA). D) Thermosome (THS) (PDB: 1A6D). E) Cowpea mosaic virus (CPMV) (PDB: 1NY7). F) Brome mosaic virus (BMV) (PDB: 1JS9). G) Cowpea chlorotic mottle virus (CCMV) (PDB: 1CWP). H) Bacteriophage lambda (PDB: 1QBE). I) Bacteriophage MS2 (PDB: 2MS2). J) Human adenovirus (AdV) (PDB: 1VSZ). K) Vault particle (PDB: 4V60). L) Bacteriophage P22 (PDB: 2XYY). Reproduced from Ref. [83] with permission from the Centre National de la Recherche Scientifique (CNRS) and The Royal Society of Chemistry.

3.2 The ferritin containers as drug delivery vehicles

3.2.1 Structure and properties

Ferritin is a protein family that is ubiquitous in almost all kinds of organisms. Its natural function is to regulate the iron level and store iron in a bioavailable and safe form.[83] The ferritin family can be classified into three subfamilies: (1) classical or maxi-ferritin, the most common ferritin which consists of 24 subunits; (2) bacterioferritin, which also consists of 24 subunits but has a heme group covalently attached to the protein; and (3) DNA-binding protein from starved cells (Dps) or mini-ferritin, that only

consists of 12 subunits.[82,102,103] All the ferritin subfamilies share many structural similarities.[104,105] In this work, I will focus on classical ferritin, in particular the human heavy-chain ferritin (HF) and its derivatives.

The classical ferritin consists of 24 subunits, which assemble to form a protein cage with an outer diameter of 12 nm and an inner cavity of 7 – 8 nm (Figure 3.4A-B).[82] Each subunit is composed of about 180 amino acids, which form four bundles of parallel helixes and a small helix (E helix) orientated at 60° relative to the four helixes (Figure 3.4C). The ferritin cages are usually formed by a mixture of two types of subunits: the heavy-chain (H) subunits (21 kDa) and the light-chain (L) subunits (19 kDa). Both of the subunits are highly similar in structure. Therefore, they can form ferritin cages in any ratio or composition. This ratio varies in different organisms and also in different tissues, e.g. in humans, the H-chain is predominant in the heart, while the L-chain is predominant in the spleen and liver.[88] The H-chain possesses a ferroxidase-center that binds and catalyzes the oxidation of Fe^{2+} ions. The L-chain lacks this catalytic site, but it provides a favorable nucleation site to form the iron mineral crystal.[22] In this way, ferritin protects cells from the oxidative damages that may be caused by the reactive oxygen species produced by the free Fe^{2+} via the Fenton reaction.[103] Human ferritin that is composed of only the H-chains is called human heavy-chain ferritin. Moreover, the intersection of ferritin subunits forms channels/pores with the size of 4 Å, through which ions or guest molecules can enter or leave the ferritin cage. In total, there are six channels with 4-fold symmetry, which are hydrophobic (Figure 3.4A), and eight channels with 3-fold symmetry, which are hydrophilic (Figure 3.4B).[106]

The cavity inside the ferritin cages can be used to load a broad range of materials, such as small drugs,[17–20] therapeutic protein,[13] photosensitizers,[21] fluorophores,[22,23] and NPs[24] among others. There are two major strategies to perform such an encapsulation. The first strategy is by opening and closing ferritin cages in a solution containing the cargo molecules, thereby some molecules will be trapped inside the cages. Several conditions can be used to open the ferritin cages: (1) by acidic conditions (pH 2-3),[107] (2) basic conditions (pH 11-12),[14] or using (3) chaotropic agents such as urea or guanidine hydrochloride (Gua-HCl, > 6 M).[108] The reassembly of ferritin cages then can be performed by returning the solution to physiological pH (7.4) or diluting the solution to a low concentration of the chaotropic agent, e.g. to 0.5 M.

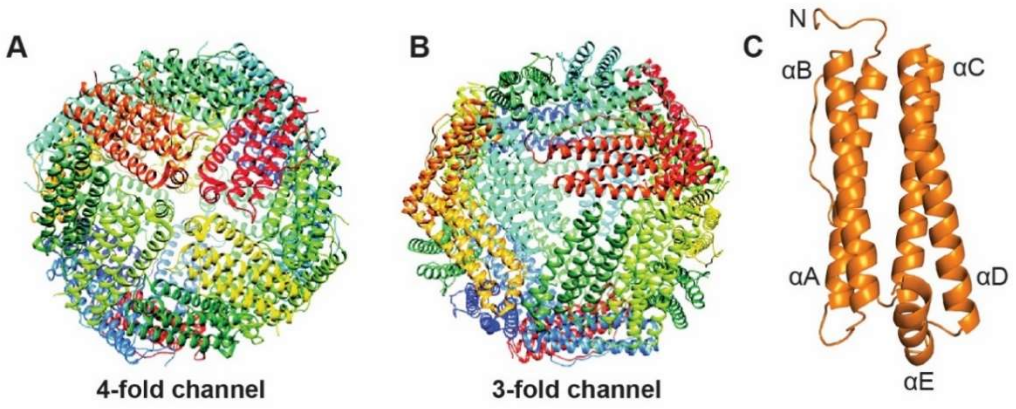

Figure 3.4 Structure of human heavy-chain ferritin. A) The four-fold channel. B) The 3-fold channel. C) A single ferritin subunit. Here, the four bundles of helixes were annotated as αA to αE, starting from the N terminus. The C terminus is located at the end of αE helix (PDB: 2FHA). Adapted from Ref. [82] with permission from the Centre National de la Recherche Scientifique (CNRS) and The Royal Society of Chemistry.

When exposed to extreme pH, either in acidic or basic conditions, ferritin cages gradually disassemble into subunits as the intramolecular forces between subunits are broken due to the conformational changes of the protein. This process is almost reversible. The reconstitution of pH back to neutral reverses the process, in which the monomers progressively form higher oligomers and finally the fully reassembled cages. Several mechanisms have been proposed to explain this reassembly process.[16,109,110]

Chaotropic agents can also be used to disassemble ferritin cages. In this case, the ferritin subunits are completely unfolded into linear, random coil polypeptide chains. Diluting or removing the chaotropic agents via dialysis or ultrafiltration will fold back and restore the ferritin cages structure. However, since this disassembly approach involves a more drastic structural changes, the reassembly process tends to give a lower yield compared to the disassembly via pH control. Nevertheless, this approach provides an alternative way to perform encapsulation, e.g. when the encapsulation by extreme pH is not applicable.

In the second strategy, the ferritin cages are not opened. Instead, the cargo molecules are loaded into the cages by diffusion through ferritin channels. There are several ways to expand ferritin channels so that larger molecules can be encapsulated, and higher loading can be reached. For example, Ma-Ham *et al*. used pH 5 to enlarge the ferritin channels and encapsulate daunomycin, an anthracycline antibiotic, with the help of poly-L-aspartic acid (PLAA).[111] Yang *et al*. exploited the high thermal stability of ferritin to encapsulate nutritional biomolecules. They showed that thermal treatment at 60 °C also expanded ferritin channels and promoted the encapsulation of rutin and epigallocatechin gallate (EGCC).[106] However, this approach may not be suitable for thermal-sensitive cargo molecules. They also reported that 2 mM Gua-HCl worked similarly to enlarge the ferritin channels. They achieved even a higher loading of rutin and EGCC using this strategy.[112]

Recently, ferritin containers have attracted considerable interest due to their unique characteristics as DDS.[13,14] In addition to its biocompatibility and biodegradability, the ferritin cage is also robust and highly stable. Ferritin was shown to withstand a broad range of pH (3 - 10)[16] and temperature (up to 80 °C for 10 min).[113] As discussed, the cages can be opened and closed reversibly for drug encapsulation purposes. Ferritin is easily produced in high purity and monodispersity. It is also amenable to various post modifications, either by chemical reactions or genetic engineering.[26] For examples, fluorophores or drugs can be attached to the surface of ferritin by chemical conjugation,[114] targeting ligands can be easily be displayed on the surface of ferritin by genetic fusion at the N-terminus,[115] or amino acid substitutions can be performed at the desired positions by site-directed mutagenesis.[24] Interestingly, HF has been known to bind with TfR-1, which is overexpressed in many types of cancer cells, thus offering an easy way to deliver drugs to cancer cells.[22,27,28] Furthermore, Bellini et al. showed that ferritin is translocated into the nucleus and this could be exploited to create a trojan-horse effect which increases the drug delivery into the nucleus.[22] All these attractive features make ferritin a promising DDS.

3.2.2 State of the art of ferritin drug delivery

3.2.2.1 Ferritin applications in cancer therapy

Many works on the application of ferritin containers as drug carriers have been reported. Most of the applications have been focused on cancer therapy.[15] Ferritin has the natural ability to sequester metal cations, and this property has been exploited for the encapsulation of drug molecules. A few of the earliest cancer drugs encapsulated in ferritin were cisplatin[116–120] and carboplatin.[120] The encapsulation of cisplatin into antibody-functionalized ferritin was shown to increase the selectivity and efficacy of treatment against melanoma cancer cells.[119] Similarly, several anti-cancer gold(III) complexes were successfully encapsulated inside ferritin and showed cytotoxic effects towards different aggressive human cancer cells, while they are less toxic for the non-cancer cells.[121,122]

The diffusion of metal cations through ferritin channels is commonly utilized to synthesize NPs inside the ferritin cage. This approach can be used as an indirect strategy to encapsulate drug molecules. Liu *et al*. prepared gold (Au) NP inside the ferritin cages by *in situ* reductions of $AuCl_4^-$ using $NaBH_4$. In the next step, the Au NPs were applied to sequester 5-Fluorouracil (5-FU), a small anti-cancer drug, which previously could not be encapsulated effectively due to rapid leaking of 5-FU from the ferritin cavity. About 45 molecules of 5-FU were encapsulated per ferritin cage, and they showed that the Au NP also enhanced the cytotoxicity effects of 5-FU towards cancer cells.[123]

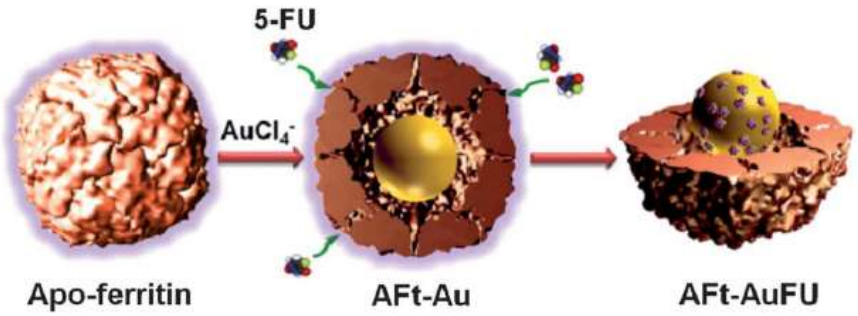

Figure 3.5 The encapsulation of 5-FU using gold NP loaded ferritin (Aft-Au). First, $AuCl_4^-$ was reduced by $NaBH_4$ inside the ferritin cavity to form a 3 nm Au NP. Subsequently, the resulting AuNPs were used to sequester the small anti-cancer drugs 5-FU, which can diffuse into the cavity through ferritin channels. Reproduced from Ref. [123] with permission from the Centre National de la Recherche Scientifique (CNRS) and The Royal Society of Chemistry.

The ability of ferritin to capture metal cations was also used to encapsulate radionuclides for imaging (radioimmunodetection) and therapy (radioimmunotherapy). Hainfeld *et al*. induced the precipitation of uranium (^{235}U) inside ferritin and functionalized the resulting ferritin NPs with Fab (antigen-binding fragment) targeting ligands. The encapsulation in ferritin reduced the immunogenicity and the toxicity of the uranium NPs in cancer radiotherapy.[124] Similarly, Lin *et al*. encapsulated yttrium (^{90}Y) and lutetium (^{177}Lu) in ferritin and modified the surface with biotin as targeting ligands. Furthermore, they used avidin-functionalized magnetic beads and a fluorescein-streptavidin probe to show the targeting ability of the resulting ferritin NPs.[124,125]

DOX represents the most extensively used anti-cancer drug encapsulated in ferritin and applied for cancer treatments. Various systems, applications, and DOX encapsulation strategies have been developed over the past 15 years. Details regarding DOX will be discussed in a separate chapter (3.2.3) because of its high importance for the present work.

Ferritin also has been reported to improve the solubility, stability, and bioavailability of poorly soluble anticancer drugs such as curcumin[126–129] and paclitaxel.[17] Moreover, Lei *et al*. encapsulated neuronal drugs, carbachol, and atropine, into ferritin and used them to target the TfR-1 positive pancreatic tumor cells. They showed that by controlling the nervous microenvironment in the tumor tissues, they were able to regulate the progression of pancreatic cancers.[19] Ferritin has also been applied for therapeutic protein delivery to tumor cells. Bonamore *et al*. encapsulated cytochrome c into Archaeglobus ferritin, which has been grafted with the TfR-1 binding motif from human ferritin to enable specific tumor targeting.[130,131] They showed that the system induced apoptosis in a myeloid leukemia cell line, which is highly resistant to transfection by conventional methods.[13,132]

Photodynamic therapy (PDT) and photothermal therapy (PTT) are two other alternatives for cancer treatment. In PDT, light is used to activate photosensitizers that have been targeted to the tumor

tissues. As a result, the photosensitizers generate reactive oxygen species that are cytotoxic and capable of killing the nearby cancer cells.[133,134] PTT is similar to PDT, but no reactive oxygen species are involved. The photosensitizers simply generate heat on light activation, which subsequently kills the targeted cells.[135,136] Photosensitizers are known for their high immunogenicity, nonbiodegradability, long-term toxicity, and poor pharmacokinetics.[101] Ferritin containers can serve as suitable carriers to deliver photosensitizing agents to cancer cells. Zhen *et al*. demonstrated successful encapsulation of $ZnF_{16}Pc$, a potent photosensitizer, into RGD- and folic acid-modified ferritin, which subsequently exhibited excellent PDT effects towards different tumor models.[21,137] The same system was also used to perform tumor endothelium-targeted PDT, which enhanced the EPR effect for the accumulation of Doxil, a clinically approved DOX-encapsulated liposome.[138] Interestingly, by encapsulating $ZnF_{16}Pc$ into ferritin modified with Fibroblast Activation Protein (FAP) targeting ligand, they were able to create a system that induced photoimmuno therapy (PIT) in cancer cells.[139] A different photosensitizer was applied by Liu *et al*., who encapsulated sinoporphyrin sodium in RGD-modified ferritin for simultaneous PDT/PTT generated by a single wavelength.[140] Furthermore, Huang *et al*. reported the encapsulation of a near infra-red dye, IR820, in ferritin, which enables simultaneous photoacoustic/fluorescence multimodal imaging and PTT. Intriguingly, the system showed 100% tumor elimination in a breast cancer model.[101]

Nucleic acid-based drugs recently have drawn much attention due to their remarkable efficacy for treating various diseases such as viral infections and cancers.[141,142] However, they are subject to rapid degradation by endogenous nucleases and have limited ability to penetrate cell membranes.[135,143] To overcome these challenges, Li *et al*. encapsulated small interfering RNA (siRNA) in ferritin and used it as a delivery vector to induce gene silencing in tumor cells.[144] Similarly, Lee *et al*. developed siRNA DDS called proteinticles by genetic engineering, in which ferritin was redesigned to display polypeptide chains on its surface. The polypeptide chains contain parts with different functionality: a cationic peptide for binding siRNA, a cancer-targeting peptide, a cell-penetrating peptide, and an enzymatic cleavage peptide for releasing the siRNA. The proteinticles complexed poly-siRNA and showed an effective gene silencing in cancer cells.[145]

Another DDS was developed by Samanipour *et al*., who integrated ferritin into a bulk hydrogel by performing a photo-crosslinking between gelatin methacryloyl and methacryloyl functionalized ferritin. The integration was shown to improve the mechanical properties of the hydrogel. Furthermore, they encapsulated fluorescein isothiocyanate (FITC) into ferritin as a model drug and then integrated it into the hydrogel. A release study at pH 2.0 confirmed the potential of the ferritin hydrogel system for drug delivery.[146]

Recently, Yao *et al*. developed a mesoporous silica nanoparticle (MSN) DDS by using ferritin as the gatekeeper. First, DOX was loaded into MSNs, and then ferritin was used to block the pores of MSNs to prevent the DOX leakage. The attachment of ferritin into the surface of MSNs was performed either by chemical crosslinking, i.e. disulfide bond formation or by hydrophobic interactions between MSNs and the 4-fold channels in ferritin. Stimuli-responsive release of DOX was achieved by the presence of glutathione (GSH) or acidic pH inside the cells. Interestingly, ferritin also provided MSNs with the TfR-1 targeting property. Both *in vitro* and *in vivo* tests showed excellent therapeutic effects of the system.[147]

3.2.2.2 Ferritin in other biomedical applications

Several works have been reported on the applications of ferritin outside tumor therapy. For example, ferritin has been used for vaccine development.[148,149] Kanekiyo et al. performed a genetic fusion of haemagglutinin protein from influenza virus to the N-terminus of *Heliobacter pylori* ferritin. As a result, three viral protein spikes emerged on each of the eight 3-fold channels. In this way, ferritin was used as a platform to display the antigen protein to induce the formation of antibodies. Immunization with these ferritin NPs increased the antibody titer production by a factor of 10 compared with the immunization with the licensed inactivated vaccine.[149]

Some groups have developed stimuli-responsive ferritin containers for DDS. Choi *et al*. performed genetic engineering to substitute the E-helixes at the 4-fold channels of ferritin with GALA, a cell-penetrating peptide. The reversible structural transformation of GALA peptides from random coil to α-helix at pH 6.0 allows reversible dis/reassembly of the ferritin cages. This switching property can be used for drug loading or release at a milder acidic condition.[150] Kang *et al*. designed a protease-sensitive DDS from *Pyrococcus furiosus* ferritin. They inserted a thrombin cleavage peptide between the D- and E-helixes and coupled fluorophore to the genetically added cysteines at the C-terminus. Furthermore, the surface of ferritin was modified with biotin targeting ligands. They showed that upon the administration of thrombin, the fluorophore attached E-helixes was released, leading to the formation of 1.8 nm holes at the 4-fold channels. This strategy may be used to trigger the release of encapsulated drugs or genetically fused therapeutic peptides at the C-terminus.[151]

Moreover, ferritin has also found many applications in bioimaging. For example, ferritin has been used to encapsulate iron oxide,[115,152,153] gadolinium complex,[154] gadolinium oxide-hydroxide NPs,[155] and manganese oxide-hydroxide NPs[156] for the application as magnetic resonance imaging (MRI) contrast agents. Furthermore, ferritin has been conjugated with fluorophores for various applications in optical imaging: Cy5.5,[26,157] ZW800,[21,158] Alexa Fluor 750,[159] green fluorescent protein (GFP).[157]

3.2.3 The encapsulation of doxorubicin in ferritin

DOX is a clinical anticancer drug widely used for the treatment of various solid tumors.[160] However, its application is limited by severe side effects, such as cardiotoxicity and the development of drug-resistant tumors.[161,162] Moreover, free DOX is subjected to rapid metabolic degradation in the systemic circulation.[163] To reduce the toxicity and increase the efficacy by selective delivery to cancer cells, DOX has been encapsulated in various ferritin-based DDS.

The first encapsulation of DOX in ferritin was reported by Kilic *et al*.[20,164] Horse-spleen ferritin was disassembled in pH 2.5 in the presence of DOX, and then slowly reassembled by gradual pH changes from 4.0 to 7.4 using dialysis. They were able to encapsulate 28 DOX molecules per ferritin cage, but the overall yield of DOX-ferritin was low due to the severe precipitation of DOX and ferritin at the neutral pH.[20]

Bellini *et al*. encapsulated DOX in HF by a very similar approach: disassembly in pH 2.0 followed by immediate reassembly at pH 7.5. Furthermore, they used a low concentration of DOX and ferritin, as well as a certain ionic strength, to circumvent the aggregation of DOX and ferritin. The encapsulation resulted in a very similar loading: 28.3 DOX/cage. Interestingly, they also showed that DOX-ferritin caused the ”Trojan horse” effect in cancer cells: the damages caused by DOX inside the nucleus trigger the cells to invite more ferritin into the cells to fix the damages. Importantly, this brought even more DOX into the cells.[22]

The encapsulation of DOX was improved by Liang *et al*. They disassembled HF in 8 M urea containing DOX, and then slowly reassembled the ferritin cages at 4 °C by stepwise dialysis with a gradual decrease of the urea concentration in the presence of the same concentration of DOX solution. With this technique, they encapsulated 33 DOX molecules per ferritin cage.[27] However, this approach wastes a lot of DOX in the process.

Zhen *et al*. utilized ferritin’s natural tendency to sequester metal cations to increase the loading efficiency. They showed that pre-complexation of DOX with transition metal ions such as copper (II) could significantly improve the DOX loading into ferritin, even without opening the ferritin cages. The DOX loading was 73.49 % (w/w), while the encapsulation of free DOX only resulted in 14.14 % (w/w) loading.[158] Despite setting a new direction in ferritin drug encapsulation, this strategy also raised concerns about its biocompatibility as it introduces heavy metal ions to the body.[164] However, the authors argued that the toxicity of Cu(II) usually occurs when the copper ions exist in their free form and not as complexes.[165]

To improve drug loading, Ahn *et al*. developed a new ferritin variant with partially enlarged 4-fold channels called nicked-ferritin. For this, first, they truncated the E-helixes at the 4-fold channels of ferritin, which leads to the formation of a ferritin variant with the fully enlarged 4-fold channels (F160).

However, F160 was not stable enough for drug encapsulation. Therefore, they incorporated the subunits of F160 into partially disassembled HF to form the stable nicked-HF. Following the previous approach, they pre-complexed three kinds of cancer drugs with Fe (II) to effectively load them into the nicked-HF. They showed that this strategy was able to stably internalize a high dose of drug molecules just by simple incubation. About 121, 26, and 440 molecules of DOX, curcumin, and quercetin were successfully encapsulated in nicked ferritin, respectively.[25]

One major problem associated with drug encapsulation in ferritin is the low yield of ferritin recovery after the encapsulation due to protein aggregation. To address this problem, Wang *et al*. proposed drug encapsulation by applying high hydrostatic pressure. Encapsulation was achieved by incubating ferritin and DOX at pH 5.5 and 500 MPa for 16 h. Moreover, the addition of 20 mM arginine as an additive increased the ferritin recovery almost to 100%. They also found that stepwise decompression and post-incubation at neutral pH in the presence of DOX increased the loading ratio further to 32 molecules per ferritin cage. The benefits of this encapsulation strategy are high recovery yield and reduced consumption of DOX compared to DOX encapsulation via urea disassembly described above.[166] However, this approach is impractical as it requires sophisticated experimental settings.

Another challenge for the application of ferritin as DDS is the short plasma half-life after systemic administration (~1 h) due to proteolytic degradation or liver clearance. To overcome this problem, Falvo *et al*. modified the surface of ferritin with polypeptide chains rich in proline, serine, and alanine (PSA) by genetic fusion at the N-terminus. This construct not only prolonged the plasma half-life of ferritin to 15 h but also improved the drug loading. DOX encapsulation into this ferritin variant via acidic dis/reassembly approach produced a loading of 90 DOX/cage. The high loading was attributed to the increased stability of ferritin subunits during the reassembly process. Moreover, the PSA polypeptides might prevent drug leakage through ferritin channels that could occur after the reassociation of ferritin subunits.[34] Despite its beneficial features, this external surface modification may result in the loss of TfR-1 targeting property, and this strategy also raised concern about its biosafety and biocompatibility during in vivo application.[164]

An ideal DDS should carry the drugs tightly and release them only at the required site. One way to prevent premature drug release is using chemical conjugation. Huang *et al*. functionalized the surface of ferritin with PEG chains to overcome the biological barrier in airway mucus and tumor tissue. Subsequently, they covalently conjugated acid-cleavable DOX to the surface of ferritin and about 88 DOX molecules were attached. This design ensured that DOX molecules were released only after cellular internalization. Interestingly, despite of having so many surface modifications that might interfere with the TfR-1 mediated endocytosis, this construct exhibited good performance in lung cancer treatment.[114]

3.3 Stimuli-responsive microgel systems

Microgels are colloidal systems that consist of crosslinked polymer networks and are swollen by a solvent (Figure 3.6). In the swollen state, they have open and porous structures with a fuzzy surface, therefore they are soft, deformable, and penetrable.[167] Still, they can maintain their structural integrity due to the presence of crosslinking. As stimuli-responsive materials, various conditions, e.g. a change in temperature (Figure 3.6), can be applied to trigger the collapse of microgels. In the collapsed state, the microgel structures shrink and resemble hard colloids. Microgels have the size ranging from 50 nm to 5 µm.[168] Therefore, depending on the size, sometimes the term nanogels is more precise instead of microgels. Nevertheless, in this work, I will use microgels as the general term. The color of microgel dispersions depends on the sizes and the degree of swelling. Microgels with small sizes or collapsed microgels are milky white (opaque), while the large sizes and highly swollen microgels are more transparent because their refractive index is closer to water.[169]

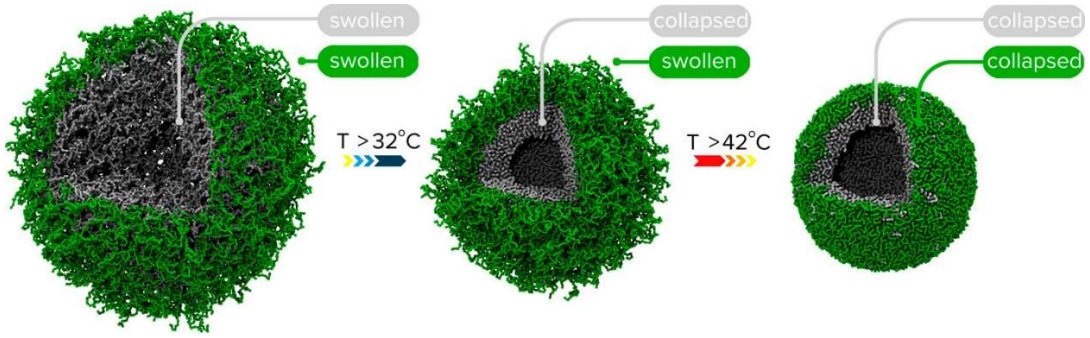

Figure 3.6 An example of microgel systems. The collapse of a hollow core-shell-shell microgel induced by heating. Adapted with permission from Ref. [170]. Copyright 2016 Macmillan Publishers Ltd.

3.3.1 The synthesis of microgels: precipitation polymerization

There are several synthesis methods to prepare microgels with tailored properties, but the most important method for the synthesis of thermo-responsive microgels is precipitation polymerization.[37] This method is facile, versatile, and flexible. The synthesis is performed at moderate temperatures, usually around 50 – 80 °C, and microgels with different sizes are easily produced with high monodispersity. A wide variety of monomers are available to equip microgels with different properties and functionalities.

Several components are necessary for precipitation polymerization: monomers, crosslinkers, initiators, and surfactants. The requirement for the main monomers is that: the material must have low solubility at high temperature, which will enable the precipitation of the polymers during synthesis. A broad range of main monomers can be selected from the family of acrylamide or N-vinyllactam monomers. The typical representatives of the two families are NIPAM[171] and N-vinylcaprolactam (VCL),[172]

respectively (Figure 3.7). Furthermore, co-monomers can be added to provide microgels with certain properties or to add certain functional groups to the microgels. For example, by adding an acid or basic co-monomers, the microgels become pH-responsive. They swell/collapse depending on the pH of the solvent.

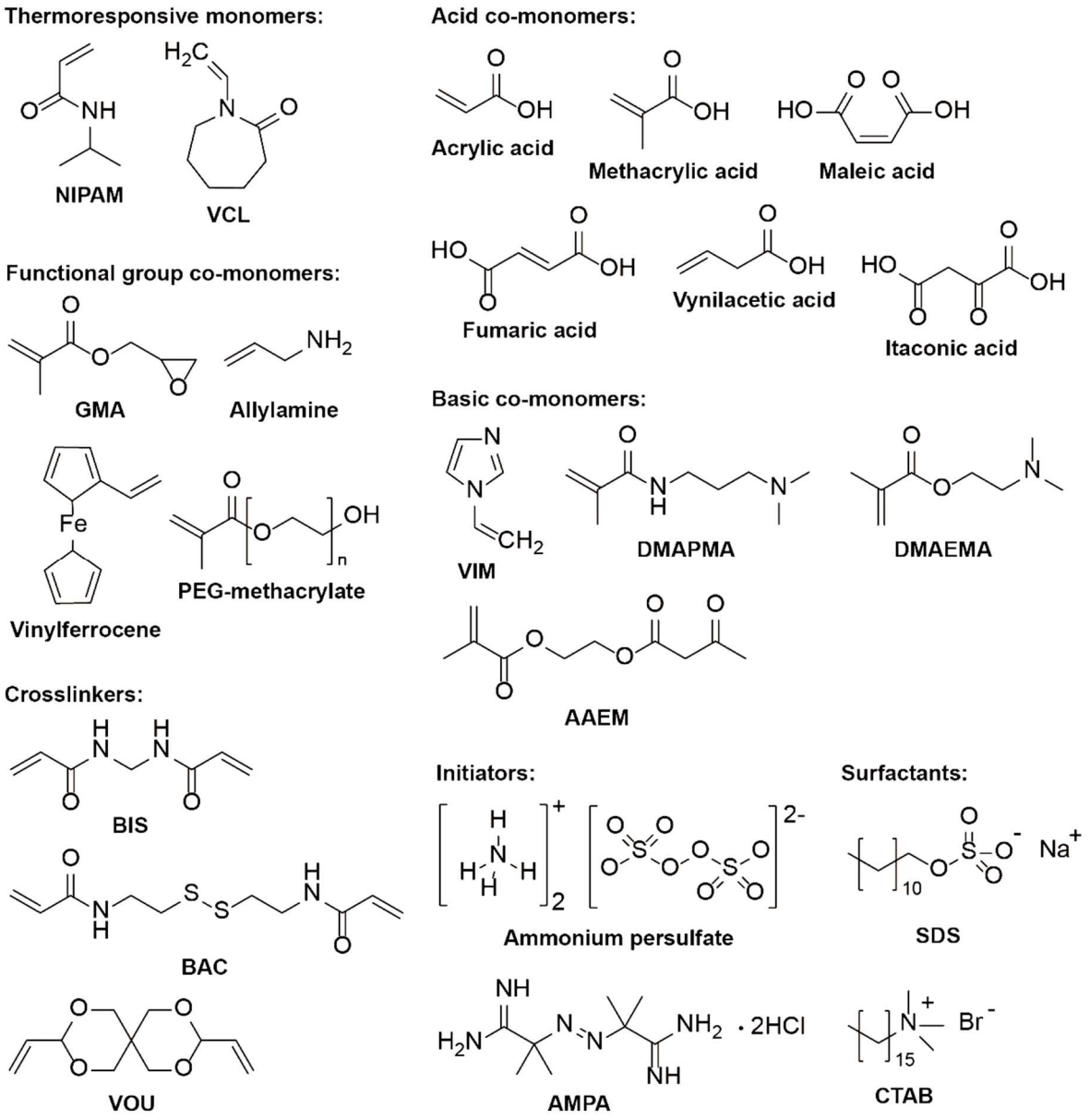

Figure 3.7 Various chemicals for precipitation polymerization. The components for precipitation polymerization are the main monomers, co-monomers, crosslinkers, initiators, and surfactants.

Some examples of acid monomers (Figure 3.7) are acrylic acid (AA), methacrylic acid (MAA), maleic acid (MA), fumaric acid (FA), vinyl acetic acid (VA),[173] and itaconic acid (IA);[174] examples for basic monomers (Figure 3.7) are 1-vinyl imidazole (VIM),[48] N-[3-(Dimethylamino)propyl]methacrylamide (DMAPMA),[175] acetoacetoxyethyl methacrylate (AAEM),[176] and dimethylaminoethyl methacrylate (DMAEMA).[177] The microgels containing these co-monomers are also referred to as polyelectolyte

microgels. Upon ionization in basic condition, microgels with the acid monomers become negatively charged. Likewise, in acidic conditions, microgels with the basic monomers become positively charged. Due to the presence of similar charges, these functional groups repel each other, therefore the microgels swell and increase in size. On the other hand, when these functional groups are neutralized, no repulsion is present, therefore the microgels shrink and become smaller. These interactions are the reason behind the pH responsiveness of the microgels. The addition of salt into microgel dispersion screens the electrostatic repulsion, thereby the microgels also shrink with the addition of salt.

Co-polymerization is also a suitable strategy to add other functional groups for specific purposes or for further post modifications of the microgels. For example, glycidyl methacrylate (GMA) was used to add epoxy groups into the microgels, which further can react with amine[178] or thiol[179] groups. Allylamine was used to add primary amine groups into the microgels for the subsequent coupling reaction with the carboxylic group of spyropyrane, which in turn provided the microgels with photo-sensitive properties.[180] Vinyl ferrocene was copolymerized to add redox-responsive properties into the microgels.[181] PEG-methacrylate was incorporated to increase the colloidal stability of microgels.[180]

The second component for the precipitation polymerization reactions is the crosslinker. Crosslinkers are also monomers, but their main function is to form the polymer networks by connecting one polymer chain to others. The crosslinkers keep the structural integrity of the microgels and prevent microgels from being completely dissolved by the solvent. One of the most common crosslinkers used in the microgel synthesis is N,N'-Methylenebis(acrylamide) (BIS).[182,183] Some crosslinkers also contain cleavable bonds that can be used to prepare degradable microgels. For example, bisacryloylcystamine (BAC)[184] has a disulfide bond that can be cleaved by glutathione inside the cells, or 3,9-Divinyl-2,4,8,10-tetra-oxaspiro[5.5]undecane (VOU) which is cleavable in acidic conditions (pH < 5).[185,186] The crosslinking can also be done with non-covalent interactions: Here, the crosslinking originates from hydrogen bonds,[187] electrostatic interactions,[169] supramolecular interactions,[188] or polymer chains entanglement.[189]

The third component for the microgel synthesis is the initiator. The initiator is mainly used to produce the free radicals required to start polymerization reactions. Some of the commonly used initiators are ammonium persulfate (APS) or potassium persulfate (KPS) and 2,2'-Azobis(2-methylpropionamidine) dihydrochloride (AMPA or V50). These initiators undergo thermal decomposition at the typical reaction temperatures (70° - 80 °C) to produce the free radicals. At lower temperatures, the production of free radicals can also be initiated by other strategies. For example, persulfate initiators can be initiated, even at room temperature, by redox reaction with tetraethylmethylendiamine (TEMED); or AMPA can be initiated by UV exposure (365 nm).[190] Furthermore, as these initiators produce ionic radicals at which the polymer chains grow, their charges are incorporated into the microgels and

contribute to the stability of microgels. For this reason, negatively charged initiators like APS or KPS are more suitable for the synthesis of microgels with negatively charged monomers. Similarly, positively charged initiators such as AMPA are more suitable for the synthesis of microgels involving positively charged monomers. Synthesis using the oppositely charged initiators and monomers is prone to aggregation and precipitation.

The fourth component for the synthesis, surfactant, can be considered optional. It is used to increase the stability of the microgels and also to reduce the size of microgels. Sodium dodecyl sulfate (SDS) is the typical example of a negatively charged surfactant, while cetyltrimethylammonium bromide (CTAB) is the example of a positively charged surfactant. Non-ionic surfactants such as poly(vinyl alcohol) have also been reported for the synthesis of microgels.[191] A higher concentration of surfactant leads to even smaller microgels. Another way to reduce the size of microgels is by increasing the reaction temperature.[192,193] On the other hand, if microgels with larger sizes are desired, lower temperatures can be applied or sodium chloride can be added.[194] However, the polydispersity usually increases with the sizes of microgels. Still *et al*. overcame this problem by semi-batch precipitation polymerization. As the microgel sizes increase linearly with reaction time, the size can be adjusted simply by adjusting the reaction time.[183]

In the typical precipitation polymerization, the reaction is started by the initiation step, in which the initiators are thermally decomposed to form the free radicals (Figure 3.8). For this, the reaction mixture must be heated (70° - 80 °C) and degassed with nitrogen, because the presence of oxygen in the reaction mixture inhibits the free radical formation. This step is then followed by propagation, in which the free radicals react with the available monomers to form oligomers. As the length of the oligomers increases, their solubility decreases. After reaching a critical length, the oligomers become insoluble and form the unstable primary particles (precursors). These precursors then coagulate together to form the stable primary particles. This nucleation process occurs simultaneously and rapidly (< 4 min). The next step is the growth of the particles. Here, the particles grow through three different processes: (1) the monomers react directly with the particles; (2) or oligomers are captured by the particles via adsorption or crosslinking; (3) primary particles aggregate with the growing particles. This growing process reaches a plateau in less than 10 min. This is the final step, termination, in which the reaction stops. The narrow size distribution of the microgels formed by precipitation polymerization suggests that the number of the growing nuclei is constant throughout the reaction.[195]

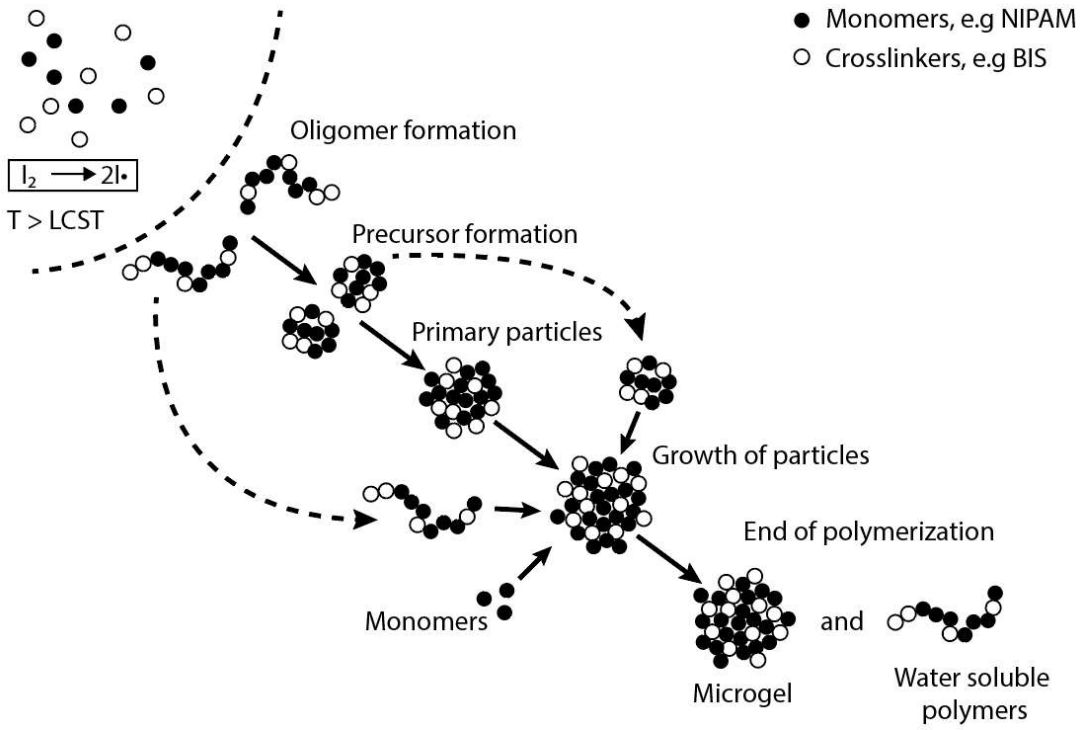

Figure 3.8 Precipitation polymerization reaction mechanism. There are four steps in the reaction mechanism: initiation, propagation, growth of the particles, and termination. Redrawn from Ref. [195], Chapter 6, Figure 16.

Microgels with more complex architectures, such as core-shell microgels or hollow microgels, have also been reported. Core-shell microgels are synthesized by seed-and-feed polymerization technique.[196] This technique has two steps. First, the core microgels are synthesized by precipitation polymerization. The resulting core microgels then are used as seeds in the second round of precipitation polymerization for the formation of the shell. Various polyelectrolyte microgel systems have been prepared by this technique, e.g. charged-core neutral-shell microgels or neutral-core charged-shell microgels.[197–200] Hollow microgels are prepared by using silica NPs as seeds during microgel synthesis. Subsequently, the silica cores are dissolved completely by sodium hydroxide solution to produce hollow microgels.[201]

In addition to precipitation polymerization, various synthesis methods are also available for the preparation of microgels: emulsion polymerization,[202] inverse emulsion polymerization,[203] microfluidic polymerization,[204] photolithography,[205] and self-assembly or crosslinking of prepolymers.[206]

3.3.2 Protein encapsulation in microgels

In drug delivery, microgels have been used to deliver small organic molecules,[207–209] siRNA,[62,210,211] DNA,[203] peptides,[212,213] and protein therapeutics.[214] Recently, there is a growing interest in the encapsulation of protein inside microgels, as the polymeric network of microgels offers potential

protection against unfavorable environments such as degradation by protease or clearance by the immune system. Therefore, such a microgel system can increase the protein bioavailability in the body.[30] Moreover, it also has been reported that the microgel environment can also enhance protein activity.[215]

Several approaches have been applied to integrate protein into microgel systems. In general, protein can be loaded during microgel synthesis or after the synthesis through covalent bonding or non-covalent interactions. For example, Garcia *et al*. employed microfluidics to synthesize protease degradable microgels. Vascular endothelial growth factor (VEGF) was encapsulated by crosslinking maleimeide-4-arm star-PEG with dithiol-crosslinkers and protease cleavable peptides.[214] Microfluidics allows for an efficient protein encapsulation, but the resulting microgels are in the µm range. As µm size microgels are not likely to be taken up by cells, thus it is not favorable if the protein release is expected to occur after the microgels are internalized by cells.

Some groups used the crosslinking of reactive prepolymers to encapsulate protein inside microgels. For example, Peng *et al*. synthesized N-hydroxysuccinimide (NHS) functionalized poly(N-vinylpyrrolidone) prepolymer by reversible addition-fragmentation chain-transfer (RAFT) polymerization and subsequently crosslinked it with GFP and cellulase in a water in oil emulsion to form catalytically active microgels.[216] Similarly, Engel *et al*. synthesized polyglycidol reactive polymers to physically entrap *Candida Antarctica* lipase B (CaLB) in a microgel after photo-polymerization with UV light in an oil in water mini emulsion.[217] While these approaches are beneficial for proteins as they avoid high temperatures, the preparation of reactive copolymers is extensive and laborious. The syntheses also involve organic solvents which may be difficult to remove, therefore potentially imposing toxicity to the cells.

Murthy *et al*. encapsulated an antigen protein, ovalbumin, into acid-degradable microgels by inverse emulsion polymerization.[218,219] In this technique, monomers, acid-cleavable crosslinkers, ovalbumin, and initiators were dissolved in an aqueous phase, while water in oil surfactant was dissolved in an organic solvent. Both phases were degassed, mixed, sonicated, and then the polymerization reaction was initiated by the addition of TEMED. They showed successful encapsulation and release of ovalbumin in an acidic condition (pH 5). Furthermore, *in vitro* test demonstrated that the antigen-presenting-cells which phagocytosed the microgels were able to activate ovalbumin-specific cytotoxic T lymphocytes. Therefore, they showed that the system has the potential for the delivery of protein-based vaccines.

Precipitation polymerization represents the easiest way for the synthesis of monodisperse microgels. However, the harsh conditions involved during the synthesis are detrimental to most proteins, hence the integration of protein is usually performed post-synthesis. To facilitate the uptake, microgels are

co-polymerized with ionizable groups (acid/base) to enable protein integration by electrostatic interactions. The subsequent protein release can be triggered by pH change or increasing ionic strength. For example, Welsch *et al*. showed that core-shell microgels, which have neutral polystyrene in the core and negatively charge P(NIPAM-co-AA) in the shell, could take up the positively charged lysozyme.[215] Furthermore, Xu *et al*. demonstrated the uptake and release of cytochrome c from polyampholyte microgels with different distribution of ionic groups.[40] Despite very promising results, these approaches are susceptible to protein leakage, which is a common problem found in carrier systems that rely on non-covalent interactions.

3.3.3 Degradable microgel systems

As mentioned in the earlier section, cleavable crosslinkers can be introduced into the microgel system to produce degradable microgels. Several cleavable crosslinkers have been successfully applied in microgel synthesis: acid-cleavable, redox-cleavable, enzyme-cleavable, and photo-cleavable crosslinkers, among others. Extensive reviews concerning these stimuli-responsive systems are available in the literature.[38,220] Here, some of the works will be highlighted to give a brief description of the systems.

In biological systems, pH gradients sometimes present and can be used to trigger the release of cargo molecules from microgels. For example, the pH value in the normal tissue is 7.4, while the pH in the tumor or inflammatory tissues is shifted towards acidic pH (6.5 – 7.0). If the microgels are internalized by cells, the pH drops to 6.0 in the early endosome, 5.0 - 6.0 in the late endosome, and 4.0 – 5.0 inside the lysosome.[185,221] Various crosslinkers are cleavable by these pH values, e.g. acetal or ketal cross-linkers, esters crosslinkers, hydrazone crosslinkers, etc.

The work by Murthy *et al*. that has been discussed in the previous section is an example of microgels prepared by an acetal crosslinker. They developed benzaldehyde acetal crosslinkers to allow rapid hydrolysis of microgels at pH 5.0 with a half-time of 5.5 min.[218,219] Another example is the work by Sunasse *et al*. They developed degradable cationic nanogels for effective gene delivery by using a ketal crosslinker (2,2-dimethacroyloxy-1-ethoxypropane). They showed that the nanogels are degraded inside the cells, releasing the complexed DNA, which then leads to the gene expression.[222]

Microgels containing hydrazone crosslinkers have also been reported. Hoare *et al*. developed degradable microgels by the self-assembly of P(NIPAM) hydrazide and P(NIPAM) aldehyde oligomers, which formed the hydrazone bonds. Interestingly, the dynamic nature of hydrazone bonds allows the formation of homogeneously crosslinked internal structures.[223] Agrawal *et al*. performed precipitation polymerization using diacetone acrylamide (DAAM) as the main monomers, dimethyl itaconate (IADME) as co-monomers to introduce negatively charged groups to the microgels, and

adipic acid dihydrazide as crosslinkers. The crosslinkers reacted with the ketone group from DAAM to form hydrazone bonds. They showed that the resulting P(VCL-co-IADME) microgels were able to effectively encapsulate DOX, and a rapid release of DOX was possible at low pH. Furthermore, the cytotoxicity tests showed an effective anti-tumor activity of DOX-microgels against HeLa cells.[208]

In addition to pH gradients, redox gradients are also present between the extracellular fluid and the intracellular environment. Glutathione (GSH), a biological reducing agent, exists in the micromolar range (~ 10 µM) in the bloodstream, while present in the millimolar range inside cytosol (~1 - 11 mM).[224,225] Moreover, the GSH level inside cancer cells is even higher than in the normal cells.[226,227] This redox gradient can be used to cleave disulfide-based crosslinkers to release cargo molecules once the microgels are internalized by cells. Various microgels systems have also been prepared by using disulfide crosslinkers.[228–231]

As an alternative strategy, degradable microgels can also be prepared using biodegradable materials, such as hyaluronic acid (HA). The benefit of this approach is that the degradation can occur on the whole microgels and does not rely only on the scission of degradable crosslinkers. Zhu *et al*. recently reported self-degradable HA nanogels for systemic delivery of anti-cancer proteins. The system is composed of deactivated hyaluronidase (HAase, an enzyme to degrade hyaluronic acid) and DNAse I (anti-cancer protein) encapsulated in HA polymer matrix. Cholesteryl moieties were grafted on the HA oligomers to enable the crosslinking of the oligomer chains for the formation of the nanogels. In the tumor microenvironment, the mildly acidic condition reactivated the HAase, which swelled the microgels and released the HAase. As HA is also the major constituent of tumor extracellular matrix, its degradation by the released HAase improved the permeation of nanogels into the tumor tissues. Inside the cells, HAase was fully reactivated. It degraded the nanogels completely and release DNase I to the nucleus to cause cancer cell death.[232]

In this chapter, the general knowledge and the state of the art of ferritin as a DDS has been discussed thoroughly. Although some promising systems have been developed to increase the bioavailability of ferritin containers in the systemic circulation, the stimuli-responsive microgel systems have not been explored for this purpose. The integration of protein containers into the microgel system via electrostatic interactions is a promising way to realize this objective.

4 Results and discussion

This chapter is divided into two major parts. The first part deals with the integration of protein containers into polyelectrolyte microgels (Chapter 4.1). Initially, ferritin was labeled with fluorophores and NPs to enable tracking of the integration and release of ferritin from microgels (Chapter 4.1.1). Subsequently, the labeled ferritin was integrated into various microgel systems to find the suitable system for drug delivery application (Chapter 4.1.2). Having established the integration of ferritin into microgel systems, the ferritin release was studied in an acidic environment (Chapter 4.1.3). Finally, a stability test was performed to investigate the ability of microgels to protect ferritin against degradation by protease (Chapter 4.1.4).

In the second part, the ferritin-microgel system was applied for drug delivery and release (Chapter 4.2). For this, DOX was encapsulated into different variants of ferritin (Chapter 4.2.1). Afterward, the DOX-ferritin variants were integrated into microgels using the protocol established in the first part of this chapter, and their DOX release properties were investigated (Chapter 4.2.2). Finally, the cytotoxicity of DOX-Ferritin variants was determined in cell experiments (Chapter 4.2.3).

4.1 The integration and release of ferritin containers from polyelectrolyte microgels

4.1.1 Ferritin labeling by fluorophores and nanoparticles

To be able to monitor the integration and release of ferritin from microgels, the ferritin needs to be labeled by fluorophores or NPs. For example, with fluorophores labeling, ferritin can be tracked by fluorescence microscopy or quantified by UV/Vis. Moreover, the encapsulation of fluorophores may serve as the basis for understanding the encapsulation of small organic molecules in ferritin. On the other hand, with NPs labeling, the presence of ferritin inside the microgels can be observed by TEM. In the future, NPs loaded ferritin can also be used for other potential microgel applications, e.g. as an MRI contrast agent for tumor imaging[233] or for generating heat[234] to trigger the stimuli responsiveness of microgels.

4.1.1.1 Fluorophore encapsulation in ferritin

Ferritin labeling with dyes or fluorophores has been discussed in the literature.[22,23,26,29,101,127,235–237] In principle, the labeling can be performed either by encapsulation[22,23,101,127,235–237] or by chemical conjugation to amino acid residues located on the outer surface of ferritin.[26,29] The latter approach, however, is non-specific and potentially unfavorable for ferritin binding to the TfR-1 as it alters the surface of ferritin. For this reason, here the ferritin labeling was performed by encapsulation.

To systematically study the encapsulation of fluorophores in ferritin, fluorophores with different charges were encapsulated into two variants of supercharged ferritin: $Ftn^{(pos)}$ and $Ftn^{(neg)}$ (Figure 4.1A-B). Three kinds of fluorophores were used: fluorescein (Fscn), rhodamine B (Rho B), and rhodamine 6G (Rho 6G). For $Ftn^{(neg)}$, the encapsulation was performed via an acidic dis/reassembly approach (Figure 4.1C), while for $Ftn^{(pos)}$ the encapsulation was conducted via diffusion through channels. After the encapsulation, ferritin was purified from the excess fluorophore molecules by size exclusion chromatography (SEC, Figure 4.1D).

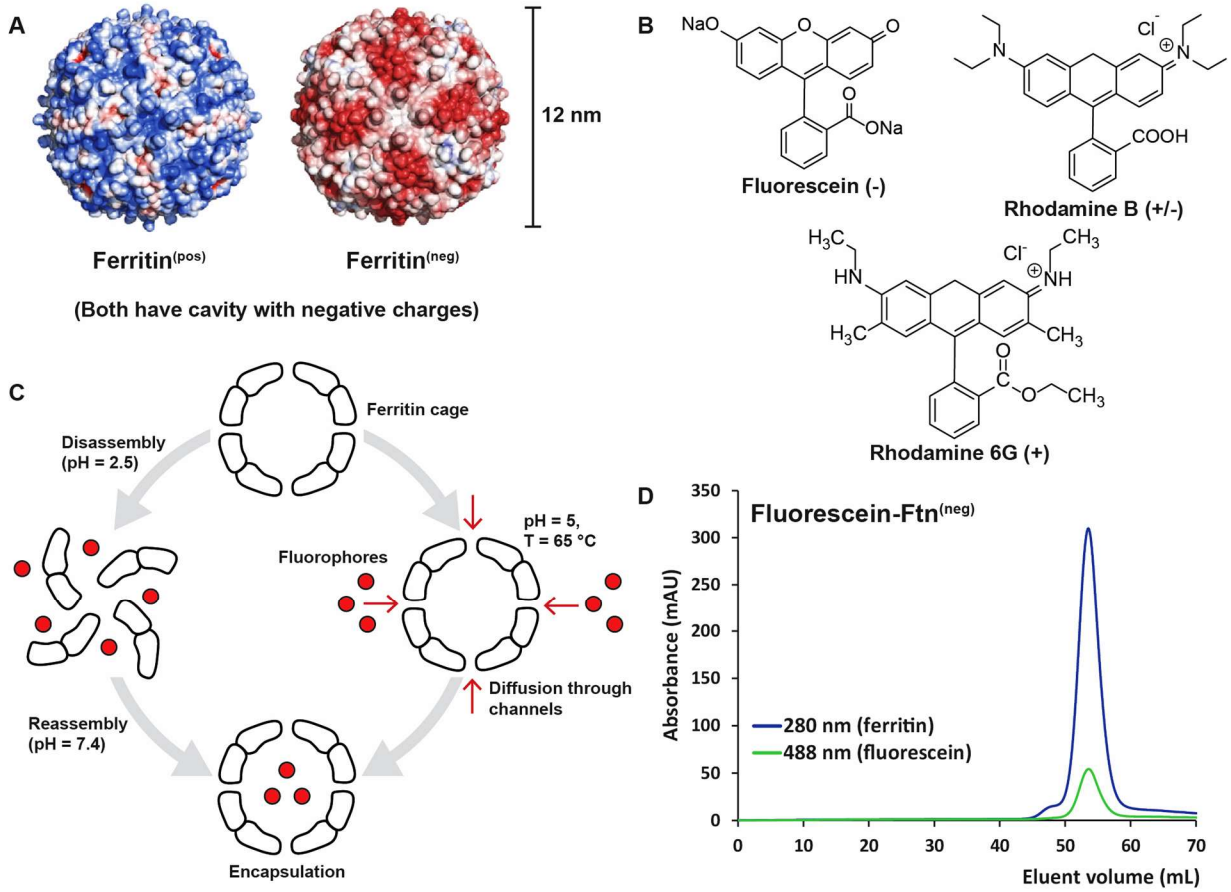

Figure 4.1 The encapsulation of fluorophores in supercharged ferritin variants. A) Electrostatic potential of redesigned ferritin containers: positively charged ferritin and negatively charged ferritin (blue, +5 kT/e; red, −5 kT/e). B) Fluorophores with different charges used for the encapsulation. C) Encapsulation strategies. D) Purification of Fluorescein-$Ftn^{(neg)}$ by SEC.

Two key factors determine the loading of fluorophore in ferritin. The first is the concentration of the fluorophore. In general, higher concentration leads to higher loading (Figure 4.2). However, at a certain point, high concentrations of fluorophore start to disturb the reassembly process (Figure 4.2C). A similar observation was also reported by Webb *et al.*[26] Another issue to consider is that each fluorophore has different solubility, and this limits the maximum concentration of fluorophore that can be applied in the encapsulation. For this reason, neutral dyes were not used for labeling the ferritin.

Neutral dyes, such as curcumin, usually have low solubility.[236] Therefore, it was presumed that the encapsulation will not result in a high loading.

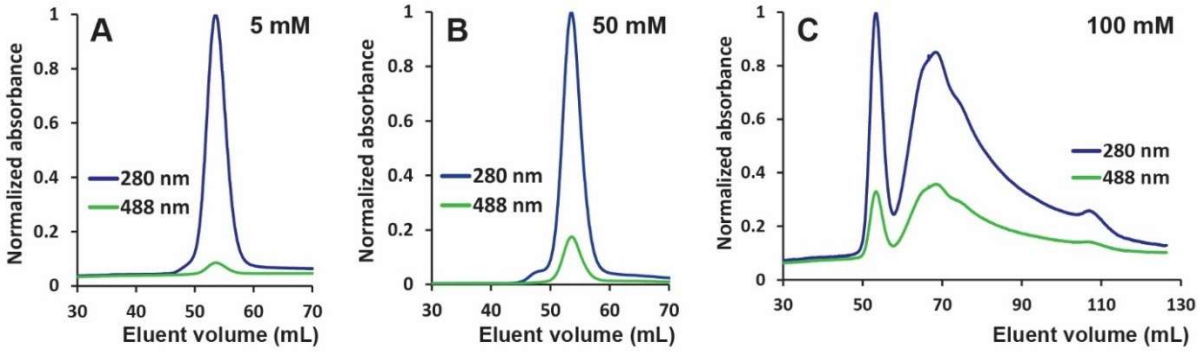

Figure 4.2 The effect of increasing fluorophore concentration. These are SEC chromatograms of Fscn-Ftn$^{(neg)}$, obtained from the encapsulation of: A) 5 mM, B) 50 mM, and C) 100 mM fluorescein. All the chromatograms were normalized against the maximum ferritin peak. The blue line is the protein signal (280 nm), while the green line is the fluorescein signal (488 nm).

The second key factor that determines the encapsulation into the ferritin container is the charge of the fluorophore. As a hollow cage, ferritin containers have an outer surface and an inner surface. The outer surface of Ftn$^{(pos)}$ is positively charged, while the outer surface of Ftn$^{(neg)}$ is negatively charged. However, both have an identical inner surface, which is negatively charged. If fluorophore and the outer surface of ferritin have the same kind of charges, they will repel each other. This is not beneficial for obtaining high loading, but helpful for the protein stability during encapsulation: It produces ferritin with encapsulated fluorophores in high yield. Next, if fluorophore and the inner surface of ferritin having the opposite charges, they will attract each other, thereby producing high loading. Table 4.1 shows that the encapsulation of Rho 6G (+) into Ftn$^{(pos)}$ and Fscn (-) into Ftn$^{(neg)}$ both produced high yields. Moreover, the loading of Rho 6G (+) in Ftn$^{(pos)}$ was twice the loading of Fscn (-) in Ftn$^{(neg)}$, although I used 0.3x lower concentration of fluorophore. As both Ftn$^{(pos)}$ and Ftn$^{(neg)}$ have exactly the same cavity, these results clearly indicate that the positively charged fluorophore has a higher affinity towards the negatively charged ferritin cavity, thereby it produced higher loading. Finally, if fluorophore and the outer surface of ferritin having the opposite charges, they will attract each other and cause precipitation, therefore the yield decreases. Table 4.1 shows that the yield dropped drastically when Rho 6G (+) was encapsulated into Ftn$^{(neg)}$. Furthermore, the precipitation limits the applicable fluorophore concentration. 0.325 mM was the highest concentration of Rho 6G (+) that still produced a reasonable yield. Higher concentrations of Rho 6G (+) caused heavier precipitation.

Table 4.1 The loading and yield of different fluorophores encapsulation

Fluorophore (and its charge)	Ferritin variants	Used fluorophore concentration (mM)*	Loading (molecules/cage)	Yield (%)	Encapsulation strategy
Fluorescein (-)	$Ftn^{(neg)}$	50	1	78.8	Acidic dis/reassembly
Rhodamine B (±)	$Ftn^{(neg)}$	20	0.5	33.4	Acidic dis/reassembly
Rhodamine 6G (+)	$Ftn^{(neg)}$	0.325	0.5	40.8	Acidic dis/reassembly
Rhodamine 6G (+)	$Ftn^{(pos)}$	15	2	73.0	Diffusion through channels

*The highest concentration of fluorophore that still gives a reasonable yield. Higher concentration caused worse precipitation.

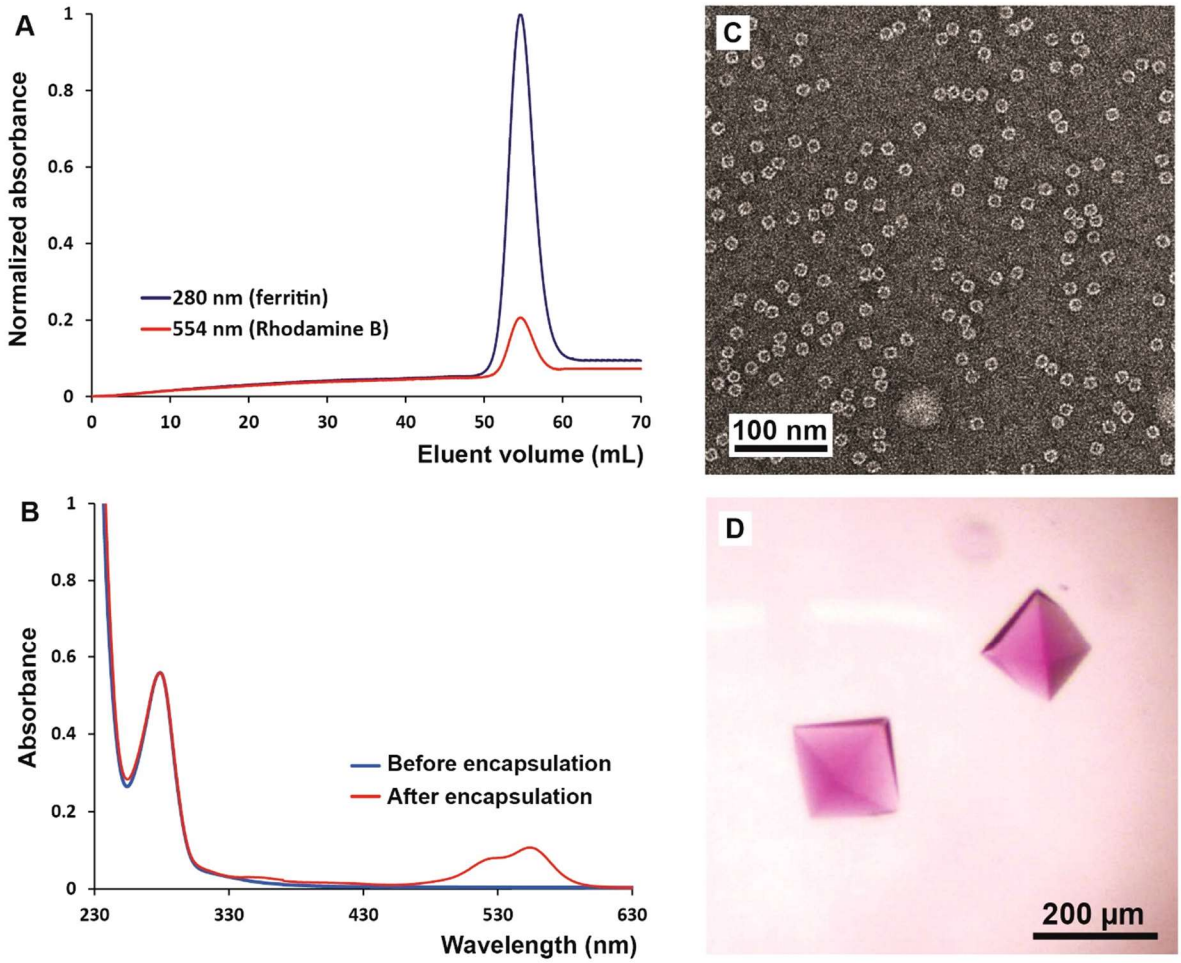

Figure 4.3 The characterization of Rho B-$Ftn^{(neg)}$. A) SEC chromatogram B) UV/Vis spectra before and after the encapsulation. C) TEM image after purification. D) Optical microscopy image of Rho B-$Ftn^{(neg)}$ single crystals.

To prove the successful encapsulation, several characterizations were performed for Rho B-$Ftn^{(neg)}$. The SEC chromatogram (Figure 4.3A) and the UV/Vis spectra before and after the encapsulation (Figure 4.3B) indicate a successful encapsulation of Rho B. Furthermore, TEM confirms that ferritin

cages reformed after the reassembly process (Figure 4.3C). I was also able to crystalize Rho B-Ftn$^{(neg)}$ as single crystals (Figure 4.3D), which indicates the monodispersity of Rho B-Ftn$^{(neg)}$. The crystallization only works if monodisperse protein containers are present. While the encapsulation worked, the loading was quite low although I have already used a high concentration of fluorophores (Table 4.1). A similar result was also reported by Yan *et al.*, who managed to encapsulate on average 1 molecule of methylene blue per ferritin cage for photodynamic therapy application.[237] These results indicate the weak molecular interactions between fluorophores and the ferritin subunits, and that the encapsulation most likely occurred via a statistically driven process. A better encapsulation strategy is needed to achieve high loading, as it will be important for the drug delivery application later.

4.1.1.2 Fluorophore encapsulation by chemical conjugation

In the previous section, it was shown that the encapsulation of fluorophores in ferritin containers by a simple molecular entrapment could not result in high loading due to the weak molecular interactions. To obtain a higher loading, I performed chemical conjugation inside the ferritin cavity by the cysteine-maleimide coupling reaction (Figure 4.4). As this encapsulation strategy requires the opening and closing of ferritin cages via acidic dis/reassembly approach, which currently is not favorable for Ftn$^{(pos)}$, this strategy was applied only to Ftn$^{(neg)}$.

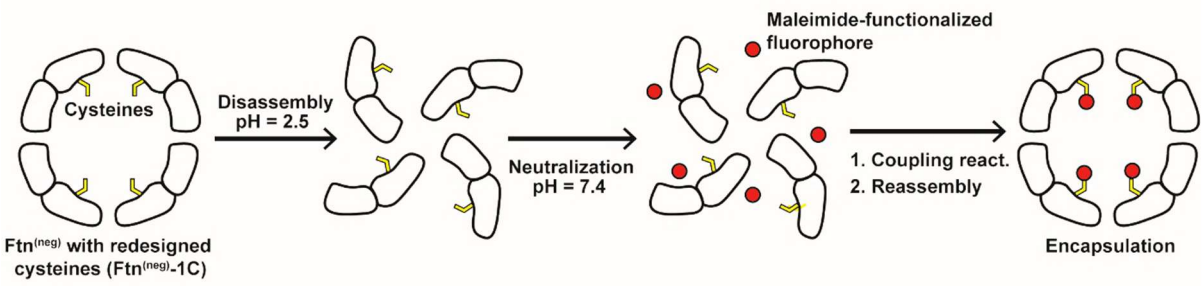

Figure 4.4 Strategy to encapsulate fluorophores in ferritin via chemical conjugation. Ferritin variant with redesigned cysteine positions was first disassembled in an acidic condition. After neutralization, a cysteine-maleimide coupling reaction was performed to attach fluorophores to the ferritin subunits. Finally, the reassembly of ferritin cages results in a successful fluorophore encapsulation.

To ensure effective coupling reactions, the location of cysteines inside the Ftn$^{(neg)}$ cavity needs to be optimized. The Ftn$^{(neg)}$ subunit only has one cysteine left at the three-fold channels (Figure 4.5A). Here, three cysteines are located in close proximity. However, coupling at these positions is not ideal as the attached fluorophore molecules may produce steric hindrance, thereby potentially hindering the reassembly process. For this reason, the cysteines at the 3-fold channels need to be removed to enable an effective encapsulation. Site-directed mutagenesis was applied to mutate this cysteine into alanine (C130A). The resulting ferritin variant is referred to as Ftn$^{(neg)}$-0C.

Furthermore, to know where to add the new cysteines in the cavity, an online program called GETAREA[238] was used to calculate the solvent-accessible surface area of each amino acid residues in ferritin. The results show how exposed the amino acid residues are to the solvent, and thus in our case, the accessibility for the coupling reaction. The solvent-accessible surface area is expressed in the term of "ratio value", which is the ratio between the side-chain surface area in the protein structure and the side-chain surface area in a random coil conformation. Multiplication by 100% gives the ratio value in percentage. An amino acid residue with a ratio value more than 50% is considered as solvent-exposed, while residue with a ratio value less than 20% is considered as buried and not easily accessible to the solvent. GETAREA showed four amino acid residues inside the ferritin cavity which have the highest solvent-accessible surface area (Table 4.2). Lysine-53, which has a ratio value of 78.1%, was found to be the best position to add the new cysteine (Figure 4.5B). Therefore, site-directed mutagenesis was performed to mutate lysine-53 into cysteine (K53C). The resulting ferritin variant was referred to as $Ftn^{(neg)}$-1C.

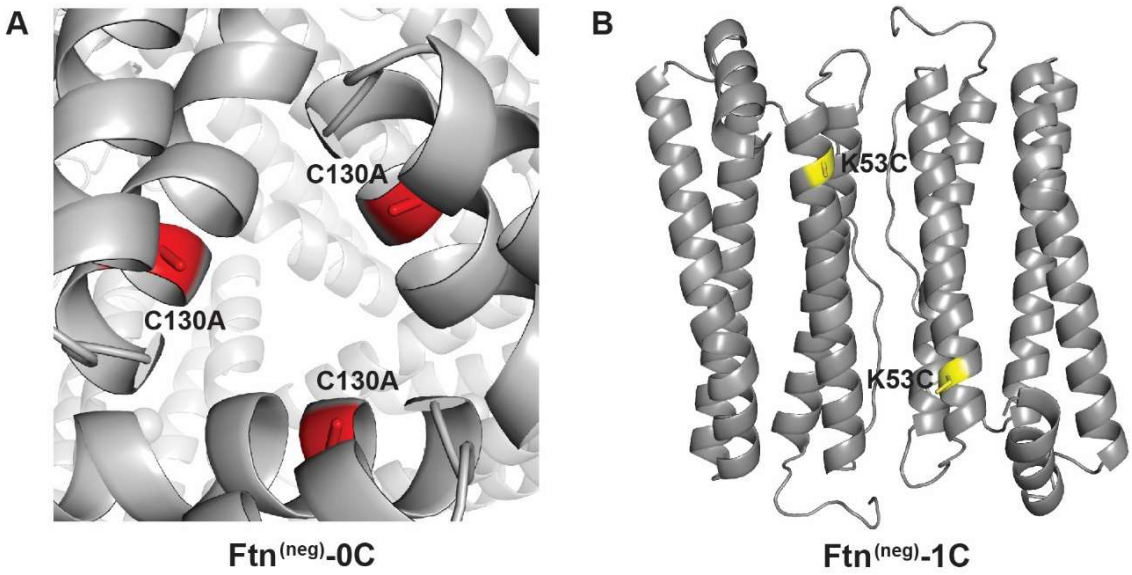

Figure 4.5 Relocation of cysteine positions in $Ftn^{(neg)}$ to enable an efficient encapsulation via chemical conjugation. A) Removal of cysteines at the three-fold channels by mutation into alanines (C130A, red). The new variant of ferritin is called $Ftn^{(neg)}$-0C. B) The subsequent mutation to add the new cysteine. Lysine-53 was mutated into cysteines (K53C, yellow). The resulting ferritin variant is called $Ftn^{(neg)}$-1C. Here, two ferritin subunits that form one side of the inner cavity are shown. In total, twelve dimers form the cavity.

Table 4.2 Solvent accessible surface area

Amino acids	Ratio (%)
K53	78.1
E64	65.7
T135	50.6
K143	53.2

To encapsulate the fluorophores, first, the ferritin cages were opened by using an acidic condition to expose the cysteines inside the ferritin cavity to the coupling reaction (Figure 4.4). After reconstitution to pH 7.4, the coupling reaction was performed and the ferritin cages were subsequently reassembled. Reassembly is a slow process because each of the ferritin subunits needs to find the right position to fully form the cages, therefore it will not interfere with the fast coupling reaction.

Nevertheless, a few issues are crucial for this new encapsulation strategy. First, a sufficient salt concentration (0.5 M) is needed to screen the electrostatic interactions during the reassembly process. Otherwise, the reassembly will not occur smoothly, and a nice SEC chromatogram profile will not be obtained. Next, it is important to dissolve the maleimide functionalized fluorophores in anhydrous DMSO (or acetonitrile) and store them in an air-tight container (or with drying silica gel) at -20 °C whenever they are not in use. Water molecules from the ambient air can react with the maleimide groups and thus will reduce the effectiveness of the coupling reaction. The low temperature efficiently helps to suppress this side reaction. Moreover, the maleimide fluorophore stock solutions need to be thawed completely to room temperature before use to minimize the condensation of water vapor on the stock solution.

Tris(2-carboxyethyl)phosphine (TCEP) is commonly used in cysteine-maleimide coupling reactions to cleave or to prevent the formation of disulfide bridges between cysteine residues.[239] However, some publications reported that TCEP also reacts with the maleimide groups, therefore competing with the intended coupling reactions.[240,241] The ferritin variant, $Ftn^{(neg)}$-1C, only has one cysteine per ferritin subunit. In the cavity, the cysteine residues are separated from each other by distances, hence no disulfide bridges are present in this system. Although theoretically, the cysteines can form disulfide bridges when the ferritin cages are disassembled into subunits, this has never been observed during the dis/reassembly process. For these reasons, TCEP is not needed for the coupling reaction with fluorophores.

The encapsulation of fluorophores via chemical conjugation was very efficient and successful. With this approach, it was possible to encapsulate both positively and negatively charged fluorophores with

high loading and yield, at much lower fluorophore concentrations (Table 4.3). On the SEC chromatogram, the intensity of fluorophore signals was even much higher than the protein signal (Figure 4.6). Compared to the statistical encapsulation, chemical conjugation produced a more intense color in the samples (Figure 4.7). This strategy has been proven to be very helpful to encapsulate small organic molecules which have weak interactions with ferritin. Therefore, this strategy could also be extended for drug encapsulation, provided there is a mechanism to cleave the drug afterward.

Table 4.3 The loading and yield from the encapsulation of fluorophores via chemical conjugation

Fluorophore (and its charge)	Ferritin variants	Used fluorophore concentration (μM)	Loading (molecules/cage)	Yield (%)
Atto Rhodamine 6G (+)	$Ftn^{(neg)}$-1C	15.8	10.9	97.9
Alexa Fluor 488 (-)	$Ftn^{(neg)}$-1C	15.8	19.1	89.5
Alexa Fluor 647 (-)	$Ftn^{(neg)}$-1C	15.8	14.8	97.6

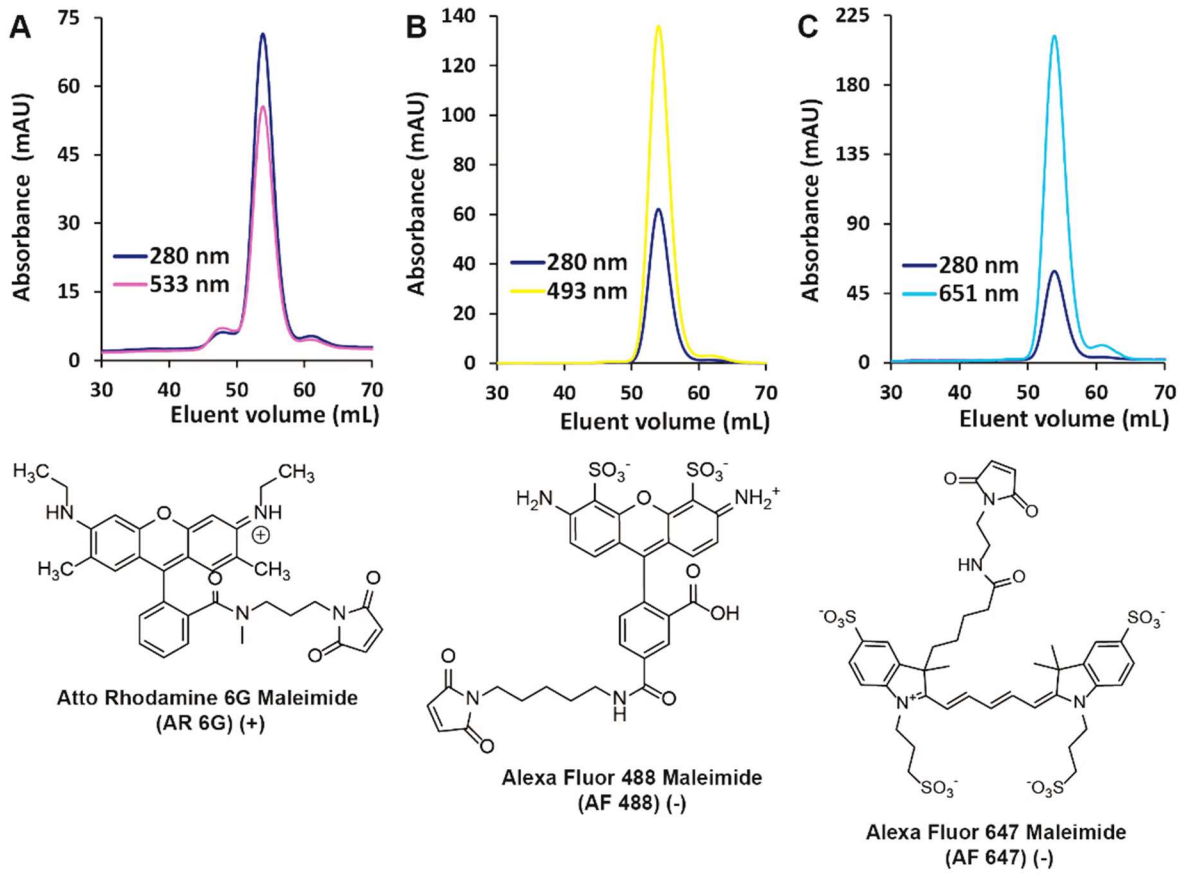

Figure 4.6 SEC chromatograms obtained from the encapsulation of fluorophores by chemical conjugation. $Ftn^{(neg)}$-1C was labeled with maleimide functionalized fluorophores: A) AR 6G (+), B) AF 488 (-), C) AF 647 (-).

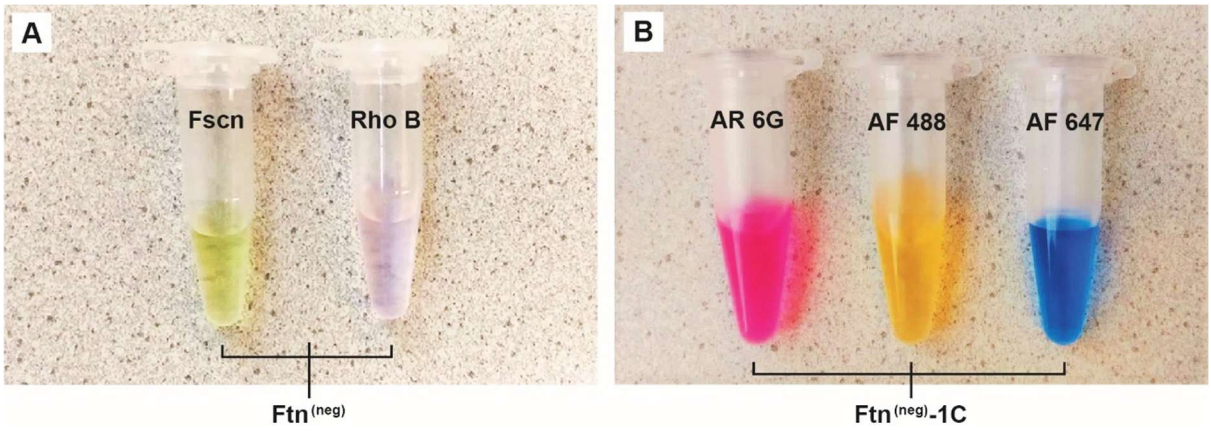

Figure 4.7 Comparison of fluorophore-labeled ferritin obtained via different encapsulation strategies. A) statistical encapsulation. B) chemical conjugation. All the solutions have a concentration of 2 mg/mL.

4.1.1.3 Synthesis and characterization of nanoparticles loaded ferritin

In addition to fluorophores, ferritin was also labeled NPs. NP-filled ferritin containers are suitable as markers for studying the integration and release of ferritin from microgels by TEM. The synthesis of metal oxide NPs within the redesigned protein containers has been established previously in our group.[24] In this synthesis, elevated temperatures are applied to facilitate the diffusion of Fe^{2+} or Ce^{3+} cations into ferritin cages. Subsequently, the cations were oxidized by H_2O_2. As a result, iron oxide or cerium oxide NPs formed inside the ferritin cages, respectively (Figure 4.8A).

Several types of NP-loaded ferritin were synthesized (Table 4.4). However, here only the characterization results of Ce-Ftn$^{(neg)}$ are shown as examples. The presence of NPs inside ferritin containers was confirmed by TEM, SEC, and UV/Vis (Figure 4.8B-D). The yield of the synthesis was 78.7%. For TEM imaging, cerium oxide ferritin was used because it produces more contrast than iron oxide ferritin. However, iron oxide ferritin has another advantage. As mentioned earlier, the magnetic property of iron oxide can be utilized for generating heat in future applications.

Table 4.4 Nanoparticles-loaded ferritin containers

Nanoparticles	Ferritin variants	Name
FeO_x	Ftn$^{(neg)}$	(Fe-Ftn$^{(neg)}$)
CeO_2	Ftn$^{(neg)}$	Ce-Ftn$^{(neg)}$
CeO_2	HF	Ce-HF
CeO_2	Ftn$^{(pos)}$	Ce-Ftn$^{(pos)}$

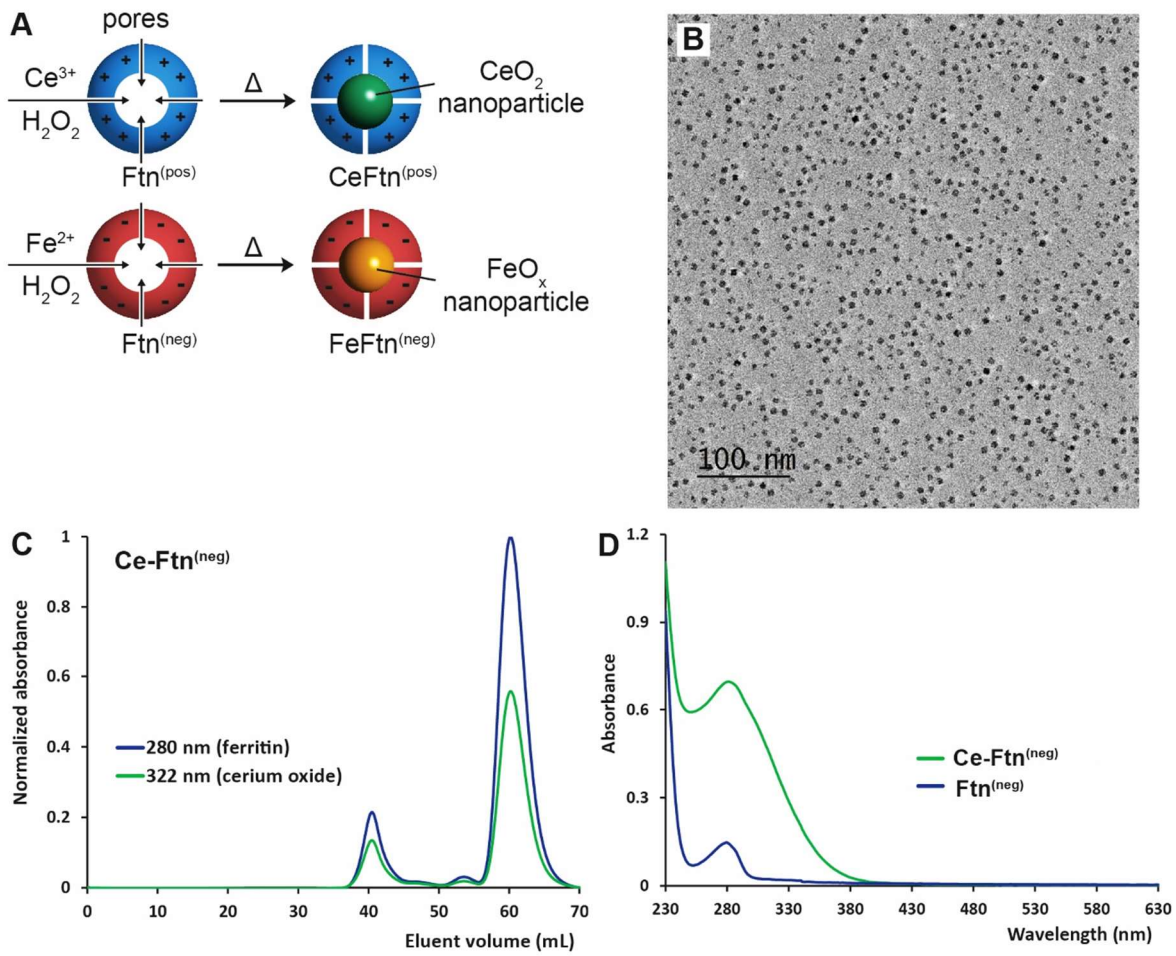

Figure 4.8 The synthesis and characterization of Ce-Ftn$^{(neg)}$. A) Synthesis scheme. B) TEM characterization without staining agent. The cerium oxide cores are clearly visible. However, staining would be required to visualize the protein containers (cf. Figure 4.3C). C) SEC chromatogram from the purification of Ce-Ftn$^{(neg)}$. D) UV/Vis spectra before and after the synthesis.

4.1.2 The integration of ferritin containers into microgel system

Having established the ferritin labeling with fluorophores and NPs, the labeled ferritin was integrated into microgel systems using electrostatic interactions between the surface charges of ferritin and the ionizable groups inside polyelectrolyte microgels. This section describes the integration of ferritin into various microgel systems to find the right system that is suitable for the envisioned drug delivery application. Initially, ferritin was integrated into readily prepared microgels. The first system tested were microgels with randomly distributed ionizable groups (Chapter 4.1.2.1). Some challenges were encountered in this system. To address the problems, a core-shell microgel system was investigated (Chapter 4.1.2.2). Although this system is better than the previous one in a certain aspect, ferritin could leak out from the microgels after purification. Finally, to overcome this problem, ferritin was integrated into microgels by adding the ferritin during the synthesis of degradable microgels (Chapter 4.1.2.3).

4.1.2.1 Integration into microgel with randomly distributed ionizable groups

A microgel with randomly distributed ionizable groups is the simplest polyelectrolyte microgel system, therefore I started with this system. All the microgels used in this sub-section were supplied by Wenjing Xu (Institute of Technical and Macromolecular Chemistry, RWTH Aachen). To perform the integration, NPs-labeled ferritin were added into microgels containing the opposite charges in a buffer solution of a certain pH (Figure 4.9A-B). Ferritin showed strong interactions with the microgels, and the microgels precipitated immediately (Figure 4.9C). This precipitation could be prevented by changing pH or by adding salts, which confirmed that the precipitation was due to electrostatic interactions (Table 4.5).

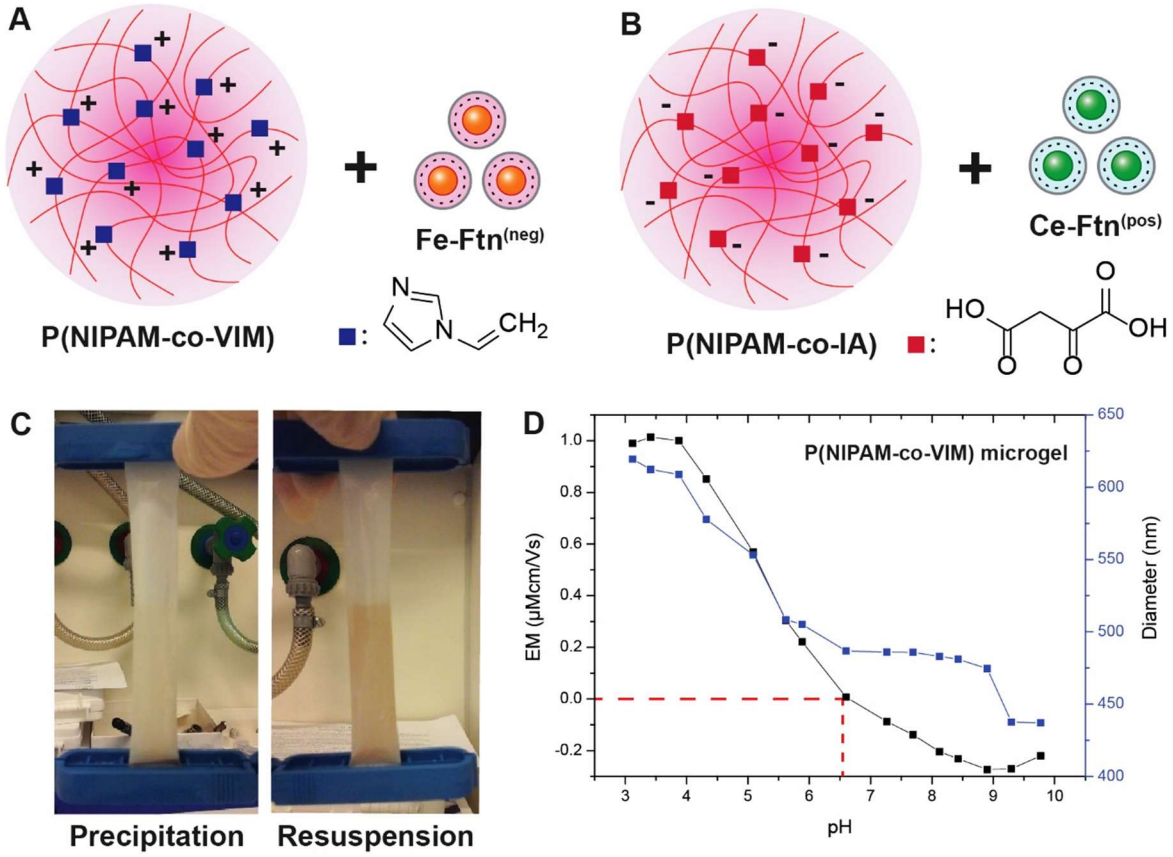

Figure 4.9 Integration of ferritin into microgel with randomly distributed ionizable groups. A) Fe-Ftn$^{(neg)}$ was added to the positively charged microgels P(NIPAM-co-VIM). The positively charged VIM groups are depicted as the blue squares. B) Ce-Ftn$^{(pos)}$ was added to the negatively charged microgels P(NIPAM-co-IA). The negatively charged IA groups are depicted by the red squares. Both microgels contain 2% mol crosslinker BIS. C) Fe-Ftn$^{(neg)}$ and P(NIPAM-co-VIM) precipitated during dialysis. D) The charges and sizes of P(NIPAM-co-VIM) microgels at different pH (a work by Wenjing Xu). The charges are indirectly shown by the electrophoretic mobility (EM). The positive value of EM indicates positive charges and vice versa.

Table 4.5 Conditions leading to the precipitation of microgels and ferritin

Microgels*	Labeled ferritin	Precipitation	No precipitation
P(NIPAM-co-VIM) (+)	Fe-Ftn$^{(neg)}$	pH (4 – 6)	[NaCl] > 80 mM
P(NIPAM-co-IA) (-)	Ce-Ftn$^{(pos)}$	pH (8 – 10)	[NaCl] > 250 mM

* Both microgels contain 2% mol BIS crosslinker and 10% mol charged monomers.

The precipitation only occurred within a certain pH range because ferritin and microgels have the opposite charges only in that pH range. For example, Fe-Ftn$^{(neg)}$ and P(NIPAM-co-VIM) precipitated only in the pH range between 4 – 6 because in this pH range they have the opposite charges. Fe-Ftn$^{(neg)}$ has an isoelectric point (pI) between 4.2 - 4.8. Below pH 4.2 Fe-Ftn$^{(neg)}$ becomes positively charged, and therefore it did not precipitate when mixed with the positively charged P(NIPAM-co-VIM). On the other hand, P(NIPAM-co-VIM) microgels become negatively charged above pH 6.5 (Figure 4.9D), and therefore they did not precipitate when mixed with Fe-Ftn$^{(neg)}$, which stays negatively charged above pH 4.8. The pH range, in which the precipitation occurred, turns out to be the suitable pH to perform the integration because the electrostatic attractions between ferritin and the microgels only exist in that pH range.

The addition of salt prevented the precipitation because the Na^+ and Cl^- ions screen the electrostatic interactions between ferritin and microgels. Although the precipitation can be avoided by changing pH or adding salt, these two approaches are not the proper way to perform the integration because they eliminate the interactions between ferritin and microgels.

In solution, microgels are stabilized by the electrostatic repulsion between the charges which are present on the surface of microgels (charge stabilization) and by the free movement of its polymeric chains (steric stabilization). Related to these two stabilization mechanisms, two possible reasons are hypothesized for explaining the precipitation. First, the precipitation occurred because ferritin bridged the microgels to form large aggregates, or in other words, ferritin caused flocculation in the microgels (Figure 4.10A). Second, the adsorption of ferritin on the surface of microgels caused the microgels to lose the free movement of their polymeric chain, and consequently, they precipitated (Figure 4.10B). This second hypothesis is supported by the fact that the precipitation could also be prevented if less crosslinked microgels are used. For example, P(NIPAM-co-VIM) with 0.2% mol BIS crosslinker did not precipitate when mixed with Fe-Ftn$^{(neg)}$ in buffer pH 5. It is assumed that Fe-Ftn$^{(neg)}$ could penetrate more to the interior of the microgels, and thus the microgels could retain their steric stabilization and remain stable in solution.

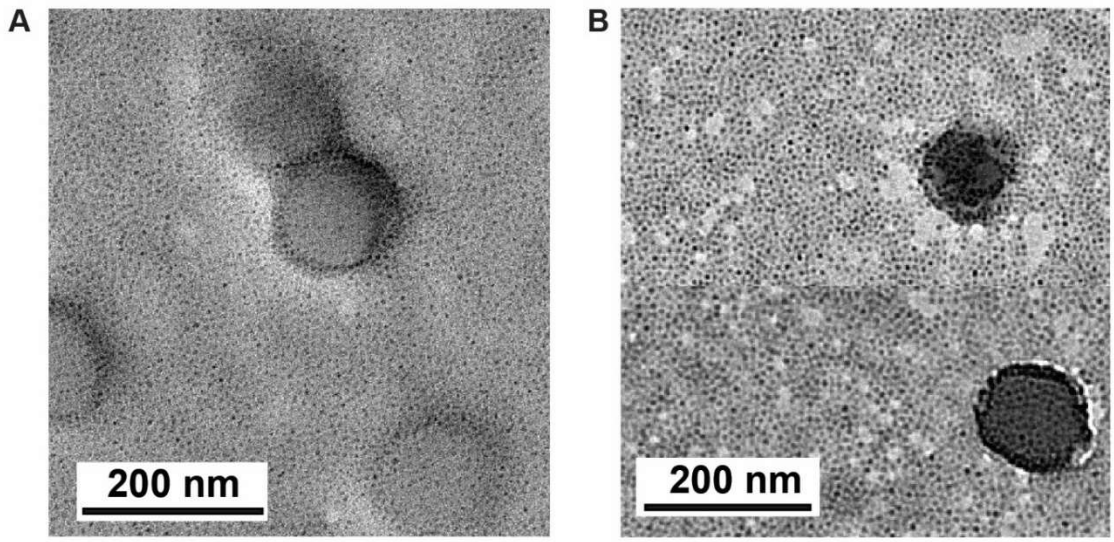

Figure 4.10 TEM characterization of the precipitated ferritin-microgel sample. In these images, the small black dots are Fe-Ftn$^{(neg)}$, while the large-round objects are P(NIPAM-co-VIM) microgels. A) Fe-Ftn$^{(neg)}$ bridged the microgels and caused flocculation. B) The adsorption of Fe-Ftn$^{(neg)}$ on the surface of microgels caused microgels to lose their steric stabilization. In this early experiment too high Fe-Ftn$^{(neg)}$ concentration was used. However, later we found that the precipitation also occurred at low Fe-Ftn$^{(neg)}$ concentration.

As mentioned in the previous paragraph, the precipitation problem was solved by integrating Fe-Ftn$^{(neg)}$ into P(NIPAM-co-VIM) microgels with 0.2% mol BIS crosslinker. However, another challenge was encountered in the purification of the microgels after the integration. Normally, microgels are purified either by centrifugation or dialysis. In our case, centrifugation could not completely clean microgels from the unbound Fe-Ftn$^{(neg)}$ even after several consecutive runs. Dialysis did not work as Fe-Ftn$^{(neg)}$ could not pass through the pores of the dialysis bag. The largest molecular weight cut-off (MWCO) of dialysis bags is 1000 kDa, while Fe-Ftn$^{(neg)}$ has a molecular weight of 508.8 kDa. To have a successful separation, the dialysis bag should have an MWCO of at least 20x larger than the molecular weight of the molecules to be removed.

Concentrators were also tested to purify the microgels. Similar to the dialysis bag, the largest MWCO of filter membrane in concentrators are 1000 kDa and 0.2 µm. However, due to the centrifugal force, Fe-Ftn$^{(neg)}$ was able to pass through the filter membrane. Unfortunately, the soft microgels ended in the membrane, blocked the pores, and could not be re-dispersed.

Finally, sucrose cushion centrifugation was tested to purify the microgels. This is a separation technique based on the difference in densities. First, several layers of sucrose solutions with different densities are established inside a centrifuge tube. Next, the samples to be separated are placed on the top of the sucrose solutions and then spun at a very high speed for several hours. During the centrifugation, a density gradient forms and each sample moves downward and finally stops at different positions according to their density. Subsequently, the resulting solution is fractionated into several fractions by repeatedly pipetting 1 mL of the solution from the top layer and placing them in

different containers. These fractions are analyzed, for example by UV/Vis, to detect the presence of ferritin containers within the samples.

By optimizing the composition of the sucrose layers, it is possible to make Fe-Ftn$^{(neg)}$ and the microgels stop in different positions within the density gradient (Figure 4.11). Accordingly, the ferritin-microgels fraction also stopped at a position between the pure ferritin and the pure microgels layers. Based on these results, I was convinced that the purification would work. The ferritin-microgels fraction was collected and analyzed by TEM. Surprisingly, the microgels were not clean from the unbound ferritin (Figure 4.12). This might be because flocculation still occurred in the ferritin-microgel fraction. Probably, the observed free ferritin is the one that bridged the microgels. The presence of the flocculation was supported by Dynamic Light Scattering (DLS) measurement (Figure 4.13).

As a summary, the integration of NPs-labeled ferritin into polyelectrolyte microgels with randomly distributed ionizable groups was characterized by several challenges. First, ferritin and microgels precipitated during the integration. Although later, the precipitation could be avoided by using less crosslinked microgels, ferritin and microgels still flocculated and formed larger aggregates in the solution. Moreover, some challenges were encountered in the purification of the microgels from the excess ferritin after the integration. Several purification techniques have been applied, however, the microgels were not completely clean from the unbound ferritin.

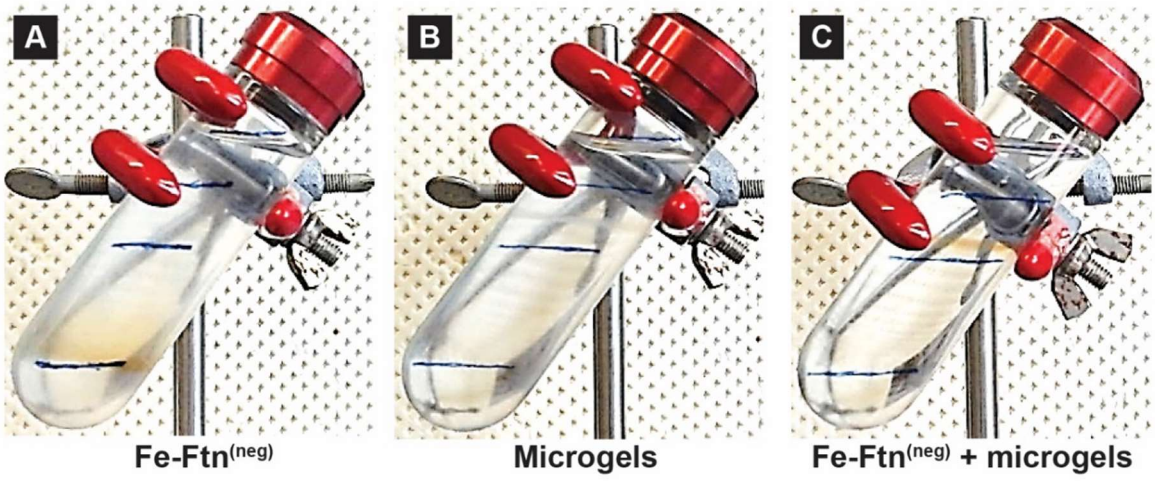

Figure 4.11 Purification by sucrose cushion centrifugation. The composition of the sucrose solutions from top to bottom were: 0% (sample), 20%, 30%, and 70% (w/w). After the centrifugation, A) the pure Fe-Ftn$^{(neg)}$ solution stopped near the 70% sucrose layer. B) the pure P(NIPAM-co-VIM) microgels with 0.2% BIS crosslinker stopped in the middle of the 20% sucrose layer. C) the ferritin-microgels mixture also stopped in the 20% sucrose layer, but at a slightly lower position.

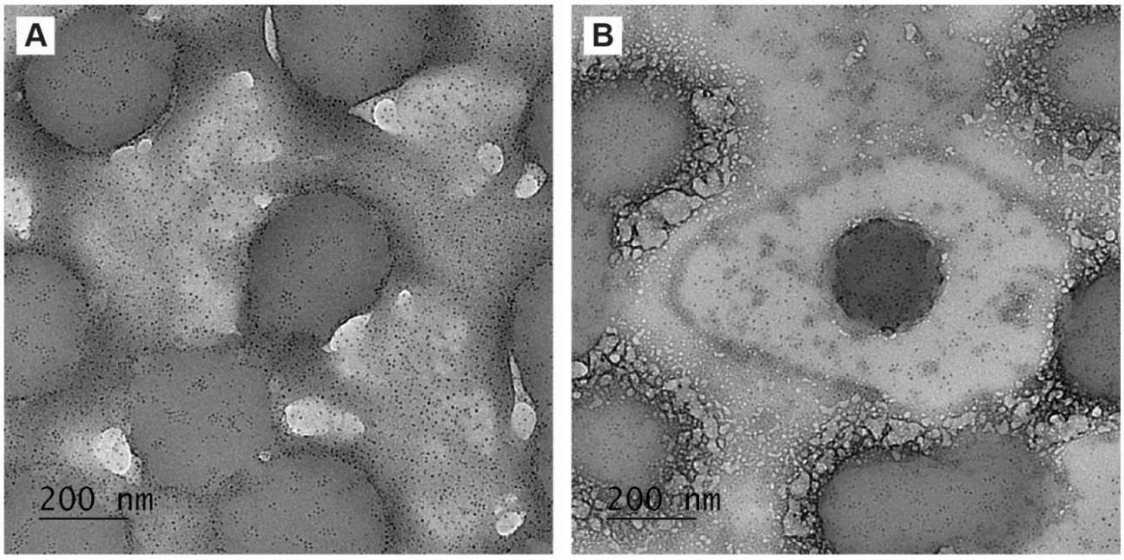

Figure 4.12 TEM characterization of the ferritin-microgels reaction mixture. A) Before purification. B) After the sucrose cushion centrifugation. Shown here, is the ferritin-microgels fraction obtained from Fig. 4.11C. The purification indeed removed a lot of the unbound ferritin but the system was not clean.

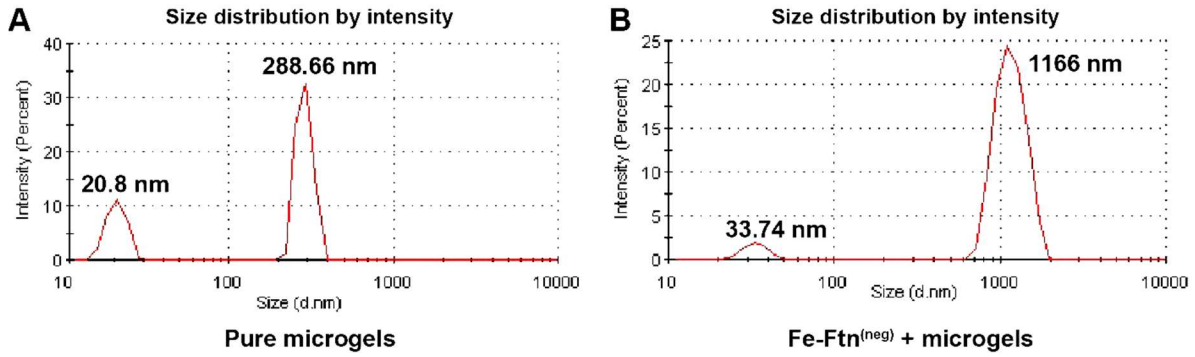

Figure 4.13 The size of P(NIPAM-co-VIM) microgels with 0.2% BIS at pH 5 as determined by DLS. A) Pure microgels. B) Microgels and Fe-Ftn$^{(neg)}$ reaction mixture. After the integration, the size of the microgels increased drastically. This result indicates that ferritin and microgels flocculated to form larger aggregates.

4.1.2.2 Integration into core-shell microgels

In the previous section, it was shown that the integration of ferritin into polyelectrolyte microgels with a random distribution of ionizable groups suffered from flocculation, which may lead to precipitation. Regarding this, it was envisioned that polyelectrolyte microgels with a core-shell structure could overcome this problem. For example, a charged core can be used for binding the ferritin containers and a neutral shell can be used to prevent the flocculation between the microgels. Therefore, here the integration of ferritin into a core-shell microgel system was investigated.

As a short overview, this section first describes the integration of ferritin into a core-shell microgel system. Two problems were identified in this system: the inhomogeneous distribution of ferritin among the microgels and the ferritin leakage from microgels. Later, thorough investigations were

performed to identify the cause of the first problem. Finally, various approaches were applied to solve both of the problems.

4.1.2.2.1 The integration of Ce-Ftn$^{(pos)}$ into the charged core-neutral shell microgels

The core-shell microgels used in this section were supplied by Sarah Wypysek (Institute of Physical Chemistry, RWTH Aachen). The microgels consist of a negatively charged core P(NIPAM-co-MAA-co-MRB) (90.985% : 5% : 0.015% : 4% mol BIS), surrounded by a neutral shell P(NIPAM) (96.1% : 3.9% mol BIS) (Figure 4.14A). To perform the integration, the cerium-oxide NPs labeled ferritin (Ce-Ftn$^{(pos)}$) was added to the core-shell microgels in buffer pH 8.0. The reaction mixture was very stable, and no precipitation was observed. TEM characterization showed that the microgels were well separated from each other (Figure 4.14B). The neutral shell indeed prevented the flocculation. Interestingly, ferritin was inhomogeneously distributed among the microgels. Only a few microgels were filled by Ce-Ftn$^{(pos)}$, and most of the microgels were empty.

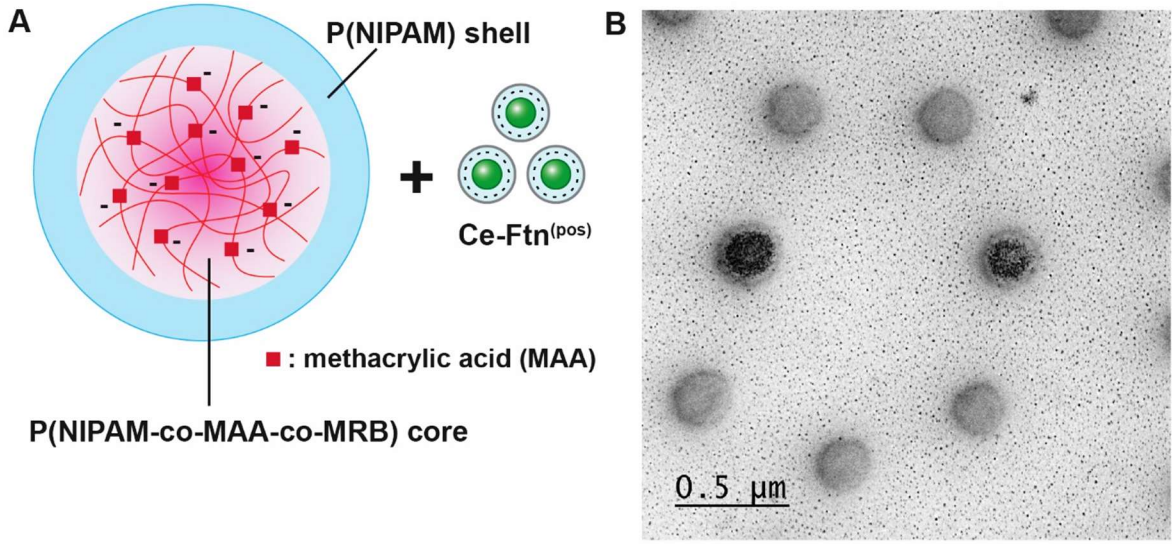

Figure 4.14 The integration of NPs-labeled ferritin into core-shell microgels. A) Reaction scheme. The positively charged Ce-Ftn$^{(pos)}$ was added into microgels with a negatively charged core and neutral shell. The core of the microgels contains methacryloxyethylthiocarbamoyl-Rhodamine B (MRB) fluorophore. B) TEM characterization of the reaction mixture without purification. The microgels were well separated from each other. However, only a few microgels were filled by Ce-Ftn$^{(pos)}$, which appeared as the small black dots. Most of the microgels were empty. As the reaction mixture was not purified, an abundance of Ce-Ftn$^{(pos)}$ was observed outside the microgels.

Although not all of the microgels were filled, I tried to purify the microgels from the unbound ferritin. This was also intended for learning more about the properties of this microgel system. First, three times consecutive ultracentrifugation were applied. The ultracentrifugation removed a lot of Ce-Ftn$^{(pos}$, however the system was not completely clean (Figure 4.15). Some free Ce-Ftn$^{(pos)}$ were still observed outside the microgels.

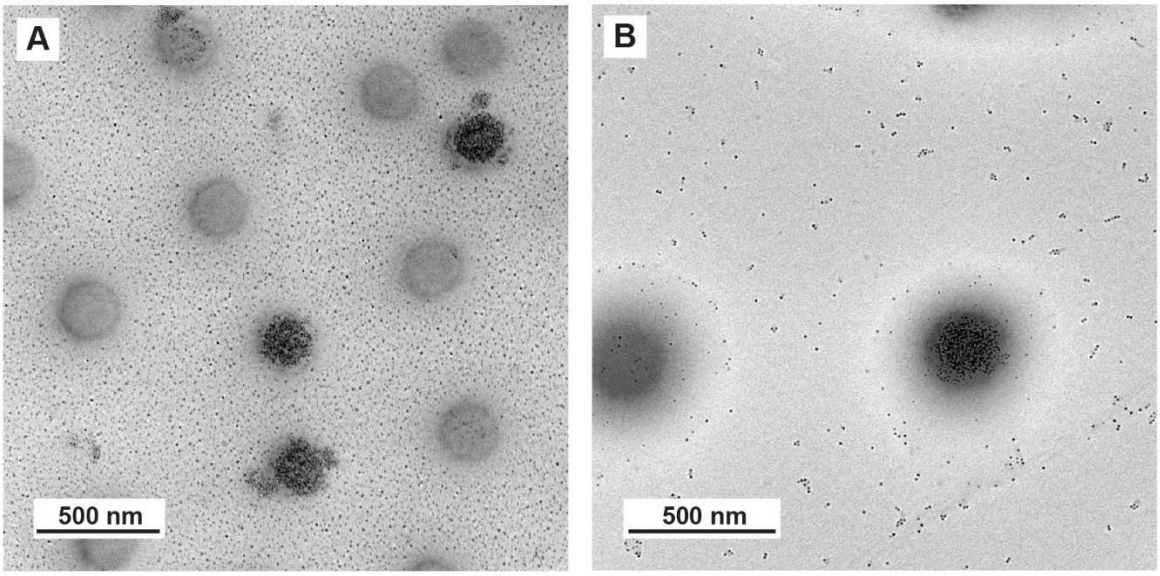

Figure 4.15 Purification of the core-shell microgels by ultracentrifugation. This was to remove the unbound ferritin after the integration. These are the TEM images: A) Before purification. B) After 3x consecutive ultracentrifugation. Here, the core-shell structure of the microgels was clearly visible. The purification removed a lot of ferritin containers but the system was not completely clean from the free ferritin.

Next, the microgels were purified by ion-exchange chromatography (IEC) and SEC, which are the common techniques for protein purification. In summary, IEC is a separation technique based on charge differences. The samples to be separated are injected into a positively or negatively charged IEC column. As a result, samples with the opposite charges will bind to the column, while samples with neutral or the same charges as the IEC column will flow through the column. Later, a gradient concentration of salt solution can be applied to the column to release the samples which are bound to the column.

First, microgels and ferritin were injected separately into a negatively charged IEC column to study their behavior and interaction with the column. As the microgels have a neutral shell, they did not bind to the column and immediately flowed through the column (Figure 4.16A). In contrast, Ce-Ftn$^{(pos)}$ was strongly bound to the column and only came out after salt elution (Figure 4.16B). Without salt elution, they remained in the column. Next, the reaction mixture of microgels and Ce-Ftn$^{(pos)}$ was injected to the column (Figure 4.16C). Two fractions were obtained. Fraction 01 (Fr-01) immediately flowed through the column, while fraction 02 (Fr-02) only came out only after the salt elution. Based on the previous results, it was predicted that Fr-01 was the microgels and Fr-02 was the Ce-Ftn$^{(pos)}$. To confirm this, both fractions were analyzed by TEM (Figure 4.16D-E). Fr-01 indeed was the microgel fraction, and it was almost clean from the Ce-Ftn$^{(pos)}$. Most of the Ce-Ftn$^{(pos)}$ has been removed and was found in Fr-02. Interestingly, Fr-02 also contained microgels that were heavily loaded with Ce-Ftn$^{(pos)}$.

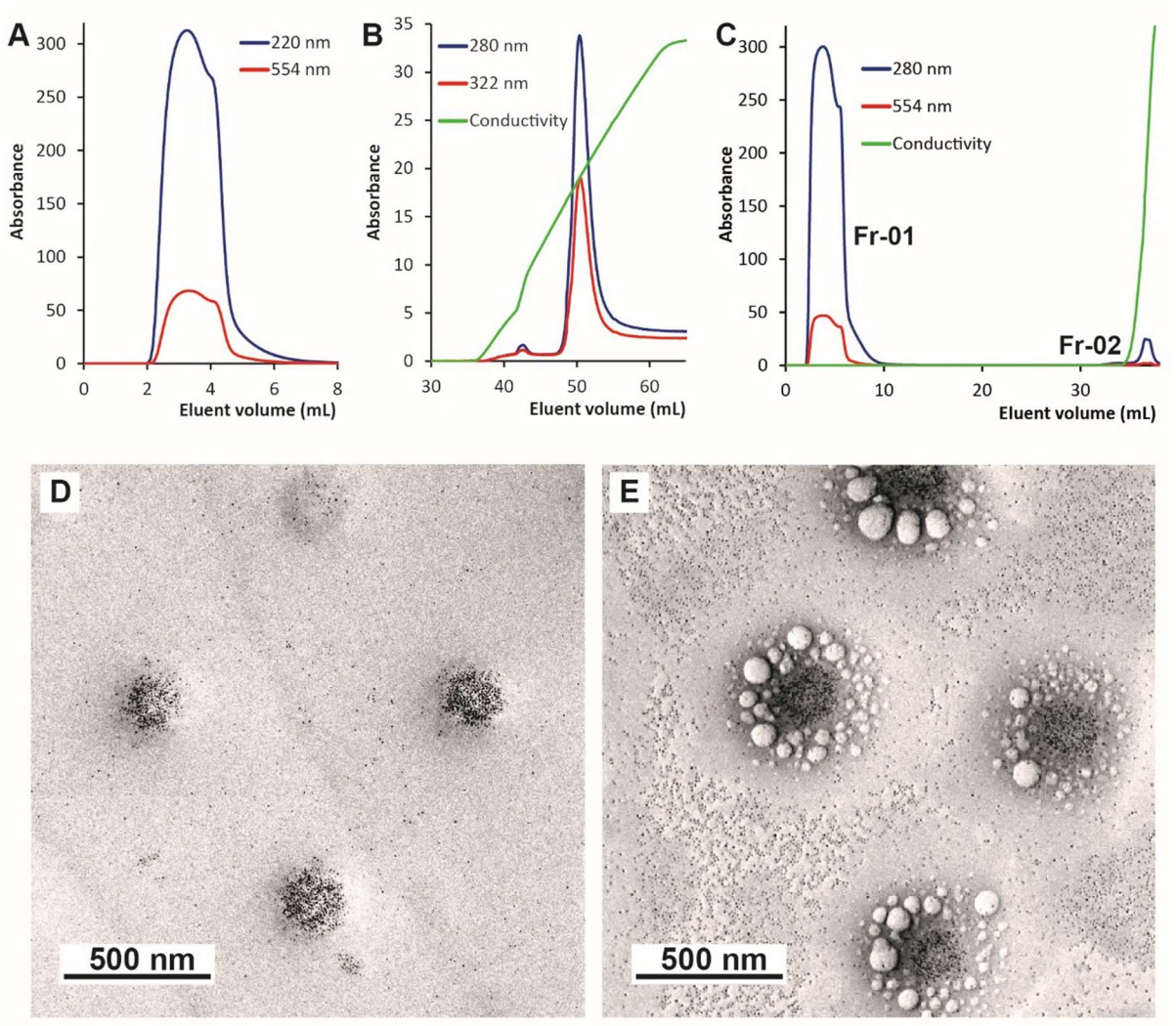

Figure 4.16 Purification of the core-shell microgels by IEC. A) The IEC chromatogram of the pure microgels. The signal at 220 nm originates from the carbon backbone of the microgels, while the signal at 554 nm comes from the fluorophore MRB, which was integrated into the core of the microgels. B) The IEC chromatogram of the pure Ce-Ftn$^{(pos)}$. The signal at 280 nm originates from ferritin, while the signal at 320 nm comes from CeO_2 NPs. C) The IEC chromatogram of the ferritin-microgel reaction mixture. The purification produced two fractions, which subsequently were characterized by TEM. The TEM results are shown in: D) Fraction 01 and E) Fraction 02. The TEM image of the sample before purification is shown in Figure 4.14B or Figure 4.15A.

Subsequently, two additional consecutive IEC runs were performed for fraction 01. Moreover, in each run, two IEC columns were connected in series to improve the purification. Surprisingly, TEM results show that there was no significant improvement in the 2nd and the 3rd IEC runs (Figure 4.17). Only the first IEC run cleaned the microgels from most of the unbound ferritin. Based on these results, it is concluded that Ce-Ftn$^{(pos)}$ leaked out from the microgels after the purification. This ferritin leakage is not ideal for drug delivery application, as it means ferritin can be released anywhere during the circulation of microgels in the bloodstream, therefore potentially causing off-target toxicity.

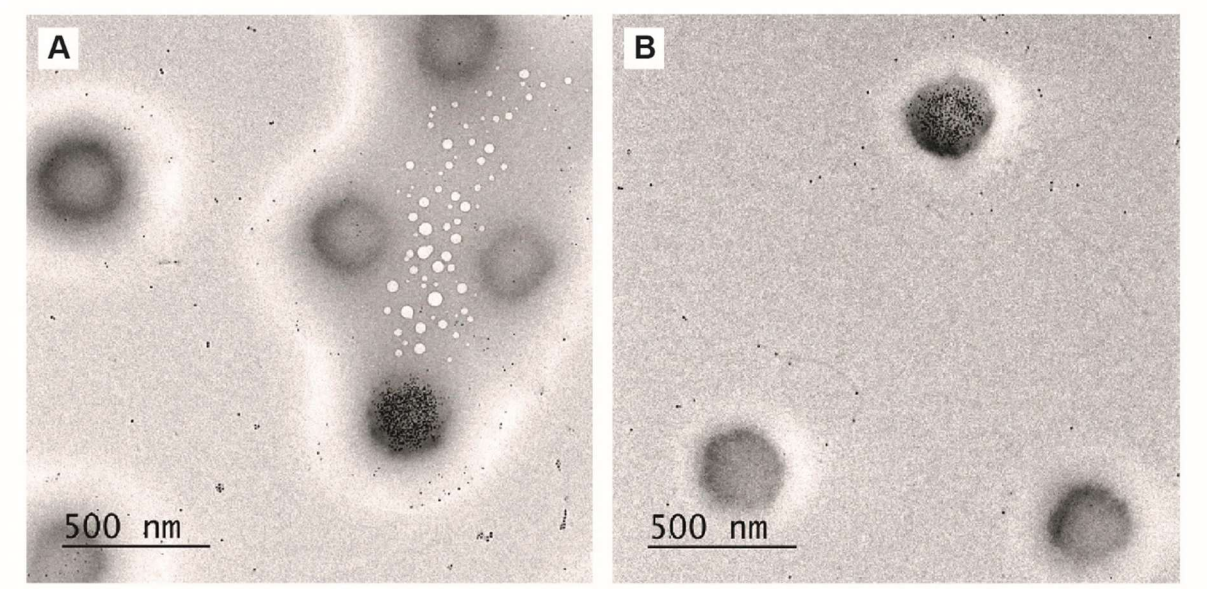

Figure 4.17 Further purification of the core-shell microgels by consecutive IEC runs. TEM characterization after: A) The second and B) The third IEC runs. The TEM image from the first IEC run is shown in Figure 4.16D.

Finally, SEC was tested to purify the microgels. Similarly, first, SEC was performed to microgels and ferritin separately to study their behavior. The microgels came out of the column at around 40 mL and produced a sharp peak (Figure 4.18A). On the contrary, the Ce-Ftn$^{(pos)}$ did not come out of the column under the applied elution condition (no salt). The SEC chromatogram is not shown here because it was only a flat line. In general, at least 0.15 M salt is needed to overcome the interaction of proteins with the column. Here, the SEC was performed with a buffer containing no salt because it would release ferritin from the microgels. Based on these results, it was predicted that SEC could purify the microgels from the unbound ferritin. Therefore, next, SEC was performed to the microgels fraction obtained from the 3rd IEC run. The result only shows a single peak at 40 mL, which is the microgels peak, and no other peak was observed (Figure 4.18B). However, the TEM characterization shows that the microgels were not clean from ferritin (Figure 4.18C). This fact can only be explained by the ferritin leakage as observed in the IEC purification.

As a summary, the integration of Ce-Ftn$^{(pos)}$ into the charged core-neutral shell microgels shows that the flocculation of microgels could be prevented by the neutral shell of the microgels. Moreover, this microgel system could be purified from the unbound ferritin by IEC or SEC. However, two problems need to be addressed before this system can be used for drug delivery applications. The first is the inhomogeneous distribution of ferritin among the microgels, and the second is the ferritin leakage from microgels after purification.

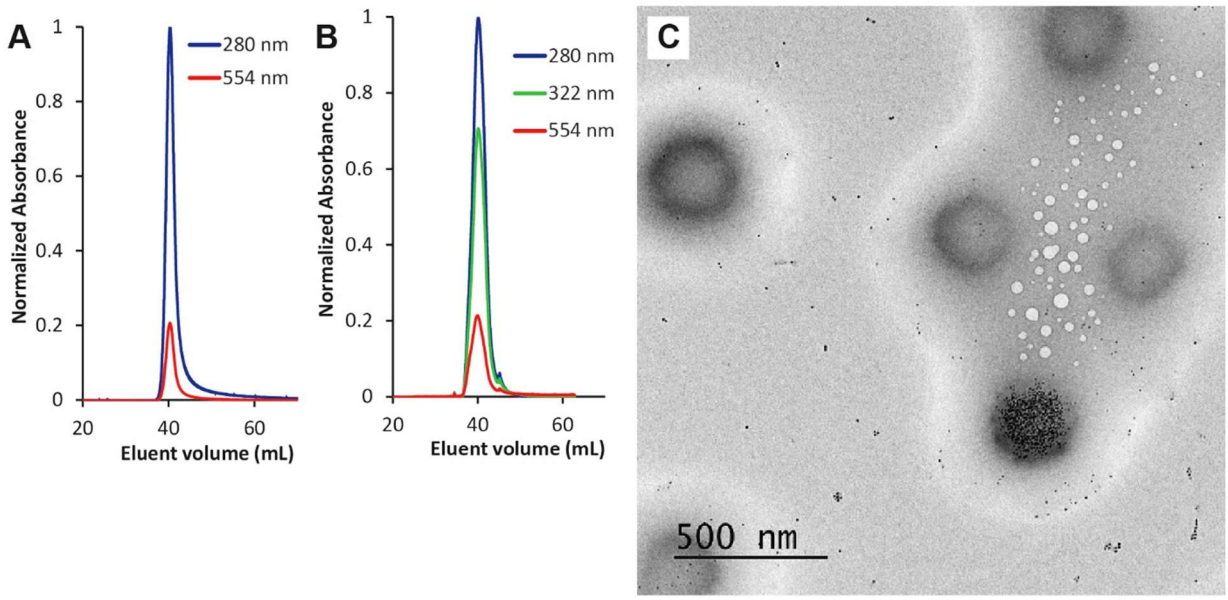

Figure 4.18 Further purification of the core-shell microgels by SEC. A) The SEC chromatogram of the pure microgels. The signal at 280 nm originates from the carbon backbone of the microgels, while the signal at 554 nm comes from the fluorophore MRB, which was integrated into the core of the microgels. B) The SEC chromatogram of the ferritin- microgel fraction obtained from the 3rd IEC run. The signal at 280 nm originates from microgels and ferritin, while the signal at 322 nm comes from the CeO_2 NPs. C) TEM characterization of the peak shown in B).

4.1.2.2.2 Investigations on the inhomogeneous distribution of ferritin among the microgels

In this section, several tests were conducted to identify the cause of the inhomogeneous distribution of ferritin among the microgels. From the previous observations, it is strongly believed that this problem lies in the core and not in the shell of the microgels. Therefore, here the synthesis of the core microgels was repeated, first by reducing the amount of BIS crosslinker, and second by increasing the amount of the charged monomer MAA. TEM characterizations showed that reducing the amount of crosslinker produced no significant differences (Figure 4.19A-C) and the problem remained. These results remove the hypothesis that the problem was due to the inhomogeneous distribution of BIS crosslinker. If it is the case, the problem should be overcome or at least reduced when less amount of crosslinker was applied. This is because ferritin should be able to penetrate better into most of the microgels. However, no significant changes were observed with reduced amounts of crosslinker. On the other hand, increasing the amount of the charged monomer MAA caused the inhomogeneous distribution of ferritin among the microgels even more pronounced (Figure 4.19D-F). Based on these results, it is believed that the problem was due to the inhomogeneous distribution of MAA in the microgels.

This result was surprising because the synthesis was performed using the common synthesis protocol of methacrylic acid microgels, and so far no inhomogeneous distribution of MAA among microgels has ever been reported. Previously, Hoare et al. investigated the distribution of MAA in P(NIPAM-co-MAA)

microgels, which have been synthesized by a very similar protocol, and they reported that MAA was homogenously distributed among the microgels, but the MAA was located more in the core than in the periphery region of the microgels.[173] Nevertheless, their method for determining the location of the MAA carboxylic groups has a weakness, which will be discussed in more detail below (see Figure 4.21).

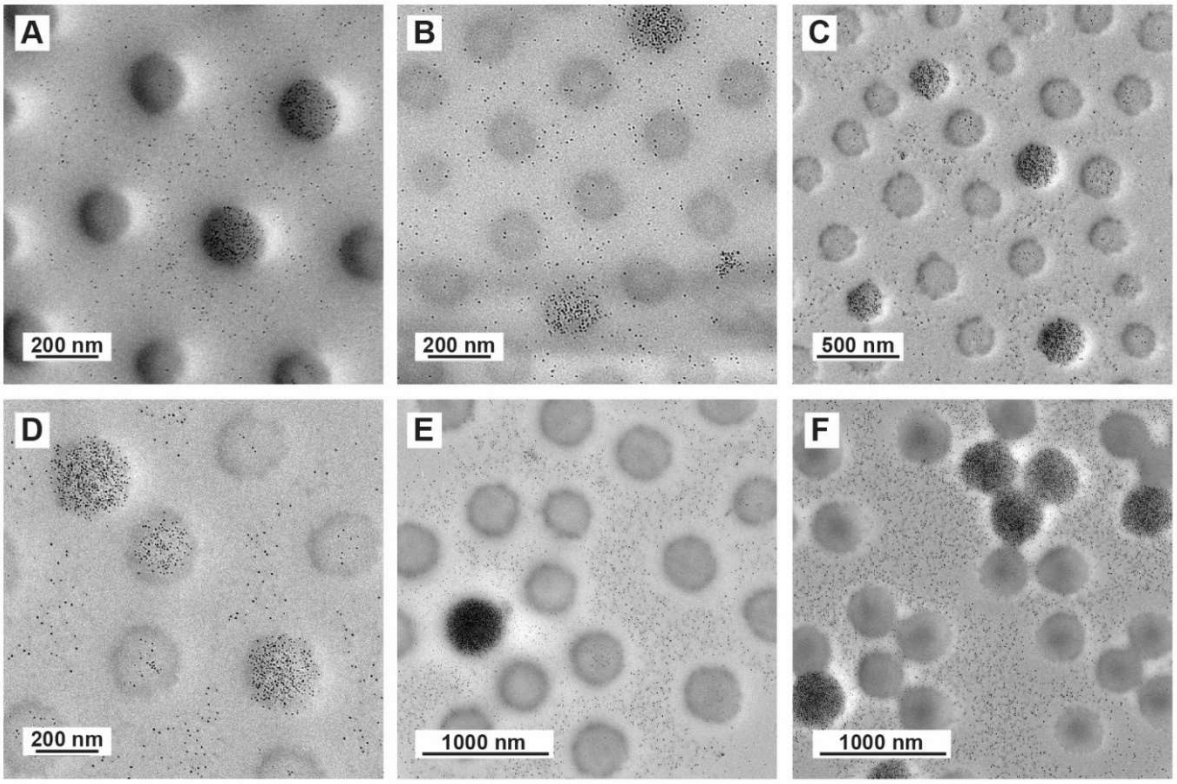

Figure 4.19 P(NIPAM-co-MAA) core microgels synthesized with different chemical compositions. These microgels were prepared with 5% mol MAA and different amounts of crosslinker: A) 5%, B) 4%, and C) 1% mol BIS. On the other hand, these microgels were prepared with 1% mol BIS and different amounts of charged monomer: D) 5%, E) 15%, and F) 30% MAA. All images were taken by regular TEM measurement.

To remove any doubt regarding the inhomogeneous distribution of MAA among the microgels, additional characterizations using various methods were performed. First, cryo-TEM was used to image the microgels in their native condition. It turns out that the inhomogeneous distribution of ferritin in microgels was also observed in the cryo-TEM image (Figure 4.20A). The result proves that the problem was not due to a drying effect, which probably occurred when the microgel sample was prepared on the TEM grid. Next, gold nanoparticles (AuNPs), which are stabilized with a mixture of neutral and positively charged ligands (Figure 4.20B), were used as a substitute for Ce-Ftn$^{(pos)}$ during the integration into microgels. Here, the AuNPs were also inhomogeneously distributed among the microgels (Figure 4.20C). This result indicates that Ce-Ftn$^{(pos)}$ is not the cause of the problem. The problem remained even if we substituted Ce-Ftn$^{(pos)}$ with AuNPs.

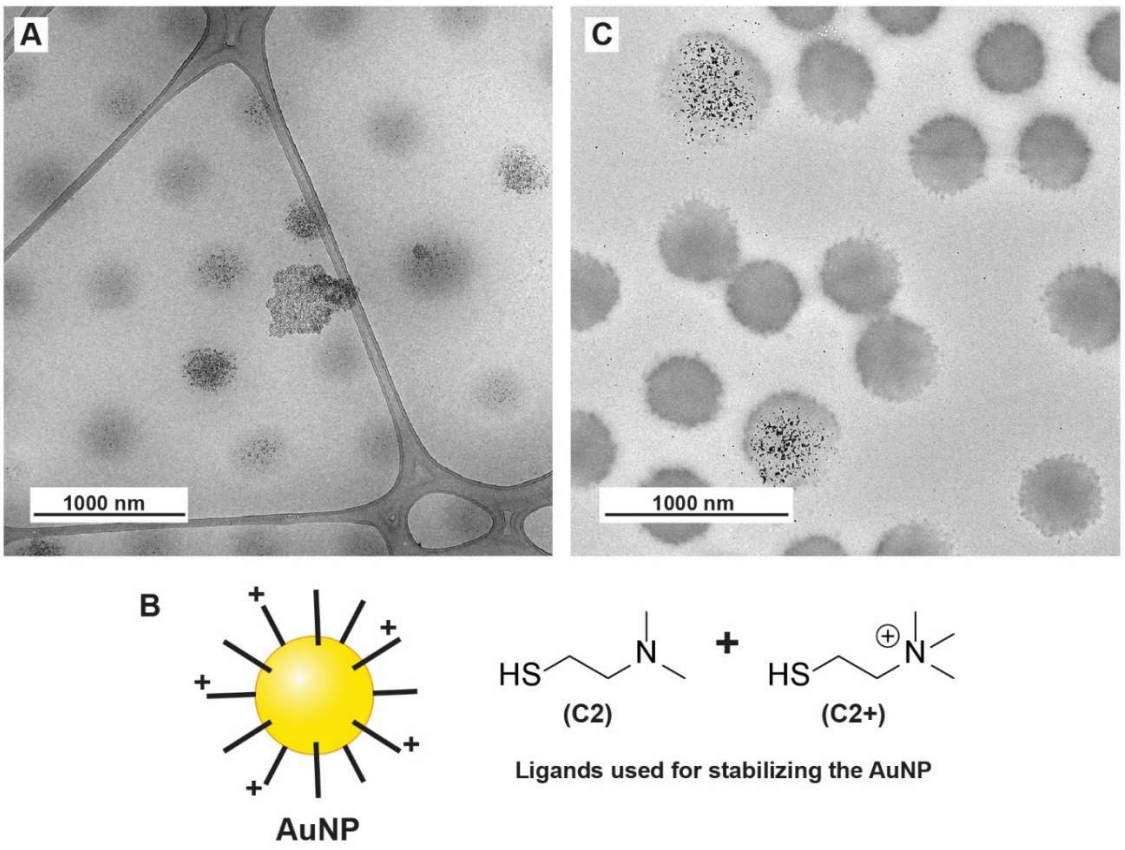

Figure 4.20 Further experiments to confirm the inhomogeneous distribution of ferritin in microgels. A) The integration of Ce-Ftn$^{(pos)}$ into P(NIPAM-co-MAA) (94% : 5% : 1% mol BIS) microgels as characterized by cryo-TEM. B) Positively charged AuNP used in the subsequent experiment. The ligands are: 2-(Dimethylamino)ethanethiol (C2) and (2-mercaptoethyl)-N,N,Ntrimethylammonium (C2+). C) The integration of AuNPs into P(NIPAM-co-MAA) (84% : 15% : 1% mol BIS) microgels as characterized by regular TEM.

Subsequently, the microgels were stained with uranyl acetate solution and imaged with regular TEM measurement. In principle, the positively charged uranyl cations will bind to the negatively charged carboxylic group of MAA in the microgels and produce darker color in TEM measurement. In this way, the position of MAA in the microgels can be localized. Again, here two types of microgel populations were observed (Figure 4.21A). It is believed that these two microgel populations originated from the microgels that contained a large number and a few number of MAA groups.

For comparison, the microgels were also stained with the staining protocol used by Hoare *et al*. (Figure 4.21B).[173] With this staining protocol, the microgels became smaller and resembled the result reported by Hoare (Figure 4.21C). However, this staining protocol may lead to an incorrect conclusion, as the microgels were immersed in uranyl acetate for two hours before dropped and left dried on a TEM grid. With a long contact time, all microgels were filled with uranyl acetate solution, and during the drying process, the uranyl cations remained inside the microgels. Above, we only applied a brief contact time between uranyl acetate solution and the microgels, therefore the uranyl cations mainly stained the microgels which contained a lot of MAA groups. In this way, the two microgel populations can be distinguished.

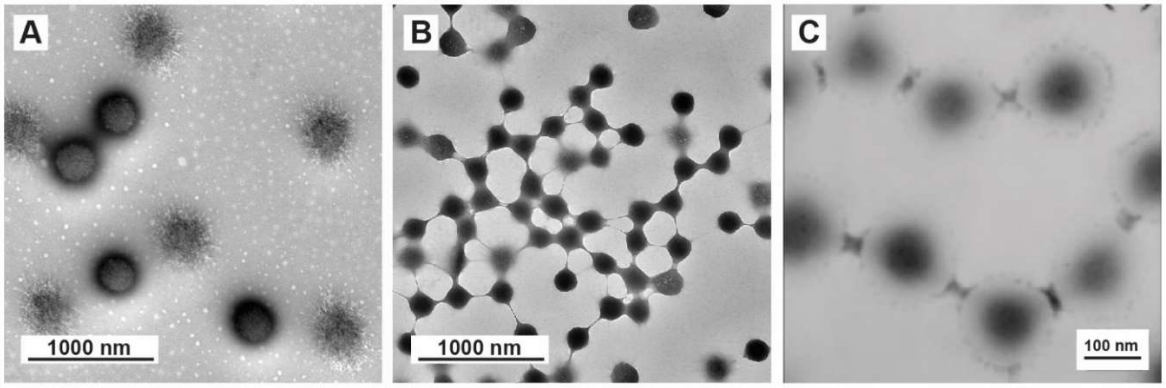

Figure 4.21 Probing the location of MAA groups in microgels by uranyl acetate staining. P(NIPAM-co-MAA) (84% : 15% : 1% mol BIS) microgels stained by: A) Brief-contact staining protocol, B) Immersion staining protocol. C) P(NIPAM-co-MAA) (89.55% : 5.7% : 4.75% mol BIS) microgels stained by uranyl acetate as reported by Hoare *et al.*[173] According to the publisher, the reuse of this image requires no license as it is only a part of a figure. All images were taken by regular TEM measurements.

Next, DLS was used to measure the size of P(NIPAM-co-MAA) microgels in solutions of different pH. At higher pH values, the carboxylic groups of MAA are ionized and they repel to each other, as a result, the size of microgels increases. If the microgels contain different numbers of MAA groups, they will have different sizes at higher pH values. In the extreme case, two peaks should be observed in the DLS measurement, which originates from the two microgel populations. This is the idea behind the characterization. The results show that the microgels were very monodisperse in water (Table 4.6). As expected, increasing the pH of the microgel solution increased the size of the microgels. However, the two distinct peaks were not observed. Probably the size difference was not large enough, and the DLS resolution was not enough to distinguish them as two peaks. Nevertheless, the PDI also increased in higher pH values. This is already an indication that the microgels contained different numbers of MAA groups. Interestingly, at a very low pH, the microgels became monodisperse again. This can be rationalized by the fact that most of the MAA groups were protonated at low pH. With fewer number of ionized carboxylic groups, the size of microgels also decreased.

Table 4.6 The sizes of P(NIPAM-co-MAA) (94% : 1% : 5% mol BIS) microgels at different pH

Solutions	PDI	Size (nm)	Solutions	PDI	Size (nm)
In water	0.008	467.2 ± 101.4	In pH 9.0	0.144	532.2 ± 139.5
	0.014	466.1 ± 102.1		0.125	534.4 ± 140.6
	0.033	466 ± 102.9		0.136	534.8 ± 144.3
In pH 8.0	0.114	496.3 ± 126.8	In pH 2.5	0.023	381.8 ± 91.38
	0.125	495.4 ± 130		0.056	375.2 ± 97.95
	0.129	502.6 ± 126.1		0.024	372.5 ± 78.56

Finally, the microgels were characterized by fluorescence microscopy. Here, P(NIPAM-co-MAA) microgels were loaded with a positively charged polypeptide labeled by GFP: GFP-[Val-Pro-Gly-Lys-Gly]$_{36}$, which is abbreviated as K36-GFP. The polypeptide chain forms a coil with a length of about 10 nm and a diameter of 3 nm. It has a molecular weight of 46521.435 g/mol, which is about eleven times lighter than ferritin. The integration was performed similarly to the Ce-Ftn$^{(pos)}$. The resulting microgels then were spin-coated on a coverslip and observed under fluorescence microscopy. The results show that all the microgels were labeled with the protein (Figure 4.22B). However, they show different brightness (fluorescence intensity), which also an indication of the different loading of K36-GFP inside the microgels. Again, this is only possible if the microgels contain different numbers of MAA groups.

As a summary, the cause of the inhomogeneous distribution of ferritin among the microgels has been identified. This is due to the inhomogeneous distribution of MAA groups among the microgels. Additional evidence was also obtained from various characterizations: cryo-TEM, staining the microgels with positively charged AuNPs or uranyl acetate, DLS measurement, and fluorescence microscopy. Although the last two characterizations did not give very strong evidence compared to the first characterizations, they also indicate the inhomogeneous distribution of MAA groups among the microgels.

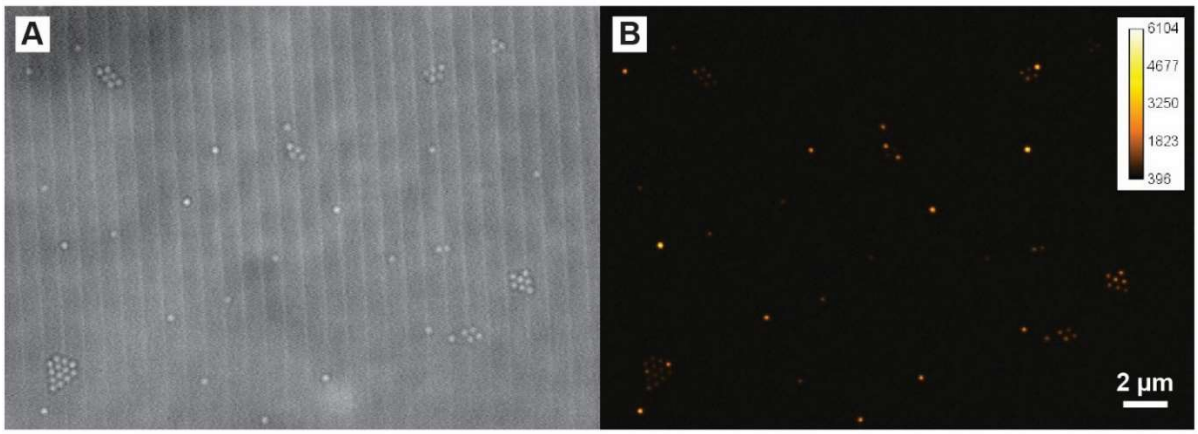

Figure 4.22 P(NIPAM-co-MAA) (84% : 15% : 1% mol BIS) microgels loaded with K36-GFP. A) Brightfield image of the resulting microgels, which appeared as white circles. B) The fluorescence image of the same area observed in A), taken with an excitation wavelength of 488 nm.

4.1.2.2.3 Overcoming the inhomogeneous distribution of charged groups in microgels

Having discovered the causes of the inhomogeneous distribution of ferritin among the microgels, the next question is how to produce charged core microgels with a homogeneous distribution of charged monomers. This section describes our attempts in this direction. First, microgel synthesis with a semi-batch approach was tested. Next, the microgel synthesis was performed at different pH. Finally, a purification technique was applied to separate the charged microgels from the uncharged microgels.

First of all, it is necessary to understand how the MAA groups could end up only in certain microgels and not in all the microgels. For this, I hypothesized that the MAA monomers prefer to react with themselves than with NIPAM monomers. As MAA is present in a limited amount in the solution (5% - 30%), it is used up faster than NIPAM, and finally, it ends up only in certain microgels. This hypothesis was supported by the following experiments.

Here, a semi-batch microgel synthesis was used. The MAA monomer was injected into the polymerization reaction over a certain period. The idea was to spread the MAA among the microgels. Ce-Ftn$^{(pos)}$ then were integrated into the resulting microgels to detect the distribution of MAA groups in the microgels. With the semi-batch approach, no obvious accumulation of MAA groups in certain microgels was detected (Figure 4.23B-E). By increasing the MAA feeding time, more MAA was found on the periphery of the microgels (Figure 4.23E). On the other hand, if NIPAM was injected into the polymerization reaction instead of MAA, the inhomogeneous distribution of MAA groups among the microgels was observed (Figure 4.23F). Based on these results, it is concluded that MAA groups accumulated in certain microgels only when they were present in the solution at high concentrations. This fact supports our hypothesis that MAA prefers to react with itself than with NIPAM.

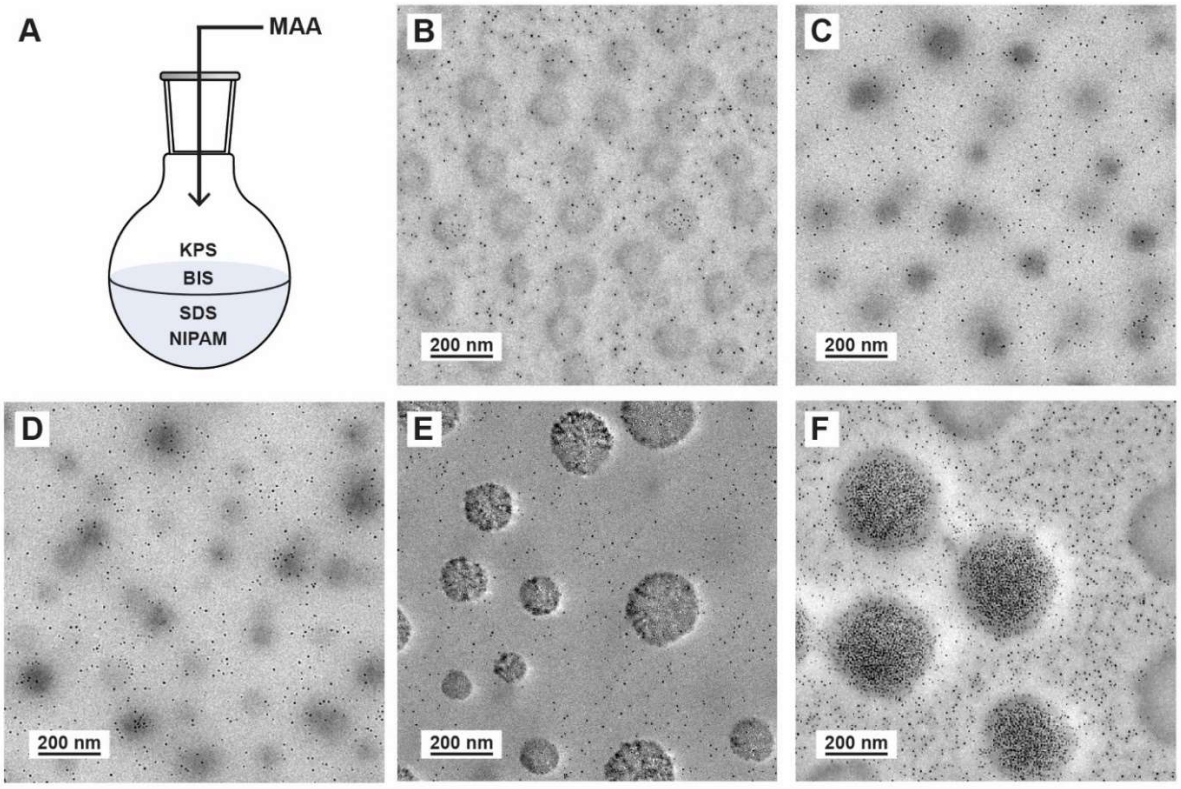

Figure 4.23 Synthesis of P(NIPAM-co-MAA) microgels by semi-batch approach. A) Semi-batch synthesis. MAA was injected dropwise to the polymerization reaction over a certain period of feeding time: B) 5 min, C) 10 min, D) 20 min, E) 30 min. F) MAA was put in the flask, and NIPAM was injected into the polymerization reaction in 10 minutes. All the electron micrographs were taken by regular TEM measurement.

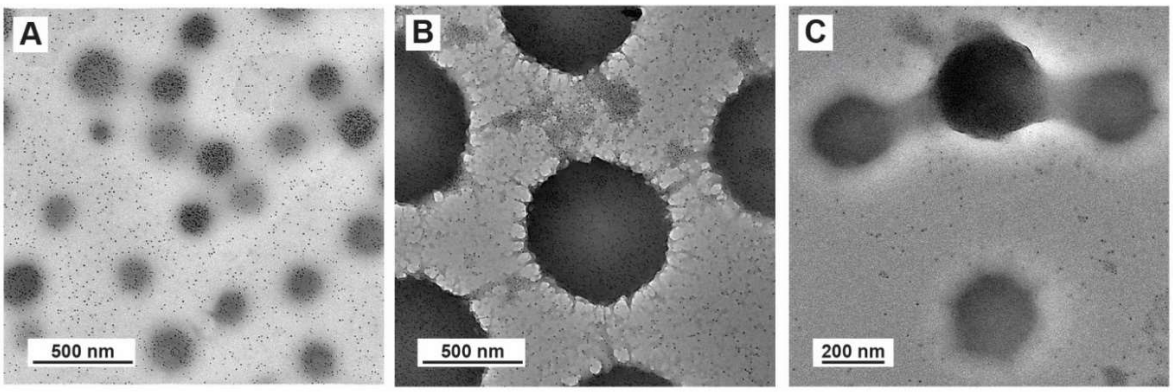

Figure 4.24 Inhomogeneous distribution of ferritin observed in other microgels. A) P(NIPMAM-co-AA) (88% : 10% : 2% mol BAC) microgels integrated with Ce-Ftn$^{(pos)}$. Inhomogeneous distribution of ferritin was observed in this microgel, although not as severe as in P(NIPAM-co-MAA) microgels. B) P(NIPAM-co-VIM) (89% : 10% : 1% BIS) microgels, synthesized without pH adjustment (at pH 8.3). Ferritin was homogeneously distributed among the microgels. C) P(NIPAM-co-VIM) (89% : 10% : 1% BIS) microgels synthesized at pH 3.0. The inhomogeneous distribution of ferritin was also observed in this microgel. For B) and C) the microgels were integrated with Fe-Ftn$^{(neg)}$.

It is also important to note that the inhomogeneous distribution of charged monomers among the microgels are mainly found in microgels with negatively charged monomers: P(NIPAM-co-MAA) or P(NIPAM-co-AA) microgels (Figure 4.24A). This problem usually does not occur in microgels with positively charged monomers, such as P(NIPAM-co-VIM) microgels (Figure 4.24B). However, in certain cases, the inhomogeneous distribution of VIM among the microgels was also observed. For example, when the microgel synthesis was performed at pH 3.0, instead of at the natural pH of VIM at 8.3 (Figure 4.24C).

Seeing this result, next I tried to perform the synthesis of P(NIPAM-co-MAA) microgels at different pH. As before, Ce-(Ftn)^{pos} was integrated into the resulting microgels to locate the distribution of MAA groups in the microgels. The results show that the inhomogeneous distribution of MAA also occurred in microgels synthesized at higher pH value, although the number of MAA groups incorporated in the microgels decreased with increasing pH (Figure 4.25). This can be related to the fact that more MAA groups are ionized at higher pH values. With more repulsion between the carboxylic groups, the tendency of MAA groups to react with each other decreases, therefore in the end fewer MAA groups are located in the microgels. Moreover, the resulting microgels solution became more transparent with the increasing pH. This is because the size of microgels decreased when synthesized at higher pH values.

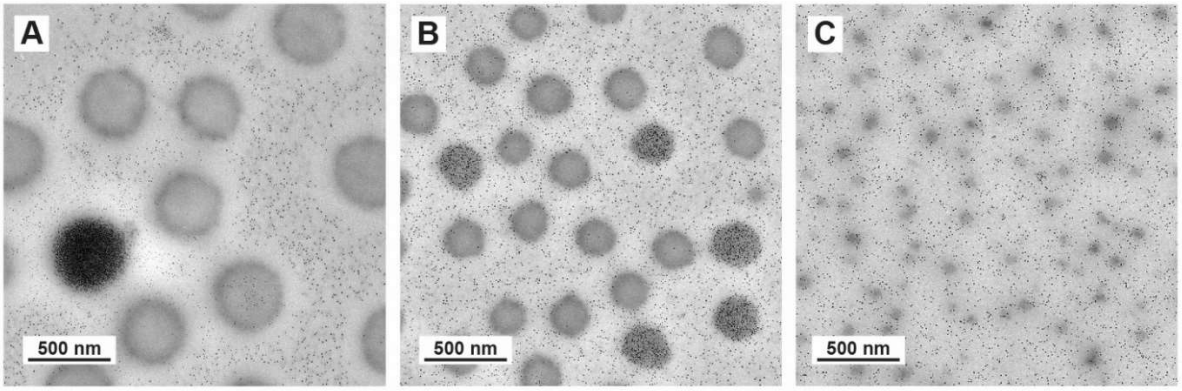

Figure 4.25 Synthesis of P(NIPAM-co-MAA)(84% : 15% : 1% mol BIS) microgels at different pH. A) Synthesis without pH adjustment (at pH 2.5). B) Synthesis at pH 4.0. C) Synthesis at pH 5.0. The resulting microgels then were integrated with Ce-Ftn$^{(pos)}$. All images were taken by regular TEM measurements.

The optimization of microgel synthesis by trial and errors to obtain the desired microgel properties is laborious and ineffective. However, Schneider *et al.* has recently reported the synthesis of vinyl-ferrocene (VFc) containing PNIPAM microgels (P(NIPAM-co-VFc)) by using a model-based design synthesis.[181] With this approach, they could determine the synthesis procedures required to produce microgels with the desired localization of the VFc monomers. For example, they could produce microgels with VFc monomers localized in the core, in the shell, or homogenously distributed in the microgels. Model-based design synthesis could be a solution to overcome the inhomogeneous distribution of charged monomers among the microgels. Therefore, for future work, a collaboration could help to build a suitable model-based design synthesis for our system. This was originally planned. However, due to the time constraints and also related to the Covid-19 outbreak, it was not carried out.

As currently core microgels with a homogeneous distribution of negatively charged monomers cannot be produced, I investigated the possibility to separate the charged microgels from the uncharged microgels by IEC. First, P(NIPAM-co-MAA) microgel solution was injected into a positively charged IEC column. The IEC chromatogram (Figure 4.26A) shows that most of the microgels just flowed through the column (Fraction 01, Fr-01). Only a small fraction of the microgels bound to the column, which later could be released by a gradient salt elution (Fraction 02, Fr-02). Both microgel fractions were collected separately. Next, Ce-Ftn$^{(pos)}$ was integrated into both of the microgel fractions to investigate the distribution of MAA groups in the microgels.

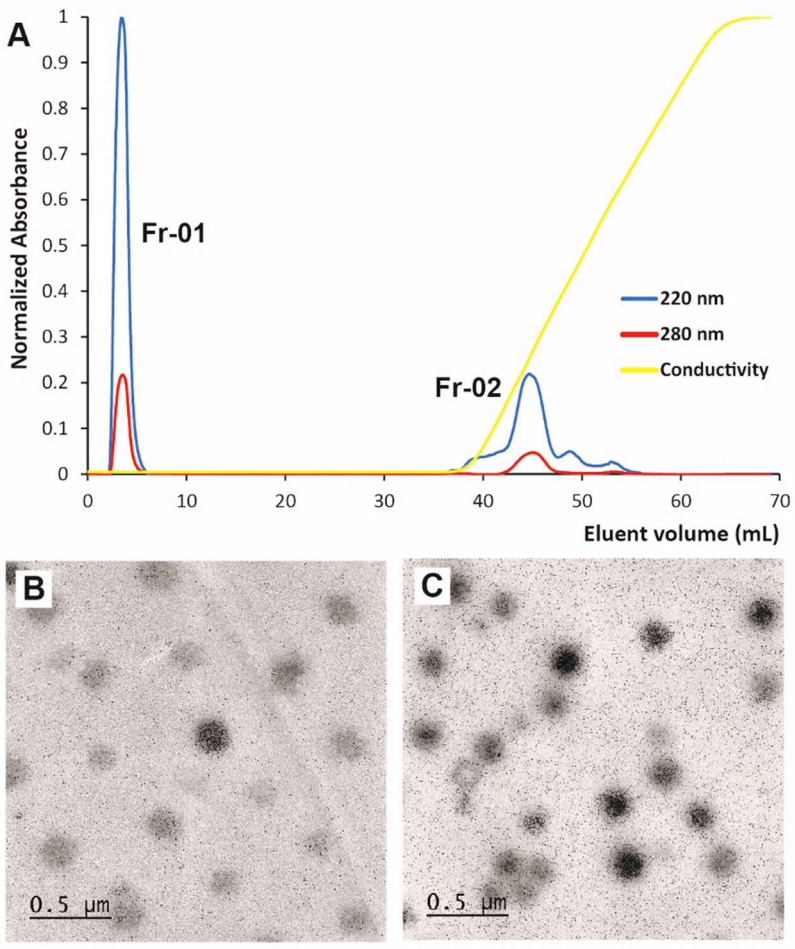

Figure 4.26 Separation of charged and uncharged microgel fractions by IEC. A) IEC chromatogram of P(NIPAM-co-MAA) (94% : 5% : 1% mol BIS) microgels. Both fractions were collected separately, integrated with Ce-Ftn$^{(pos)}$, and characterized by TEM: B) Fraction 01, C) Fraction 02.

As predicted, the TEM characterizations show that Fr-01 and Fr-02 mainly contained the uncharged and the charged microgels fractions, respectively (Figure 4.26B-C). However, the ideal separation between the two microgel fractions was not obtained. A few charged microgels were observed in Fr-01, and likewise, a few uncharged (or less charged) microgels were observed in Fr-02. This is because only the charges on the surface of microgels are required for the binding with the IEC column, while the charges in the interior of microgels do not play a role in binding. In other words, the charged microgels observed in Fr-01 directly flowed through the column because they do not have MAA groups on their surface. On the other hand, the uncharged microgels observed in Fr-02 bound to the column because they have MAA groups on the surface, while do not have many MAA groups in their interior. The result of this experiment is another proof of the inhomogeneous distribution of MAA groups among the microgels.

As the charged microgels can be separated from the uncharged microgels, for future experiments, microgels with a more homogeneous distribution of MAA groups among the microgels can be produced. Furthermore, they can be used as seeds in the subsequent microgels synthesis to add the

neutral shell. In this way, a homogeneous charged core and neutral shell microgels could be obtained. However, it must be admitted that this approach is not so efficient. As only a small fraction of the resulting microgels are charged, a large-scale microgel synthesis is required to produce enough charged core microgels. Moreover, most of the resulting microgels are uncharged and thus wasteful.

In summary, various approaches have been tried to produce microgels with a homogeneous distribution of charged monomers. The semi-batch approach did not solve the problem, but it provided further insight into the synthesis: MAA groups only accumulate in certain microgels when they are present in the solution at high concentrations. Changing the pH of microgel synthesis was not the solution either. Model-based design synthesis could be a way to solve this problem. As an alternative, the charged and the uncharged microgels can be separated by IEC. Although this approach worked, it has low efficiency.

4.1.2.2.4 Overcoming ferritin leakage from the microgels

In the earlier section (Chapter 4.1.2.2.1), it was shown that the integration of ferritin into core-shell microgels also suffered from ferritin leakage. To address this problem, Sarah Wypysek came up with an idea to synthesize charged core microgels that have locking-shells to prevent ferritin leakage (Figure 4.27A). One way to produce this locking shell is by copolymerizing NIPAM with a more nonpolar monomer such as *tert*-butyl acrylamide (tBAM). It has been reported that the copolymerization of NIPAM with more than 40% mol tBAM decreased the volume phase transition temperature (VPTT) of microgels to below room temperature. If this material is used as a shell for a charged core microgel, the integration of ferritin into the microgels can be performed at low temperatures. Later, if the microgels are raised to room temperature, the shell will collapse and prevent ferritin leakage. To enable ferritin release, a degradable crosslinker can be introduced during the microgel synthesis. However, one possible challenge that may be encountered in this system is the instability of the microgels. Because the shell collapses, the stability of the microgels decreases. To overcome this potential problem, a second PNIPAM shell or PEG chains can be introduced to the microgels after the locking shell. This research plan was developed in collaboration with Sarah Wypysek and Simon Schog (Institute of Physical Chemistry, RWTH Aachen).

First, charged core microgels were produced by the copolymerization of N-isopropylmethacrylamide (NIPMAM) and the positively charged monomer DMAPMA. Here NIPMAM was used instead of NIPAM because it has a higher VPTT (45 °C) than NIPAM (32 °C). With higher VPTT, the resulting microgels will not collapse when used as drug delivery vehicles in the body. Moreover, the positively charged DMAPMA is used instead of the negatively charged MAA because it is easier to obtain a homogeneous distribution of charged monomers among the microgels with positively charged monomers. Fe-Ftn$^{(neg)}$ then was integrated into the resulting microgels to localize the distribution of DMAPMA in the

microgels. TEM characterization shows that DMAPMA was homogeneously distributed among the microgels (Figure 4.27B). Next, these P(NIPMAM-co-DMAPMA) microgels were used as core seeds in the subsequent synthesis of the locking shell composed of 60% NIPAM and 40% mol tBAM. However, the synthesis of the shell was not successful. Instead of building shells on the existing core seeds, the reacting monomers preferred to undergo secondary nucleation and formed smaller microgels (Figure 4.27C), which is a common problem in the synthesis of core-shell microgels.

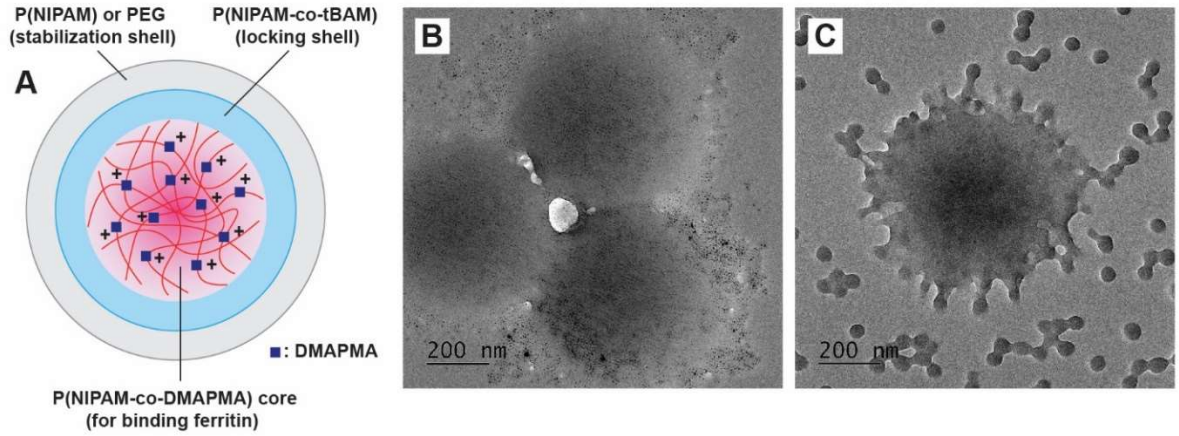

Figure 4.27 Microgel with a locking shell. A) Schematic drawing of the core-shell-shell microgel. B) P(NIPMAM-co-DMAPMA) (88% : 10% : 2% BAC) microgel core, integrated with Fe-Ftn$^{(neg)}$ to locate the distribution of DMAPMA in the microgels. C) The resulting microgels after the synthesis of the locking shell P(NIPAM-co-tBAM).

This research plan was not pursued further. However, recently Brugnoni *et al*. reported the synthesis of temperature-sensitive nano-capsules composed of hollow microgels stabilized by P(NIPAM) shells.[242] This system is very similar to our system because the hollow microgels, which were produced by the copolymerization of NIPAM and DAAM, also have a low VPTT below room temperature. This property enables the hollow microgels to control their permeability: It swells on moderate cooling and de-swells at room temperature. Therefore, DAAM potentially could be used as locking-shells in our system if the research plan will be continued in the future.

4.1.2.3 Immobilization of ferritin during microgel synthesis

The integration of ferritin into core-shell microgels, as described in the previous section, was characterized by the inhomogeneous distribution of ferritin among the microgels and the ferritin leakage. To overcome this problem, another approach was used. Previously, ferritin was integrated into readily synthesized microgels. Here, ferritin was immobilized during the microgel synthesis. It is expected that ferritin will be trapped inside microgels, therefore solves the leakage problem.

For the integration of ferritin into microgels, the favorable interactions between the outer surface of ferritin and the charged co-monomers were utilized. In particular, the positively charged co-monomer

(VIM) was used to facilitate the integration of Ce-Ftn$^{(neg)}$ into microgels (Figure 4.28). To obtain a stimuli-responsive material, an acid cleavable crosslinker (VOU) was used in the synthesis. This crosslinker will enable ferritin release in acidic environments. This could be useful for drug delivery application as ferritin can be released in the acidic environment of the lysosome (pH 4-5)[221] once the microgels are internalized by cells.

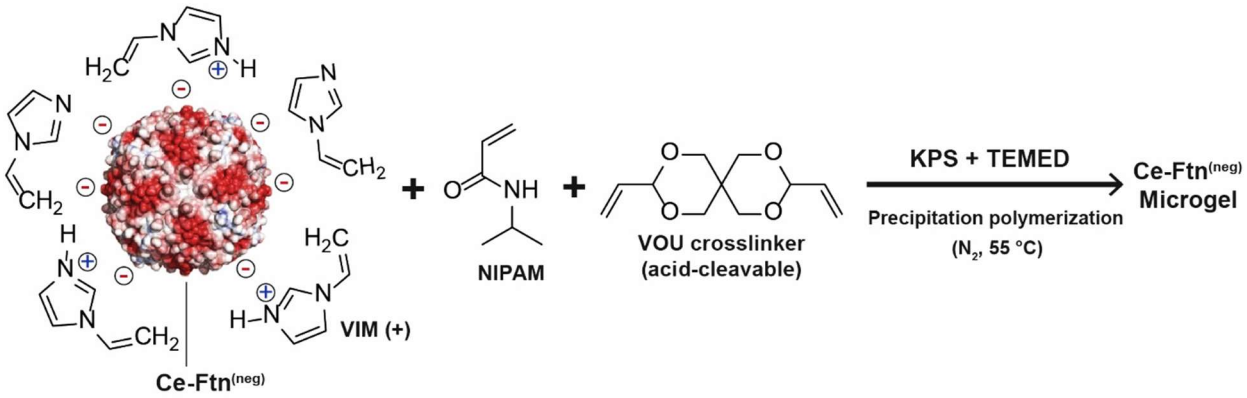

Figure 4.28 The synthesis scheme of Ce-Ftn$^{(neg)}$ microgel. This figure illustrates the strategy to immobilize ferritin during the microgel synthesis.

For the microgel synthesis, several optimizations were necessary to achieve a procedure ideally suited for the integration of ferritin containers. KPS is commonly used to initiate the precipitation polymerization at high temperatures (> 70 °C). However, these reaction conditions were known to cause self-crosslinking in PNIPAM microgels.[243,244] Self-crosslinking is unfavorable for a microgel that is supposed to be degraded to enable cargo release. To overcome this limitation, the precipitation polymerization was performed at a lower temperature (55 °C) using a redox initiator system composed of KPS and TEMED. These reaction conditions were reported to prevent NIPAM self-crosslinking.[190]

However, the synthesis of microgels at lower temperatures often results in large microgels in the range of 0.8 – 4 µm, in particular when semi-batch approaches are used.[183] For drug delivery applications, small-size microgels are advantageous as cells prefer to internalize small objects. Recently, Switacz *et al.* has reported that the size of microgels and the amount of crosslinker are crucial for the uptake by cells. They showed that microgels with sizes larger than 800 nm and containing 10-15 % mol crosslinkers were not taken up by cells.[245] Moreover, smaller size microgels are favorable for the enhanced permeability and retention (EPR) effect, which has been reported to improve the accumulation of DDS in tumor tissues.[246,247] Surfactants, such as SDS, can be applied to reduce the size of microgels.[248] Nevertheless, this is not suitable for my system as SDS reduced ferritin loading in microgels (Figure 4.29) and denatures protein at higher concentrations.[249]

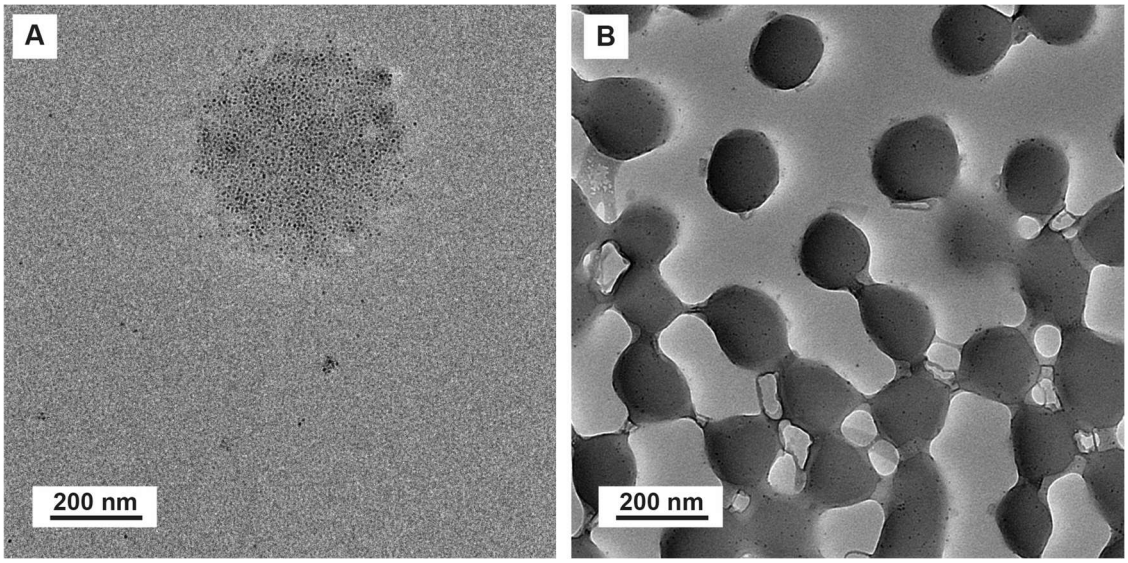

Figure 4.29 Influence of SDS for the synthesis of ferritin microgels. These TEM images show the earlier attempts to synthesis Fe-Ftn$^{(neg)}$ microgel by semi-batch approach at high temperature: A) Without SDS. B) With 0.23 mM SDS. Later, Ce-Ftn$^{(neg)}$ was used to get a better contrast.

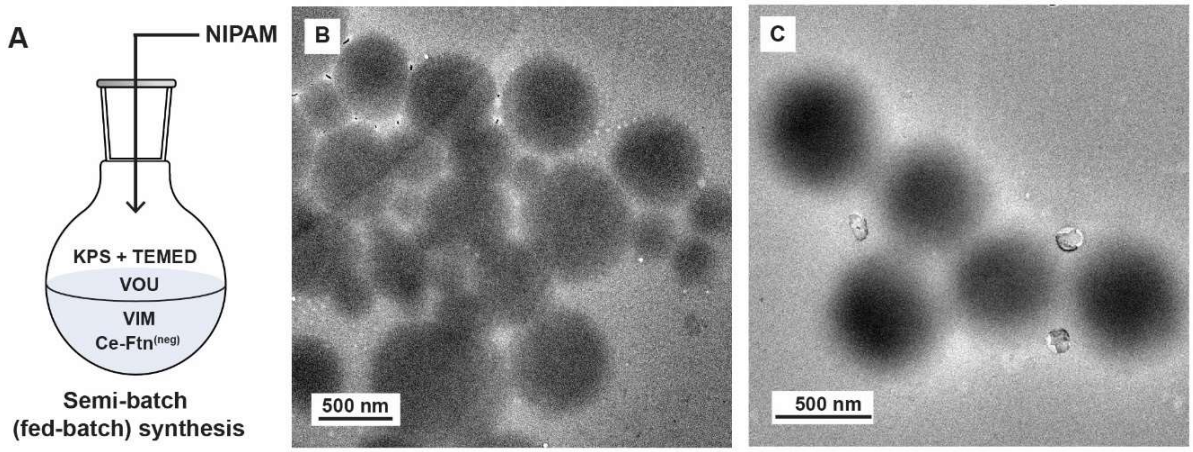

Figure 4.30 Semi-batch microgel synthesis. A) Reaction scheme. These are TEM images of: B) Microgels obtained by semi-batch synthesis if the reaction was started with no NIPAM in the pot. C) Microgels that were obtained if the reaction was started with a certain concentration of NIPAM in the pot. Both reactions were performed with empty Ftn$^{(neg)}$ instead of Ce-Ftn$^{(neg)}$ to save some material. The amount of NIPAM was kept constant in both reactions.

To obtain microgels smaller than 1 µm, both the number of the growing nuclei and the volume of NIPAM feed were controlled during the semi-batch synthesis (Figure 4.30A). Here, NIPAM was added dropwise into the pot (reaction mixture) over a certain period. If the reaction was started with no NIPAM in the pot, polydisperse microgels were obtained (Figure 4.30B). This is because, during the NIPAM injection, new nucleation occurred continuously along with the growth of the microgel. As a result, nuclei that formed earlier in the reaction produced microgels with larger sizes than nuclei that formed later in the reaction. However, monodisperse microgels can be achieved if the reaction was started with a certain concentration of NIPAM in the pot and the remaining NIPAM was injected after the solution became cloudy. Here, the nucleation occurred simultaneously at the beginning of the

reaction. The later injection mainly helped the existing nuclei to grow, therefore monodisperse microgels were obtained (Figure 4.30C).

The synthesis in Figure 4.30C was repeated by using Ce-Ftn$^{(neg)}$ and the resulting microgels are shown in Figure 4.31. All the microgels were filled with Ce-Ftn$^{(neg)}$, which indicates that Ce-Ftn$^{(neg)}$ was successfully integrated into microgels. Due to the effective integration, only a few ferritin containers were found outside microgels, and they were easily removed by simple centrifugation. Importantly, there was no sign of ferritin leakage from the microgel. If ferritin leaked out, microgels could not be completely purified from the unbound ferritin.

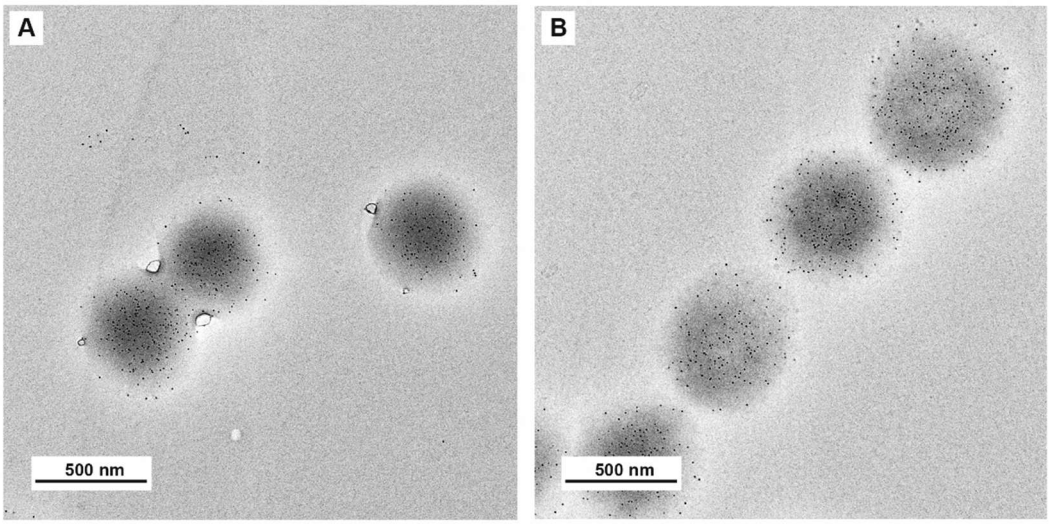

Figure 4.31 Ce-Ftn$^{(neg)}$ microgels obtained from semi-batch synthesis. A) Before purification. B) After purification by centrifugation. All images were taken by regular TEM measurement.

Next, the resulting microgels were characterized with DLS measurements. The results show that the resulting microgel was monodisperse with a hydrodynamic diameter of ~1000 nm (Table 4.7). The obtained diameter is larger than what was observed in the TEM image. A possible explanation is that microgels swelled in solution and collapsed in the dried state on the TEM grid. However, further confirmation by cryo-TEM shows that the size of the microgel is only around 600 nm (Figure 4.32A). To explain this size discrepancy, I hypothesize that the microgels can form clusters in solution, which sizes were averaged in DLS measurement. The ζ-potential and the electrophoretic mobility of the microgels as measured by DLS were ~+18.4 mV and 1.44 µmcm/Vs, respectively (Table 4.8). These results can be rationalized with the surface exposure of the positively charged imidazole groups of the VIM monomer. Furthermore, the microgels collapsed with increasing temperature, and the VPTT was determined as about 36 °C (Figure 4.32B).

Table 4.7 The size of Ce-Ftn$^{(neg)}$ microgels at 20 °C as determined by DLS

PDI	Size (nm)	Std. dev. (nm)
0.039	1025	179.1
0.049	1033	175.5
0.005	1056	180.2

Table 4.8 ζ-potential and electrophoretic mobility of Ce-Ftn$^{(neg)}$ microgels as measured by DLS

ζ-Potential (mV)	Standard dev. (mV)	Electrophoretic mobility (µmcm/Vs)	Standard dev. (µmcm/Vs)
+18.2	3.43	1.425	0.269
+18.7	3.51	1.469	0.275
+18.4	2.64	1.440	0.207

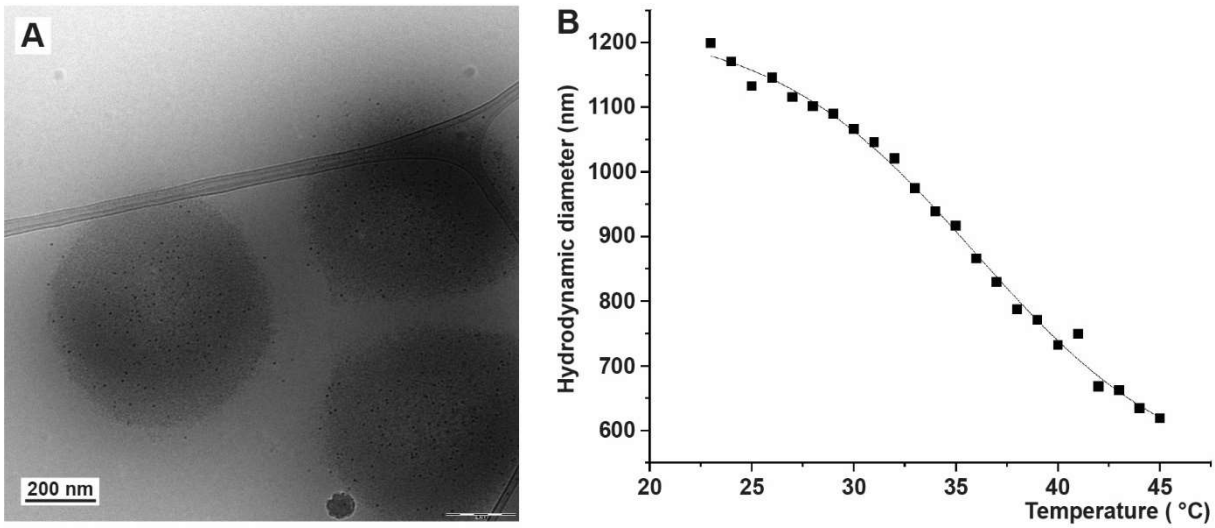

Figure 4.32 Further characterizations of Ce-Ftn$^{(neg)}$ microgels. A) Cryo-TEM image of Ce-Ftn$^{(neg)}$ microgels. B) The size-temperature dependence of Ce-Ftn$^{(neg)}$ microgels. The VPTT was determined from the inflection point of the Sigmoidal-Boltzman curve fit (black line): 35.96 ± 5.02 °C.

As conventional TEM images are 2D projections of a 3D object, they could not provide us the information about the 3D distribution of Ce-Ftn$^{(neg)}$ inside the microgels. To obtain this information, electron tomography was applied. In this technique, microgels were deposited on a TEM grid, and then a tilt series of High-Angle Annular Dark-Field Scanning Transmission Electron Microscopy (HAADF-STEM) images were recorded. These images then were used to reconstruct the 3D volume of the microgel, which can be presented as a still image or a rotating video of the microgels viewed from different angles.

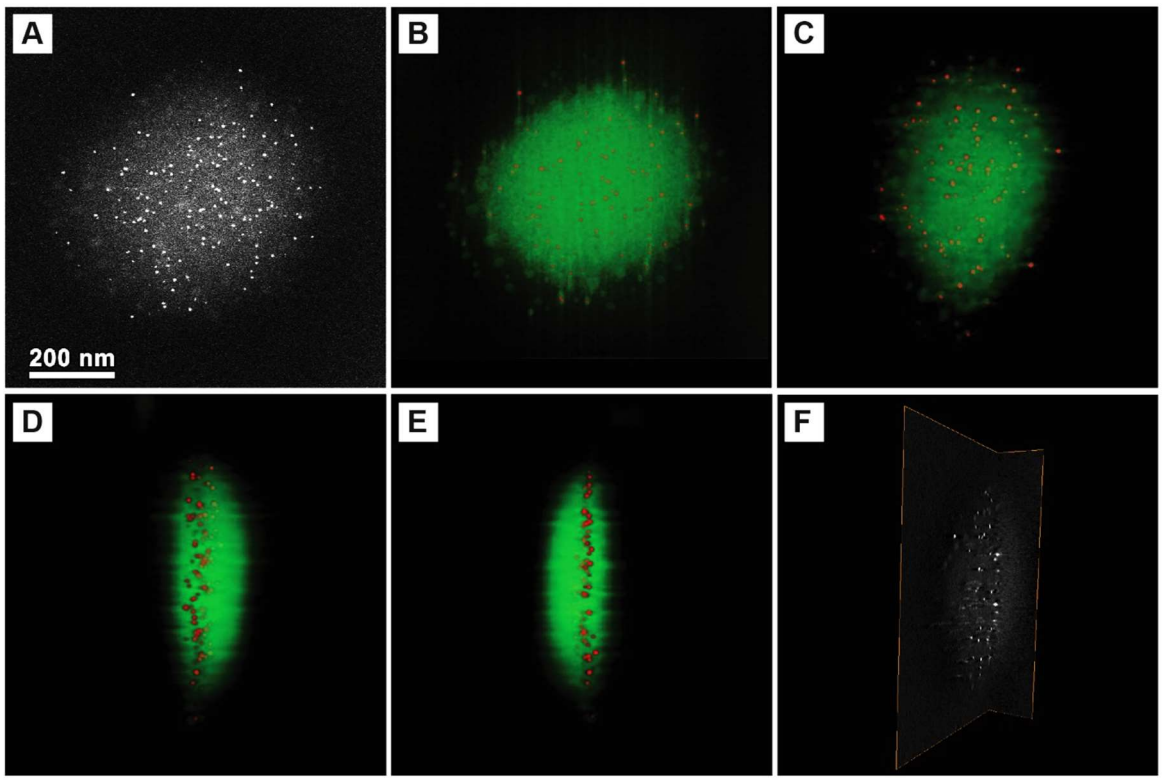

Figure 4.33 Electron tomography analysis of Ce-Ftn$^{(neg)}$ microgel. A) Z-contrast HAADF-STEM image of a Ce-Ftn$^{(neg)}$ microgel. B) Reconstructed volume of the same Ce-Ftn$^{(neg}$ microgel, frontal view. The microgel volume was colored green, while the cerium oxide NPs were highlighted in red. In figures C-E, the reconstructed volume was rotated counterclockwise and viewed from different angles. F) Orthoslice through the reconstructed volume confirming the Ce-Ftn$^{(neg)}$ to be inside the microgel matrix.

Figure 4.33A is an example of the Z-contrast HAADF-STEM images of Ce-Ftn$^{(neg)}$ microgels that were used to reconstruct the final volume. In HAADF STEM mode, elements with higher atomic numbers appear brighter than elements with lower atomic numbers. The bright dots are the cerium oxide NPs inside the ferritin containers, while the lower contrast object corresponds to the polymeric material of the microgel. Figure 4.33B-E shows the reconstructed volume looked from different angles. These images show that due to its nature as a soft material, the microgel was heavily deformed when deposited on the TEM grid. It looks like an egg on a frying pan. Because of the heavy deformation, almost all the NPs were located nearly on the same plane close to the TEM grid. As a result, the information about the 3D distribution of Ce-Ftn$^{(neg)}$ within the microgel was lost. Nevertheless, the results give another information. The ortho-slice through the reconstructed volume provides clear and direct evidence of the integration of Ce-Ftn$^{(neg)}$ inside the volume of microgel Figure 4.33F).

Microgels with sizes smaller than 1 µm were also achievable by batch synthesis (Figure 4.34A). In this approach, NIPAM and all the other ingredients were put in the pot and the reaction was started at once by adding the initiator. The benefit of this approach is that the nucleation occurs simultaneously at the beginning of the reaction and the growing process follows afterward, therefore the resulting microgels were highly monodisperse (Figure 4.34B-C). In Figure 4.34D-E, Ce-Ftn$^{(neg)}$ microgels obtained

by batch and semi-batch approaches were compared. Under the employed reaction conditions, batch approaches produced smaller and more monodisperse microgels than the semi-batch approaches. However, the amount of ferritin loading also greatly depends on the volume of microgels. Larger microgels contained more ferritin per microgel volume than the smaller ones. Therefore, for future applications in drug delivery, it is advisable to use larger size microgels.

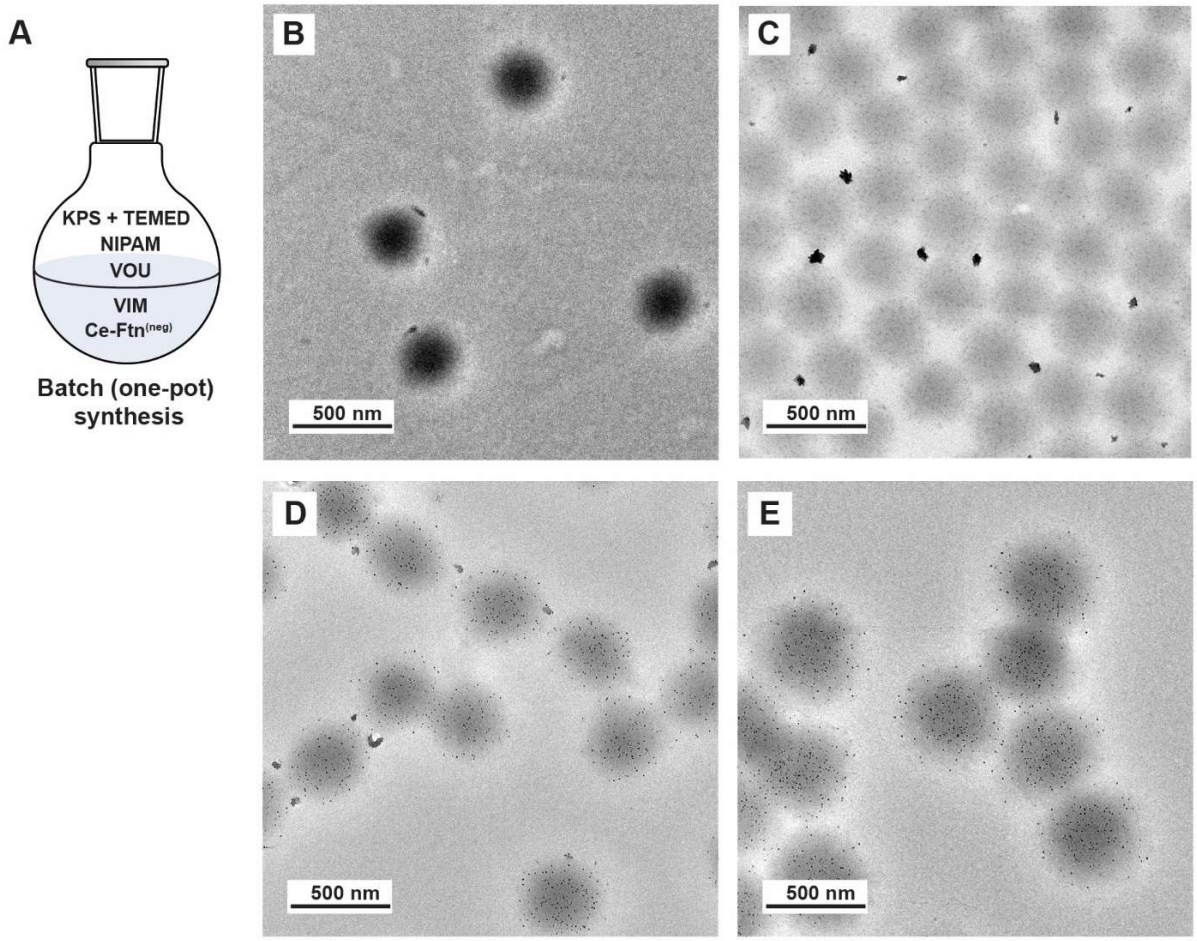

Figure 4.34 Batch microgel synthesis. A) Reaction scheme. B) and C) Microgels obtained from batch synthesis. Here, the reaction was performed with empty Ftn$^{(neg)}$ instead of Ce-Ftn$^{(neg)}$ to save some material. D) Ce-Ftn$^{(neg)}$ microgels obtained from batch synthesis. E) Ce-Ftn$^{(neg)}$ microgels obtained from semi-batch synthesis. All the electron micrographs were taken by regular TEM measurements.

As a control reaction, a semi-batch synthesis was performed without VIM. The result shows that Ce-Ftn$^{(neg)}$ was not integrated into the microgels due to the weak molecular interactions between NIPAM and Ce-Ftn$^{(neg)}$ (Figure 4.35). This control reaction indicates that VIM is necessary for the integration of Ce-Ftn$^{(neg)}$ into the microgels. A similar result was also reported by Hu *et al.*, who were able to integrate avidin protein into PNIPAM microgel only by using an acrylated version of avidin. Without the acrylation, the integration did not work.[190]

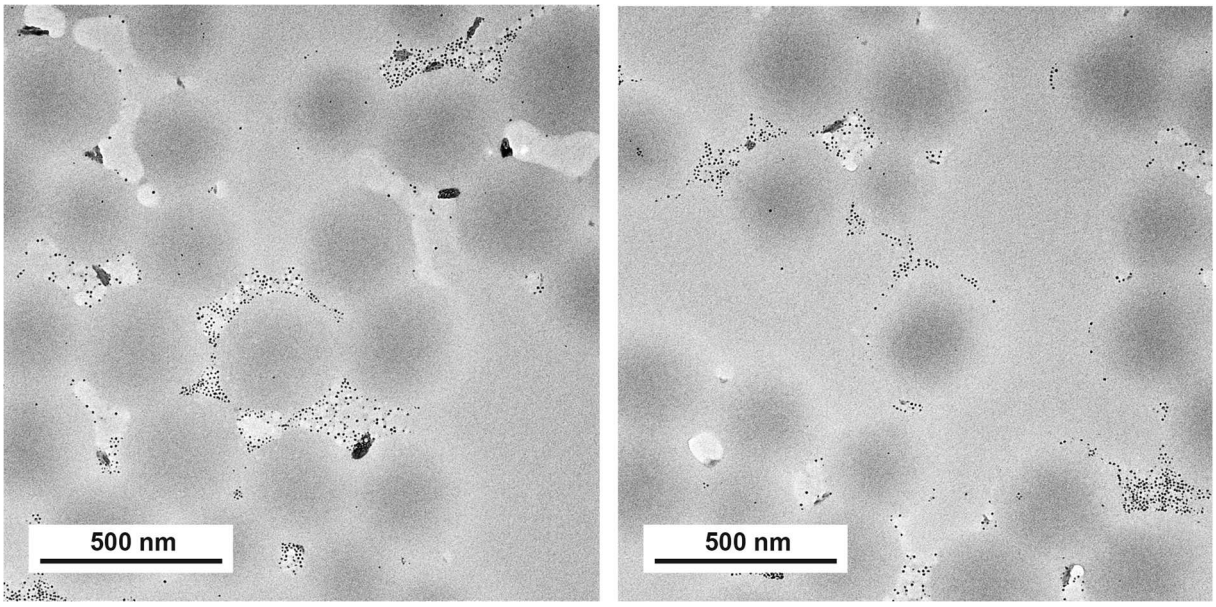

Figure 4.35 Ce-Ftn$^{(neg)}$ microgels synthesized without using the positively charged co-monomer VIM. Most of Ce-Ftn$^{(neg)}$ were found outside the microgels. The integration of Ce-Ftn$^{(neg)}$ into the microgels was not successful. Both images were taken by regular TEM measurements.

In summary, by performing the integration of ferritin during the microgel synthesis, several problems were overcome simultaneously. First, ferritin leakage was not observed in this system as the microgels bound the ferritin tightly inside. Ferritin was also homogeneously distributed among the microgels. This is because they were bound to the VIM monomer, which is well distributed among the microgels. Moreover, the resulting microgels can easily be purified from the unbound ferritin by centrifugation. To obtain microgels with favorable sizes for cell internalization, both batch and semi-batch synthesis can be applied. In general, batch synthesis results in smaller microgels. However, the amount of ferritin loading is also related to the size of microgels. Larger microgels can integrate more ferritin. One disadvantage that was observed in this system is that the microgels tend to cluster together in solution, which reminds us about the flocculation that occurred when ferritin was integrated into microgels with randomly distributed ionic groups. I hypothesize that this problem can be overcome by adding a stabilization shell, as previously observed in the core-shell microgels.

4.1.3 Ferritin release from microgels

In the previous section, the synthesis of a protein-microgel system with an acid-degradable crosslinker has been established. To investigate the stimuli-responsiveness of this system, the release of ferritin from microgels in acidic solution will be studied in this section. The VOU crosslinker is expected to be cleaved in acidic conditions and ferritin can be released because the microgels are degraded or their mesh sizes become larger. This section is divided into three parts according to the characterization methods that were used to study the ferritin release.

4.1.3.1 Study of ferritin release by TEM

The release of NPs-loaded ferritin from microgels can easily be followed by TEM. First, the Ce-Ftn$^{(neg)}$ microgels prepared by semi-batch synthesis were incubated in acidic solutions for certain periods. Afterward, the Ce-Ftn$^{(neg)}$ release was analyzed by TEM. Two acidic buffer solutions were used. Buffer pH 4.0 was used to mimic the acidic environment in the lysosome, while buffer pH 2.5 was used to obtain accelerated release. VOU was reported to be cleaved faster in a more acidic solution.[186]

TEM measurements show that the Ce-Ftn$^{(neg)}$ was already released from microgels within 5 minutes (Figure 4.36B-C). The free ferritin was observed as black dots next to the microgels. Furthermore, the release increased if lower pH or longer incubation time was used (Figure 4.36B-D). These results indicate a successful release, although it was not possible to fully degrade the microgels and release all the Ce-Ftn$^{(neg)}$ even by prolonged incubation in pH = 2.5 for 5 days (Figure 4.36D). Although reaction conditions leading to the self-crosslinking of NIPAM have been avoided by using low reaction temperature and a redox initiator system, it seems that self-crosslinking could also occur through other mechanisms.[244] For example, Mc Phee *et al.* explained it by polymer chain entanglement.[189]

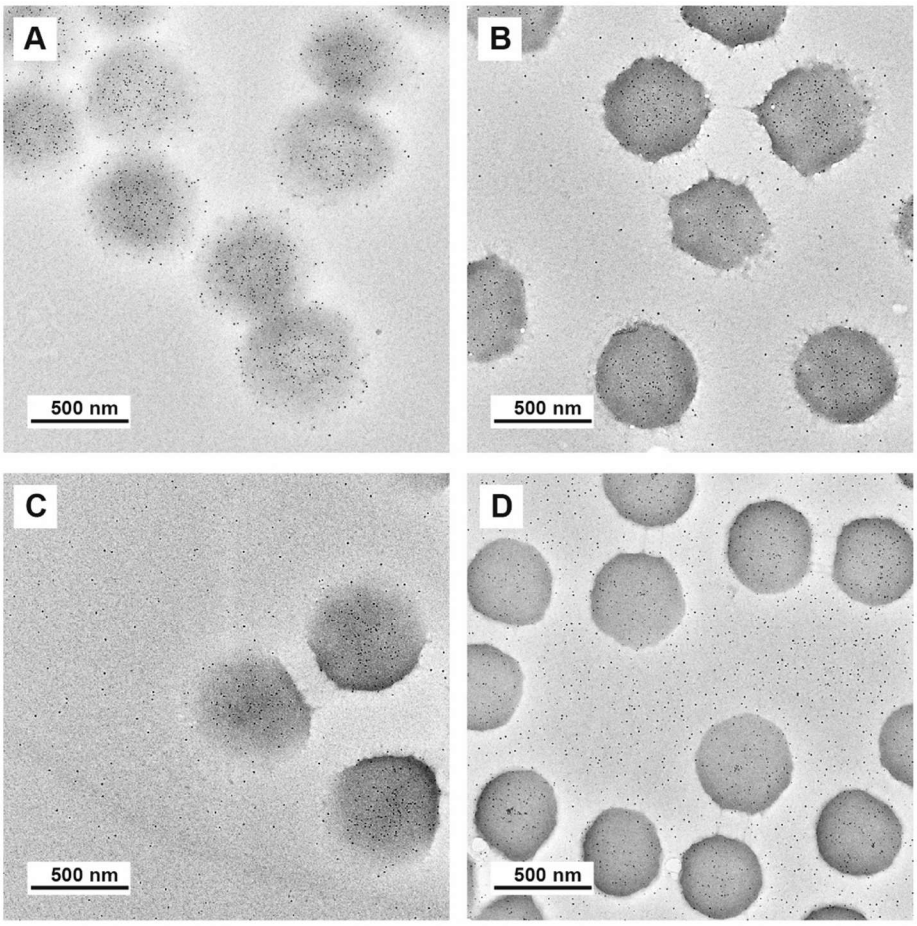

Figure 4.36 Ce-Ftn$^{(neg)}$ release from microgels after incubation in acidic solution. A) Before release. B) pH = 4, 5 min. C) pH = 2.5, 5 min. D) pH = 2.5, 5 days. All images were taken by regular TEM measurements.

4.1.3.2 Study of ferritin release by UV/Vis spectroscopy

Compared to NPs-loaded ferritin, fluorophore-loaded ferritin also offers some benefits for studying ferritin release from microgels. First, the ferritin loading and release can be quantified by UV/Vis. Furthermore, it also allows us to follow the release process *in situ*. Therefore, here two types of fluorophore-loaded ferritin microgels were synthesized: AF 488-(Ftn$^{(neg)}$-1C) and AR 6G-(Ftn$^{(neg)}$-1C) microgels. The microgel syntheses were performed in a similar way as the synthesis of Ce-Ftn$^{(neg)}$ microgels and they yielded a successful integration of ferritin containers (Figure 4.37). This is the first proof that ferritin can be used as a modular approach in this hybrid system: Different cargos can be loaded into the ferritin containers and later integrated into the microgels. The AF 488-(Ftn$^{(neg)}$-1C) microgels were also synthesized under reaction conditions that caused NIPAM self-crosslinking (KPS, at 70 °C). This was to investigate if the current synthesis method by redox initiator system (KPS and TEMED, at 55 °C) improved the release properties of the microgels.

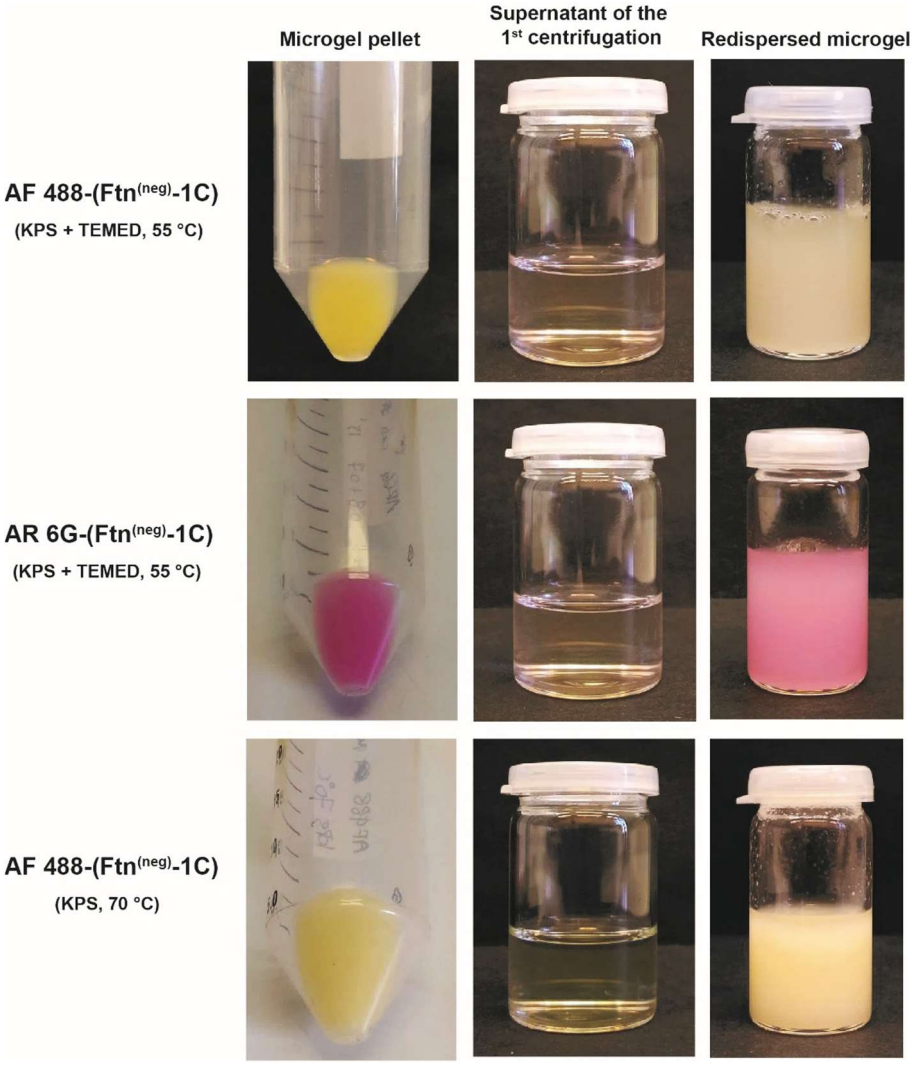

Figure 4.37 Fluorophore-loaded ferritin-loaded microgels. These microgels were synthesized to quantify ferritin loading and release from microgels by UV/Vis spectrometry, and also to study *in-situ* ferritin release by fluorescence microscopy. The intense color of the microgel pellet and the faint color of the supernatant after the first centrifugation indicate successful ferritin integration to the microgels.

To get more insight into the ferritin release, the release under different incubation solutions was first investigated (Table 4.9). Here, the AR 6G-(Ftn$^{(neg)}$-1C) microgels were used because it has an intense red color, which is easier to be recognized by eyes, compared to the AF 488-(Ftn$^{(neg)}$-1C) microgels which have a yellow color. The same amount of AR 6G-(Ftn$^{(neg)}$-1C) microgels were incubated for 5 minutes in different solutions and then centrifuged down (Figure 4.38A). As a result, the microgels formed a pellet at the bottom of the Eppendorf tubes. The absorption of the supernatant then was measured at 536 nm, which indicates the amount of ferritin release from microgels.

Table 4.9 AR 6G-(Ftn$^{(neg)}$-1C) release from microgels after incubation in different solutions

Solutions	Absorption (@536 nm)
Water	negligible
Salt (150 mM NaCl)	0.0224
Acid only (50 mM glycine buffer pH 2.5)	0.2460
Acid + Salt (50 mM glycine buffer pH 2.5; 150 mM NaCl)	0.2472

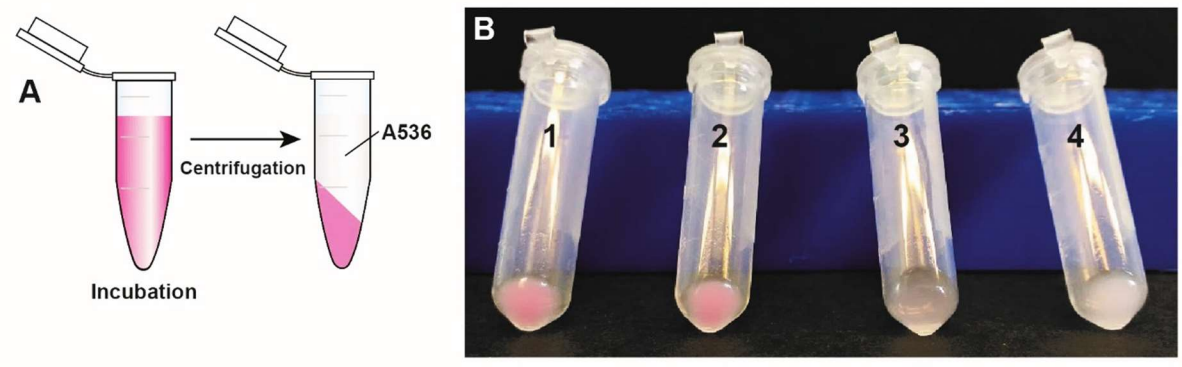

Figure 4.38 Ferritin release in different solutions. A) Experimental scheme. B) The color of microgel pellets obtained after ferritin release in different solutions: 1) Water, 2) Salt (150 mM NaCl), 3) Acid only (50 mM glycine buffer pH 2.5), 4) Acid + salt (50 mM glycine buffer pH 2.5; 150 mM NaCl).

The results show that in water no ferritin was released (Table 4.9). This finding is in accordance with our previous observation in TEM, that there was no Ce-Ftn$^{(neg)}$ leakage after the purification, which is important for the later drug delivery applications. The addition of salt at the physiological concentration (150 mM NaCl) caused some ferritin release, which probably comes from the ferritin containers bound by electrostatic interactions to the surface of microgels or loosely trapped inside the microgels. The release increased drastically when microgels were incubated in an acidic solution. However, further salt addition did not significantly improve the release. It is believed that this is because below its isoelectric point (pI ~4.2) Ftn$^{(neg)}$-1C becomes positively charged. This means that in pH 2.5 both VIM and ferritin have a positive charge and will repel each other. As there was no

electrostatic attraction present anymore, the addition of salt did not significantly improve the release. The results presented in Table 4.9 are also confirmed by the color of the pellet (Figure 4.38). With more ferritin release, the pink color of the pellets is reduced.

Next, the time-dependent release of ferritin in acidic solutions was investigated (Table 4.10). The experiments were performed similarly as depicted in Figure 4.38A. Here, the incubation times were varied. The results show that there was no significant difference in ferritin release between 5 minutes and longer incubation times. This finding was observed both at pH 4.0 and pH 2.5, which means that the cleavage of VOU crosslinkers occurred very fast, within 5 minutes. This observation, however, is different from the results reported by Zhang *et al.*, who developed acid-degradable micelles with the same VOU crosslinkers. They observed a complete degradation of their micelles in 30 minutes and 12 hours under incubation in pH 2.0 and 4.0, respectively.[186] A slight increase in ferritin release was noticed after the incubation for 6 days in pH 2.5. To explain this, it is hypothesized that some ferritin containers were deeply trapped inside the microgels and require more time to diffuse out of the microgels.

Table 4.10 Time-dependent release of AF 488-(Ftn$^{(neg)}$-1C) in acidic solutions

Release in glycine buffer pH 2.5		**Release in acetate buffer pH 4.0**	
Incubation time	**Absorption (@500 nm)**	**Incubation time**	**Absorption (@500 nm)**
0 min	negligible	0 h	negligible
5 min	0.2010	1 h	0.1120
10 min	0.2154	2 h	0.1103
20 min	0.2083	4 h	0.1110
30 min	0.2016		
20 h	0.2173		
6 days	0.2670		

Furthermore, the amount of ferritin loading and release from microgels was quantified by UV/Vis spectroscopy. In this experiment, the AF 488-(Ftn$^{(neg)}$-1C) microgels were used because the UV/Vis spectrum of AF 488 before and after the maleimide coupling reaction with cysteines inside ferritin are almost the same. Therefore, AF 488 is more reliable than AR 6G to be used for quantification. For the AR 6G-(Ftn$^{(neg)}$-1C), a shoulder peak was formed after the coupling reactions. It was concerned that this shoulder peak could affect the intensity of the main peak, and thus the reliability of the quantification.

The amount of ferritin loading into the microgel was estimated as follows. After the synthesis, the resulting microgel solution was centrifuged to separate microgels from the unbound ferritin. As a result, the microgels formed pellet at the bottom of the centrifuge tube, while the unbound ferritin remained in the supernatant. Next, the amount of the unbound ferritin was determined by measuring the UV/Vis absorption of the supernatant. By subtracting the initial amount of ferritin used in the synthesis and the amount of the remaining ferritin in the supernatant, the ferritin loading was obtained. Here, it was assumed that all the unbound ferritin was removed from the microgels during centrifugation. Subsequently, by dividing the amount of ferritin loading with the total mass of the resulting microgels, the mass percentage of ferritin content was obtained. Moreover, ferritin release was estimated similarly as the experiment explained in Figure 4.38A. However, the absorption of the supernatant was further used to determine the amount of ferritin release. By dividing the amount of released ferritin by the amount of ferritin integrated into the microgels, the percentage of ferritin release or more precisely the percentage of releasable ferritin was obtained. For the release conditions, similarly as before, 5 minutes incubation in buffer pH 2.5 or 4.0 was used.

As shown in Table 4.11, ferritin was effectively integrated into microgels. Almost 80% of the ferritin containers used during synthesis were integrated into the microgels. Interestingly, almost 85% of the integrated ferritin was releasable in pH 2.5. Moreover, compared to the synthesis using KPS at 70 °C, the synthesis with a redox initiator system at a lower temperature improved both the ferritin content and the release of ferritin. It is believed that the release improved due to the suppression of the self-crosslinking in NIPAM. The results also show that ferritin release in pH 2.5 is higher than the release in pH 4.0. This can be attributed to the faster cleavage of VOU in lower pH or to the fact that ferritin cages also disassemble in pH 2.5.

Table 4.11 Estimation of ferritin uptake and release from microgels in acidic solutions

Microgels	Initiator	Ftn loading[a]	Ftn content[b]	Release pH	Ftn release[c]
AF 488-(Ftn$^{(neg)}$-1C)	KPS, 70 °C	71.8%	1.4 % (w/w)	2.5	68.2%
AF 488-(Ftn$^{(neg)}$-1C)	(KPS + TEMED), 55 °C	77.82%	4.7% (w/w)	2.5	84.8%
AF 488-(Ftn$^{(neg)}$-1C)	(KPS + TEMED), 55 °C	77.82%	4.7% (w/w)	4.0	52.1%

[a] Relative to the initial amount of ferritin used during synthesis. [b] Relative to the total mass of the material (ferritin-microgels). [c]Relative to the amount of incorporated ferritin in the microgel.

4.1.3.3 Study of ferritin release by fluorescence microscopy

Complementary to the study of ferritin release by TEM measurements, here ferritin release was analyzed by Widefield Fluorescence Microscopy. Figure 4.39 shows panels of a brightfield image displaying a cluster of microgels and the corresponding fluorescence images at the same area. The

dark spots in Figure 4.39A indicate the microgels' positions, which then show fluorescence in Figure 4.39B-D due to the presence of AF488-(Ftn$^{(neg)}$-1C) inside the microgels. The intensity of these fluorescence signals was analyzed to compare the relative amount of ferritin that remained in the microgels. The microscopy images in Figure 4.39A-B were recorded immediately after the spin-coating, whereas the images shown in Figure 4.39C-D were recorded in acetic buffer pH 4.0 to trigger the ferritin release. The incubation time in the buffer was 10 min and 15 min, respectively.

Before ferritin release, the microgels showed fluorescence signals with an average intensity of 15831 counts/µm² (Figure 4.39B). After adding the buffer with pH 4.0, the microgels showed a drastically reduced fluorescence intensity (Figure 4.39C: 11225 counts/µm², Figure 4.39D: 6890 counts/µm²), which indicates the release of ferritin. It is also important to note that in Figure 4.39B-D, only single images were taken with reduced laser intensity (LPD = 0,47 kW/cm², 20 ms exposure time, electron-multiplying gain of 200). This setting was chosen to reduce the illumination time of the sample and thereby prevent the bleaching of fluorophores. The observed decreased intensity of the microgels is therefore only caused by the release of ferritin. As already shown by TEM and fluorescence microscopy, the ferritin release from microgels under acidic conditions was a rather fast process.

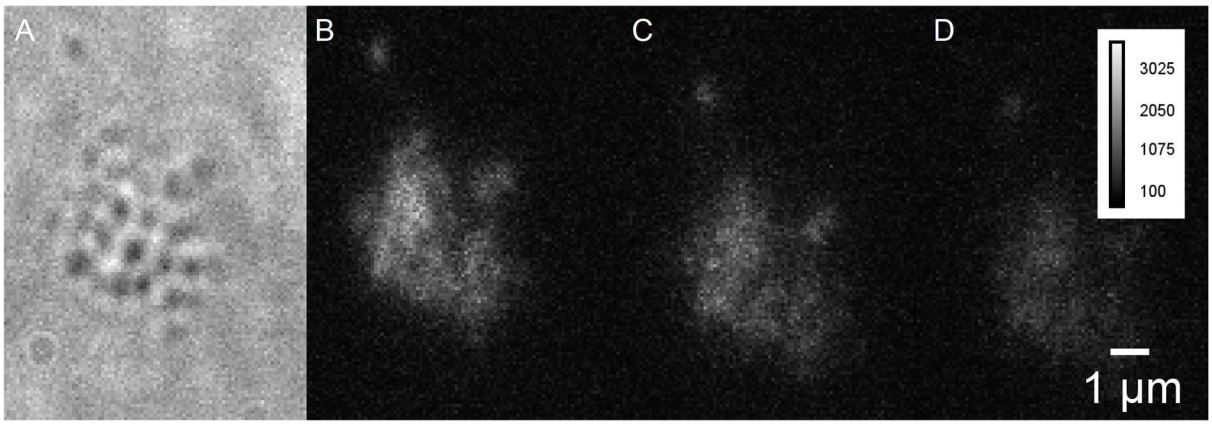

Figure 4.39 Widefield fluorescence microscopy images of AF 488-(Ftn$^{(neg)}$-1C) loaded microgels. A) Brightfield image. B) Fluorescence before the release. The average intensity was 15831 counts/µm^2. C) Fluorescence after 10 min incubation in buffer pH 4.0 (11225 counts/µm^2). D) Fluorescence after 15 min incubation in buffer pH 4.0 (6890 counts/µm^2). The calibration bar shows the fluorescence intensity counts for images (B-D).

As a summary, TEM and fluorescence microscopy results qualitatively show that ferritin can be released from microgels in acidic conditions. The release was a rather fast process and increased in lower pH and with longer incubation time. A complete release and total degradation of microgels, however, was not achieved due to the self-crosslinking of NIPAM. Furthermore, the estimation of ferritin loading and release by UV/Vis indicates that ferritin was very effectively integrated into microgels and a large amount of ferritin can be released from microgels.

4.1.4 Proteolytic degradation of ferritin-microgels

As discussed in the introduction, the application of ferritin containers in biomedical settings is hampered by the degradation of the protein shell in blood plasma. Therefore, the ferritin containers were incorporated into a microgel that should function as a protection shield against proteases. In this section, the stability of the ferritin container, both isolated in solution and integrated into microgel, against proteolytic degradation was investigated. For this purpose, chymotrypsin was used as a model protease. Chymotrypsin is a non-specific protease that can cleave proteins at many different sites, mainly the carboxyl site of large-hydrophobic amino acids (tyrosine, phenylalanine, and tryptophan).[250]

First, the AR 6G-(Ftn$^{(neg)}$-1C) solution was digested with chymotrypsin at 37 °C and the digestion mixture was analyzed by SEC after certain digestion periods (Figure 4.40). The intensity of ferritin peak on the chromatogram decreased with the digestion time. The results indicate that ferritin was digested by chymotrypsin. To estimate the amount of ferritin that remained after the digestion, the area under ferritin peak on the chromatograms was integrated. The results show that only 36% and 12.8% ferritin remained intact after 24 h and 48 h digestion by chymotrypsin, respectively (Table 4.12).

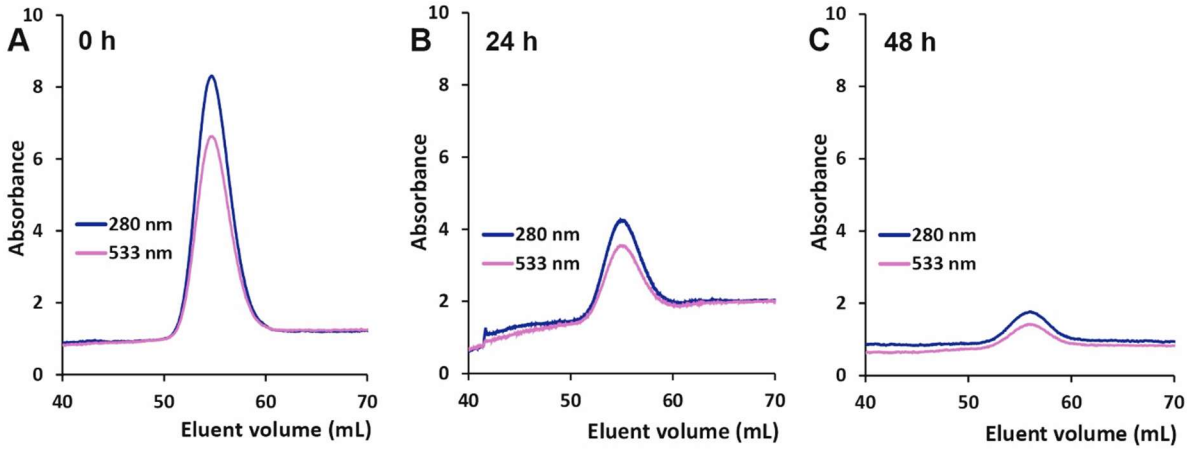

Figure 4.40 SEC chromatograms of AR 6G-(Ftn$^{(neg)}$-1C) before and after digestion by chymotrypsin at 37 °C. A) Before digestion. B) After 24 h. C) After 48 h. The signals at 280 and 533 nm are the signals from ferritin and AR 6G, respectively.

Table 4.12 Analysis of the remaining AR 6G-(Ftn$^{(neg)}$-1C) before and after digestion by chymotrypsin at 37 °C

Digestion time	Ferritin peak area - A280 (mL.mAU)	% Remaining protein	% Digestion
0 h	28.97	100 %	0 %
24 h	10.44	36 %	64 %
48 h	3.71	12.8 %	87.2 %

Next, similar digestion was performed to the AR 6G-(Ftn$^{(neg)}$-1C) that was integrated in the microgels. After a certain period of incubation, the release of AR 6G-(Ftn$^{(neg)}$-1C) from microgels in pH 2.5 was investigated (Figure 4.41). If the microgels cannot protect ferritin from the digestion by chymotrypsin, the ferritin release in pH 2.5 will be reduced as some ferritin have already been degraded and released from the microgels. As a reaction control, the ferritin release from non-digested microgels was also examined.

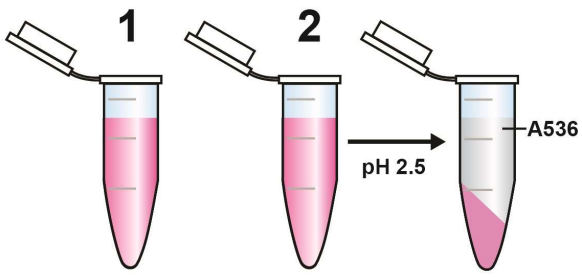

Figure 4.41 Stability test of AR 6G-(Ftn$^{(neg)}$-1C) inside the microgels against degradation by chymotrypsin. This test was performed in two steps: 1) Incubation of AR 6G-(Ftn$^{(neg)}$-1C) microgels by chymotrypsin. 2) Investigation of the ferritin release in pH 2.5.

The results show that after digestion by chymotrypsin, the release of AR 6G-(Ftn$^{(neg)}$-1C) from microgels did not change significantly (Table 4.13, Figure 4.42). This indicates that microgels protect ferritin from the digestion by chymotrypsin. The result can be explained by the fact that the polymer network provided steric hindrances for chymotrypsin to access ferritin. This is even more true at the digestion temperature (37 °C) as the microgels collapsed and therefore protect ferritin even better.

Table 4.13 Comparison of AR 6G-(Ftn$^{(neg)}$-1C) release from microgels in buffer pH 2.5 after digestion by chymotrypsin at 37 °C

	The absorption of the supernatant at 536 nm obtained from		
Step	**Non-digested microgels**	**24 h digested microgels**	**48 h digested microgels**
Release in pH 2.5	0.2494	0.2253	0.2195

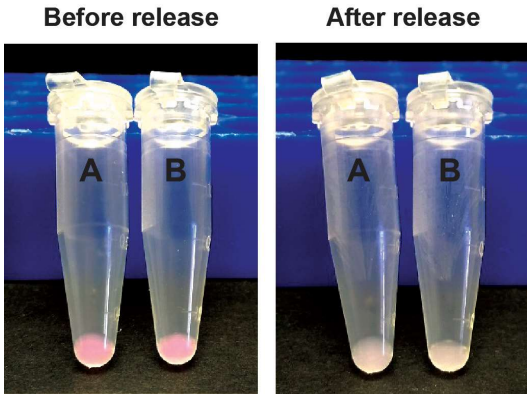

Figure 4.42 The appearance of AR 6G-(Ftn$^{(neg)}$-1C) microgels before and after ferritin release in pH 2.5. A) Non-digested microgels. B) 24 h digested microgels.

4.2 The application of the ferritin-microgel system for drug release and delivery

In this section, the ferritin-microgel system obtained in the previous section will be applied for drug release and delivery. This section is divided into three parts. The first part is about the encapsulation of DOX in ferritin containers. The second part covers the integration of DOX-Ftn into the microgel system. In the last part, the cytotoxicity of DOX-Ftn variants will be investigated.

4.2.1 Encapsulation of doxorubicin in ferritin

For the application of ferritin in drug delivery, first of all, drugs need to be encapsulated in ferritin containers. DOX, one of the most studied cancer drugs, was chosen as a model drug. As described in the earlier section, redesigned and supercharged ferritin containers ($Ftn^{(pos)}$ and $Ftn^{(neg)}$) were used to facilitate the integration of ferritin into microgels. However, because surface modifications were performed to obtain these ferritin variants, there was a concern that the modifications might alter the binding of ferritin to TfR-1 and the subsequent cell uptake. Therefore, in addition to those two variants, DOX was also encapsulated in wild-type ferritin and wild-type ferritin with redesigned cysteine positions. This section will elaborate on the encapsulation of DOX in these ferritin variants.

4.2.1.1 Encapsulation of DOX in $Ftn^{(pos)}$

It has been discussed previously in Chapter 4.1.1.1 that the encapsulation via dis/reassembly approach in acidic conditions cannot be applied to $Ftn^{(pos)}$ as it causes protein precipitation. Therefore, the encapsulation in $Ftn^{(pos)}$ must be performed via diffusion through ferritin channels. In Chapter 3.2.3, some previous works related to this approach have been summarized. For example, Zhen *et al.* employed metal pre-complexation of DOX with Cu(II) cations to facilitate the encapsulation of DOX in HF.[158] Similarly, Ahn *et al.* pre-complexed DOX with Fe(II) cations and encapsulated them into nicked ferritin.[25] Some other treatments, such as pH 5.0,[111] temperature (60 °C),[106] and low concentration of chaotropic salts (2 mM Gua-HCl),[112] also have been reported to enlarge the ferritin channels. It was hypothesized that one or the combination of these approaches could work for the encapsulation of DOX in $Ftn^{(pos)}$. Here, several optimizations were performed to find the best way to encapsulate DOX in $Ftn^{(pos)}$.

First, the best experimental conditions to enlarge the channels of $Ftn^{(pos)}$ need to be determined. For this, $Ftn^{(pos)}$ was initially incubated with the Fe(II)-DOX complex in different conditions known to enlarge the ferritin channels. Fe(II)-DOX was expected to diffuse through the ferritin channels and produced encapsulation. Next, the reaction mixtures were purified by SEC to estimate the loading and yield of the encapsulation (Figure 4.43). The loading can be estimated from the relative intensity of signals detected on the chromatogram (A490/A280), while the yield can be estimated from the

intensity of the signal at 280 nm (A280). The SEC chromatograms show that the best conditions to load ferritin with Fe(II)-DOX via enlarged $Ftn^{(pos)}$ channels are the combination of pH 5.0 and 65 °C. These conditions produced a nice peak with good loading and yield. For the next experiments, these reaction conditions will be used.

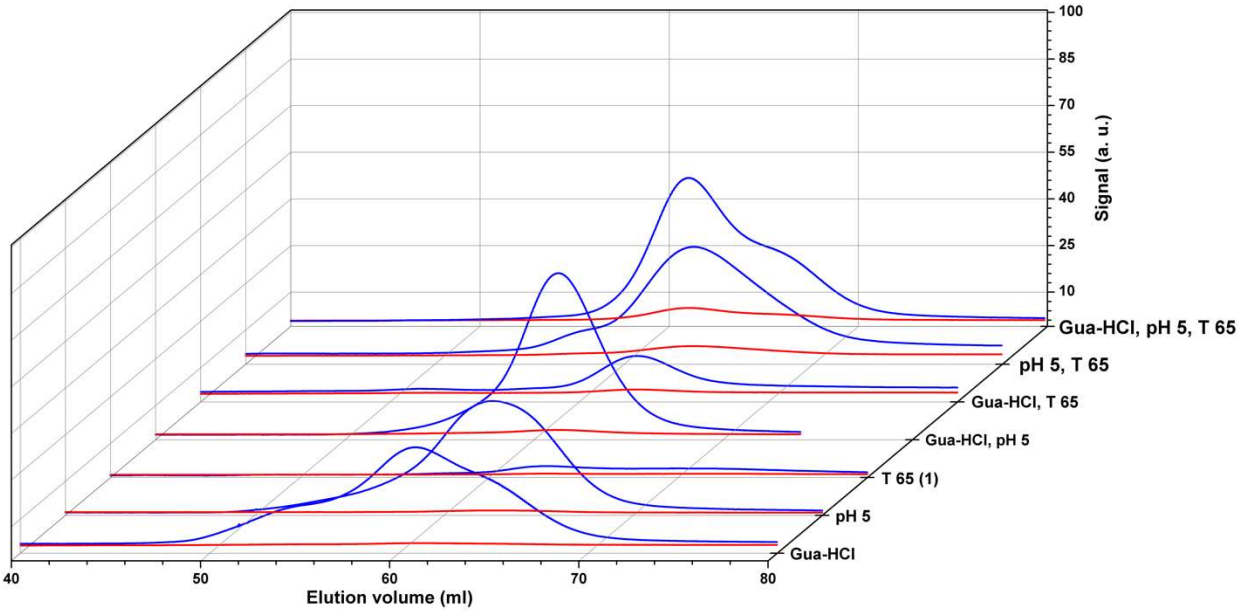

Figure 4.43 Experiments to determine the best conditions to enlarge $Ftn^{(pos)}$ channels. These are SEC chromatograms obtained from the encapsulation of Fe(II)-DOX in $Ftn^{(pos)}$ via diffusion through channels. Different experimental conditions were applied to enlarge the ferritin channels.

Next, the influence of the metal cations used in the pre-complexation of DOX for the loading and the yield was investigated. For this, Fe(II) was substituted with other metal cations in the pre-complexation: Fe(III) and Cu(II), and then the encapsulation was performed. The results show that Cu(II) produced the highest loading, but the total yield of DOX-ferritin is lower than the total yield obtained using Fe(II) and Fe(III) cations (Figure 4.44). As currently, loading is the highest priority, Cu(II) was used in the subsequent experiments.

In the next step, the influence of Cu (II) to DOX ratio used in the pre-complexation was investigated The results show that changing the ratio of Cu(II) to DOX did not significantly change the loading (Figure 4.45), which indicates that the Cu(II)-DOX complex only involves one metal cation and one ligand. Moreover, a shoulder peak formed as the ratio of Cu(II) to DOX increased. Based on these results, it is concluded that the best ratio of Cu(II) to DOX for the encapsulation is 1 : 1. This ratio then was used for the following experiments.

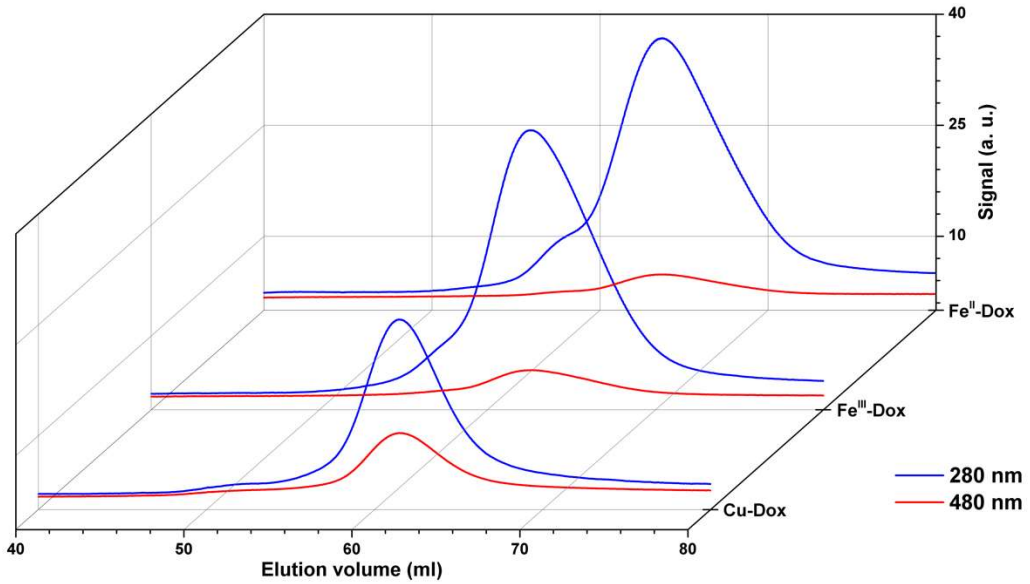

Figure 4.44 The influence of metal cations used in the complexation of DOX for the encapsulation. These are SEC chromatograms from the encapsulation of metal-DOX in Ftn$^{(pos)}$ via diffusion through channels (pH 5, 65 °C).

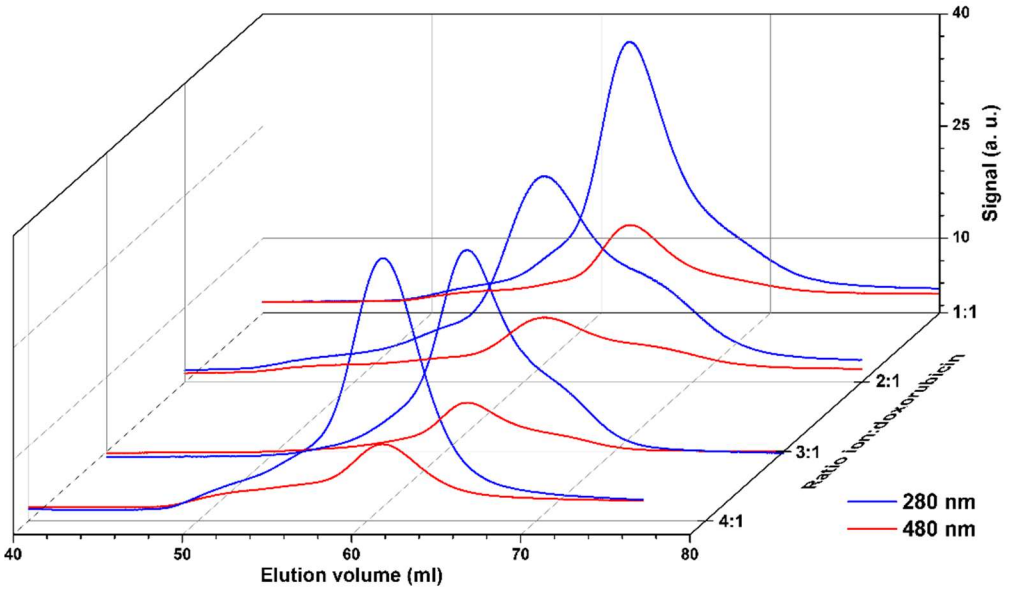

Figure 4.45 The influence of Cu(II) to DOX ratio used in the pre-complexation for the encapsulation. These SEC chromatograms were obtained from the encapsulation of Cu(II)-DOX complexes in Ftn$^{(pos)}$ via diffusion through channels (pH 5, 65 °C). The Cu(II)-DOX complexes were produced by different metal cation to DOX ratios.

Afterward, the concentration of Cu(II)-DOX complex used in the encapsulation was increased to improve the loading further. The results show that, although the loading slightly improved by increasing Cu(II)-DOX concentration, the protein aggregation also increased with higher Cu(II)-DOX concentration (Figure 4.46). Therefore, for the next experiments, Ftn$^{(pos)}$ to Cu(II)-DOX concentrations with a ratio of 1 : 200 was used.

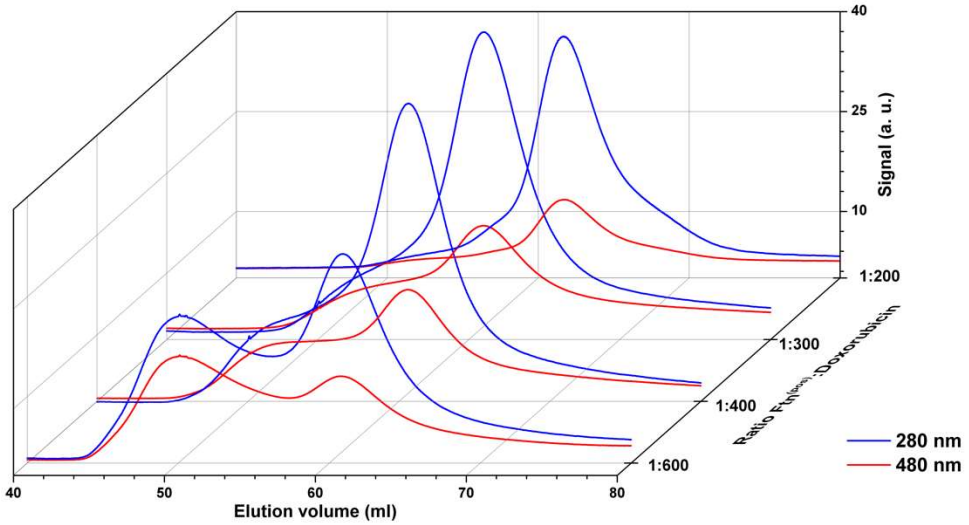

Figure 4.46 The influence of increasing the Cu(II)-DOX concentration for the encapsulation. These are SEC chromatograms obtained by increasing the concentration of Cu(II)-DOX during the encapsulation of Cu(II)-DOX in $Ftn^{(pos)}$ via diffusion through channels (pH 5, 65 °C, Cu : DOX = 1 : 1).

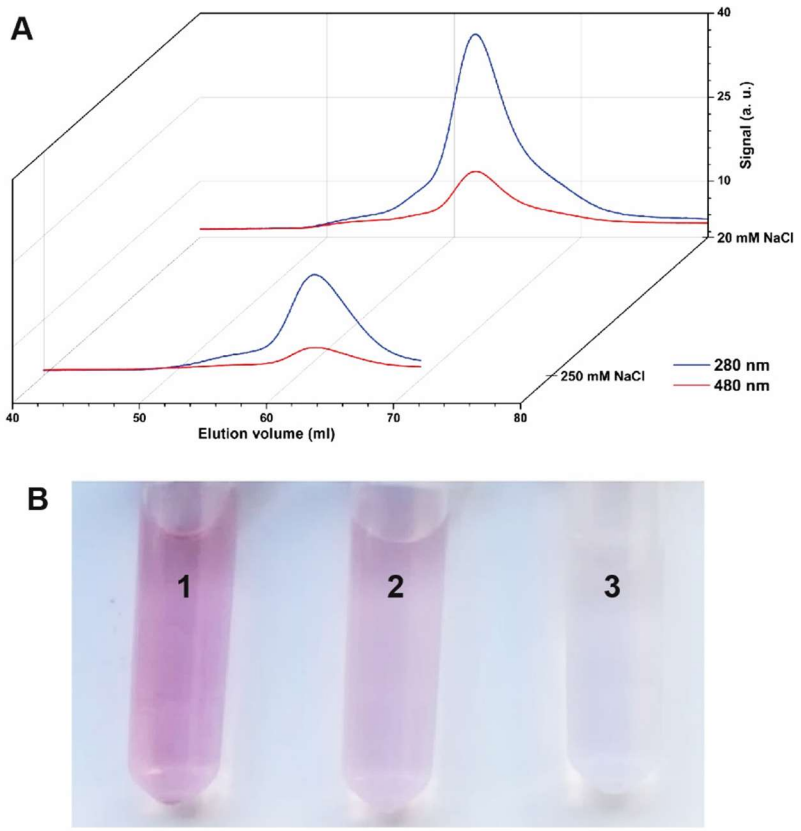

Figure 4.47 The influence of increasing salt concentration for the encapsulation of Cu(II)-DOX in $Ftn^{(pos)}$. A) The SEC chromatograms obtained by increasing the salt concentration during the encapsulation of Cu(II)-DOX in $Ftn^{(pos)}$ via diffusion through channels (pH 5, 65 °C, Cu : DOX = 1 : 1, $Ftn^{(pos)}$: Cu(II)-DOX = 1 : 200). B) Visual appearance of the samples after the encapsulation using: 1) 250 mM, 2) 500 mM, 3) 1 M NaCl.

In the next set of experiments, the encapsulation experiment was performed in various salt concentrations to investigate if the yield of the encapsulation can be improved: 40 mM, 250 mM, 500 mM, and 1 M. The results show that more protein aggregation occurred when the salt concentration increased (Figure 4.47). This can be attributed to the salt screening of the repulsion between Cu(II)-DOX and the outer surface charges of $Ftn^{(pos)}$ and to the increased hydrophobic interactions between $Ftn^{(pos)}$ cages. SEC was not performed for the samples with 500 mM and 1 M NaCl because the low yield can be noticed by simple visual observation. It is concluded that 40 mM salt concentration is the best for the encapsulation.

Finally, the incubation time for the diffusion of Cu(II)-DOX into the $Ftn^{(pos)}$ cavity was varied to improve the loading further: 1 h, 2.5 h, 5 h, and 24 h. Ideally, the incubation time should be the shortest time possible, while still having a high loading and yield. The results show that 1 h incubation time was not enough to get a high loading (Figure 4.48). On the contrary, incubation for 24 h resulted in the precipitation of most of the protein, and therefore the reaction mixture was not analyzed by SEC. Incubation time for 2.5 h was found to be the best for producing a high loading and yield in the encapsulation.

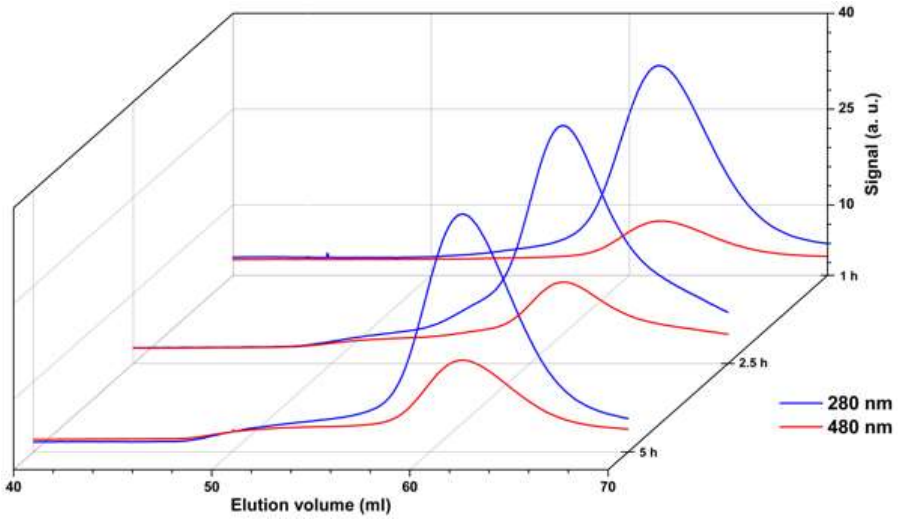

Figure 4.48 Optimization of the incubation time for the diffusion of Cu(II)-DOX into $Ftn^{(pos)}$. These are SEC chromatograms obtained by varying the incubation time during the encapsulation of Cu(II)-DOX in $Ftn^{(pos)}$ via diffusion through channels (pH 5, 65 °C, Cu : DOX = 1 : 1, $Ftn^{(pos)}$: Cu(II)-DOX = 1 : 200, 40 mM NaCl).

To confirm that the encapsulation worked well, the Cu(II)-DOX $Ftn^{(pos)}$ fractions were collected and analyzed by TEM (Figure 4.49). The result shows that most of the protein containers were intact, but a few cages were broken. It will be difficult to separate these broken cages from the intact ferritin cages by SEC. To overcome this problem, one suggestion is to digest the sample with trypsin before the purification by SEC. The intact cages will not be digested by trypsin, while the broken cages will be digested into smaller fragments. In this way, a better separation will be obtained in the subsequent SEC. Moreover, the DOX loading in $Ftn^{(pos)}$ was determined by UV/Vis: 31 DOX/cage.

In this section, several optimizations were performed to find out the best conditions to encapsulate DOX into Ftn$^{(pos)}$. As a summary, DOX was pre-complexed with Cu(II) (1 : 1 ratio) to facilitate the encapsulation of DOX to the Ftn$^{(pos)}$ cage. Compared to the other metal-DOX complexes, Cu(II)-DOX was taken better by the Ftn$^{(pos)}$. The appropriate ratio of protein to Cu(II)-DOX concentration is 1 : 200. And finally, the best conditions for the diffusion of Cu(II)-DOX into Ftn$^{(pos)}$ are: pH 5, 65 °C, 40 mM salt, and 2.5 h incubation time.

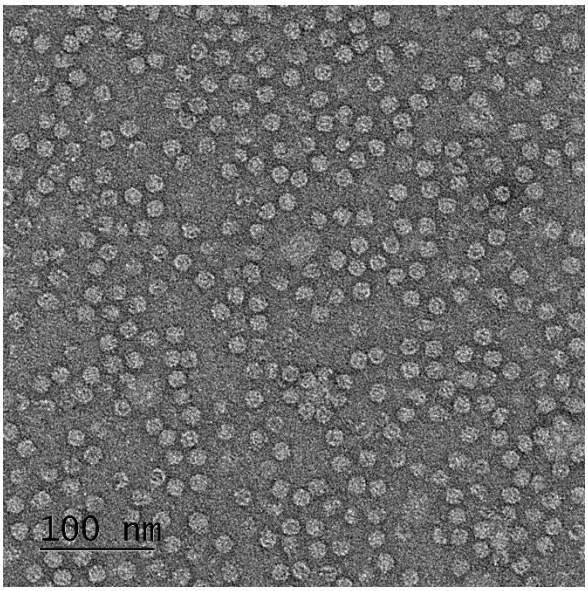

Figure 4.49 TEM image of Cu(II)-DOX Ftn$^{(pos)}$. Most of the ferritin cages were intact, while a few cages were broken.

4.2.1.2 Encapsulation of DOX in Ftn$^{(neg)}$-1C

The previous encapsulation strategy used for the Ftn$^{(pos)}$ could not be applied for the encapsulation of DOX in Ftn$^{(neg)}$, because the positively charged Cu(II)-DOX complex immediately precipitated with the Ftn$^{(neg)}$. The other option is to encapsulate DOX by opening and closing the Ftn$^{(neg)}$ cage. However, the same problem also occurred when DOX was encapsulated via dis/reassembly approach in acidic conditions: DOX and Ftn$^{(neg)}$ heavily precipitated. In the earlier section, a new encapsulation strategy was developed for the encapsulation of fluorophores, i.e. by cys-maleimide coupling reactions. It was hypothesized that this approach could also work for encapsulating DOX because a much lower concentration of DOX would be applied in this approach. Protein aggregation would be reduced if a lower concentration of DOX was used.

For this encapsulation strategy, Ftn$^{(neg)}$ with the redesigned cysteine positions (Ftn$^{(neg)}$-1C) was used. Furthermore, DOX was substituted with aldoxorubicin, a maleimide derivative of DOX containing an acid-cleavable hydrazone bond (Figure 4.50).[251] This acid-sensitive bond will enable DOX release when ferritin is degraded in the acidic environment of the lysosome.

The encapsulation was performed in a similar way as in the encapsulation of fluorophore via chemical conjugation (Figure 4.4). To optimize the coupling reaction, different concentrations of aldoxorubicin were tested: 1, 2, 5, and 10 eq. Unexpectedly, very high loadings were obtained with higher concentrations of aldoxorubicin (Figure 4.51 and Figure 4.52). These loadings were even higher than the maximum number of cysteines in the cage, which is only 24 (Table 4.14). This means, in addition to chemical conjugation, the DOX encapsulation also occurred via non-specific binding: electrostatic or hydrophobic interactions.

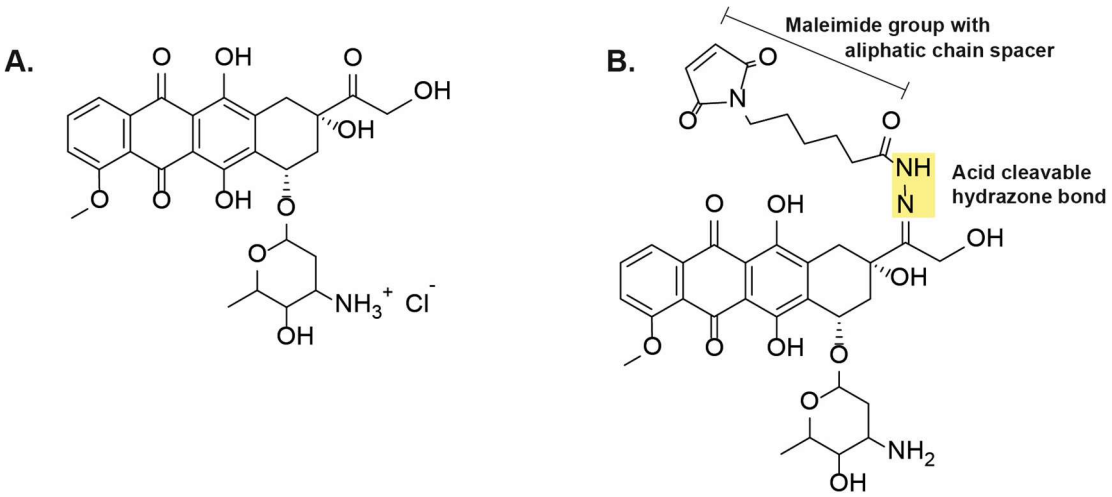

Figure 4.50 The molecular structures of DOX and aldoxorubicin. A) Doxorubicin as its hydrochloride salt (Dox-HCl). B) Maleimide-functionalized doxorubicin (aldoxorubicin).

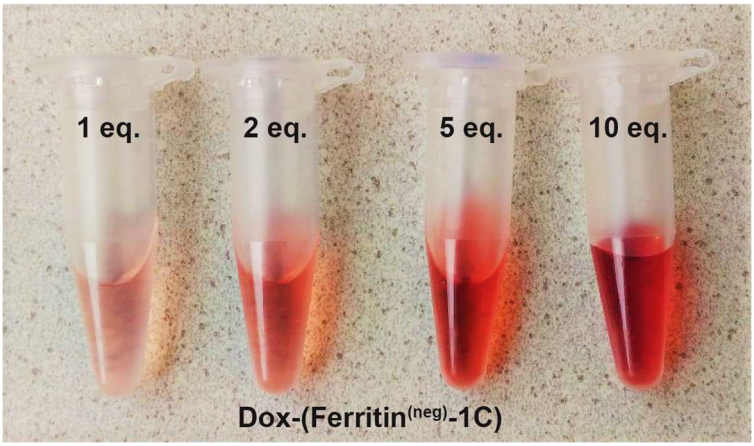

Figure 4.51 DOX-(Ftn$^{(neg)}$-1C) solutions obtained from the optimization of the coupling reaction. All the solutions were prepared at 2.5 mg/mL protein concentration.

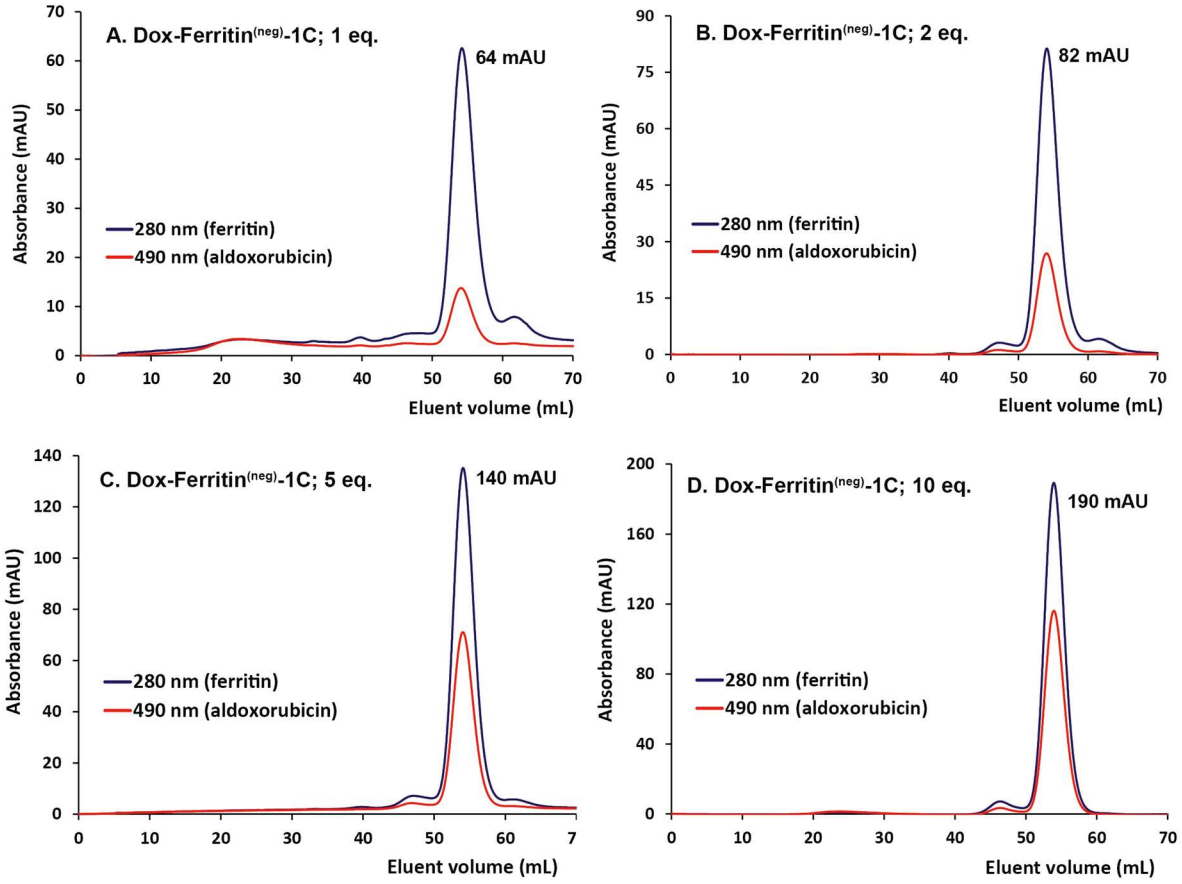

Figure 4.52 The optimization of Ferritin$^{(neg)}$-1C coupling reaction with aldoxorubicin. These SEC chromatograms were obtained by reacting the same concentration of cysteines (in Ferritin$^{(neg)}$-1C) with various concentrations of aldoxorubicin: A) 1 eq. B) 2 eq. C) 5 eq. D) 10 eq.

Table 4.14 The loading and yield from the optimization of Ftn$^{(neg)}$-1C coupling reaction with aldoxorubicin

Aldoxorubicin concentration	Loading (molecules/cage)	Yield (%)
1 eq.	18.6	69.6
2 eq.	38.4	76.3
5 eq.	76.3	92.1
10 eq.	91.7	82.1

To investigate whether chemical conjugation is necessary to achieve the encapsulation of a large amount of DOX in Ftn$^{(neg)}$-1C, several reaction controls were performed. First, the encapsulation of DOX and aldoxorubicin in Ftn$^{(neg)}$-1C were compared (Figure 4.53A-B). The results show that it was possible to get high loading without chemical conjugation, but the yield drastically decreased due to heavy precipitation (Table 4.15). In other words, chemical conjugation stabilizes ferritin subunits during the reassembly process, and this leads to high loading and yield. Next, the encapsulation of aldoxorubicin in Ftn$^{(neg)}$-1C and Ftn$^{(neg)}$-0C were compared (Figure 4.53A and Figure 4.53C). The results show that the encapsulation still worked without cysteine, but both the loading and the yield decreased. Figure 4.53C

basically shows the encapsulation that purely worked via non-specific interactions. Finally, the encapsulation of DOX and aldoxorubicin in Ftn$^{(neg)}$-0C were compared (Figure 4.53C-D). The yield also decreased when DOX was used in the encapsulation. Interestingly, this result indicates that the maleimide aliphatic chain also helps to stabilize the ferritin subunits. It is suggested that probably the hydrophobic moiety of aldoxorubicin attached to ferritin subunits, while the maleimide aliphatic chain remained free to move to give steric stabilization.

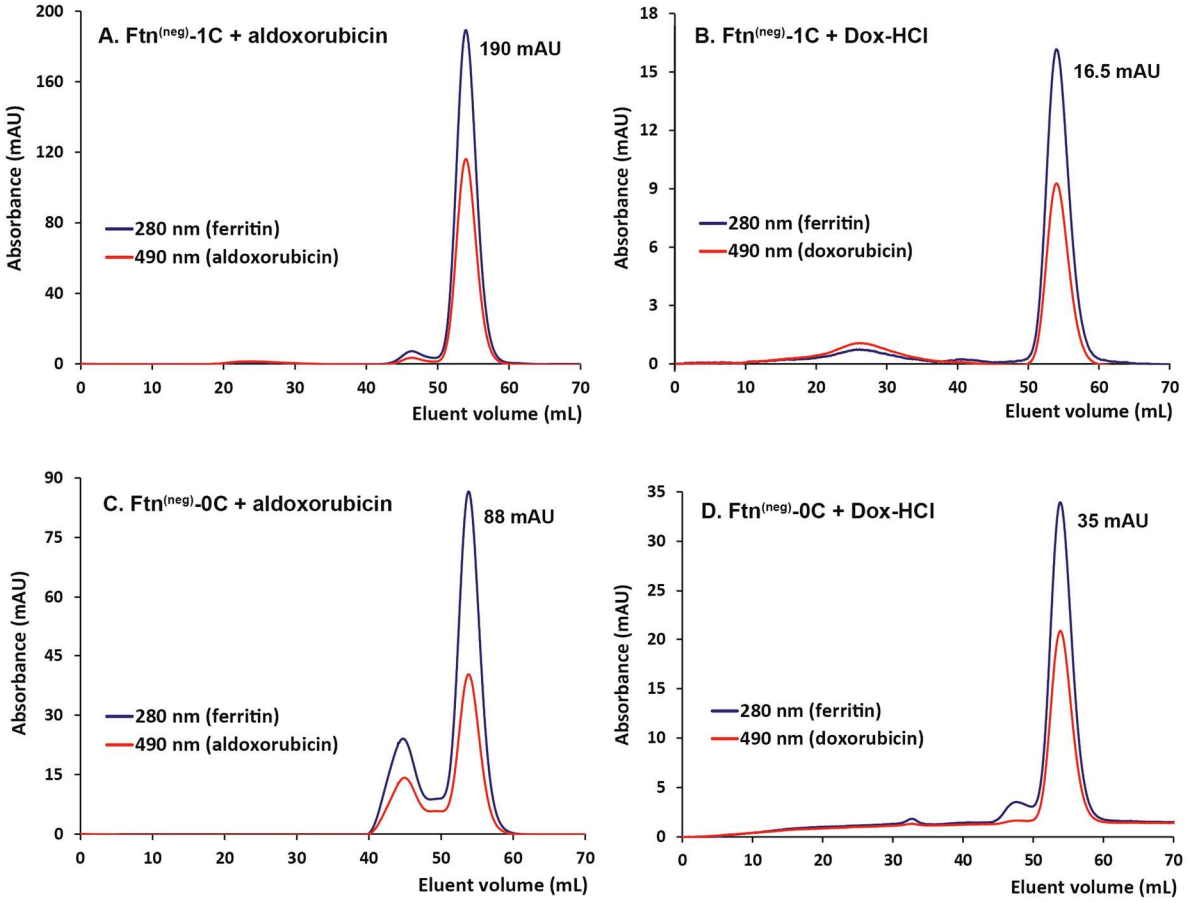

Figure 4.53 Reaction controls to investigate if cysteine is needed to achieve good encapsulation of DOX. Ftn$^{(neg)}$ containing 1 cysteine per subunit (Ftn$^{(neg)}$-1C) was used to encapsulate: A) aldoxorubicin. B) DOX-HCl. These SEC chromatograms then are compared with the SEC chromatograms from Ftn$^{(neg)}$ without cysteine (Ftn$^{(neg)}$-0C) that was used to encapsulate: C) aldoxorubicin and D) DOX-HCl. All the reactions used 10 eq. concentration of DOX variants relative to cysteine or to the Ftn$^{(neg)}$ subunit.

Table 4.15 The loading and yield from the control experiments in Figure 4.53

Ferritin variants	Doxorubicin variants	Loading (molecules/cage)	Yield (%)
Ftn$^{(neg)}$-1C	Aldoxorubicin	91.7	82.1
Ftn$^{(neg)}$-1C	DOX-HCl	77.4	12.2
Ftn$^{(neg)}$-0C	Aldoxorubicin	43.7	82.3
Ftn$^{(neg)}$-0C	DOX-HCl	86.8	23.4

To confirm that the encapsulation worked well, DOX-(Ftn$^{(neg)}$-1C) 10 eq. was characterized by DLS (Table 4.16) and TEM (Figure 4.54). The results indicate successful encapsulation. The cages reformed after the encapsulation and the sizes of the cages are reasonable.

Table 4.16 The size of DOX-(Ftn$^{(neg)}$-1C) 10 eq. as measured by DLS

Size (nm)	PDI
14.19	0.074
14.05	0.078
13.99	0.061

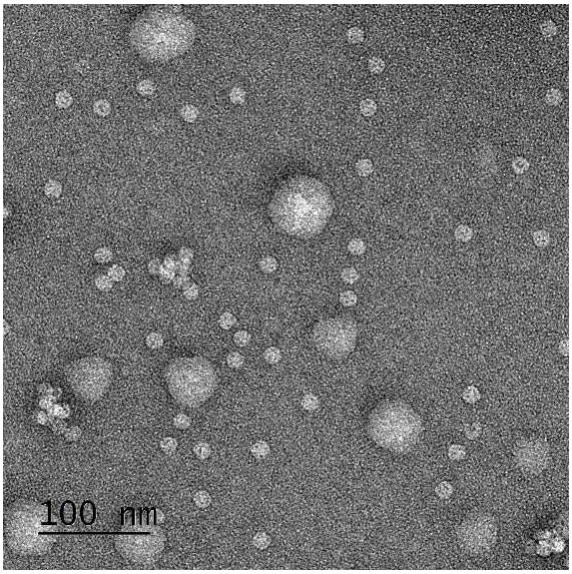

Figure 4.54 TEM characterization of DOX-(Ftn$^{(neg)}$-1C) 10 eq. with staining. The ferritin cages reformed after the encapsulation. The larger round objects observed here are artifacts, as they are commonly observed when ferritin is imaged by TEM with a staining agent.

In short, DOX was encapsulated in Ftn$^{(neg)}$-1C with very high loading and yield by a simple chemical conjugation approach between aldoxorubicin and cysteines inside the ferritin cavity. In the past, the DOX encapsulation in HF by acidic dis/reassembly approach could not achieve the loading level as high as here and also suffered from the low yield due to precipitation. [22][20] Moreover, this method enables us to control the DOX loading level simply by changing the concentration of aldoxorubicin.

4.2.1.3 Encapsulation of DOX in HF

As explained in the introduction to this section, the encapsulation of DOX in HF was performed because it was concerned that the surface modifications in Ftn$^{(pos)}$ and Ftn$^{(neg)}$ might alter the binding properties of ferritin to the TfR-1, and thus the uptake by cancer cells. The encapsulation of DOX in HF by various

approaches has been discussed in Chapter 3.2.3. The main challenge is that the encapsulation suffered from the heavy precipitation of DOX and HF at pH 7.4, which is caused by both electrostatic and hydrophobic interactions. Many publications recommended using 1 mg/mL DOX for the encapsulation. However, a simple mixing between DOX and HF at this concentration resulted in heavy precipitation. The addition of salts and urea for screening electrostatic and hydrophobic interactions reduced the precipitation to a certain extent, but could not completely prevent the precipitation. At a longer incubation time, they slowly precipitated.

The encapsulation strategy that was employed here is based on the work reported by Bellini *et al.* Their main idea was to use a low concentration DOX and sufficient ionic strength to prevent the precipitation. Here, HF was disassembled in glycine buffer pH 2.5 and mixed with DOX solution. After 4 hours, the solution was neutralized to pH 7.4 by adding the reassembly buffer. However, it is very critical to note that the required amount of salt solution must be combined with the reassembly buffer. If the salt solution is added to the disassembly solution, HF and DOX will precipitate when the solution is neutralized to pH 7.4. For the reassembly process, it is better to incubate the solution at room temperature overnight without stirring because the yield decreased when the incubation was performed at 4 °C. Moreover, agitation or stirring disturbed the reassembly process. To improve the yield, the encapsulation was also performed in a larger total volume, i.e. at a lower concentration of ferritin, as this suppressed the protein aggregation.

As shown by the SEC chromatogram (Figure 4.55A), a large aggregation peak is observed before the main ferritin peak. The ferritin fractions were collected and analyzed by TEM (Figure 4.55B). The result confirms that the ferritin cages were reassembled properly. Furthermore, the yield and the loading were determined by UV/Vis. The yield was only 9.7% due to the aggregation, while the loading was 28.7 DOX/cage. This loading is in accordance with the result reported by Bellini *et al.*: 28.3 DOX/cage.

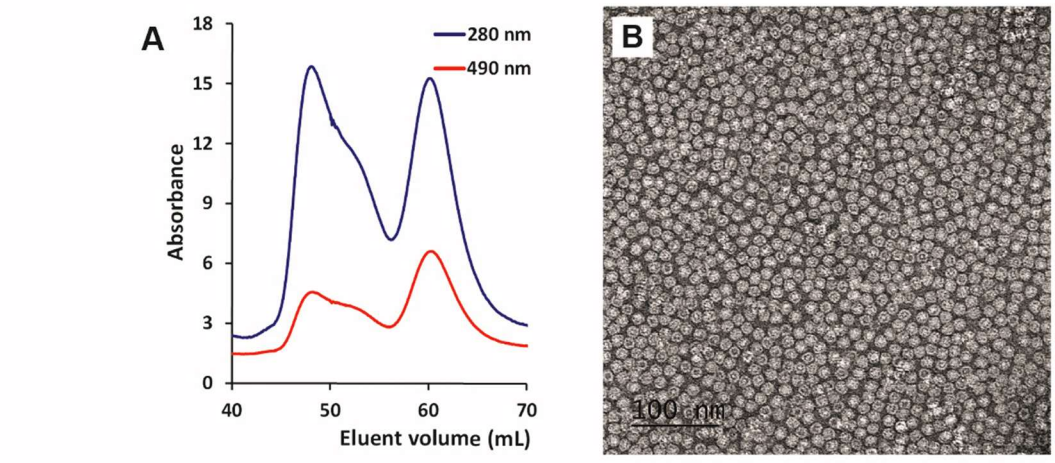

Figure 4.55 Purification and characterization of DOX-HF. A) SEC chromatogram. B) TEM image with staining.

4.2.1.4 Encapsulation of DOX in HF-7C and HF-1C

As described above, the encapsulation of DOX in HF suffered from the aggregation of DOX and ferritin. Here, the encapsulation via chemical conjugation to cysteine residues inside the ferritin cavity was applied to improve both the yield and loading. For this, two variants of ferritin were developed: HF-7C and HF-1C. Both variants have the same outer surface and contain seven and one cysteines per ferritin subunit inside the cavity, respectively. Chronologically, the variant HF-7C was developed before HF-1C. In HF-7C, the location of cysteines has not been optimized for the coupling reactions. Some of the cysteine positions were simply adopted from the work of Dmochowski.[252] Only later, it is known that one cysteine at the position 53 (K53C) is enough for the encapsulation of fluorophores (Chapter 4.1.1.2) and DOX (Chapter 4.2.1.2). HF-1C was developed to contain this necessary cysteine. Nevertheless, here the encapsulation of DOX in HF-7C needs to be reported because in the next section DOX (HF-7C) is also applied in the cell experiments.

Structurally, the ferritin cages in HF-1C and HF-7C have identical outer surfaces, therefore they have the same binding properties to TfR-1. However, the outer cages of HF-1C and HF-7C are slightly different compared to HF. Two cysteines on the outer surface (C90 and C102) and one cysteine at the 3-fold channels (C130) that are present in each HF subunit were mutated into alanines in both HF-1C and HF-7C. This was done to make sure that the coupling reactions only occur inside the ferritin cages. If the coupling occurs at the outer cages, it may also alter the binding property of ferritin to TfR-1.

The encapsulation of DOX in HF-7C and HF-1C was performed in a similar way as in $Ftn^{(neg)}$-1C. The main difference is that a high concentration of TCEP was used for the encapsulation of DOX in HF-7C, while in HF-1C and $Ftn^{(neg)}$-1C no and a lower concentration of TCEP were used, respectively. In Chapter 4.1.1.2, it was explained that it is not necessary to use TCEP for the coupling reaction in our system. Furthermore, for the encapsulation of DOX in HF-1C, 20 mM L-arginine was applied as an additive to improve the DOX loading.[166]

The SEC chromatograms show that less aggregation formed during the encapsulation of DOX in HF-7C or HF-1C (Figure 4.56A and Figure 4.56C), i.e. when compared to the encapsulation of DOX in HF (Figure 4.55A). The DOX loading in HF-7C and HF-1C as determined by UV/Vis are 20 DOX/cage and 41.7 DOX/cage, respectively. HF-1C has higher loading than HF-7C, probably because more coupling reactions in HF-7C prevent the aldoxorubicin attachment to ferritin subunits through non-specific binding. Of the two variants, only HF-1C has a higher DOX loading compared to HF. On the other hand, the encapsulation of DOX in $Ftn^{(neg)}$-1C has a higher total yield of DOX-ferritin and loading compared to the encapsulation of DOX in HF-7C and HF-1C. To explain this, it is assumed that the surface charging in $Ftn^{(neg)}$-1C contributes to the stability of the ferritin subunits during the reassembly process, which

in turn increases the yield and loading. Finally, TEM characterizations confirm the presence of ferritin cages in both samples (Figure 4.56B and Figure 4.56D).

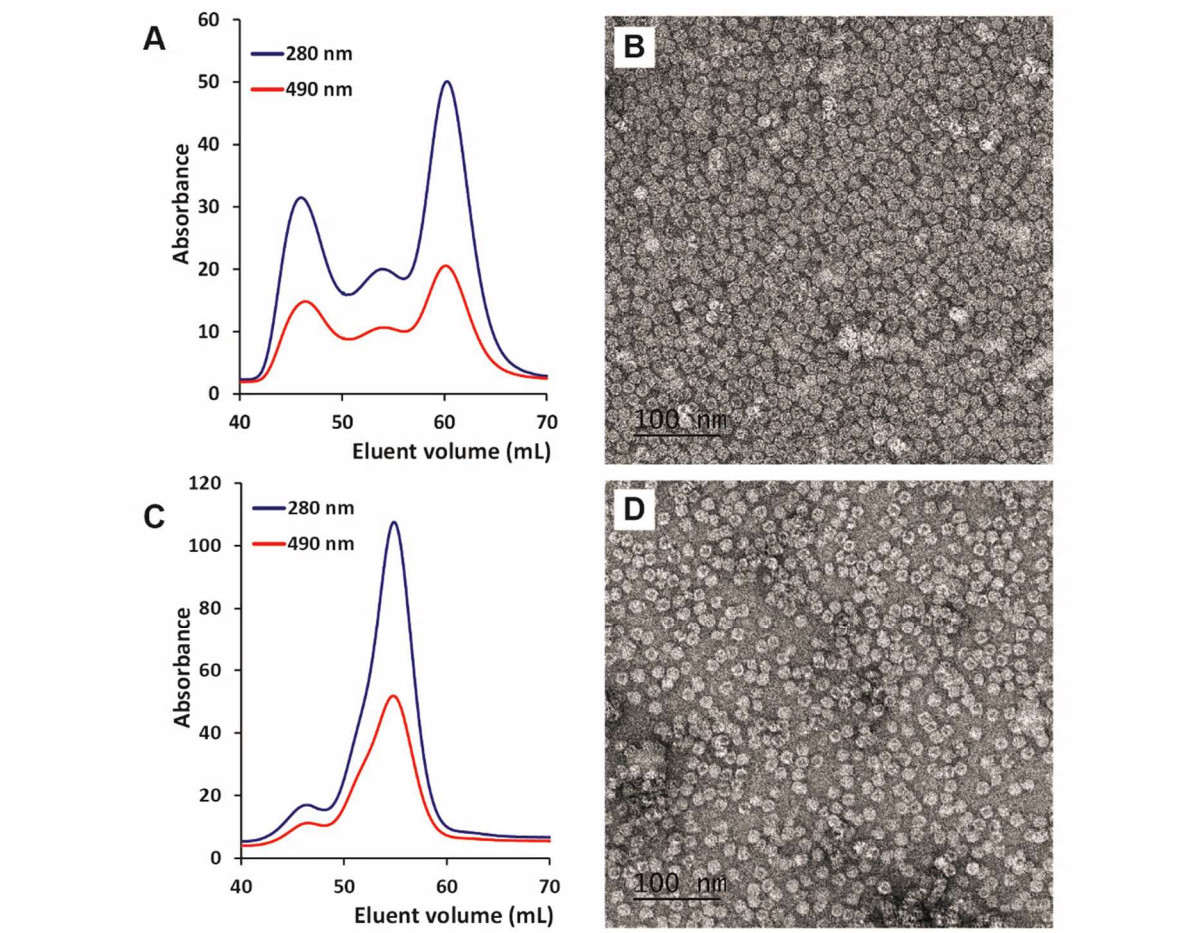

Figure 4.56 Purification and characterization of DOX-HF variants. A) SEC chromatogram of DOX (HF-7C). B) TEM image of DOX (HF-7C). C) SEC chromatogram of DOX (HF-1C). D) TEM image of DOX (HF-1C).

As a summary, DOX was encapsulated in five ferritin variants by different approaches. For the $Ftn^{(pos)}$, the encapsulation was performed by diffusion through channels. On the other hand, the encapsulation of DOX in $Ftn^{(neg)}$-1C was performed by chemical conjugation and resulted in a high yield and loading. However, here it was found that the encapsulation also occurred via non-specific binding. For HF, the encapsulation of DOX by dis/reassembly approach was achieved but the yield was low due to heavy precipitation. The encapsulation of DOX via chemical conjugation can also be extended to wild-type ferritin with redesigned cysteines: HF-7C and HF-1C, although the loading and yield were not as good as in the $Ftn^{(neg)}$-1C.

4.2.2 Synthesis of DOX-Ftn microgels and its release study

In the earlier sections, the synthesis of acid-cleavable ferritin-microgels was established and the ferritin release was studied in acidic solutions. In this section, a similar synthesis was applied to integrate DOX-Ftn variants into microgels for drug delivery purposes. As the positively charged monomer, VIM, was

used in the synthesis, only the negatively charged DOX-Ftn variants can be integrated into the microgels. For integrating DOX-Ftn$^{(pos)}$, microgels with negatively charged monomer are required. However, it was shown in the earlier sections that the synthesis is still hampered by the inhomogeneous distribution of the negatively charged monomers among the microgels. In this section, the synthesis of DOX-(Ftn$^{(neg)}$-1C) microgels and its release study in acidic solutions are described. In the later section, a similar synthesis was used to produce DOX (HF-1C) microgels.

The synthesis of DOX-(Ftn$^{(neg)}$-1C) microgels was performed by a semi-batch approach, just as the synthesis of Ce-Ftn$^{(neg)}$ microgels. First, DOX-(Ftn$^{(neg)}$-1C) with the highest loading (10 eq.) was used in the synthesis. However, this caused a lot of aggregation. A possible explanation is that the cages disassemble during the synthesis due to the high loading and the elevated temperature. Later, DOX-(Ftn$^{(neg)}$-1C) with the second-best loading (5 eq.) was used and the synthesis worked very well (Figure 4.57). Next, the ferritin loading and release were estimated by UV/Vis spectroscopy. The results show that almost all of the ferritin present during synthesis was integrated into the microgels (Table 4.17). And similar to before, ferritin release at pH 4.0 is lower than the release at pH 2.5, with about 75% of the ferritins being released at pH 2.5.

Next, a similar synthesis was applied to integrate DOX-containing wild-type ferritin into the microgels. For this, we chose to use DOX (HF-1C), the wild-type ferritin with the highest DOX-loading. However, a lot of aggregation occurred during the synthesis, which was not observed in the synthesis of DOX-(Ftn$^{(neg)}$-1C) microgels. This is probably related to the surface charge difference between HF-1C and Ftn$^{(neg)}$-1C. The stability of polyelectrolyte microgels during synthesis largely depends on the charged species (charged monomer VIM, ferritin, and persulfate initiator). Therefore, by reducing the initiator concentration, the synthesis of DOX (HF-1C) microgels was stabilized. However, the yield was reduced. Probably this is because fewer nuclei formed with a reduced concentration of initiators. Moreover, the integration of DOX (HF-1C) into the microgels was poor, not as good as DOX-(Ftn$^{(neg)}$-1C) (Figure 4.58).

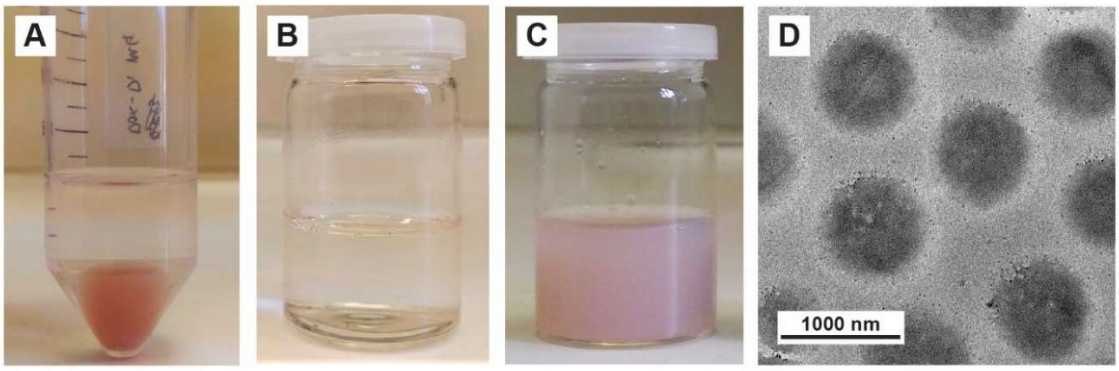

Figure 4.57 The synthesis of DOX-(Ftn$^{(neg)}$-1C) 5eq. microgels. A) Microgel pellet. B) Supernatant after the first centrifugation. C) Re-dispersed microgels. D) TEM characterization of the microgels.

Table 4.17 Estimation of DOX-(Ftn$^{(neg)}$-1C) 5eq. loading and release in microgels

Microgels	Initiator	Ftn loading[a]	Ftn content[b]	Ftn release at pH 2.5[c]	Ftn release at pH 4.0[c]
DOX-(Ftn$^{(neg)}$-1C) 5eq.	(KPS + TEMED), 55 °C	95.4%	3.2% (w/w)	75.44%	22.15%

[a] Relative to the initial amount of ferritin used during synthesis. [b] Relative to the total mass of the material (ferritin-microgels). [c]Relative to the amount of incorporated ferritin in the microgel.

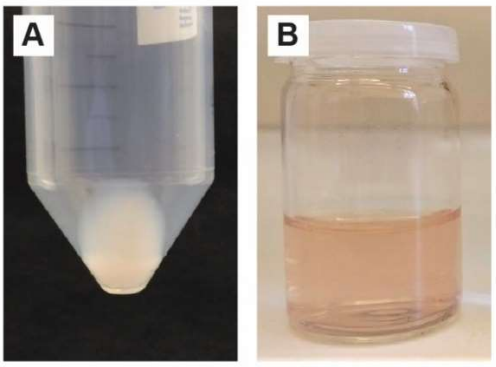

Figure 4.58 The synthesis of DOX (HF-1C) microgels. A) Microgel pellet. B) Supernatant after the first centrifugation.

From the previous syntheses, it was known that the loading of ferritin in microgels depends on: (1) the amount of the charged monomer VIM used in the synthesis; (2) the surface charge of ferritin; and also (3) the size of the microgels. The amount of VIM was not the problem because the same amount of VIM was used during the synthesis of DOX-(Ftn$^{(neg)}$-1C) microgels and DOX (HF-1C) microgels. To examine where the problem comes from, the synthesis was repeated by replacing DOX (HF-1C) with cerium oxide loaded HF-1C (Ce(HF-1C)). In this way, the presence of HF-1C in the microgels can be observed by TEM. The results show that Ce(HF-1C) was integrated well in the microgels and the size of the microgels was also large enough for taking a large number of ferritin (Figure 4.59). As Ce(HF-1C) was integrated well into the microgels while DOX (HF-1C) is not, this indicates that both ferritin cages have different surface properties. Moreover, this leads to a hypothesis that probably not all of the DOX molecules were located inside the cages. Maybe some DOX molecules are also bound to the surface of HF-1C. This prevented the electrostatic interactions between VIM and HF-1C, thereby a poor ferritin loading was obtained. This hypothesis is supported by the cell experimental results, which will be discussed in the following section.

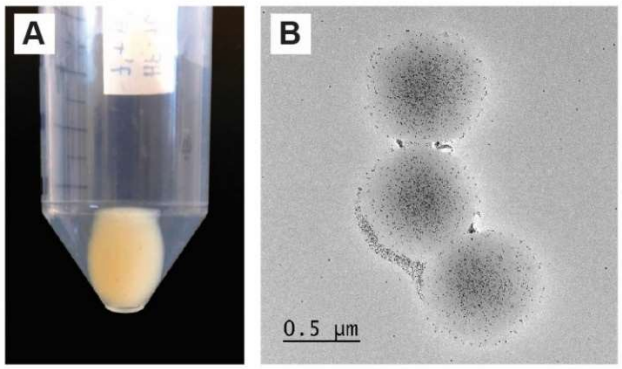

Figure 4.59 The synthesis of Ce(HF-1C) microgels. A) Microgel pellet. B) TEM characterization of Ce(HF-1C) microgels after synthesis, without purification.

As a summary, DOX-(Ftn$^{(neg)}$-1C) was successfully integrated into microgels using the synthesis protocol established for Ce-Ftn$^{(neg)}$. About 75% of the integrated DOX-(Ftn$^{(neg)}$-1C) was released in pH 2.5. However, the synthesis did not work well for the integration of DOX (HF-1C). Further investigation revealed that this is probably because some DOX molecules bound to the surface of ferritin, thus interfering with the integration of DOX (HF-1C) into the microgels.

4.2.3 Cytotoxicity of DOX-Ftn variants

As described above, DOX has been successfully encapsulated in various ferritin variants through different approaches. The next step is to test the biological performance of these DOX-ferritin variants in cell experiments. For this, first, a suitable cancer cell line and a control cell line were selected by monitoring the presence/absence of the TfR-1 on the cell surface. Next, the cytotoxicity assays were established. Here, the proper concentration of DOX required in the cell experiments was determined. Finally, the cytotoxicity assays were performed for the DOX-Ftn variants. This section is developed according to these three sets of experiments. All the cell experiments were performed by Sarah Boesveld (Medizinische Klinik III, Uniklinik RWTH Aachen).

To select the suitable cell lines, real-time polymerase chain reactions (real-time PCR) were performed with various cell lines to determine the cancer cell lines that show a high expression of TfR-1. At the same time, the cell lines that have no expression of TfR-1 were selected as the candidates for the control cell line. The results of the real-time PCR are shown in Figure 4.60. Three mouse-hepatocellular-carcinoma (HCC) cell lines were found to have an abundance expression of TfR-1 on their surface: Hepa 1-6, Hepa 55.1c, and Hepa 56.1D. On the other hand, L292 and 3T3 fibroblast cells show no expression of TfR-1, therefore they are suitable as the control cell lines. Based on these results, Hepa 1-6 cells and 3T3 fibroblasts were chosen as cancer and control cell lines for the subsequent cell experiments, respectively.

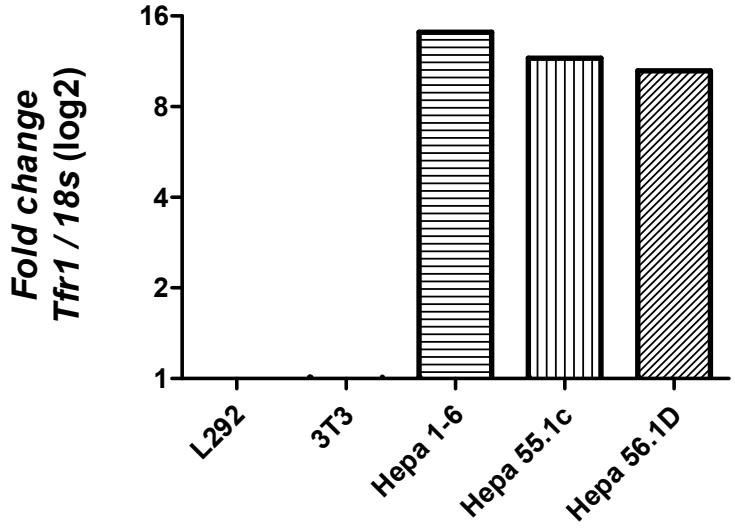

Figure 4.60 Real-time PCR to determine the suitable cancer cell line and the control cell line. Cells with a high expression of TfR-1 are suitable as the cancer cell lines, while cells with no expression of TfR-1 are suitable as the control cell lines.

To measure the cell viability, a 3-(4,5-dimethylthiazol-2-yl)-2,5-diphenyltetrazolium bromide assay (MTT assay) was performed with the chosen cell lines. Both cell lines were treated with different DOX concentrations to determine the lowest DOX concentration that induces cell death. For this, DOX solutions with various concentration, ranging from 0.032 µg/mL to 100 µg/mL, was added to the cell lines and the cell viability was measured after 24 h and 48 h of incubation. The results show that 0.8 µg/mL (1.38 µM) is a suitable DOX concentration for the assay (Figure 4.61). It is the minimum concentration of DOX which significantly reduces the cell viability during 24 h and 48 h incubation time. In Figure 4.61A it is shown that the cell viability increased again when 20 µg/mL and 100 µg/mL DOX were applied. It was believed that these values could most probably result from experimental errors. One possible explanation is that these concentrations of DOX were too high so that the absorbance of DOX interfered with the absorbance measurement for the MTT assays. Furthermore, the results indicate that the control cells are more susceptible than the cancer cells against DOX treatment.

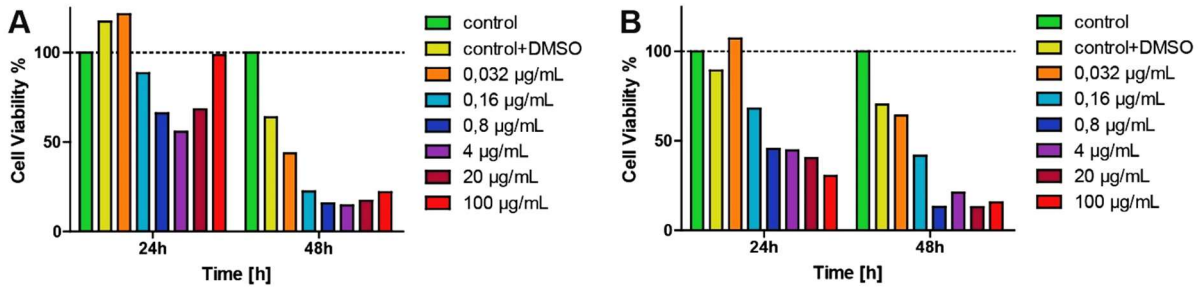

Figure 4.61 Determination of the suitable DOX concentration for the MTT assays. A) Hepa 1-6 cells (HCC). B) 3T3 cells (Fibroblasts). Treatment with water was used as a positive control.

Subsequently, cell experiments were performed using different DOX-Ftn variants, and their cytotoxicity was compared to the free DOX solution at the determined DOX concentration. For this, DOX-Ftn variants containing the same DOX concentration (0.8 µg/mL) were applied. The results show that all the DOX-Ftn variants were less cytotoxic compared to free DOX (Figure 4.62). The order of the cytotoxicity is: HF < $Ftn^{(pos)}$ < HF-7C. Surprisingly, of the three DOX-Ftn variants, HF has the lowest cytotoxicity. This finding is contrary to what has been reported in the literature: HF was shown to deliver DOX to HeLa cells more efficiently than the free DOX.[22] HeLa cells were reported to serve as a TfR-1 positive cell line and therefore used for the cell experiments. Furthermore, in our experiments, all the DOX-Ftn variants harmed the 3T3 control cells, although these cells do not express the TfR-1. This indicates that the 3T3 cells internalized DOX-Ftn through other mechanisms.

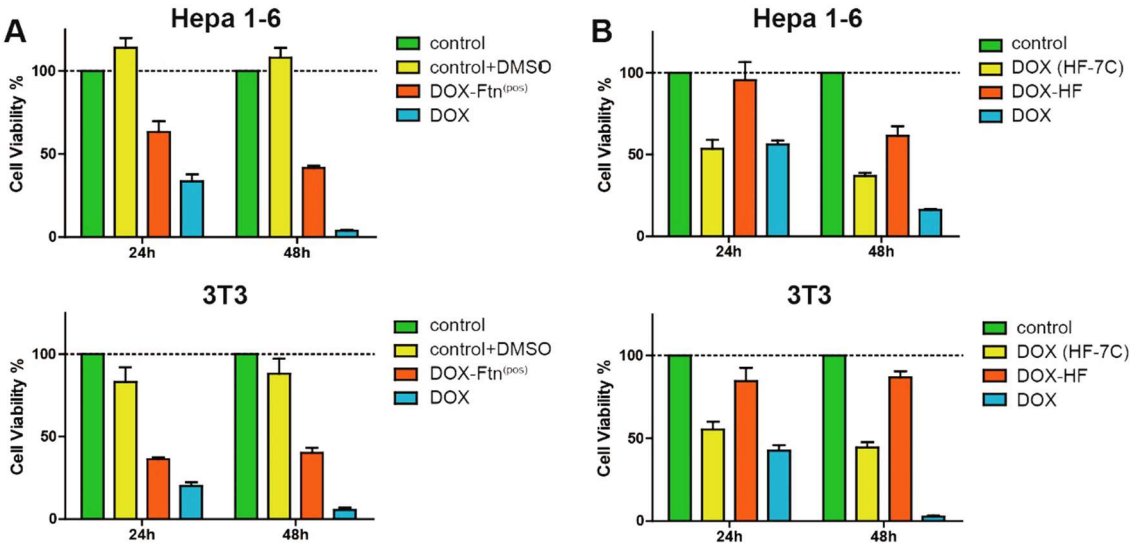

Figure 4.62 MTT assays for various DOX-Ftn variants against Hepa 1-6 and 3T3 cells. A) DOX-$Ftn^{(pos)}$. B) DOX (HF-7C) and DOX-HF. In all experiments, DOX-Ftn variants containing 0.8 µg/mL DOX were applied to both Hepa 1-6 and 3T3 cells, and then their cytotoxicity was compared to the cytotoxicity of 0.8 µg/mL free DOX.

Due to the lower cytotoxicity of DOX-Ftn variants compared to the free DOX in Hepa 1-6 and 3T3 cells, we turned to HeLa cells and used the DOX concentration reported in the literature: 0.1 µM (0.058 µg/mL).[22] However, the results reported in the literature could not be reproduced: DOX-HF was shown to be more toxic than the free DOX for the HeLa cells. Because of the lower concentration of DOX applied in these cell experiments, the cell viability remained high even after 48 h incubation time (Figure 4.63). Nevertheless, the cytotoxicity of various DOX-Ftn variants could be compared. The order of the cytotoxicity is very similar to the previous results: HF < $Ftn^{(neg)}$ < $Ftn^{(pos)}$ < HF-7C. Only HF-7C shows comparable cytotoxicity to the free DOX. Finally, the results show that the empty Ftn variants were not toxic to all the three cell lines.

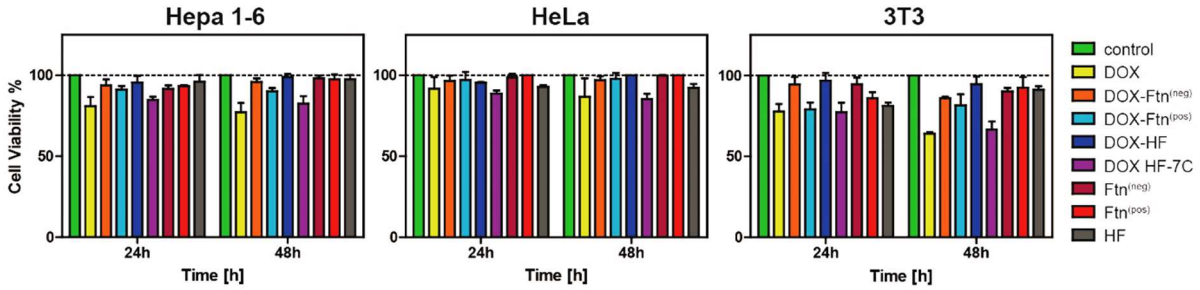

Figure 4.63 MTT assays for various DOX-Ftn variants against Hepa 1-6, HeLa, and 3T3 cells. In all experiments, DOX-Ftn variants containing 0.1 µM (0.058 µg/mL) DOX were applied to Hepa 1-6, HeLa, and 3T3 cells, and then their cytotoxicity was compared to the cytotoxicity of 0.1 µM free DOX. Control reactions were performed by applying the same concentration of empty Ftn cages.

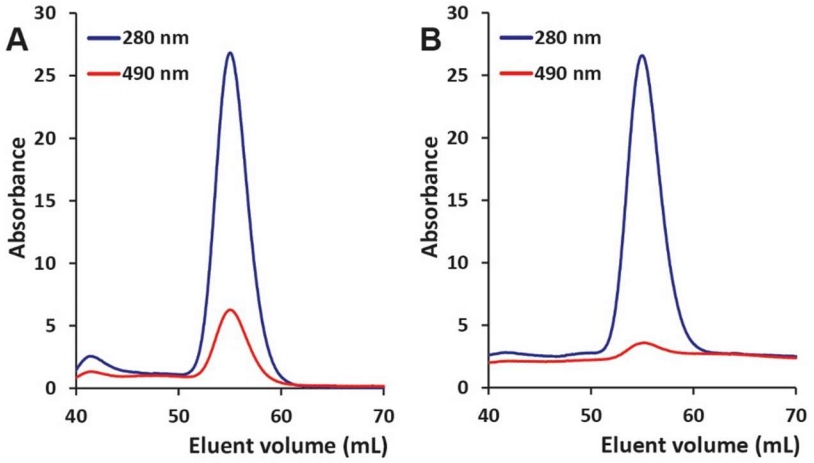

Figure 4.64 Control reactions indicating DOX attachment on the surface of ferritin cages. These are SEC chromatograms of samples that were obtained by simply mixing aldoxorubicin and HF-7C, without opening the ferritin cages. A) Without TCEP. B) With TCEP added during the mixing. Theoretically, no encapsulation should occur without opening the cages, therefore no DOX signal (490 nm) should appear along with the ferritin signal (280 nm). However, here, the co-elution of DOX and ferritin signals was observed, which indicates the association of DOX on the surface of ferritin cages. In B) fewer DOX molecules were associated with ferritin when TCEP was added during the mixing.

Several possible reasons were suggested for explaining the lower cytotoxicity of DOX-Ftn variants compared to the free DOX. First, this might be because DOX-Ftn variants and the free DOX were taken by cells through different mechanisms. Free DOX are small organic molecules that are taken by cells by fast passive diffusion,[35] while DOX-Ftn is macromolecules that are taken by cells through TfR-1 mediated endocytosis.[28] Second, recently, some experimental evidence shows that not all of the DOX molecules were encapsulated inside the ferritin cages (Figure 4.64). The SEC chromatograms show that a simple mixing of DOX and ferritin without opening the cages resulted in the association of DOX and ferritin. This indicates that during the encapsulation, some DOX molecules will also attach to the surface of ferritin cages. This might alter the binding properties of DOX-Ftn to the TfR-1, which in turn affects the uptake and the cytotoxicity of DOX-Ftn. This result is very important as the attachment of DOX to the outer surface of ferritin so far has not been reported in the literature. Interestingly, if TCEP was added during the mixing of DOX and ferritin, fewer DOX molecules were associated with ferritin.

Somehow the TCEP could reduce the interaction between DOX and the outer cages of ferritin. This would explain why DOX (HF-7C) has the highest cytotoxicity of all the other DOX-Ftn variants. This is because, in the present experiments, only DOX (HF-7C) was prepared with a high concentration of TCEP.

Furthermore, DOX must be released from the ferritin cages before it can exert its cytotoxic action by targeting DNA in the nucleus. As this process also takes some time, perhaps this process can be related to the lower cytotoxicity of the DOX-Ftn cage compared to the free DOX.

Another thing to note is, the DOX-Ftn variants show different levels of cytotoxicity. This fact implies that Ftn variants have different binding properties to the TfR-1. However, although the cell experiments were performed by applying DOX-Ftn variants containing the same concentration of DOX, all the DOX-Ftn variants have different loading (Table 4.18) which means different concentrations of ferritin containers were applied to the cells. It is believed that this also determines the efficacy of DOX uptake into the cells. Therefore, the current cytotoxicity results do not exclusively illustrate the binding properties of different ferritin variants to the TfR-1. To get this particular information, the DOX-Ftn variants could be prepared with the same level of DOX loading. Or the binding affinity of each ferritin variant to the TfR-1 could be determined directly, for example by flow cytometry or isothermal titration calorimetry (ITC). Another possibility is to use confocal microscopy to observe and compare how fast the different variants of fluorophore-loaded ferritin are taken by cells having TfR-1 on their surface.

Table 4.18 DOX-Ftn variants and their DOX loading

DOX-Ftn variants	DOX to Ftn ratio in synthesis	Loading
DOX-Ftn$^{(pos)}$	200 eq.	31
DOX (Ftn$^{(neg)}$-1C)	10 eq.	91.7
DOX-HF	1000 eq.	28.7
DOX (HF-7C)	5.25 eq.	20
DOX (HF-1C)	7 eq.	41.7

As a summary, the cytotoxicity assays for testing the biological performance of various DOX-Ftn variants were established. However, the DOX-Ftn variants showed lower cytotoxicity compared to the free DOX solution. Several possible reasons have been discussed. One possible reason is due to the attachment of DOX molecules on the surface of ferritin cages. However, more experiments are needed to investigate and overcome this problem.

5 Summary and perspectives

One of the challenges for the application of ferritin containers in biomedical settings is the degradation by protease in blood circulation. It was envisaged that the integration of ferritin into the polymeric network of microgel could overcome this limitation. For this, first, the ferritin needs to be labeled by fluorophores and NPs to enable the tracking of their integration and release from microgels by fluorescence microscopy and TEM, respectively. Fluorophores with three different charges were encapsulated into $Ftn^{(pos)}$ and $Ftn^{(neg)}$. However, the results show low loadings due to the weak molecular interactions between ferritin and fluorophore molecules. To overcome this problem, the encapsulation was performed by cysteine-maleimide coupling reaction using a $Ftn^{(neg)}$ variant with redesigned cysteine positions. The encapsulation was very efficient and successful. It produced high loading and total yield at a much lower fluorophore concentration. This encapsulation strategy is very helpful for the encapsulation of small organic molecules which have weak interactions with ferritin. The synthesis of NPs inside ferritin was performed by the oxidation of metal cations inside ferritin cages. Iron oxide and cerium oxide NPs were successfully synthesized in various ferritin variants.

For the integration of ferritin into microgels, first, NPs-labeled ferritin was integrated into the simplest polyelectrolyte system: microgels with randomly distributed ionizable groups. The integration was characterized by several problems. First, ferritin and microgels precipitated during the integration. Although later the precipitation could be avoided by using less crosslinked microgels, ferritin and microgels still flocculated and formed larger aggregates in the solution. Moreover, after the integration, the microgels could not be purified from the excess ferritin. Various purification techniques have been applied, but the microgels were not completely clean, probably due to leakage of ferritin containers.

Subsequently, ferritin was integrated into a core-shell microgel system. The results show that the neutral shell of the microgels prevented the flocculation of ferritin and microgels. Furthermore, this microgel system could be purified from the excess ferritin by IEC or SEC. However, it was observed that ferritin leaked out from the microgels and only a few microgels were abundantly filled with ferritin while the others were almost empty. Several tests were performed, and it was found that the inhomogeneous distribution of ferritin among the microgels was caused by the inhomogeneous distribution of MAA groups among the microgels. Additional evidence was also obtained from other characterizations: cryo-TEM, staining the microgels with positively charged AuNPs or uranyl acetate, DLS measurement, and fluorescence microscopy.

Various approaches then were applied to produce microgels with homogeneous distribution MAA. The semi-batch reactions were used to adjust the kinetics with the goal to distribute the MAA evenly among the microgels. Although it did not produce the expected result, it was observed that MAA groups only accumulate in certain microgels when they are present in solution at high concentration. Another approach, changing the reaction pH, also did not solve the problem. Rather than performing laborious trial and error experiments, a model-based design synthesis could be a way to solve this problem. Furthermore, it was found that the charged and the uncharged microgels could be separated by IEC. However, the yield of the charged microgels was rather low.

To overcome ferritin leakage from microgels, an idea to synthesize a charged core microgel with a locking shell was proposed. The locking shell could be prepared by using non-polar monomers, such as tBAM, that would collapse at room temperature. In this case, the integration with ferritin could be performed at low temperatures. When the temperature is raised to room temperature, the shell would collapse and prevent ferritin leakage. However, this plan did not work because tBAM tends to form new microgels instead of building shells on the existing core microgels used as seeds in the reaction.

Finally, ferritin was integrated during the microgel synthesis. This approach solved several problems at once. The resulting microgels integrated the ferritin tightly and no ferritin leakage was observed. Moreover, ferritin was homogeneously distributed among the microgels and the microgels can easily be purified from the excess ferritin by centrifugation. Ferritin-microgels with the favorable size for cell-internalization can be obtained by batch or semi-batch synthesis, but the batch synthesis usually produces smaller microgels. The size of microgels is also related to the ferritin loading. Larger microgels contained more ferritin per microgel volume than the smaller ones. However, it was also observed that the microgels tend to cluster together in solution, which probably can be solved by adding stabilization shells, as observed in the core-shell microgel system.

Afterward, the ferritin release was studied in acidic conditions by TEM and fluorescence microscopy. Ferritin was rapidly released from microgels in acidic conditions and the release increased in lower pH and with longer incubation time. However, a complete release and total degradation of microgels were not achieved due to the self-crosslinking of NIPAM. We also estimated the ferritin loading and release from the microgels by UV/Vis spectrometry. The results show that ferritin was effectively integrated into the microgels and a large amount of ferritin can be released from microgels.

Finally, the first part of this thesis was concluded by showing that the microgels could protect ferritin from proteolytic degradation by chymotrypsin, a model protease. This result is very important for the application of ferritin as a drug delivery vehicle because it shows the potential of microgels to increase the half-life of ferritin in systemic circulation.

In the second part of the thesis, an anti-cancer drug (DOX) was encapsulated in various ferritin variants. The encapsulation of DOX in $Ftn^{(pos)}$ was performed by the diffusion of Cu(II)-DOX through ferritin channels. Several optimizations were performed to obtain a high loading and yield. Moreover, the encapsulation of DOX in $Ftn^{(neg)}$-1C was performed by chemical conjugations, and it produced a high yield and loading. Here, it was found that the encapsulation also occurred via a non-specific binding. Next, DOX was encapsulated in HF using a modified version of the established protocol in the literature. The reported loading could be reproduced, but the yield was rather low. To address this problem, DOX encapsulation by chemical conjugation then was applied to HF with redesigned cysteines: HF-7C and HF-1C. In general, the loading and the yield increased, but they were not as good as the loading and the yield obtained in $Ftn^{(neg)}$-1C.

Subsequently, DOX ($Ftn^{(neg)}$-1C) was integrated into microgels using the same protocols as established in the first part of the thesis. The integration was successful and DOX can be released in acidic conditions. However, the integration of DOX (HF-1C) into microgels produced a lot of aggregation and the loading was poor. Further investigations indicated that some of the DOX molecules were probably attached to the surface of HF-1C, which interfered with their binding to the charged co-monomer VIM.

Next, the cytotoxicity of DOX-Ftn variants was tested and compared to the cytotoxicity of the free-DOX solution. Hepa 1-6 hepatocarcinoma and 3T3 fibroblast were chosen as cancer and control cell lines, respectively. However, the results show that DOX-Ftn variants have lower cytotoxicity compared to the free DOX solution. Several possible reasons have been discussed. One possible reason is due to the attachment of DOX molecules on the surface of ferritin cages, which prevents the ferritin binding with the TfR-1. Further investigations are needed to confirm and overcome this problem. Due to time limitations, the work was concluded for this dissertation at this point.

In this thesis, the integration of ferritin containers into microgel systems by electrostatic interactions has been established. Moreover, it was shown that ferritin can be loaded with different cargo materials (fluorophore, NPs, drugs) and successfully integrated into microgels. This opens new possibilities to combine different materials into microgels for new applications. For example, in drug delivery, different drugs can be delivered; multiple drugs can be combined; or drugs can be coupled with NPs for theranostic purpose. It is envisaged that magnetic- or photo-thermal heating of iron-oxide or gold NPs loaded ferritin can trigger the collapse of the microgels. Moreover, the integration strategy established here will also be applicable for protein containers with larger sizes than ferritin, such as encapsulin, therefore adding the versatility of the system.

As an alternative strategy to integrate protein containers into microgel systems, chemical conjugation can be used instead of electrostatic interactions. It has several advantages compared to electrostatic interactions. Chemical conjugation will prevent the ferritin leakage, but at the same time, the ferritin

can be released easier as there is no physical entrapment involved in this approach. Furthermore, the integration based on electrostatic interactions is often restricted by precipitation or flocculation, or stability problems. These should be reduced in a chemical conjugation approach. However, a suitable cleavable crosslinker should be found for connecting ferritin containers and the microgels. Moreover, a suitable biological stimulus needs to be present to trigger the release of ferritin from microgels.

To improve the degradability of the microgels, a more degradable polymeric material such as polysaccharides[253] can be used instead of synthetic polymers like P(NIPAM). In this case, the microgels themselves can be degraded and not only the crosslinkers.

In the current system, because pH 4.0 - 5.0 is present inside the lysosome, the microgels need to be internalized by cells to be able to release ferritin. This means, in this system the TfR-1 targeting property of ferritin has not been exploited yet. In the future, a ferritin-microgel system that can be degraded extracellularly can be designed, for example by using a peptide crosslinker that is cleavable by matrix metalloproteinase-9, a cancer biomarker known to be present in tumor tissues.[254]

The ferritin cages can also be developed further. For example, integrating stimuli-responsive ferritin cages that can release drugs at a moderate environmental condition into the microgel system could be interesting. Furthermore, currently, our group is developing ferritin cages with a hydrophobic cavity which potentially could be used to efficiently load various hydrophobic drugs. The integration of this novel ferritin variant into the microgel system could serve as a way to load the insoluble drug molecules into the microgels.

6 Experimental section

6.1 General

All syntheses, reactions, and purifications were conducted in ultrapure water from the Purelab Plus (ELGA LabWater). The electrical conductivity of the ultrapure water is 0.055 µS/mL. Samples for DLS measurement were prepared in HPLC grade water LiChrosolv (Merck) when applicable. All glassware and magnetic stirrer bars were washed thoroughly and then rinsed with deionized water. Harvested cell pellets after protein expression and nucleic acids were stored in the freezer at -20 °C. Competent cells and cryo-cultures were stored at -80 °C. Centrifugation was performed in 50 mL or 15 mL falcon tubes with a 5810R centrifuge (Eppendorf). Smaller volumes were centrifuged in 1.5 mL or 2 mL Eppendorf tubes with a Heraeus Fresco 21 microcentrifuge (Thermo Scientific). Centrifugation of bacterial cultures was performed in 500 mL bottles with a Sorval RC 6 Plus centrifuge (Thermo Scientific). Ultracentrifugation was performed in 20 mL polycarbonate bottles with an Optima XPN-80 ultracentrifuge (Beckman Coulter). For concentrating, washing, and exchanging buffer, Amicon Ultra-15 or Amicon Ultra-0.5 centrifugal filter units (Merck) were used. An MWCO of 30 kDa was used for protein production and encapsulation experiments. Unless stated otherwise, dialysis was performed using a dialysis bag with MWCO of 14 kDa (ZelluTrans, Carl Roth). Purification of protein containers by IEC or SEC was performed with an Äkta Pure 25 chromatography system (Cytiva). All the elution buffers were degassed and filtered with a 0.22 µm filter membrane before used. Concentrations of the protein solutions were determined with a NanoDrop 2000 spectrophotometer (Thermo Scientific). The concentrations (mg/mL) always refer to the concentrations of assembled containers and not to the individual subunits, unless stated otherwise. All the purified protein solutions were stored in the dark at 4 °C.

6.2 Chemicals

2,2'-Azobis(2-methylpropionamidine) dihydrochloride, N-isopropylacrylamide, and Rhodamine 6G were purchased from Acros Organics. Rhodamine B was purchased from Alfa Aesar. Ammonium sulfate, Bradford reagent, 2-(*N*-morpholino)ethanesulfonic acid monohydrate, RNase A, tryptone, and yeast extract were purchased from Applichem. Maleimide functionalized Atto Rhodamine 6G was purchased from Atto-tec. Agar was purchased from Beco. 4-(2-hydroxyethyl)-1-piperazineethanesulfonic acid, isopropyl β-D-1-thiogalactopyranoside, and tris(hydroxymethyl)amino-methane were purchased from Carl Roth. MTT cell proliferation assay kit was purchased from Cayman Chemical. $T7_{FOR}$, $T7_{REV}$, QuickChange primers, and ferritin genes were purchased from Eurofins Genomics. Hydrochloric acid was purchased from Fisher Chemicals. Sodium dodecyl sulfate and

sucrose were purchased from Fluka. Magnesium acetate, sodium acetate, sodium chloride, and sodium hydroxide were purchased from Grüssing. NucleoSpin® Gel and PCR clean-up kit and NucleoSpin® Plasmid miniprep kit were purchased from Macherey-Nagel. Doxorubicin hydrochloride and Doxorubicin(6-maleimidocaproyl)hydrazine were purchased from Med Chem Express. Acrylic acid, ammonium iron(II) sulfate hexahydrate, di-potassium hydrogen phosphate trihydrate, Methacrylic acid, N-[3-(dimethylamino) propyl] methacrylamides, N,N'-Bis(acryloyl)cystamine, N,N'-Methylenebis-(acrylamides), sodium fluorescein, and trisodium citrate dihydrate were purchased from Merck. Potassium dihydrogen phosphate was purchased from Riedel. Calcium chloride, cerium(III) chloride heptahydrate, chymotrypsin, copper sulfate pentahydrate, disodium EDTA, glycine, Guanidine hydrochloride, hexadecyltrimethylammonium bromide, iron(III) chloride, potassium persulfate, L-arginine, methanol, 1-Methylpiperazine, N-isopropylmethacrylamide, N-tert-Butylacrylamide, sodium ampicillin, tetramethylethylendiamine, Tween-20, uranyl acetate, 1-Vinylimidazole, and 3,9-Divinyl-2,4,8,10-tetra-oxaspiro[5.5]undecane were purchased from Sigma-Aldrich. Dpn1, dNTP mix, maleimide functionalized Alexa Fluor 488, maleimide functionalized Alexa Fluor 647, Pfu DNA polymerase, and (tris(2-carboxyethyl)phosphine) hydrochloride were purchased from Thermofisher Scientific. Hydrogen peroxide was purchased from Th. Geyer. Anhydrous dimethyl sulfoxide was purchased from VWR Chemicals. All chemicals used without further purifications, unless stated otherwise.

6.3 *E. coli* strains

E. coli strains used for protein expression and plasmid replication are listed below in Table 6.1.

Table 6.1 List of *E. coli* strains

Strain	Genotype	Supplier
BL21-Gold(DE3)	E. coli B F- dcm ompT hsdS(rB- mB-) gal λ(DE3)	Agilent
DH5α	F^- Φ80*lac*ZΔM15 Δ(*lac*ZYA-*arg*F) U169 *rec*A1 *end*A1 *hsd*R17(rk^-, mk^+) *pho*A *sup*E44 *thi*-1 *gyr*A96 *rel*A1 λ	Invitrogen

6.4 Solution recipes

LB medium: 4 g yeast extract, 8 g tryptone, 8 g NaCl were dissolved in 800 mL Milli-Q water and autoclaved.

Agar plate: 4 g yeast extract, 8 g tryptone, 8 g NaCl, and 12 g agar were dissolved in 800 mL Milli-Q water using a magnetic stirrer and then autoclaved. The solution was cooled down in a water bath to

55 °C. 1.2 mL Ampicillin stock solution was added to the solution, mixed well, and poured to the plates inside the laminar hood. The agar plate was let to solidified at RT for about 1h, and then stored at -4 °C.

Sodium ampicillin stock solution: 2 g sodium ampicillin was dissolved in 20 mL Milli-Q water and then filtered with a 0.22 µM syringe filter to sterilize it. The solution was distributed into small aliquots in 10 Eppendorf tubes and stored at -20 °C.

IPTG stock solution: 0.48 g IPTG was dissolved in 10 mL Milli-Q water and then filtered with a 0.22 µM syringe filter to sterilize it. The solution was distributed into 5 small Eppendorf tubes and stored at -20 °C.

6.5 Analytical methods

6.5.1 Transmission electron microscopy (TEM)

Ferritin samples were prepared at 0.3 mg/mL concentration, while microgel samples were prepared at 0.1 mg/mL concentration. To prepare a TEM grid for the sample without staining, 2 µL sample solution was dropped on a Formvar carbon-coated copper grid (400 mesh, Ted Pella, 01814-F) and then left dried in air. To prepare a TEM grid for the sample with staining, a Formvar carbon-coated copper grid was incubated face-down to a 20 µL droplet of sample solution for 1 minute. Then, the grid was washed 3x in Milli-Q water, followed by 1x wash and 1x incubation for 45 s on 2% uranyl acetate drops, blotted with filter paper, and then left dried in air. The TEM measurements were carried out on a Zeiss Libra 200 FE transmission electron microscope and operated at 200 kV.

6.5.2 Cryo-TEM

For sample preparation, one drop of microgel solution (0.1 mg/mL) was placed onto a plasma-treated 300-mesh carbon-coated copper grid (EMS). The drop was thinned into a film less than 300 nm thick, by blotting away the excess solution with a filter paper wrapped on a metal strip. The grid was then plunged into liquid ethane at its freezing point (-183°C) and cooled by liquid nitrogen at its boiling point (-196 °C). Until imaging, the vitrified specimens were stored under liquid nitrogen. For morphological observation, zero-loss energy-filtered TEM images were recorded with a LIBRA 120 operating at 120 kV using a bottom-mounted CCD camera.

6.5.3 Electron tomography

The electron tomography measurement and the post-processing were performed by Maria Meledina and Alexander Meledin (Central facility for electron microscopy, RWTH Aachen University), respectively. The sample preparation was similar to the preparation of the TEM grid without staining. In electron tomography, a HAADF-STEM tilt series was recorded using an FEI Tecnai microscope operated at 200 kV. The sample was tilted from -76° to 70° and images were taken every 2°. FEI

Inspect3D software was used for the reconstruction with the SIRT algorithm. Thermo Fisher Avizo software was further used for the visualization.

6.5.4 Wide-field fluorescence microscopy

Wide-field fluorescence microscopy was performed by Lukas Schubert (Institute of Physical Chemistry, RWTH Aachen University). 50 µL microgels solution with a concentration of 0.1 mg/mL was spin-coated on a plasma cleaned coverslip (Marienfeld Superior 170 µm, cleaned overnight using Hellmanex III solution, 15 min in plasma oven). As a result, the microgels were immobilized to the surface of the coverslip. For introducing liquid to the sample, a sticky slide (ibidi GmbH, sticky-Slide 8 Well, dimensions each well: 9.4 × 10.7 × 6.8 mm) was glued on the prepared coverslip. The fluorescence signals were captured by using an Olympus IX83 inverted fluorescence microscope equipped with an Olympus 100x APO Objective (100x magnification, NA: 1.3, WD: 0.2 mm, oil immersive). The excitation light from a 488 nm laser (Cobolt MLD, 200 mW) can be separated using a 500 nm long-pass emission filter (Chroma, 500 LP ET). Between microscope and camera, a 2x magnification path with 2 convex lenses (150 mm & 300 mm focal length) was introduced to increase the image size. The resulting image size is 80 nm per pixel. The fluorescence signals were increased using an electron-multiplying gain of 200 by the camera (Andor XIon Ultra 897 EMCCD). To calculate the average fluorescence intensity, the dark background was subtracted from each pixel, followed by the integration of the intensities.

6.5.5 Dynamic light scattering (DLS) and ζ-potential measurements

The hydrodynamic radius of ferritin and microgels were measured at 20 °C in water by Dynamic Light Scattering (Malvern Zetasizer Nano S, equipped with a He–Ne laser at 633 nm and θ= 173°). For this, ferritin and microgel solutions with a concentration of 0.5 mg/mL and 0.1 mg/mL were prepared, respectively. The samples were measured in PMMA micro cuvettes (Brand). All the measurements were performed in triplicates with 120 s equilibration time. Data analysis was performed with the Zetasizer software by cumulant analysis. The size-temperature dependence of the microgels was also measured with DLS. The volume phase transition temperature (VPTT) was determined from the inflection point of its sigmoidal-Boltzman curve fit (OriginPro®).

ζ-potential and electrophoretic mobility of microgels were also conducted with the same instrument (Malvern Zetasizer Nano S, equipped with a He–Ne laser at 633 nm and θ= 173°) at 20°C in micro zeta disposable capillary cells (PMMA, DTS1070, Malvern Instrument). Before the measurement, the samples were equilibrated for 120 s and the microgel concentration was also 0.1 mg/mL. Data analysis was performed with the Smoluchowski approximation to convert electrophoretic mobility to the ζ-potential. The measurements were performed in triplicates.

6.5.6 Optical microscopy

Crystals were observed and imaged using a CrysCam digital microscope (Art Robbins).

6.5.7 UV/Vis spectroscopy

The UV/Vis spectra were recorded in disposable UV micro cuvettes (Brand) or quartz cuvette (Hellma Analytics) with a 1 cm path length on a Jasco V-630 spectrophotometer. Water was used as a reference.

6.6 Experimental protocols

6.6.1 Production and purification of supercharged ferritin variants.

$Ftn^{(pos)}$ and $Ftn^{(neg)}$ were produced and purified as described before.[24]

Production of $Ftn^{(pos)}$: A cryo-stock of *E. coli* BL21-Gold(DE3) containing pET-22b(+) plasmid embedded with $Ftn^{(pos)}$ gene was used to prepare a preculture in 5 mL sterile LB medium supplemented with 150 µg/mL sodium ampicillin and incubated overnight at 37 °C and 250 rpm. 4 mL of this preculture was diluted into 400 mL LB medium containing 150 µg/mL sodium ampicillin and incubated at 37°C and 250 rpm. After reaching an optical density at 600 nm (OD_{600}) of 0.2, protein expression was induced by adding IPTG to a final concentration of 0.25 mM. The protein expression was continued at 37 °C for 5 h. Cells were harvested by 10 min centrifugation at 14000 g and 4 °C. The pellet was washed with Milli-Q water and stored at -20 °C.

Purification of $Ftn^{(pos)}$: The pellet was resuspended in 10 mL buffer A (50 mM Tris buffer pH 7.5; 1.5 M NaCl) and sonicated in ice (60% amplitude; 4 x 1 min) with a Vibra-Cell VCX-130 ultrasonic processor (Sonics). The suspension was centrifuged at 14000 g and 4 °C for 15 min to remove cell debris. Next, the supernatant was incubated with 1.5 mg/mL RNase A for 3 h at 37°C. Note that incomplete digestion of RNA reduced $Ftn^{(pos)}$ binding to the cation exchange column in later purification steps. Subsequently, the solution was heated at 65 °C for 15 min in a water bath. Denatured *E. coli* proteins were removed by centrifugation at 14000 g and 4 °C for 15 min. The supernatant was subjected to precipitation with ammonium sulfate at a final concentration of 70% of its saturation and followed by centrifugation at 14000 g and 4 °C for 15 min. The pellet was re-dissolved in 10 mL buffer A and purified by ammonium sulfate precipitation once again for further removal of nucleic acids. The pellet was then dissolved in 50 mL buffer B (50 mM MES buffer pH 6; 0.5 M NaCl) and filtered with a 0.22 µm syringe filter. Afterward, the sample was purified by IEC. For this, the sample was loaded to a 5 mL Sepharose HiTrap SP HP column (Cytiva) and eluted with a salt gradient from 0.5 to 1.5 M NaCl. The $Ftn^{(pos)}$ fractions were collected and washed 5x with Milli-Q water using an Amicon Ultra-15 centrifugal filter unit (MWCO 100 kDa). The final solution was concentrated to 2 mL and further purified by SEC. For this, the sample was loaded into HiLoad 16/600 Superdex PG column (Cytiva) with buffer C (50 mM Tris Buffer pH 7.5;

1 M NaCl) as elution buffer. The $Ftn^{(pos)}$ fractions were collected and washed 5x with Milli-Q water as before and stored at 4 °C. The protein concentration was determined by NanoDrop.

Production of $Ftn^{(neg)}$: It is similar to $Ftn^{(pos)}$, but here the cryo-stock used to prepare preculture contains pET-22b(+) plasmid embedded with the $Ftn^{(neg)}$ gene. Protein expression was induced after an OD_{600} of 0.7 and followed by incubation at 18 °C for 48 h.

Purification of $Ftn^{(neg)}$: It resembles the purification of $Ftn^{(pos)}$ but with minor changes. The pellet was resuspended in 20 mL buffer D (50 mM Tris buffer pH 7.5; 0.15 M NaCl) and sonicated (8 x 1 min) in ice. RNA digestion was omitted, and the solution was divided into two falcon tubes before performing the ammonium sulfate precipitation. For IEC, the protein was resuspended in 50 mL buffer D and purified by a salt gradient from 0.15 to 1 M NaCl using a 5mL Sepharose HiTrap Q HP anion exchange column (Cytiva). Finally, SEC was conducted with buffer E (50 mM Tris Buffer pH 7.5; 0.3 M NaCl) as elution buffer.

6.6.2 Fluorophore encapsulation in ferritin

6.6.2.1 Encapsulation of fluorophores in $Ftn^{(neg)}$ and $Ftn^{(pos)}$

The encapsulation of fluorophores in $Ftn^{(neg)}$ was achieved by an acidic dis/reassembly approach. First, 1.5 mg $Ftn^{(neg)}$ was incubated in 1.5 mL disassembly buffer (20 mM PBS buffer pH 2.0; 50 mM NaCl) for 4 h to ensure complete disassembly. Next, the appropriate amount of fluorophore was dissolved in reassembly buffer (50 mM PBS buffer pH 7.4; 50 mM NaCl). 3 mL of this solution then was added to the first solution, and the final pH was adjusted to 7.4 by adding a few µL of 1 M NaOH or HCl. Afterward, this solution was incubated overnight at 4 °C. The next day, the solution was washed 5x with reassembly buffer, concentrated to 2 mL, and purified by SEC with buffer E as elution buffer. The final concentration of fluorescein was: 5 mM, 50 mM, and 100 mM. For Rho B and Rho 6G, the concentration was 20 mM and 0.325 mM, respectively.

The encapsulation of fluorophore in $Ftn^{(pos)}$ was performed by diffusion through channels.[106] For this, 1.5 mg $Ftn^{(pos)}$ was dissolved in 2.883 mL of incubation buffer (20 mM acetate buffer pH 5.0; 40 mM NaCl) and heated at 60 °C for 30 minutes with gentle stirring. Next, 20 mg Rho 6G was dissolved in 1 mL incubation buffer to make a stock solution of 41.75 mM. Then, 1.617 mL of this stock solution was dropwise added to the first solution, and the incubation was continued for another 2.5 h. This solution was cooled down to RT, washed 5x with Milli-Q water, concentrated to 2 mL, and purified by SEC with buffer C as elution buffer.

6.6.2.2 Characterization of Rho B-Ftn$^{(neg)}$

The UV/Vis spectra of Ftn$^{(neg)}$ and Rho B-Ftn$^{(neg)}$ were measured using solutions with a concentration of 0.5 mg/mL. To confirm that the ferritin cages formed after the reassembly, the Rho B-Ftn$^{(neg)}$ solution was imaged by TEM with staining.

The crystallization of Rho B-Ftn$^{(neg)}$ was carried out by the hanging drop method in pre-greased 24 well plates (Crystalgen).[255] The well was filled with a reservoir solution containing: 50 µL 1 M Tris buffer pH 8.5, 120 µL 2 M magnesium acetate, and 330 µL Milli-Q water. Next, a drop was prepared on a glass cover slide (Jena Bioscience) by mixing: 2 µL reservoir solution, 1 µL buffer C, and 1 µL of 4 mg/mL Rho B-Ftn$^{(neg)}$ dissolved in buffer E. The cover slide then was placed drop-side-down onto the pre-greased well, sealed tight, and equilibrated against reservoir solution at 20 °C. The crystals were imaged by CrysCam digital microscope.

6.6.2.3 Loading and yield determination.

The fluorophore loading was determined by UV/Vis spectrometry in pH 2.5 to avoid reduced absorption or fluorescence quenching.[22] The concentration of fluorophore was determined from the absorption at λ_{max} (Fscn = 488 nm, Rho B = 554 nm, and Rho 6G = 530 nm). For this, standard calibration curves were prepared for each fluorophore in the range of 1 – 10 µM. Next, the concentration of protein was determined from the absorption at 280 nm, after subtracting the absorption of fluorophore at 280 nm.[29] This value can be calculated based on assumption that the ratio A280/Aλ_{max} is constant at any concentration. Similarly, a standard calibration curve was also established for the protein in the range of 0.1 – 1.0 mg/mL. Finally, the loading is the ratio of fluorophore concentration to protein concentration. The yield was calculated using the protein concentration.

6.6.3 Fluorophore encapsulation by chemical conjugation

6.6.3.1 Mutagenesis to relocate cysteine position in Ftn$^{(neg)}$

The relocation of cysteine position in Ftn$^{(neg)}$ was performed in two mutation steps: C130A and K53C. The second mutation was found from the calculation of solvent-accessible surface area by GETAREA.[238] The protein database (PDB) file of Ferritin$^{(neg)}$ was inserted into the program and based on the results (% ratio) amino acids were categorized into several classes (e.g. 90-100%, 80-90%, …, 50-60%). Next, PyMOL (Schrödinger) was used to check the location of amino acids in each class, starting from classes with the highest % ratio. In this way, lysine-53 was found as the amino acid with the highest % ratio in the cavity.

The mutation was performed by QuickChange™ site-directed mutagenesis using a two-steps polymerase chain reaction (PCR) protocol.[256] First, two sets of primers were designed using

QuickChange™ Primer Design Program (Agilent). The primer sequences for C130A and K53C were: 5'-C AAG AAC GAT CCG CAT CTG GCC GAT TTC ATC GAA ACC CAC-3' and 5'-T GTT GCA CTG AAG AAC TTT GCG TGT TAC TTT CTG CAT CAG TCC CAT G-3', respectively (ordered from Eurofins Genomics).

Next, a master mix was prepared by combining: 2.9 µL pET-22b(+) plasmid containing $Ftn^{(neg)}$ gene (7 ng/µL), 1 µL dNTP mix, 5 µL buffer 10x, 1 µL Pfu DNA polymerase, and 38.1 µL sterile Milli-Q water. This master mix was divided into two microtubes and added with 1 µL C130A FOR or REV primer. This recipe can be tripled to get a higher amount of plasmid. Subsequently, a PCR (Eppendorf Mastercycler Nexus PCR Cycler) was performed with the following parameters. Initiation: heating for 30 s at 95 °C. Step 1 (3 cycles): denaturation for 30 s at 95 °C, annealing for 1 min at 61 °C, and elongation for 6 min at 68 °C, hold for an infinite time at 4 °C. The two microtubes were combined and PCR was continued with Step2 (16 cycles): denaturation for 30 s at 95 °C, annealing for 1 min at 61 °C, and elongation for 6 min at 68 °C. Final elongation: for 10 min at 68 °C. Storage: for an infinite time at 4 °C.

Afterward, 1 µL Dpn1 was added to digest the parental plasmid overnight at 37 °C. The following day, Dpn1 was deactivated by heating for 20 min at 80 °C. This was followed by purification using NucleoSpin® Gel and PCR clean-up kit according to the manufacturer's instructions. Next, 200 ng of the plasmid was transformed by heat-shock into *E. Coli* DH5α competent cell, plated onto LB agar plate with ampicillin, and incubated at 37 °C for 16 h. A single colony was picked up and incubated overnight in 5 mL sterile LB medium supplemented with 150 µg/mL ampicillin at 37 °C and 250 rpm. 4 mL of the culture then was used for plasmid extraction by NucleoSpin® Plasmid miniprep kit according to the manufacturer's instructions. The plasmid DNA was eluted in 50 µL sterile Milli-Q water and the concentration was determined by NanoDrop.

To confirm the sequence, 500 ng plasmid was mixed with 25 pmol $T7_{FOR}$ or $T7_{REV}$ primer in 10 µL solution and sent for DNA sequencing (Eurofins Genomics). The result was analyzed by CLC Sequence Viewer (QIAGEN Bioinformatics). The correct plasmid then was used as a template for the second-round mutation, along with K53C primers, in the same way as described above.

For protein production, the plasmid was further transformed by heat shock into *E. coli* BL21-Gold(DE3) competent cells. Both the production and purification were performed in the same way as for $Ftn^{(neg)}$.

6.6.3.2 Encapsulation of fluorophore by chemical conjugation.

1.5 mg $Ftn^{(neg)}$-1C was incubated in 1.5 mL disassembly buffer (10 mM glycine buffer pH 2.5) for 4 h to ensure complete disassembly. In the meantime, 1 mg AR 6G, AF 488, and AF 647 were dissolved separately in 200 µL anhydrous DMSO to prepare stock solutions. After 4 h, 3 mL reassembly buffer (50 mM Tris buffer pH 7.5; 0.5 M NaCl) was added to ferritin solution, and the final pH was adjusted to 7.4 by adding a few µL of NaOH or HCl 1 M. Next, the exposed cysteines were reacted with 1 eq.

fluorophore and incubated at RT overnight. The next day, the solution was washed 1x with Milli-Q water, concentrated to 2 mL, and purified by SEC with buffer E as elution buffer. The loading was determined in the same way as above. The maximum absorption of AR 6G, AF 488, and AF 647 were at 533 nm, 496 nm, and 650 nm, respectively.

6.6.4 Synthesis and characterization of nanoparticles loaded ferritin

NPs loaded ferritin were synthesized according to the previously reported protocol.[24] **Synthesis and characterizations of Ce-Ftn$^{(neg)}$**: Buffer E, 15 mM H_2O_2, and 30 mM $CeCl_3$ were depleted of O_2 by bubbling N_2 through the solutions for at least 15 min. 25 mg Ftn$^{(neg)}$ was dissolved in buffer E to make a concentration of 0.4 mg/mL and then heated in an oil bath at 65 °C for 20 min under an oxygen-free atmosphere with constant stirring. 3.625 mL of $CeCl_3$ and 3.625 mL H_2O_2 were injected into Ftn$^{(neg)}$ solution at the same time with a speed of 3.625 mL/h by using two separate syringe pumps (Fischer Scientific). Once the injection was completed, the reaction was continued for another 15 min. Finally, 2.344 mL disodium EDTA 500 mM was added to chelate the residual cerium ions. After 15 min, the solution was cooled down to RT and centrifuged for 15 min at 14000 g and 4°C. The supernatant was washed 1x with Milli-Q water, concentrated to 2 mL, and purified with SEC as described above. The concentration of Ce-Ftn$^{(neg)}$ was estimated with Bradford assay.[257] Additionally, the UV/Vis spectrum was measured, and the nanoparticle formation was analyzed by TEM.

Synthesis of Ce-Ftn$^{(pos)}$: The synthesis was performed in a similar way as Ce-Ftn$^{(neg)}$. However, here buffer C was used to dissolve Ftn$^{(pos)}$ instead of buffer E.

Synthesis of Ce(HF-1C): The synthesis was performed exactly in the same way as Ce-Ftn$^{(neg)}$ above.

Synthesis of Fe-Ftn$^{(neg)}$: Buffer F (200 mM HEPES buffer pH 8.6), 25 mM H_2O_2, 75 mM $(NH_4)_2Fe(SO_4)_2$, and Milli-Q water were depleted of O_2 by bubbling N_2 through the solutions for at least 15 min. 25 mg Ftn$^{(neg)}$ was dissolved in 18.25 mL buffer F, diluted with Milli-Q water to 36.5 mL, and heated in an oil bath at 65 °C for 20 min under an oxygen-free atmosphere using a 100 mL two-neck round-bottom flask with constant stirring. 2.33 mL of $(NH_4)_2Fe(SO_4)_2$ and 2.33 mL H_2O_2 were injected into Ftn$^{(neg)}$ solution at the same time with a speed of 0.78 mL/h by using two separate syringe-pumps. At this setting, about 3500 Fe (II) ions were injected into a ferritin cage at a flow rate of 100 ions per minute. Once the injection was complete, the reaction was continued for another 15 min. Finally, 2 mL sodium citrate 300 mM was added to chelate the residual iron ions. After 15 min, the solution was cooled down to RT and centrifuged for 10 min at 14000 g and 4°C. The supernatant was washed 5x with Milli-Q water, concentrated to 2 mL, and purified with SEC as described above.

6.6.5 Integration of ferritin into microgels with randomly distributed ionizable groups

The integration of P(NIPAM-co-VIM) and Fe-Ftn$^{(neg)}$: P(NIPAM-co-VIM) (88% : 10% : 2% mol BIS) solid microgels were dissolved in Milli-Q water to prepare a stock solution of 10 mg/mL. This solution was run overnight on a roller mixer to fully redisperse the microgels. 30 µL microgels stock solution (0.3 mg) and 0.15 mg Fe-Ftn$^{(neg)}$ was added into 20 mM PBS buffer solution (pH 3-10) to make a total volume of 0.5 mL. The solutions were observed for precipitation. One of the precipitated solutions then was analyzed by TEM without further purification.

The integration of P(NIPAM-co-IA) and Ce-Ftn$^{(pos)}$: This was performed in a similar way as described above, but the microgels and ferritin were replaced with P(NIPAM-co-IA) (88% : 10% : 2% mol BIS) and Ce-Ftn$^{(pos)}$.

The effect of salt addition: The integration of P(NIPAM-co-VIM) and Fe-Ftn$^{(neg)}$ were repeated at pH 5.0 but with different salt concentrations (0-500 mM). Similarly, the integration of P(NIPAM-co-IA) and Ce-Ftn$^{(pos)}$ were also repeated at pH 8.0 with different salt concentrations (0-500 mM).

DLS measurements: The size and electrophoretic mobility of 0.1 mg/mL P(NIPAM-co-VIM) microgel solution were measured in 10 mM PBS buffer with different pH from 3-10.

Integration into less crosslinked microgels: The integration of Fe-Ftn$^{(neg)}$ into P(NIPAM-co-VIM) microgels with 0.2% mol BIS was performed at pH 5.0, similar to the integration into P(NIPAM-co-VIM) microgels with 2% mol BIS.

Microgel purifications: To purify microgels from the unbound ferritin after the integration, several separation techniques were tested: centrifugation (5x @5000 g, 1 h), dialysis (MWCO 1000 kDa), ultrafiltration centrifugation (MWCO: 1000 kDa and 0.2 µm; Vivaspin, Sartorius), and sucrose cushion centrifugation. The composition of the sucrose cushion from bottom to the top was: 3 mL (70% w/w), 10 mL (30% w/w), 5 mL (20% w/w), and finally 4 mL sample solution.

Microgel flocculation: To investigate whether flocculation occurred during the integration of P(NIPAM-co-VIM) (89.8% : 10% : 0.2% mol BIS) microgels and Fe-Ftn$^{(neg)}$, we measured the size of microgels before and after the integration by DLS. Both solutions contained the same concentration of microgels (0.1 mg/mL).

6.6.6 Integration of Ce-Ftn$^{(pos)}$ into the charged core-neutral shell microgels

Integration protocol: The microgels used here were charged core and neutral shell microgels. The core consists of P(NIPAM-co-MAA-co-MRB) (90.985% : 5% : 0.015% : 4% mol BIS) while the shell consists of P(NIPAM) (96.1% : 3.9% mol BIS). The solid microgels were dissolved in Milli-Q water to prepare a stock solution of 10 mg/mL. This solution was run overnight on a roller mixer to fully redisperse the

microgels. 200 µL microgel stock solution was added to 1.4 mL buffer pH 8.0 (20 mM Tris buffer) in a 15 mL falcon tube. Next, 0.25 mg Ce-Ftn$^{(pos)}$, 200 µL buffer pH 8.0, and Milli-Q water were added into a separate falcon tube to make a total volume of 400 µL. Finally, the microgel solution was added dropwise into the ferritin solution with gentle stirring. This solution then was left on the roller mixer overnight. The following day, the reaction mixture was analyzed by TEM without further purification.

Purification by ultracentrifugation: The microgels were purified by 3 cycles of centrifugation (257300 g, 45 min) and redispersion in Milli-Q water. The redispersion was performed overnight on a roller mixer.

Purification by IEC: Here, the IEC was performed by using a 5 mL Sepharose HiTrap SP HP column, with 20 mM Tris buffer pH 8.0 as loading buffer and buffer A as elution buffer. First, 2 mg of pure microgels was dissolved in 2 mL of loading buffer and purified by IEC. Similarly, 0.25 mg of pure Ce-Ftn$^{(pos)}$ was dissolved in 2 mL of loading buffer and then purified by IEC. Finally, Ce-Ftn$^{(pos)}$ was integrated into microgels as described above, and the resulting solution was purified by IEC. Two fractions were collected and analyzed by TEM. The resulting microgel fraction then was further purified by two consecutive IEC runs. In each run, two IEC columns were connected in series, and the purified microgels were analyzed by TEM.

Purification by SEC: Here, the SEC was performed by using HiPrep 16/60 Sephacryl S-500 HR column, with 50 mM Tris buffer pH 8.0 used as elution buffer. First, 2 mg of pure microgels was dissolved in 2 mL elution buffer and purified by SEC. Next, 0.25 mg of pure Ce-Ftn$^{(pos)}$ was dissolved in 2 mL elution buffer and then purified by SEC. Finally, the purified microgel fraction obtained from 3x consecutive IEC purifications is purified further by SEC. The resulting microgel fractions were collected and analyzed by TEM.

6.6.7 Investigation of the inhomogeneous distribution of ferritin in microgels

One-pot synthesis of P(NIPAM-co-MAA) core microgels: The precipitation polymerization was performed in total monomer concentration of 150 mM and total volume of 30 mL. 478.7 mg NIPAM (94 mol%), 19 µL MAA (5 mol %), 7 mg BIS (1 mol %), and 13 mg SDS (1.5 mM) were dissolved in 25 mL water in a 100 mL three-neck round-bottom flask equipped with a reflux condenser. The mixture was stirred with a magnetic bar at 300 rpm and preheated to 80 C. Degassing was accomplished by purging with nitrogen for 1 h. 24.4 mg KPS (3 mM) was dissolved in 5 mL water and likewise degassed with nitrogen at RT. The reaction was started by injecting the initiator, and it was let to proceed for 2 h with constant stirring, temperature, and nitrogen flow. Purification was performed by 5x dialysis, each for at least 4h, against 5 L fresh deionized water. The microgels were lyophilized for storage. The synthesis was repeated for 5% and 4% mol BIS. Furthermore, the synthesis was also repeated at 1 % BIS

crosslinker but with different amounts of charged monomer: 10% and 15% mol MAA. The integration of Ce-Ftn$^{(pos)}$ into these microgels was conducted similarly as described in section 6.6.6.

The inhomogeneous distribution of ferritin in microgels was confirmed by several characterizations. **Cryo-TEM**: Ce-Ftn$^{(pos)}$ integrated P(NIPAM-co-MAA) (94% : 5% : 1% mol BIS) microgel solution with a concentration of 0.1 mg/mL was recorded by cryo-TEM.

Replacement of Ce-Ftn$^{(pos)}$ by AuNPs: The AuNPs were obtained from Marcel Lach, a coworker in our group. The integration of AuNPs into P(NIPAM-co-MAA) (84% : 15% : 1% mol BIS) microgels was performed in a similar fashion as described for Ce-Ftn$^{(pos)}$ in section 6.6.6. The reaction mixture (0.1 mg/mL) was characterized by regular TEM.

Microgel staining with uranyl acetate: P(NIPAM-co-MAA) (84% : 15% : 1% mol BIS) microgel solution with a concentration of 0.1 mg/mL was stained by 2% uranyl acetate as described in the general section (6.5.1) and then imaged by regular TEM. For comparison, the same microgel solution was stained according to the protocol published by Hoare *et al*.[173]

DLS characterization: The size of P(NIPAM-co-MAA) (94% : 1% : 5% mol BIS) microgels was measured by DLS: (1) in water, (2) in 10 mM Tris buffer pH 8.0 and 9.0, and (3) in 10 mM glycine buffer pH 2.5.

Fluorescence microscopy: K36-GFP protein was obtained from Sarah Wypysek. 0.5 mg K36-GFP protein was integrated into P(NIPAM-co-MAA) (84% : 15% : 1% mol BIS) microgels in a similar way as described for Ce-Ftn$^{(pos)}$ in section 6.6.6. The reaction mixture was diluted 10x and then spin-coated on a coverslip. The microgels were imaged in the bright field and the fluorescence of the same area was recorded using an excitation wavelength of 488 nm.

6.6.8 Overcoming the inhomogeneous distribution of charged groups in microgels

Semi-batch synthesis of P(NIPAM-co-MAA) core microgels: The precipitation polymerization was performed in a total monomer concentration of 150 mM and total volume of 30 mL. 478.7 mg NIPAM (94 mol%), 7 mg BIS (1 mol %), and 13 mg SDS (1.5 mM) were dissolved in 20 mL water in a 100 mL three-neck round-bottom flask equipped with a reflux condenser. The mixture was stirred with a magnetic bar at 300 rpm and preheated to 80 C. Degassing was accomplished by purging with nitrogen for 1 h. 19 µL MAA (5 mol %) and 24.4 mg KPS (3 mM) were dissolved separately, each in 5 mL water, and likewise degassed with nitrogen at RT. The reaction was started by injecting the initiator. The MAA solution was added dropwise in 5 min by a syringe pump and the reaction was let to proceed for 2 h with constant stirring, temperature, and nitrogen flow. Purification was performed by 5x dialysis, each for at least 4h, against 5 L fresh deionized water. The microgels were lyophilized for storage. The synthesis was repeated for 10 min, 20 min, and 30 min MAA feeding time. Finally, the synthesis was repeated with MAA placed in the flask, and NIPAM was added dropwise to the flask in 10 min (after

the reaction has been started). The integration of Ce-Ftn$^{(pos)}$ into these microgels was conducted similarly as described in section 6.6.6.

One-pot synthesis of P(NIPMAM-co-AA) core microgels: The precipitation polymerization was performed in a total monomer concentration of 140 mM and a total volume of 250 mL. In a 500 mL three-necked flask, NIPMAM (88% mol) and AA (10%) were dissolved in 210 mL of Milli-Q water. The solution was heated to 55 °C and stirred at 300 rpm. KPS, TEMED, and SDS were dissolved separately, each in 10 mL Milli-Q water, to give the final concentration in solution 5 mM, 2 mM, and 2.05 mM, respectively. BAC (2% mol) was dissolved separately in 10 mL MeOH. All solutions were degassed with N_2 for at least an hour. To start the reaction, SDS, KPS, TEMED, and BAC solutions were added to the flask in this order and rapid succession. After 3 hours, the flask was removed from the oil baths to cool it down. The warm solution was filtered through glass wool to remove any aggregates. Next, the solution was dialyzed against Milli-Q water with daily changes for at least one week. Afterward, the solution was lyophilized. Prior used, the solid microgels were redispersed in Milli-Q water to make a 10 mg/mL stock solution. The integration of Ce-Ftn$^{(pos)}$ into these microgels was conducted similarly as described in section 6.6.6.

One-pot synthesis of P(NIPAM-co-VIM) core microgels: The precipitation polymerization was performed in a total monomer concentration of 150 mM and a total volume of 30 mL. 453.2 mg NIPAM (89 mol%), 7 mg BIS (1 mol %), and 42.3 mg VIM (10 mol %) were dissolved in 25 mL water in a 100 mL three-neck round-bottom flask equipped with a reflux condenser. The mixture was stirred with a magnetic bar at 300 rpm and preheated to 80 °C. Degassing was accomplished by purging with nitrogen for 1 h. 24.4 mg AMPA (3 mM) was dissolved in 5 mL water and likewise degassed with nitrogen at RT. The reaction was started by adding the initiator AMPA. The reaction was let to proceed for 2 h with constant stirring, temperature, and nitrogen flow. Purification was performed by 5x dialysis, each for at least 4 h, against 5 L fresh deionized water. The microgels were lyophilized for storage. The synthesis was repeated, but the pH of the solution in the flask was adjusted to pH 3.0 before heating and degassing. The integration of Fe-Ftn$^{(neg)}$ into these microgels was conducted as described in section 6.6.6, but using 20 mM NMP buffer pH 5.0.

One-pot synthesis of P(NIPAM-co-MAA) microgels at different pH: Here, P(NIPAM-co-MAA)(84% : 15% : 1% mol BIS) microgels were synthesis at different pH according to the protocol described in section 6.6.7. Before heating and degassing, the pH of the solution was adjusted to pH 4.0 and 5.0. The integration of Ce-Ftn$^{(pos)}$ into these microgels was conducted similarly as described in section 6.6.6.

Separation of the charged and uncharged microgels by IEC: P(NIPAM-co-MAA) (94% : 5% : 1% mol BIS) microgels were purified by IEC using 5 mL Sepharose HiTrap Q HP column, with Milli-Q water as the loading buffer and buffer A as the elution buffer. First, 2 mg of pure microgels was dissolved in 2

mL of loading buffer and purified by IEC. Two fractions were collected separately and purified by 5x dialysis, each for at least 4 h, against 5 L fresh deionized water. Next, Ce-Ftn$^{(pos)}$ was integrated into these two microgel fractions as described in section 6.6.6. Finally, both of the reaction mixtures were analyzed by TEM.

6.6.9 Overcoming the ferritin leakage from microgels

One-pot synthesis of P(NIPMAM-co-DMAPMA) core microgels: The precipitation polymerization was performed in a total monomer concentration of 140 mM and a total volume of 250 mL. In a 500 mL three-necked flask, NIPMAM (88% mol) and DMAPMA (10%) were dissolved in 220 mL of Milli-Q water. The solution was heated to 55 °C and stirred at 300 rpm. V50 and CTAB were dissolved separately, each in 10 mL Milli-Q water, to give the final concentration in solution 2 mM and 0.115 mM, respectively. BAC (2% mol) was dissolved separately in 10 mL MeOH. All solutions were degassed with N_2 for at least an hour. V50, CTAB, and BAC solutions were added to the flask and the reaction was started by irradiation with UV light (365 nm). After 3 hours, the flask was removed from the oil baths to cool it down. The warm solution was filtered through glass wool to remove any aggregates. Next, the solution was dialyzed against Milli-Q water with daily changes for at least one week. Afterward, the solution was lyophilized. Prior used, the solid microgels were redispersed in Milli-Q water to make a 10 mg/mL solution. The integration of Fe-Ftn$^{(neg)}$ into these microgels was conducted as described in section 6.6.6, but using 20 mM NMP buffer pH 5.0.

Synthesis of the locking shell: The locking shell was designed to consist of P(NIPAM-co-tBAM) (59% : 39% : 2% mol BAC). A series of mini-batch syntheses were conducted to optimize the mass ratio between microgel cores and the shell monomer. For the shell, a 25 mL stock solution with a total monomer concentration of 65 mM was prepared. The BAC was first dissolved in 3 mL of MeOH before added to the stock solution. CTAB and V50 were also added to the stock solution to give the final concentration of 0.115 mM and 2 mM, respectively. Next, 3 mL of the stock solution was added separately into seven vials. Then, different amounts of core microgel solution (16.89 mg/mL) were added to each sample to set the predetermined core to monomer ratios ((0 – 0.8) : 1). Milli-Q water was added to each sample to ensure the same volume across all samples. All samples were heated to 55 °C, stirred at 300 rpm, and degassed with N_2 for at least an hour. The reaction was started by irradiation with UV light (365 nm). After 3 hours, the vials were removed from the oil bath to cool down. The resulting microgel solution was purified by dialysis against Milli-Q water with daily changes for at least one week. The size of the resulting microgels was plotted against the mass ratio. The best ratio was chosen from the maximum point of the curve. The corresponding sample then were analyzed by TEM.

6.6.10 Immobilization of ferritin during microgel synthesis

Synthesis of Ce-Ftn$^{(neg)}$ microgels using KPS & TEMED redox initiator: The synthesis was performed by semi-batch precipitation polymerization. NIPAM, KPS, and TEMED stock solutions were prepared separately with a concentration of 66.5 mg/mL, 11.85 mg/mL, and 10 % (v/v), respectively. All the three stock solutions were degassed with N_2 for 30 min at RT. Next, 0.8 mL NIPAM, 1.197 mg Ce-Ftn$^{(neg)}$, 6.65 mg VIM, and 2.7 mg VOU crosslinker were dissolved in Milli-Q water to make a total volume of 8.6 mL. This solution was prepared inside a 25 mL round-bottom flask and degassed for 30 min by purging N_2 at 55 °C with gentle stirring at 300 rpm. 0.5 mL TEMED solution was added to the flask, and 10 minutes later the reaction was initiated by adding 0.2 mL KPS to the flask in a single shot. After 5 minutes, when the solution became cloudy, 0.7 mL NIPAM was injected dropwise to the flask by a syringe pump at a speed of 4 mL/h. After the injection was completed, the reaction was continued for another 15 min. The reaction was quenched in flowing cold water, gently vortexed (Heidolph), and stirred on a roller mixer (Stuart, STR 9D). Subsequently, the microgel was purified by 3 cycles of centrifugation (14000 g, RT, 15 min) and redispersion in Milli-Q water. The final solution was diluted to 5 mL. 0.5 mL of this solution was dried at 70 °C in the oven (BINDER) and then weighted to determine the concentration of the microgel solution. For the synthesis without VIM, all the steps are the same, except the VIM was replaced with water. One-pot synthesis was also performed in the same way, but all 1.5 mL NIPAM was put in the flask along with the other reactants at the beginning of the reaction.

Synthesis of Ce-Ftn$^{(neg)}$ microgels using KPS at 70 °C: The synthesis was performed similarly. 1.197 mg Fe-Ftn$^{(neg)}$, 6.65 mg VIM, and 2.7 mg VOU crosslinker were dissolved in Milli-Q water to make a total volume of 7.8 mL. This solution was prepared inside a 25 mL round-bottom flask and degassed for 30 min by purging N_2 at 70 °C with gentle stirring at 300 rpm. NIPAM and KPS stock solutions were prepared separately at a concentration of 66.5 mg/mL and 11.85 mg/mL, respectively. These two stock solutions were also degassed with N_2 for 30 min at RT. The reaction then was initiated by adding 0.2 mL KPS to the flask in a single shot. Subsequently, 2 mL NIPAM was injected dropwise to the flask by a syringe pump at a speed of 4 mL/h. After the injection was completed, the reaction was continued for another 15 min. The reaction was quenched in flowing cold water, gently vortexed, and stirred on a roller mixer. Subsequently, the microgel was purified by 3 cycles of centrifugation (14000 g, RT, 15 min) and redispersion in Milli-Q water. The final solution was diluted to 5 mL. 0.5 mL of this solution were dried at 70 °C in the oven and then weighted to determine the concentration of the microgel solution. For the microgel synthesis with a surfactant, 0.665 mg SDS was added to the flask along with the other reactants at the beginning of the reaction.

Microgel characterizations: The presence of Ce-Ftn$^{(neg)}$ inside microgel was observed by TEM without applying a staining agent. Ce-Ftn$^{(neg)}$ microgels were also characterized by electron tomography and

cryo-TEM as described in the analytical methods (section 6.5). The size, ζ-potential, electrophoretic mobility, and the size-temperature dependence of the microgels were measured at 20 °C by DLS.

6.6.11 Ferritin release from microgels

6.6.11.1 Study of ferritin release by TEM

To study the release, Ce-Ftn$^{(neg)}$ microgel was incubated in an acidic solution under different conditions. First, 250 µL Ce-Ftn$^{(neg)}$ microgel (5 mg/mL) was mixed with 50 µL of buffer F (300 mM acetate buffer pH 4.0). For the accelerated release, the buffer was replaced with buffer G (300 mM glycine buffer pH 2.5). Both were incubated for 5 min at RT. To check if the microgels can be completely degraded, another batch was incubated in pH 2.5 at RT for 5 days. After the incubation, 2 µL of each sample was analyzed by TEM.

6.6.11.2 Study of ferritin release by UV/Vis

Synthesis of fluorophore-loaded ferritin microgels: AF 488-(Ftn$^{(neg)}$-1C) and AR 6G-(Ftn$^{(neg)}$-1C) microgels were synthesized with KPS and TEMED redox initiator at 55 °C as described above. Moreover, for comparison, one batch of AF 488-(Ftn$^{(neg)}$-1C) microgel was prepared using KPS initiator at 70 °C.

Ferritin release from microgels in different solutions: 250 µL of AR 6G-(Ftn$^{(neg)}$-1C) microgels was mixed with 70 µL incubating solutions. After 5 min, the microgel solutions were centrifuged at 14000 g for 15 min. The supernatant was carefully pipetted out and analyzed by UV/Vis at 536 nm. The incubating solutions were: (1) water, (2) 150 mM NaCl, (3) 50 mM glycine buffer pH 2.5, and (4) a solution containing both 50 mM glycine buffer pH 2.5 and 150 mM NaCl. All are the final concentrations in 320 µL solution. For the last incubating solution, NaCl was added after 5 min incubation with acid, and then the incubation was continued for another 5 min.

Time-dependent release of ferritin in acidic solution: 250 µL of AF 488-(Ftn$^{(neg)}$-1C) microgels was mixed with 70 µL glycine buffer pH 2.5 to make a final buffer concentration of 50 mM. The incubation was performed for 5, 10, 20, 30 min, 20 h, and 6 days. After the incubation, the microgel solutions were centrifuged at 14000 g for 15 min. The supernatant was carefully pipetted out and analyzed by UV/Vis at 500 nm. For the release at pH 4.0, acetate buffer with a final concentration of 50 mM was used and the incubation was performed for 1, 2, and 4 h.

Estimation of ferritin uptake and release from microgels: To estimate ferritin uptake, we assumed that all the unbound ferritin was removed during the first centrifugation. The microgels formed pellet, while ferritin remained in solution. This supernatant was concentrated, and the amount of ferritin was determined by UV/Vis. By subtracting the initial amount of ferritin and the remaining ferritin in the supernatant, we obtained the ferritin uptake. The value was expressed in % relative to the initial

amount of ferritin. If the amount of ferritin uptake is divided by the total mass of the resulting microgels, we obtained % ferritin content. Ferritin release was estimated at pH 2.5 after 5 min incubation in acid. For AF 488-(Ftn$^{(neg)}$-1C), we also estimated the ferritin release at pH 4.0 in a similar fashion. The value was expressed in % relative to the amount of the incorporated ferritin.

6.6.11.3 Study of ferritin release by fluorescence microscopy

50 µL of AF 488-(Ftn$^{(neg)}$-1C) microgels solution with a concentration of 0.1 mg/mL was spin-coated on a plasma cleaned coverslip. First, the microgels were imaged in brightfield. Next, the fluorescence signals were captured by a fluorescence microscope. To trigger the release of ferritin, 100 µL of 50 mM acetic buffer pH 4.0 was added to the sample. Subsequently, the fluorescence images were taken after 10- and 15-min incubation in the buffer solution.

6.6.12 Proteolytic degradation of ferritin microgels

AR 6G-(Ftn$^{(neg)}$-1C) digestion by chymotrypsin. A stock solution of 2 mg/mL chymotrypsin was prepared by dissolving chymotrypsin in a solution containing 1 mM HCl and 2 mM $CaCl_2$. Next, a stock solution of 100 mM Tris buffer pH 7.8 containing 10 mM $CaCl_2$ was prepared as digestion buffer. For the digestion, 0.1863 mg AR 6G-(Ftn$^{(neg)}$-1C) was mixed with chymotrypsin and digestion buffer to make a 1 mL solution. The protein to protease mass ratio was 2 : 1. The solution was incubated at 37 °C for 0, 24, and 48 h. After incubation, the solution was diluted with water to 2 mL, centrifuged at 14000 g for 15 min to remove any precipitation, and finally analyzed by SEC using buffer E. The amount of remaining ferritin was determined from the FPLC chromatograms by integrating the area under the curve of ferritin peaks.

AR 6G-(Ftn$^{(neg)}$-1C) microgels digestion by chymotrypsin. 1 mL microgels solution containing the same amount of 0.1863 mg AR 6G-(Ftn$^{(neg)}$-1C) was centrifuged at 14000 g for 15 min. The supernatant (water) was removed and replace with digestion buffer containing chymotrypsin to make a 1 mL solution. The protein to protease mass ratio was 2 : 1 and the solution was also incubated at 37 °C. After 0, 24, and 48 h incubation, 150 µL microgel solution was pipetted out. The solution was centrifuged at 14000 g for 15 min. The digestion buffer was removed and the microgels were re-dispersed in a washing buffer (50 mM Tris pH 7.5; 50 mM NaCl; 0.05% Tween-20) to remove any precipitated digestion product. The solution was centrifuged once again at 14000 g for 15 min and the washing buffer was removed. Finally, the microgels were re-dispersed in 250 µL water and ferritin release at pH 2.5 was investigated as described above.

6.6.13 Encapsulation of DOX in ferritin

6.6.13.1 Encapsulation of DOX in Ftn$^{(pos)}$

Determination of the best conditions to enlarge Ftn$^{(pos)}$ channels: 1.5 mg Ftn$^{(pos)}$ was dissolved in 1.5 mL incubation buffer and stirred for 30 minutes. Next, a Fe(II)-DOX stock solution was prepared by mixing 1 mM of $(NH_4)_2Fe(II)(SO_4)_2$ and 1 mM DOX-HCl (1 : 1). The Fe(II)-DOX stock solution then was added to the protein solution with a concentration ratio of (200 : 1), along with additional incubation buffer to make a total volume of 4.5 mL. The incubation was continued for another 2.5 h. The solution was cooled down to RT (when necessary), washed 5x with Milli-Q water, concentrated to 2 mL, and purified by SEC with buffer C as elution buffer. Various conditions were tested for the encapsulation: 2 mM Gua-HCl, pH 5.0 (20 mM acetate buffer pH 5.0; 40 mM NaCl), T = 65 °C, and the combinations of these conditions.

Changing the metal-cation used in the pre-complexation of DOX: Cu(II)-DOX and Fe(III)-DOX stock solutions were prepared by mixing 1 mM DOX-HCl with 1 mM $CuSO_4$ and 1 mM $FeCl_3$, respectively. The encapsulations were performed in pH 5.0 at 65 °C (for 2.5 h; 200 : 1) in a similar fashion as described above.

Changing Cu(II) to DOX ratio used in the pre-complexation: Subsequently, the ratio of Cu(II) to DOX-HCl was varied from (1 : 1) to (4 : 1), while all the other encapsulation conditions were kept the same (pH 5.0, at 65 °C, for 2.5 h; 200 : 1).

Changing Cu(II)-DOX concentration used for the encapsulation: Next, the ratio of Cu(II)-DOX to protein concentration was varied from (200 : 1) to (600 : 1), while all the other encapsulation conditions were kept the same (pH 5.0, at 65 °C, for 2.5 h; 1 : 1).

Changing the salt concentration: Here, the concentration of NaCl in the incubation buffer was varied: 40 mM, 250 mM, 500 mM, and 1 M, while all the other encapsulation conditions were kept the same (pH 5.0, at 65 °C, for 2.5 h; 1 : 1; 200 : 1).

Changing the incubation time: Finally, the incubation time was varied: 1 h, 2.5 h, 5 h, and 24 h, while all the other encapsulation conditions were kept the same (pH 5.0, at 65 °C, 2.5 h; 1 : 1; 200 : 1; 40 mM NaCl).

DOX-Ftn$^{(pos)}$ characterizations: The best result from the encapsulation of DOX in Ftn$^{(pos)}$ was characterized by TEM with staining and the DOX loading was determined as described in section 6.6.2.3, but at 490 nm.

6.6.13.2 Encapsulation of DOX in Ftn$^{(neg)}$-1C

This follows closely the protocol for the encapsulation of fluorophore by chemical conjugation. 1.5 mg Ftn$^{(neg)}$-1C was incubated in 1.5 mL disassembly buffer (10 mM glycine buffer pH 2.5) for 4 h to ensure complete disassembly. In the meantime, aldoxorubicin stock solution was prepared in anhydrous DMSO at 10 mg/mL. After 4 h, the reassembly buffer (50 mM Tris buffer pH 7.5; 50 mM NaCl) was added to ferritin solution, and the final pH was adjusted to 7.4 by adding a few µL of NaOH or HCl 1 M. Next, the exposed cysteines were reacted with 1, 2, 5, or 10 eq. of aldoxorubicin. The total volume of the solution was 4.5 mL. The solution was incubated at RT overnight. The next day, the solution was washed 1x with Milli-Q water, concentrated to 2 mL, and purified by SEC with buffer E as elution buffer. As reaction controls, Ftn$^{(neg)}$-1C was reacted with DOX-HCl, and Ftn$^{(neg)}$-0C was reacted with aldoxorubicin or DOX-HCl. All the reactions used 10 eq. concentration of DOX variants relative to the cysteine.

DOX-(Ftn$^{(neg)}$-1C) characterizations: The size of DOX-(Ftn$^{(neg)}$-1C) 10 eq. was measured by DLS. The sample was also characterized by TEM with staining. Both the loading and yield were determined as described in section 6.6.2.3, but at the DOX maximum absorption: 490 nm.

6.6.13.3 Encapsulation of DOX in HF

The protocol used here was based on the work reported by Bellini et al.[22] Several modifications were made to obtain a better encapsulation yield. 1.5 mg Ftn$^{(neg)}$-1C was incubated in 1.5 mL disassembly buffer (10 mM glycine buffer pH 2.5) for 4 h to ensure complete disassembly. In the meantime, a DOX-HCl stock solution was prepared at 10 mg/mL. Next, the appropriate amount of DOX-HCl and NaCl was mixed with the reassembly buffer (50 mM Tris buffer pH 7.5; 0.5 M NaCl) to make a total volume of 13.5 mL. After 4h, this solution was added dropwise to the ferritin solution, and the final pH was adjusted to 7.4 by adding a few µL of NaOH or HCl 1 M. Next, the reaction mixture was incubated at RT overnight. The next day, the solution was washed 1x with Milli-Q water, concentrated to 2 mL, and purified by SEC with buffer E as elution buffer.

DOX-HF characterization: The purified DOX-HF was characterized by TEM with staining. Both the loading and yield were determined as described in section 6.6.2.3, but at the DOX maximum absorption: 490 nm.

6.6.13.4 Encapsulation of DOX in HF-7C and HF-1C

The encapsulation of DOX in HF-7C: 1.5 mg HF-7C was incubated in 1.5 mL disassembly buffer (10 mM glycine buffer pH 2.5) for 4 h to ensure complete disassembly. In the meantime, aldoxorubicin stock solution was prepared in anhydrous DMSO at 10 mg/mL. Furthermore, TCEP stock solution was prepared at 10 mg/mL. After 4 h, 10 eq. TCEP was added to the protein solution and let react for 30

min. Subsequently, the reassembly buffer (50 mM Tris buffer pH 7.5; 50 mM NaCl) was added to the solution, and the final pH was adjusted to 7.4 by adding a few µL of NaOH or HCl 1 M. 5 minutes later, the exposed cysteines were reacted with 0.75 eq. aldoxorubicin. The total volume of the solution was 4.5 mL. The solution was incubated at RT overnight. The next day, the solution was washed 1x with Milli-Q water, concentrated to 2 mL, and purified by SEC with buffer E as elution buffer.

The encapsulation of DOX in HF-1C: 1.5 mg HF-1C was incubated in 1.5 mL disassembly buffer (10 mM glycine buffer pH 2.5) for 4 h to ensure complete disassembly. In the meantime, aldoxorubicin stock solution was prepared in anhydrous DMSO at 10 mg/mL. Furthermore, an L-arginine stock solution was prepared at 200 mM. After 4 h, 450 µL L-arginine stock solution and the reassembly buffer (50 mM Tris buffer pH 7.5) was added to the solution. The final pH was adjusted to 7.4 by adding a few µL of NaOH or HCl 1 M. The exposed cysteines then were reacted with 7eq. aldoxorubicin. The total volume of the solution was 4.5 mL. The solution was incubated at RT overnight. The next day, the solution was washed 1x with Milli-Q water, concentrated to 2 mL, and purified by SEC with buffer E as elution buffer.

Characterizations: Both DOX (HF-7C) and DOX (HF-1C) were characterized by TEM with staining. Furthermore, the loading and yield were determined as described in section 6.6.2.3, but at 490 nm.

6.6.14 Synthesis of DOX-Ftn microgels and its release study

Synthesis of DOX ($Ftn^{(neg)}$-1C) 5 eq. microgels: The synthesis was performed by semi-batch precipitation polymerization as described in section 6.6.10. The only difference is, here we used DOX ($Ftn^{(neg)}$-1C) 5 eq. instead of Ce-$Ftn^{(neg)}$. The ferritin loading and release was also estimated as described in section 6.6.11.2. The resulting microgels were also imaged by regular TEM without staining.

Synthesis of DOX (HF-1C) 7 eq. microgels and Ce(HF-1C) microgels: The synthesis was also performed by semi-batch precipitation polymerization as described in section 6.6.10. However, here we used DOX (HF-1C) 7 eq. or Ce(HF-1C) instead of Ce-$Ftn^{(neg)}$, and we employed half amount of the applied KPS-TEMED redox initiator in the reaction. The resulting microgels then were analyzed by TEM without staining.

6.6.15 Cytotoxicity of DOX-Ftn variants

Selection of the appropriate cell lines: The TfR-1 expression of various cell lines was determined by quantitative real-time PCR. The experiment was performed by Sarah Boesveld (Medizinische Klinik III, Uniklinik RWTH Aachen).

A general protocol for MTT assays: Hepa 1-6, 3T3, and HeLa cells were plated in 100 µL culture medium in a 96-wells microplate at a density of 3.5 x 10^5 cells/wells and allowed to grow overnight. The next day, DOX or DOX-Ftn variants were dissolved in fresh cell culture supernatant and added to the cells.

All concentrations were prepared as triplicates and water was used as control. The cells then were cultured in a CO_2 incubator at 37 °C for 24 h and 48 h. Next, the cell viability was measured by MTT Assay kit (Cayman) according to the manufacturer's instructions. 10 µL of MTT reagent was added to each well using a repeating pipettor. Afterward, the cell cultures were mixed gently for one minute on an orbital shaker and then incubated for 4 h at 37 °C in a CO_2 incubator. The formazan produced in the cells will appear as dark crystals at the bottom of the wells. 100 µL of crystal dissolving solution then was added to each well and incubated for 18 h in a 37 °C CO_2 incubator. Finally, the absorbances were measured at 570 nm using a microplate reader.

Determination of the suitable DOX concentration for MTT assays: Various DOX concentrations were tested: 0.032, 0.16, 0.8, 4, 20, and 100 µg/mL. The minimum concentration of DOX which induced a significant decrease in cell viability during 24 h and 48 h incubation was chosen as the DOX concentration for further experiments.

MTT assays for various DOX-Ftn variants: The cytotoxicity of DOX-Ftn variants were tested at DOX concentration of 0.8 µg/mL (1.38 µM) and 0.058 µg/mL (0.1 µM).

Reaction control for investigating the DOX attachment on the surface of ferritin cages: The encapsulation of DOX in HF-7C (Chapter 6.6.13.4) was repeated, but without opening the cages. This means, the glycine buffer pH 2.5 was simply replaced by the reassembly buffer (50 mM Tris buffer pH 7.5; 50 mM NaCl). The experiment was repeated once again, but this time TCEP was left out. After encapsulation, the reaction mixtures were purified by SEC and the resulting chromatograms were compared.

7 Appendix

Protein variants and characteristics

Ftn$^{(pos)}$

Molar mass: 21331 kDa; **Extinction coefficient:** 18910;

Mutation: A18K, C90K, N98R, C102K, H105K, N25R, N109K, D123K, E162R

DNA sequence:

ACCACAGCTAGTACGTCCCAAGTACGTCAGAACTATCACCAAGATAGCGAGAAAGCCATTAATCGCCAAATTC
GCTTGGAACTGTATGCATCGTATGTCTACCTGTCAATGAGCTACTACTTTGATCGTGATGATGTTGCTCTGAAG
AACTTTGCGAAATACTTTCTGCATCAGTCTCATGAAGAACGCGAACATGCCGAGAAACTGATGAAACTGCAGA
ATCAGCGTGGTGGACGCATCTTCTTACAGGACATTCAGAAACCGGATAAAGACGATTGGGAAAGCGGGTTGC
GTGCGATGGAGAAAGCACTGAAACTGGAAAAGAAAGTGAATCAGTCTCTGCTGGAACTCCACAAATTAGCGA
CGAAGAAGAACGATCCGCATCTCTGCGACTTCATCGAAACCCACTATTTAAACGAGCAAGTGAAAGCGATCAA
AGAACTTGGCGATCACGTTACCAACCTTCGGAAAATGGGTGCACCACGCAGTGGCTTGGCCGAATATCTGTTC
GACAAACATACTCTGGGCGATTCCGACAATGAGTCG

Protein sequence:

TTASTSQVRQNYHQDSEEAINRQINLELYASYVYLSMSYYFDRDDVALKNFAKYFLHQSHEEREHAEKLMKLQNQR
GGRIFLQDIQKPDEDDWESGLNAMEEALELEKNVNQSLLELHKLATDKNDPHLCDFIETHYLNEQVKAIKELGDHVT
NLRKMGAPESGLAEYLFDKHTLGDSDNES

Ftn$^{(neg)}$

Molar mass: 21196.3 kDa; **Extinction coefficient:** 18910; **Mutation:** A18E, C90E, C102E, H105E

DNA sequence:

ACCACAGCATCAACGAGCCAAGTTCGCCAAAACTATCACCAGGATTCTGAGGAAGCGATTAATCGGCAGATTA
ACCTGGAGTTATATGCGAGCTATGTGTATCTGTCGATGAGCTACTACTTTGACCGTGACGATGTTGCACTGAAG
AACTTTGCGAAATACTTTCTGCATCAGTCCCATGAAGAACGCGAACATGCCGAGAAACTGATGAAACTGCAGA
ATCAACGTGGTGGACGCATTTTCTTGCAAGATATCCAGAAACCGGATGAAGATGACTGGGAAAGTGGCTTGA
ATGCCATGGAAGAAGCACTGGAACTTGAGAAGAACGTGAATCAGTCTCTGCTTGAACTGCATAAACTGGCCAC
TGACAAGAACGATCCGCATCTGTGCGATTTCATCGAAACCCACTATCTGAACGAACAGGTCAAAGCGATCAAA
GAACTCGGGGATCACGTAACCAACCTCCGTAAAATGGGTGCTCCAGAGAGTGGCTTGGCTGAATACTTATTCG
ACAAACACACGTTAGGCGATTCGGACAATGAGTCC

Protein sequence:

TTASTSQVRQNYHQDSEEAINRQINLELYASYVYLSMSYYFDRDDVALKNFAKYFLHQSHEEREHAEKLMKLQNQR
GGRIFLQDIQKPDEDDWESGLNAMEEALELEKNVNQSLLELHKLATDKNDPHLCDFIETHYLNEQVKAIKELGDHVT
NLRKMGAPESGLAEYLFDKHTLGDSDNES

Ftn$^{(neg)}$-0C

Molar mass: 21164.31 kDa; **Extinction coefficient:** 18910;

Mutation: A18E, C90E, C102E, H105E, C130A

DNA sequence:

ACCACAGCATCAACGAGCCAAGTTCGCCAAAACTATCACCAGGATTCTGAGGAAGCGATTAATCGGCAGATTA
ACCTGGAGTTATATGCGAGCTATGTGTATCTGTCGATGAGCTACTACTTTGACCGTGACGATGTTGCACTGAAG
AACTTTGCGAAATACTTTCTGCATCAGTCCCATGAAGAACGCGAACATGCCGAGAAACTGATGAAACTGCAGA
ATCAACGTGGTGGACGCATTTTCTTGCAAGATATCCAGAAACCGGATGAAGATGACTGGGAAAGTGGCTTGA
ATGCCATGGAAGAAGCACTGGAACTTGAGAAGAACGTGAATCAGTCTCTGCTTGAACTGCATAAACTGGCCAC
TGACAAGAACGATCCGCATCTGGCCGATTTCATCGAAACCCACTATCTGAACGAACAGGTCAAAGCGATCAAA
GAACTCGGGGATCACGTAACCAACCTCCGTAAAATGGGTGCTCCAGAGAGTGGCTTGGCTGAATACTTATTCG
ACAAACACACGTTAGGCGATTCGGACAATGAGTCC

Protein sequence:

TTASTSQVRQNYHQDSEEAINRQINLELYASYVYLSMSYYFDRDDVALKNFAKYFLHQSHEEREHAEKLMKLQNQR
GGRIFLQDIQKPDEDDWESGLNAMEEALELEKNVNQSLLELHKLATDKNDPHLADFIETHYLNEQVKAIKELGDHVT
NLRKMGAPESGLAEYLFDKHTLGDSDNES

Ftn$^{(neg)}$-1C

Molar mass: 21139.27 kDa; **Extinction coefficient:** 18910;

Mutation: A18E, C90E, C102E, H105E, C130A, K53C

DNA sequence:

ACCACAGCATCAACGAGCCAAGTTCGCCAAAACTATCACCAGGATTCTGAGGAAGCGATTAATCGGCAGATTA
ACCTGGAGTTATATGCGAGCTATGTGTATCTGTCGATGAGCTACTACTTTGACCGTGACGATGTTGCACTGAAG
AACTTTGCGTGTTACTTTCTGCATCAGTCCCATGAAGAACGCGAACATGCCGAGAAACTGATGAAACTGCAGA
ATCAACGTGGTGGACGCATTTTCTTGCAAGATATCCAGAAACCGGATGAAGATGACTGGGAAAGTGGCTTGA
ATGCCATGGAAGAAGCACTGGAACTTGAGAAGAACGTGAATCAGTCTCTGCTTGAACTGCATAAACTGGCCAC
TGACAAGAACGATCCGCATCTGGCCGATTTCATCGAAACCCACTATCTGAACGAACAGGTCAAAGCGATCAAA

GAACTCGGGGATCACGTAACCAACCTCCGTAAAATGGGTGCTCCAGAGAGTGGCTTGGCTGAATACTTATTCG
ACAAACACACGTTAGGCGATTCGGACAATGAGTCC

Protein sequence:

TTASTSQVRQNYHQDSEEAINRQINLELYASYVYLSMSYYFDRDDVALKNFACYFLHQSHEEREHAEKLMKLQNQR
GGRIFLQDIQKPDEDDWESGLNAMEEALELEKNVNQSLLELHKLATDKNDPHLADFIETHYLNEQVKAIKELGDHVT
NLRKMGAPESGLAEYLFDKHTLGDSDNES

HF

Molar mass: 21094.45 kDa; **Extinction coefficient:** 18910; **Mutation:** -

DNA sequence:

ACCACCGCGTCCACTAGCCAGGTCCGTCAAAACTACCACCAGGATTCGGAAGCCGCAATCAATCGTCAGATCA
ATCTGGAGCTGTACGCGAGCTATGTCTACCTGTCAATGTCGTATTATTTTGACCGGGACGACGTAGCATTGAAA
AACTTTGCTAAATACTTCTTGCACCAGAGCCACGAAGAACGCGAACATGCAGAGAAACTGATGAAACTGCAGA
ACCAACGCGGCGGCCGTATCTTCCTGCAAGATATTAAGAAGCCCGATTGCGATGATTGGGAATCTGGCTTAAA
TGCTATGGAATGCGCACTGCATCTTGAGAAGAACGTCAACCAGAGTTTGTTAGAGCTGCATAAACTGGCGACC
GACAAAAACGACCCGCATCTGTGTGATTTTATCGAAACGCATTATCTCAATGAGCAAGTTAAAGCTATCAAGGA
ACTGGGTGATCATGTCACCAACCTCCGGAAAATGGGCGCTCCGGAAAGCGGCCTGGCAGAGTACCTCTTCGAT
AAACACACTTTGGGTGATTCAGATAATGAATCG

Protein sequence:

TTASTSQVRQNYHQDSEAAINRQINLELYASYVYLSMSYYFDRDDVALKNFAKYFLHQSHEEREHAEKLMKLQNQR
GGRIFLQDIKKPDCDDWESGLNAMECALHLEKNVNQSLLELHKLATDKNDPHLCDFIETHYLNEQVKAIKELGDHVT
NLRKMGAPESGLAEYLFDKHTLGDSDNES

HF-7C

Molar mass: 20959.48 kDa; **Extinction coefficient:** 18910;

Mutation: A52C, E64C, C90A, C102A, C130A, E140C, K143C, E147C, S178C, S182C

DNA sequence:

ACCACTGCTTCGACCAGTCAGGTTCGCCAGAACTATCACCAGGATTCTGAAGCTGCGATTAATCGGCAGATCA
ACCTGGAGTTATATGCGAGCTATGTGTACTTATCGATGTCCTACTACTTCGATCGTGACGATGTAGCCTTGAAG
AACTTCTGCAAATACTTCCTGCATCAATCCCACGAAGAACGCTGTCATGCAGAGAAACTCATGAAACTCCAGAA
TCAGCGTGGTGGTCGCATCTTTCTGCAAGACATCAAGAAGCCGGATGCAGATGACTGGGAAAGCGGCCTTAA
CGCAATGGAAGCAGCACTGCATCTGGAGAAGAACGTCAACCAGTCACTGCTGGAACTGCACAAATTGGCTACT
GACAAGAACGATCCCCATCTTGCGGACTTCATCGAAACGCATTACCTGAATTGCCAGGTTTGTGCCATTAAGTG

TCTTGGCGATCACGTGACCAATCTCCGCAAAATGGGAGCACCAGAGTCAGGGTTAGCAGAGTATCTGTTCGAC
AAACACACATTGGGCGATTGCGATAACGAATGT

Protein sequence:

TTASTSQVRQNYHQDSEAAINRQINLELYASYVYLSMSYYFDRDDVALKNFCKYFLHQSHEERCHAEKLMKLQNQR
GGRIFLQDIKKPDADDWESGLNAMEAALHLEKNVNQSLLELHKLATDKNDPHLADFIETHYLNCQVCAIKCLGDHV
TNLRKMGAPESGLAEYLFDKHTLGDCDNEC

HF-1C

Molar mass: 20973.23 kDa; **Extinction coefficient:** 18910;

Mutation: K53C, C90A, C102A, C130A

DNA sequence:

ACAACCGCATCTACGTCACAAGTTCGTCAGAACTATCACCAAGATAGTGAAGCTGCCATTAATCGCCAGATTAA
CCTGGAACTGTATGCCTCCTATGTGTATCTGAGCATGAGCTACTACTTTGATCGCGATGACGTTGCGCTCAAGA
ACTTTGCCTGCTACTTCTTGCATCAGAGCCATGAAGAACGTGAACACGCGGAAAAACTCATGAAACTGCAGAA
TCAACGTGGAGGTCGGATTTTTCTGCAGGACATCAAGAAACCGGATGCGGATGATTGGGAATCTGGGCTTAAC
GCGATGGAAGCAGCTCTGCATCTGGAGAAAAACGTGAATCAGTCGTTACTGGAGTTACACAAACTTGCGACTG
ACAAGAACGATCCGCATTTGGCGGACTTCATCGAAACCCATTACCTGAATGAACAGGTAAAAGCCATCAAAGA
GCTGGGCGATCATGTCACCAATCTGCGCAAAATGGGTGCTCCAGAATCGGGCTTGGCAGAGTATCTGTTCGAC
AAACACACGTTAGGCGATAGTGACAACGAGTCC

Protein sequence:

TTASTSQVRQNYHQDSEAAINRQINLELYASYVYLSMSYYFDRDDVALKNFACYFLHQSHEEREHAEKLMKLQNQR
GGRIFLQDIKKPDADDWESGLNAMEAALHLEKNVNQSLLELHKLATDKNDPHLADFIETHYLNEQVKAIKELGDHV
TNLRKMGAPESGLAEYLFDKHTLGDSDNES

Note: All the extinction coefficients are in units of M^{-1} cm^{-1}, at 280 nm and measured in water.

8 List of figures

9 List of tables

10 Abbreviations

AA	Acrylic acid
AF 488	Alexa Fluor 488
AF 647	Alexa Fluor 647
AMPA	2,2'-Azobis(2-methylpropionamidine) dihydrochloride
AR 6G	Atto Rhodamine 6G
BAC	N,N'-Bis(acryloyl)cystamine
BIS	N,N'-Methylenebis(acrylamides)
Ce-Ftn$^{(neg)}$	Cerium oxide nanoparticle loaded Ferritin$^{(neg)}$
Ce(HF-1C)	Cerium oxide nanoparticle loaded HF-1C
CCMV	Cowpea Chlorotic Mottle Virus
CPMV	Cowpea Mosaic Virus
CTAB	hexadecyltrimethylammonium bromide
DAAM	Diacetone acrylamide
DDS	Drug delivery systems
DLS	Dynamic Light Scattering
DOX	Doxorubicin
DMAPMA	N-[3-(dimethylamino) propyl] methacrylamides)
DMSO	Dimethylsulfoxide
EGCC	Epigallocatechin gallate
EPR	Enhanced permeability and retention
Fscn	Fluorescein
Ftn$^{(neg)}$	Ferritin$^{(neg)}$
Ftn$^{(pos)}$	Ferritin$^{(pos)}$
GFP	Green fluorescent protein
GSH	Glutathione

Gua-HCl Guanidine hydrochloride

HA Hyaluronic Acid

HAADF-STEM High-angle annular dark-field scanning transmission electron microscopy

HF Human heavy-chain ferritin

IA Itaconic Acid

IADME Dimethyl itaconate

IEC Ion Exchange Chromatography

IPTG isopropyl β-D-1-thiogalactopyranoside

KPS Potassium persulfate

MAA Methacrylic acid

Milli-Q water Ultrapure water with electrical conductivity of 0.055 µS/mL

MRI Magnetic resonance imaging

MSN Mesoporous silica nanoparticle

MWCO Molecular Weight Cut-Off

MRB Methacryloxyethylthiocarbamoyl-Rhodamine B

NHS N-Hydroxysuccinimide

NIPAM N-isopropylacrylamide

NIPMAM N-isopropylmethacrylamide

NMP 1-Methylpiperazine

NPs Nanoparticles

PCR Polymerase chain reaction

PDT Photodynamic therapy

PEG Polyethyleneglycol

pI Isoelectric point

PIT Photoimmuno therapy

PTT Photothermal therapy

QDs Quantum Dots

RAFT	Reversible addition-fragmentation chain-transfer
Rho B	Rhodamine B
Rho 6G	Rhodamine 6G
SDS	Sodium dodecyl sulfate
SEC	Size exclusion chromatography
siRNA	small interfering RNA
tBAM	N-tert-Butylacrylamide
TCEP-HCl	(tris(2-carboxyethyl)phosphine) hydrochloride
TEM	Transmission electron microscopy
TEMED	Tetramethylethylendiamine
TfR-1	Transferrin receptor 1
Tris	tris(hydroxymethyl)aminomethane
VCL	N-vinylcaprolactam
VEGF	Vascular endothelial growth factor
VFc	Vinyl Ferrocene
VIM	1-vinylimidazole
VOU	3,9-Divinyl-2,4,8,10-tetra-oxaspiro[5.5]undecane
VPTT	Volume phase transition temperature
5-FU	5-Fluorouracil

11 Bibliography

[1] D. Lombardo, M. A. Kiselev, M. T. Caccamo, Smart nanoparticles for drug delivery application: Development of versatile nanocarrier platforms in biotechnology and nanomedicine, *J. Nanomater.* **2019**, *2019*, 1–26, DOI: 10.1155/2019/3702518.

[2] M. R. Mohammadi, A. Nojoomi, M. Mozafari, A. Dubnika, M. Inayathullah, J. Rajadas, Nanomaterials engineering for drug delivery: A hybridization approach, *J. Mater. Chem. B* **2017**, *5*, 3995–4018, DOI: 10.1039/C6TB03247H.

[3] W. H. De Jong, P. J. A. Borm, Drug delivery and nanoparticles: Applications and hazards, *Int. J. Nanomedicine* **2008**, *3*, 133–149, DOI: 10.2147/IJN.S596.

[4] S. A. A. Rizvi, A. M. Saleh, Applications of nanoparticle systems in drug delivery technology, *Saudi Pharm. J.* **2018**, *26*, 64–70, DOI: 10.1016/j.jsps.2017.10.012.

[5] H. Cabral, K. Kataoka, Progress of drug-loaded polymeric micelles into clinical studies, *J. Control. Release* **2014**, *190*, 465–476, DOI: 10.1016/j.jconrel.2014.06.042.

[6] T. M. Allen, P. R. Cullis, Liposomal drug delivery systems: From concept to clinical applications, *Adv. Drug Deliv. Rev.* **2013**, *65*, 36–48, DOI: 10.1016/j.addr.2012.09.037.

[7] D. Pandita, N. Poonia, S. Kumar, V. Lather, K. Madaan, Dendrimers in drug delivery and targeting: Drug-dendrimer interactions and toxicity issues, *J. Pharm. Bioallied Sci.* **2014**, *6*, 139–150, DOI: 10.4103/0975-7406.130965.

[8] V. Patel, C. Rajani, D. Paul, P. Borisa, K. Rajpoot, S. R. Youngren-Ortiz, R. K. Tekade, Dendrimers as novel drug-delivery system and its applications, in *Drug Deliv. Syst.*, Elsevier, **2020**, pp. 333–392, DOI: 10.1016/B978-0-12-814487-9.00008-9.

[9] C. E. Probst, P. Zrazhevskiy, V. Bagalkot, X. Gao, Quantum dots as a platform for nanoparticle drug delivery vehicle design, *Adv. Drug Deliv. Rev.* **2013**, *65*, 703–718, DOI: 10.1016/j.addr.2012.09.036.

[10] M. Z. Ahmad, S. Akhter, G. K. Jain, M. Rahman, S. A. Pathan, F. J. Ahmad, R. K. Khar, Metallic nanoparticles: Technology overview & drug delivery applications in oncology, *Expert Opin. Drug Deliv.* **2010**, *7*, 927–942, DOI: 10.1517/17425247.2010.498473.

[11] W. Lohcharoenkal, L. Wang, Y. C. Chen, Y. Rojanasakul, Protein nanoparticles as drug delivery carriers for cancer therapy, *Biomed Res. Int.* **2014**, *2014*, 1–12, DOI: 10.1155/2014/180549.

[12] A. MaHam, Z. Tang, H. Wu, J. Wang, Y. Lin, Protein-based nanomedicine platforms for drug delivery, *Small* **2009**, *5*, 1706–1721, DOI: 10.1002/smll.200801602.

[13] A. Macone, S. Masciarelli, F. Palombarini, D. Quaglio, A. Boffi, M. C. Trabuco, P. Baiocco, F. Fazi, A. Bonamore, Ferritin nanovehicle for targeted delivery of cytochrome C to cancer cells, *Sci. Rep.* **2019**, *9*, 1–7, DOI: 10.1038/s41598-019-48037-z.

[14] M. Truffi, L. Fiandra, L. Sorrentino, M. Monieri, F. Corsi, S. Mazzucchelli, Ferritin nanocages: A biological platform for drug delivery, imaging and theranostics in cancer, *Pharmacol. Res.* **2016**, *107*, 57–65, DOI: 10.1016/j.phrs.2016.03.002.

[15] M. Khoshnejad, H. Parhiz, V. V. Shuvaev, I. J. Dmochowski, V. R. Muzykantov, Ferritin-based drug delivery systems: Hybrid nanocarriers for vascular immunotargeting, *J. Control. Release* **2018**, *282*, 13–24, DOI: 10.1016/j.jconrel.2018.02.042.

[16] M. Kim, Y. Rho, K. S. Jin, B. Ahn, S. Jung, H. Kim, M. Ree, pH-dependent structures of ferritin and apoferritin in solution: Disassembly and reassembly, *Biomacromolecules* **2011**, *12*, 1629–1640, DOI: 10.1021/bm200026v.

[17] R. Li, Y. Ma, Y. Dong, Z. Zhao, C. You, S. Huang, X. Li, F. Wang, Y. Zhang, Novel paclitaxel-loaded nanoparticles based on human H chain ferritin for tumor-targeted delivery, *ACS Biomater. Sci. Eng.* **2019**, *5*, 6645–6654, DOI: 10.1021/acsbiomaterials.9b01533.

[18] D. M. Monti, G. Ferraro, A. Merlino, Ferritin-based anticancer metallodrug delivery: Crystallographic, analytical and cytotoxicity studies, *Nanomedicine Nanotechnol. Biol. Med.* **2019**, *20*, 101997, DOI: 10.1016/j.nano.2019.04.001.

[19] Y. Lei, Y. Hamada, J. Li, L. Cong, N. Wang, Y. Li, W. Zheng, X. Jiang, Targeted tumor delivery and controlled release of neuronal drugs with ferritin nanoparticles to regulate pancreatic cancer progression, *J. Control. Release* **2016**, *232*, 131–142, DOI: 10.1016/j.jconrel.2016.03.023.

[20] M. A. Kilic, E. Ozlu, S. Calis, A novel protein-based anticancer drug encapsulating nanosphere: Apoferritin-doxorubicin complex, *J. Biomed. Nanotechnol.* **2012**, *8*, 508–514, DOI: 10.1166/jbn.2012.1406.

[21] Z. Zhen, W. Tang, C. Guo, H. Chen, X. Lin, G. Liu, B. Fei, X. Chen, B. Xu, J. Xie, Ferritin nanocages to encapsulate and deliver photosensitizers for efficient photodynamic therapy against cancer, *ACS Nano* **2013**, *7*, 6988–6996, DOI: 10.1021/nn402199g.

[22] M. Bellini, S. Mazzucchelli, E. Galbiati, S. Sommaruga, L. Fiandra, M. Truffi, M. A. Rizzuto, M. Colombo, P. Tortora, F. Corsi, D. Prosperi, Protein nanocages for self-triggered nuclear delivery of DNA-targeted chemotherapeutics in cancer cells, *J. Control. Release* **2014**, *196*, 184–196, DOI: 10.1016/j.jconrel.2014.10.002.

[23] G. Liu, J. Wang, S. A. Lea, Y. Lin, Bioassay labels based on apoferritin nanovehicles, *ChemBioChem* **2006**, *7*, 1315–1319, DOI: 10.1002/cbic.200600225.

[24] M. Künzle, T. Eckert, T. Beck, Binary protein crystals for the assembly of inorganic nanoparticle superlattices, *J. Am. Chem. Soc.* **2016**, *138*, 12731–12734, DOI: 10.1021/jacs.6b07260.

[25] B. Ahn, S.-G. Lee, H. R. Yoon, J. M. Lee, H. J. Oh, H. M. Kim, Y. Jung, Four-fold channel-nicked human ferritin nanocages for active drug loading and pH-responsive drug release, *Angew. Chemie Int. Ed.* **2018**, *57*, 2909–2913, DOI: 10.1002/anie.201800516.

[26] X. Lin, J. Xie, G. Niu, F. Zhang, H. Gao, M. Yang, Q. Quan, M. A. Aronova, G. Zhang, S. Lee, R. Leapman, X. Chen, Chimeric ferritin nanocages for multiple function loading and multimodal imaging, *Nano Lett.* **2011**, *11*, 814–819, DOI: 10.1021/nl104141g.

[27] M. Liang, K. Fan, M. Zhou, D. Duan, J. Zheng, D. Yang, J. Feng, X. Yan, H-ferritin-nanocaged doxorubicin nanoparticles specifically target and kill tumors with a single-dose injection, *Proc. Natl. Acad. Sci.* **2014**, *111*, 14900–14905, DOI: 10.1073/pnas.1407808111.

[28] L. Li, C. J. Fang, J. C. Ryan, E. C. Niemi, J. A. Lebrón, P. J. Björkman, H. Arase, F. M. Torti, S. V. Torti, M. C. Nakamura, W. E. Seaman, Binding and uptake of H-ferritin are mediated by human transferrin receptor-1, *Proc. Natl. Acad. Sci. U. S. A.* **2010**, *107*, 3505–3510, DOI: 10.1073/pnas.0913192107.

[29] L. Vannucci, E. Falvo, M. Fornara, P. Di Micco, O. Benada, J. Krizan, J. Svoboda, K. Hulikova-Capkova, V. Morea, A. Boffi, P. Ceci, Selective targeting of melanoma by PEG-masked protein-based multifunctional nanoparticles, *Int. J. Nanomedicine* **2012**, *7*, 1489–1509, DOI: 10.2147/IJN.S28242.

[30] A. L. Liu, A. J. García, Methods for generating hydrogel particles for protein delivery, *Ann. Biomed. Eng.* **2016**, *44*, 1946–1958, DOI: 10.1007/s10439-016-1637-z.

[31] B. J. Bruno, G. D. Miller, C. S. Lim, Basics and recent advances in peptide and protein drug delivery, *Ther. Deliv.* **2013**, *4*, 1443–1467, DOI: 10.4155/tde.13.104.

[32] M. Worwood, J. D. Cook, Serum ferritin, *Crit. Rev. Clin. Lab. Sci.* **1979**, *10*, 171–204, DOI: 10.3109/10408367909147133.

[33] P. C. Adams, L. A. Chau, Hepatic ferritin uptake and hepatic iron, *Hepatology* **1990**, *11*, 805–808, DOI: 10.1002/hep.1840110514.

[34] E. Falvo, E. Tremante, A. Arcovito, M. Papi, N. Elad, A. Boffi, V. Morea, G. Conti, G. Toffoli, G. Fracasso, P. Giacomini, P. Ceci, Improved doxorubicin encapsulation and pharmacokinetics of ferritin–fusion protein nanocarriers bearing proline, serine, and alanine elements, *Biomacromolecules* **2016**, *17*, 514–522, DOI: 10.1021/acs.biomac.5b01446.

[35] C. Wang, C. Zhang, Z. Li, S. Yin, Q. Wang, F. Guo, Y. Zhang, R. Yu, Y. Liu, Z. Su, Extending half life of H-ferritin nanoparticle by fusing albumin binding domain for doxorubicin encapsulation, *Biomacromolecules* **2018**, *19*, 773–781, DOI: 10.1021/acs.biomac.7b01545.

[36] F. A. Plamper, W. Richtering, Functional microgels and microgel systems, *Acc. Chem. Res.* **2017**, *50*, 131–140, DOI: 10.1021/acs.accounts.6b00544.

[37] M. Karg, A. Pich, T. Hellweg, T. Hoare, L. A. Lyon, J. J. Crassous, D. Suzuki, R. A. Gumerov, S. Schneider, I. I. Potemkin, W. Richtering, Nanogels and microgels: From model colloids to applications, recent developments, and future trends, *Langmuir* **2019**, *35*, 6231–6255, DOI: 10.1021/acs.langmuir.8b04304.

[38] N. M. B. Smeets, T. Hoare, Designing responsive microgels for drug delivery applications, *J. Polym. Sci. Part A Polym. Chem.* **2013**, *51*, 3027–3043, DOI: 10.1002/pola.26707.

[39] M. S. Islam, J. P. K. Tan, C. Y. Kwok, K. C. Tam, Drug release kinetics of pH-responsive microgels of different glass-transition temperatures, *J. Appl. Polym. Sci.* **2019**, *136*, 1–11, DOI: 10.1002/app.47284.

[40] W. Xu, A. A. Rudov, R. Schroeder, I. V. Portnov, W. Richtering, I. I. Potemkin, A. Pich, Distribution of ionizable groups in polyampholyte microgels controls interactions with captured proteins: From blockade and “levitation” to accelerated release, *Biomacromolecules* **2019**, *20*, 1578–1591, DOI: 10.1021/acs.biomac.8b01775.

[41] M. Dirksen, C. Dargel, L. Meier, T. Brändel, T. Hellweg, Smart microgels as drug delivery vehicles for the natural drug aescin: uptake, release and interactions, *Colloid Polym. Sci.* **2020**, *298*, 505–518, DOI: 10.1007/s00396-020-04632-5.

[42] C. M. Nolan, M. J. Serpe, L. A. Lyon, Thermally modulated insulin release from microgel thin films, *Biomacromolecules* **2004**, *5*, 1940–1946, DOI: 10.1021/bm049750h.

[43] C. C. L. Schuurmans, A. Abbadessa, M. A. Bengtson, G. Pletikapic, H. B. Eral, G. Koenderink, R. Masereeuw, W. E. Hennink, T. Vermonden, Complex coacervation-based loading and tunable release of a cationic protein from monodisperse glycosaminoglycan microgels, *Soft Matter* **2018**, *14*, 6327–6341, DOI: 10.1039/c8sm00686e.

[44] S. Walta, D. V. Pergushov, A. Oppermann, A. A. Steinschulte, K. Geisel, L. V. Sigolaeva, F. A. Plamper, D. Wöll, W. Richtering, Microgels enable capacious uptake and controlled release of architecturally complex macromolecular species, *Polym. (United Kingdom)* **2017**, *119*, 50–58, DOI: 10.1016/j.polymer.2017.05.008.

[45] Z. Gu, T. T. Dang, M. Ma, B. C. Tang, H. Cheng, S. Jiang, Y. Dong, Y. Zhang, D. G. Anderson, Glucose-responsive microgels integrated with enzyme nanocapsules for closed-loop insulin delivery, *ACS Nano* **2013**, *7*, 6758–6766, DOI: 10.1021/nn401617u.

[46] K. Kataoka, H. Miyazaki, M. Bunya, T. Okano, Y. Sakurai, Totally synthetic polymer gels responding to external glucose concentration: Their preparation and application to on−off regulation of insulin release, *J. Am. Chem. Soc.* **1998**, *120*, 12694–12695, DOI: 10.1021/ja982975d.

[47] S. Patnaik, A. K. Sharma, B. S. Garg, R. P. Gandhi, K. C. Gupta, Photoregulation of drug release in azo-dextran nanogels, *Int. J. Pharm.* **2007**, *342*, 184–193, DOI: 10.1016/j.ijpharm.2007.04.038.

[48] R. Vukićević, A. T. Neffe, K. Luetzow, B. F. Pierce, A. Lendlein, R. Vukicevic, A. T. Neffe, K. Luetzow, B. F. Pierce, A. Lendlein, R. Vukićević, A. T. Neffe, K. Luetzow, B. F. Pierce, A. Lendlein, Conditional ultrasound sensitivity of poly[(N-isopropylacrylamide)-co-(vinyl imidazole)] microgels for controlled lipase release, *Macromol. Rapid Commun.* **2015**, *36*, 1891–1896, DOI: 10.1002/marc.201500311.

[49] R. Regmi, S. R. Bhattarai, C. Sudakar, A. S. Wani, R. Cunningham, P. P. Vaishnava, R. Naik, D. Oupicky, G. Lawes, Hyperthermia controlled rapid drug release from thermosensitive magnetic microgels, *J. Mater. Chem.* **2010**, *20*, 6158–6163, DOI: 10.1039/c0jm00844c.

[50] S. Campbell, D. Maitland, T. Hoare, Enhanced pulsatile drug release from injectable magnetic hydrogels with embedded thermosensitive microgels, *ACS Macro Lett.* **2015**, *4*, 312–316, DOI: 10.1021/acsmacrolett.5b00057.

[51] D. P. Rotella, The critical role of organic chemistry in drug discovery, *ACS Chem. Neurosci.* **2016**, *7*, 1315–1316, DOI: 10.1021/acschemneuro.6b00280.

[52] D. J. Newman, G. M. Cragg, K. M. Snader, Natural products as sources of new drugs over the period 1981-2002, *J. Nat. Prod.* **2003**, *66*, 1022–1037, DOI: 10.1021/np030096l.

[53] K. T. Savjani, A. K. Gajjar, J. K. Savjani, Drug solubility: Importance and enhancement techniques, *ISRN Pharm.* **2012**, *2012*, 1–10, DOI: 10.5402/2012/195727.

[54] M. Ishikawa, Y. Hashimoto, Improvement in aqueous solubility in small molecule drug discovery programs by disruption of molecular planarity and symmetry, *J. Med. Chem.* **2011**, *54*, 1539–1554, DOI: 10.1021/jm101356p.

[55] A. Gautier, M. J. Hinner, Getting across the cell membrane: An overview for small molecules, peptides, and proteins, *Site-Specific Protein Labeling: Methods and Protocols* **2015**, *1266*, 1–267, DOI: 10.1007/978-1-4939-2272-7.

[56] G. M. Cooper, R. E. Hausman, *The Cell: A Molecular Approach*, Sinauer Associates, Oxford University Press, Oxford, Newyork, **2019**, 514–525.

[57] T. Lammers, W. E. Hennink, G. Storm, Tumour-targeted nanomedicines: Principles and practice, *Br. J. Cancer* **2008**, *99*, 392–397, DOI: 10.1038/sj.bjc.6604483.

[58] H. Jahangirian, K. Kalantari, Z. Izadiyan, R. Rafiee-Moghaddam, K. Shameli, T. J. Webster, A review of small molecules and drug delivery applications using gold and iron nanoparticles, *Int. J. Nanomedicine* **2019**, *14*, 1633–1657, DOI: 10.2147/IJN.S184723.

[59] K. Cho, X. Wang, S. Nie, Z. Chen, D. M. Shin, Therapeutic nanoparticles for drug delivery in cancer, *Clin. Cancer Res.* **2008**, *14*, 1310–1316, DOI: 10.1158/1078-0432.CCR-07-1441.

[60] J. Jeevanandam, A. Barhoum, Y. S. Chan, A. Dufresne, M. K. Danquah, Review on nanoparticles and nanostructured materials: History, sources, toxicity and regulations, *Beilstein J. Nanotechnol.* **2018**, *9*, 1050–1074, DOI: 10.3762/bjnano.9.98.

[61] D. Chenthamara, S. Subramaniam, S. G. Ramakrishnan, S. Krishnaswamy, M. M. Essa, F. H. Lin, M. W. Qoronfleh, Therapeutic efficacy of nanoparticles and routes of administration, *Biomater. Res.* **2019**, *23*, 1–29, DOI: 10.1186/s40824-019-0166-x.

[62] W. H. Blackburn, E. B. Dickerson, M. H. Smith, J. F. McDonald, L. A. Lyon, Peptide-functionalized nanogels for targeted siRNA delivery, *Bioconjug. Chem.* **2009**, *20*, 960–968, DOI: 10.1021/bc800547c.

[63] J. K. Patra, G. Das, L. F. Fraceto, E. V. R. Campos, M. D. P. Rodriguez-Torres, L. S. Acosta-Torres, L. A. Diaz-Torres, R. Grillo, M. K. Swamy, S. Sharma, S. Habtemariam, H.-S. Shin, Nano based drug delivery systems: recent developments and future prospects, *J. Nanobiotechnology* **2018**, *16*, 71, DOI: 10.1186/s12951-018-0392-8.

[64] E.-K. Lim, T. Kim, S. Paik, S. Haam, Y.-M. Huh, K. Lee, Nanomaterials for theranostics: Recent advances and future challenges, *Chem. Rev.* **2015**, *115*, 327–394, DOI: 10.1021/cr300213b.

[65] F. Yuan, M. Dellian, D. Fukumura, M. Leunig, D. A. Berk, R. K. Jain, V. P. Torchilin, Vascular permeability in a human tumor xenograft: Molecular size dependence and cutoff size, *Cancer Res.* **1995**, *55*, 3752–3756.

[66] J. D. Heidel, M. E. Davis, Clinical developments in nanotechnology for cancer therapy, *Pharm. Res.* **2011**, *28*, 187–199, DOI: 10.1007/s11095-010-0178-7.

[67] H. Kang, S. Rho, W. R. Stiles, S. Hu, Y. Baek, D. W. Hwang, S. Kashiwagi, M. S. Kim, H. S. Choi, Size-dependent EPR effect of polymeric nanoparticles on tumor targeting, *Adv. Healthc. Mater.* **2020**, *9*, 8–15, DOI: 10.1002/adhm.201901223.

[68] D. Peer, J. M. Karp, S. Hong, O. C. Farokhzad, R. Margalit, R. Langer, Nanocarriers as an emerging platform for cancer therapy, *Nat. Nanotechnol.* **2007**, *2*, 751–760, DOI: 10.1038/nnano.2007.387.

[69] M. Shi, J. Lu, M. S. Shoichet, Organic nanoscale drug carriers coupled with ligands for targeted drug delivery in cancer, *J. Mater. Chem.* **2009**, *19*, 5485–5498, DOI: 10.1039/b822319j.

[70] S. Dhar, F. X. Gu, R. Langer, O. C. Farokhza, S. J. Lippard, Targeted delivery of cisplatin to prostate cancer cells by aptamer functionalized Pt(IV) prodrug-PLGA - PEG nanoparticles, *Proc. Natl. Acad. Sci. U. S. A.* **2008**, *105*, 17356–17361, DOI: 10.1073/pnas.0809154105.

[71] R. L. Juliano, R. Alam, V. Dixit, M. Kang, Peptides for delivery of therapeutic and imaging agents, *WIREs Nanomedicine and Nanobiotechnology* **2009**, *1*, 324–335, DOI: 10.1002/wnan.004.

[72] M. M. Attwood, J. Jonsson, M. Rask-Andersen, H. B. Schiöth, Soluble ligands as drug targets, *Nat. Rev. Drug Discov.* **2020**, *19*, DOI 10.1038/s41573-020-0078-4, DOI: 10.1038/s41573-020-0078-4.

[73] D. A. Richards, A. Maruani, V. Chudasama, Antibody fragments as nanoparticle targeting ligands: A step in the right direction, *Chem. Sci.* **2016**, *8*, 63–77, DOI: 10.1039/c6sc02403c.

[74] Y. Zhang, Y. Huang, S. Li, Polymeric micelles: Nanocarriers for cancer-targeted drug delivery, *AAPS PharmSciTech* **2014**, *15*, 862–871, DOI: 10.1208/s12249-014-0113-z.

[75] M. C. I. M. Amin, A. M. Butt, M. W. Amjad, P. Kesharwani, Polymeric micelles for drug targeting and delivery, *Nanotechnology-Based Approaches for Targeting Delivery of Drugs and Genes* **2017**, 167–202, DOI: 10.1016/B978-0-12-809717-5.00006-3.

[76] G. Bozzuto, A. Molinari, Liposomes as nanomedical devices, *Int. J. Nanomedicine* **2015**, *10*, 975–999, DOI: 10.2147/IJN.S68861.

[77] S. Bamrungsap, Z. Zhao, T. Chen, L. Wang, C. Li, T. Fu, W. Tan, Nanotechnology in therapeutics: A focus on nanoparticles as a drug delivery system, *Nanomedicine* **2012**, *7*, 1253–1271, DOI: 10.2217/nnm.12.87.

[78] A. Jain, S. K. Singh, S. K. Arya, S. C. Kundu, S. Kapoor, Protein nanoparticles: Promising platforms for drug delivery applications, *ACS Biomater. Sci. Eng.* **2018**, *4*, 3939–3961, DOI: 10.1021/acsbiomaterials.8b01098.

[79] F. Kratz, Albumin as a drug carrier: Design of prodrugs, drug conjugates and nanoparticles, *J. Control. Release* **2008**, *132*, 171–183, DOI: 10.1016/j.jconrel.2008.05.010.

[80] H. Wang, G. Cheng, Y. Du, L. Ye, W. Chen, L. Zhang, T. Wang, J. Tian, F. Fu, Hypersensitivity reaction studies of a polyethoxylated castor oil-free, liposome-based alternative paclitaxel formulation, *Mol. Med. Rep.* **2013**, *7*, 947–952, DOI: 10.3892/mmr.2013.1264.

[81] M. Uchida, M. T. Klem, M. Allen, P. Suci, M. Flenniken, E. Gillitzer, Z. Varpness, L. O. Liepold, M. Young, T. Douglas, Biological containers: Protein cages as multifunctional nanoplatforms, *Adv. Mater.* **2007**, *19*, 1025–1042, DOI: 10.1002/adma.200601168.

[82] W. M. Aumiller, M. Uchida, T. Douglas, Protein cage assembly across multiple length scales, *Chem. Soc. Rev.* **2018**, *47*, 3433–3469, DOI: 10.1039/c7cs00818j.

[83] M. Rother, M. G. Nussbaumer, K. Renggli, N. Bruns, Protein cages and synthetic polymers: A fruitful symbiosis for drug delivery applications, bionanotechnology and materials science, *Chem. Soc. Rev.* **2016**, *45*, 6213–6249, DOI: 10.1039/c6cs00177g.

[84] I. W. Park, K. W. Kim, Y. Hong, H. J. Yoon, Y. Lee, D. Gwak, K. Heo, Recent developments and prospects of M13-bacteriophage based piezoelectric energy harvesting devices, *Nanomaterials* **2020**, *10*, DOI 10.3390/nano10010093, DOI: 10.3390/nano10010093.

[85] Y. Fu, J. Li, A novel delivery platform based on Bacteriophage MS2 virus-like particles, *Virus Res.* **2016**, *211*, 9–16, DOI: 10.1016/j.virusres.2015.08.022.

[86] A. S. Blum, C. M. Soto, C. D. Wilson, J. D. Cole, M. Kim, B. Gnade, A. Chatterji, W. F. Ochoa, T. Lin, J. E. Johnson, B. R. Ratna, Cowpea mosaic virus as a scaffold for 3-D patterning of gold nanoparticles, *Nano Lett.* **2004**, *4*, 867–870, DOI: 10.1021/nl0497474.

[87] L. Schoonen, R. J. M. Nolte, J. C. M. Van Hest, Highly efficient enzyme encapsulation in a protein nanocage: Towards enzyme catalysis in a cellular nanocompartment mimic, *Nanoscale* **2016**, *8*, 14467–14472, DOI: 10.1039/c6nr04181g.

[88] G. Jutz, P. van Rijn, B. Santos Miranda, A. Böker, Ferritin: A versatile building block for bionanotechnology, *Chem. Rev.* **2015**, *115*, 1653–1701, DOI: 10.1021/cr400011b.

[89] K. Namba, R. Pattanayek, G. Stubbs, Visualization of protein-nucleic acid interactions in a virus, *J. Mol. Biol.* **1989**, *208*, 307–325, DOI: 10.1016/0022-2836(89)90391-4.

[90] A. Z. Stasiak, E. Larquet, A. Stasiak, S. Müller, A. Engel, E. Van Dyck, S. C. West, E. H. Egelman, The human Rad52 protein exists as a heptameric ring, *Curr. Biol.* **2000**, *10*, 337–340, DOI: 10.1016/S0960-9822(00)00385-7.

[91] J. Heddle, Protein cages, rings and tubes: useful components of future nanodevices?, *Nanotechnol. Sci. Appl.* **2008**, *Volume 1*, 67–78, DOI: 10.2147/nsa.s4092.

[92] Y. T. Lai, E. Reading, G. L. Hura, K. L. Tsai, A. Laganowsky, F. J. Asturias, J. A. Tainer, C. V. Robinson, T. O. Yeates, Structure of a designed protein cage that self-assembles into a highly porous cube, *Nat. Chem.* **2014**, *6*, 1065–1071, DOI: 10.1038/nchem.2107.

[93] R. Ladenstein, M. Fischer, A. Bacher, The lumazine synthase/riboflavin synthase complex: Shapes and functions of a highly variable enzyme system, *FEBS J.* **2013**, *280*, 2537–2563, DOI: 10.1111/febs.12255.

[94] M. Sutter, B. Greber, C. Aussignargues, C. A. Kerfeld, Assembly principles and structure of a 6.5-MDa bacterial microcompartment shell, *Science* **2017**, *356*, 1293–1297, DOI: 10.1126/science.aan3289.

[95] S. Yuan, J. Wang, D. Zhu, N. Wang, Q. Gao, W. Chen, H. Tang, J. Wang, X. Zhang, H. Liu, Z. Rao, X. Wang, Cryo-EM structure of a herpesvirus capsid at 3.1 Å, *Science* **2018**, *360*, eaao7283, DOI: 10.1126/science.aao7283.

[96] T. Ueno, M. Suzuki, T. Goto, T. Matsumoto, K. Nagayama, Y. Watanabe, Size-selective olefin hydrogenation by a Pd nanocluster provided in an apo-ferritin cage, *Angew. Chemie - Int. Ed.* **2004**, *43*, 2527–2530, DOI: 10.1002/anie.200353436.

[97] N. Gálvez, P. Sánchez, J. M. Domínguez-Vera, Preparation of Cu and CuFe Prussian Blue derivative nanoparticles using the apoferritin cavity as nanoreactor, *Dalt. Trans.* **2005**, 2492, DOI: 10.1039/b506290j.

[98] E. C. Theil, X. S. Liu, T. Tosha, Gated pores in the ferritin protein nanocage, *Inorganica Chim. Acta* **2008**, *361*, 868–874, DOI: 10.1016/j.ica.2007.08.025.

[99] R. J. Nichols, C. Cassidy-Amstutz, T. Chaijarasphong, D. F. Savage, Encapsulins: molecular biology of the shell, *Crit. Rev. Biochem. Mol. Biol.* **2017**, *52*, 583–594, DOI: 10.1080/10409238.2017.1337709.

[100] X. Yang, N. D. Chasteen, Molecular diffusion into horse spleen ferritin: A nitroxide radical spin probe study, *Biophys. J.* **1996**, *71*, 1587–1595, DOI: 10.1016/S0006-3495(96)79361-X.

[101] P. Huang, P. Rong, A. Jin, X. Yan, M. G. Zhang, J. Lin, H. Hu, Z. Wang, X. Yue, W. Li, G. Niu, W. Zeng, W. Wang, K. Zhou, X. Chen, Dye-loaded ferritin nanocages for multimodal imaging and photothermal therapy, *Adv. Mater.* **2014**, *26*, 6401–6408, DOI: 10.1002/adma.201400914.

[102] P. Arosio, R. Ingrassia, P. Cavadini, Ferritins: A family of molecules for iron storage, antioxidation and more, *Biochim. Biophys. Acta* **2009**, *1790*, 589–599, DOI: 10.1016/j.bbagen.2008.09.004.

[103] D. He, J. Marles-Wright, Ferritin family proteins and their use in bionanotechnology, *N. Biotechnol.* **2015**, *32*, 651–657, DOI: 10.1016/j.nbt.2014.12.006.

[104] S. C. Andrews, A. K. Robinson, F. Rodríguez-Quiñones, Bacterial iron homeostasis, *FEMS Microbiol. Rev.* **2003**, *27*, 215–237, DOI: 10.1016/S0168-6445(03)00055-X.

[105] S. C. Andrews, The Ferritin-like superfamily: Evolution of the biological iron storeman from a rubrerythrin-like ancestor, *Biochim. Biophys. Acta* **2010**, *1800*, 691–705, DOI: 10.1016/j.bbagen.2010.05.010.

[106] R. Yang, J. Tian, Y. Liu, Z. Yang, D. Wu, Z. Zhou, Thermally induced encapsulation of food nutrients into phytoferritin through the flexible channels without additives, *J. Agric. Food Chem.* **2017**, *65*, 9950–9955, DOI: 10.1021/acs.jafc.7b03949.

[107] Z. Heger, S. Skalickova, O. Zitka, V. Adam, R. Kizek, Apoferritin applications in nanomedicine, *Nanomedicine* **2014**, *9*, 2233–2245, DOI: 10.2217/nnm.14.119.

[108] M. Gerl, R. Jaenicke, Mechanism of the self-assembly of apoferritin from horse spleen - Cross-linking and spectroscopic analysis, *Eur. Biophys. J.* **1987**, *15*, 103–109, DOI: 10.1007/BF00257503.

[109] N. Imai, Y. Arata, S. Fujiwara, 1 H NMR study of dissociation and re-association of apoferritin and ferritin, *Bull. Chem. Soc. Jpn.* **1981**, *54*, 1243–1244, DOI: 10.1246/bcsj.54.1243.

[110] R. R. Crichton, C. F. Bryce, Subunit interactions in horse spleen apoferritin. Dissociation by extremes of pH., *Biochem. J.* **1973**, *133*, 289–299, DOI: 10.1042/bj1330289.

[111] A. Ma-Ham, H. Wu, J. Wang, X. Kang, Y. Zhang, Y. Lin, Apoferritin-based nanomedicine platform for drug delivery: Equilibrium binding study of daunomycin with DNA, *J. Mater. Chem.* **2011**, *21*, 8700–8708, DOI: 10.1039/c0jm04321d.

[112] R. Yang, Y. Liu, C. Blanchard, Z. Zhou, Channel directed rutin nano-encapsulation in phytoferritin induced by guanidine hydrochloride, *Food Chem.* **2018**, *240*, 935–939, DOI: 10.1016/j.foodchem.2017.07.088.

[113] S. Stefanini, S. Cavallo, C.-Q. Q. Wang, P. Tataseo, P. Vecchini, A. Giartosio, E. Chiancone, Thermal stability of horse spleen apoferritin and human recombinant H apoferritin, *Arch. Biochem. Biophys.* **1996**, *325*, 58–64, DOI: 10.1006/abbi.1996.0007.

[114] X. Huang, J. Chisholm, J. Zhuang, Y. Xiao, G. Duncan, X. Chen, J. S. Suk, J. Hanes, Protein nanocages that penetrate airway mucus and tumor tissue, *Proc. Natl. Acad. Sci.* **2017**, *114*, E6595–E6602, DOI: 10.1073/pnas.1705407114.

[115] M. Uchida, M. L. Flenniken, M. Allen, D. A. Willits, B. E. Crowley, S. Brumfield, A. F. Willis, L. Jackiw, M. Jutila, M. J. Young, T. Douglas, Targeting of cancer cells with ferrimagnetic ferritin cage nanoparticles, *J. Am. Chem. Soc.* **2006**, *128*, 16626–16633, DOI: 10.1021/ja0655690.

[116] R. Xing, X. Wang, C. Zhang, Y. Zhang, Q. Wang, Z. Yang, Z. Guo, Characterization and cellular uptake of platinum anticancer drugs encapsulated in apoferritin, *J. Inorg. Biochem.* **2009**, *103*, 1039–1044, DOI: 10.1016/j.jinorgbio.2009.05.001.

[117] N. Pontillo, F. Pane, L. Messori, A. Amoresano, A. Merlino, Cisplatin encapsulation within a ferritin nanocage: A high-resolution crystallographic study, *Chem. Commun.* **2016**, *52*, 4136–4139, DOI: 10.1039/c5cc10365g.

[118] X. T. Ji, L. Huang, H. Q. Huang, Construction of nanometer cisplatin core-ferritin (NCC-F) and proteomic analysis of gastric cancer cell apoptosis induced with cisplatin released from the NCC-F, *J. Proteomics* **2012**, *75*, 3145–3157, DOI: 10.1016/j.jprot.2012.03.013.

[119] E. Falvo, E. Tremante, R. Fraioli, C. Leonetti, C. Zamparelli, A. Boffi, V. Morea, P. Ceci, P. Giacomini, Antibody-drug conjugates: Targeting melanoma with cisplatin encapsulated in protein-cage nanoparticles based on human ferritin, *Nanoscale* **2013**, *5*, 12278–12285, DOI: 10.1039/c3nr04268e.

[120] Z. Yang, X. Wang, H. Diao, J. Zhang, H. Li, H. Sun, Z. Guo, Encapsulation of platinum anticancer drugs by apoferritin, *Chem. Commun.* **2007**, *7345*, 3453–3455, DOI: 10.1039/b705326f.

[121] G. Ferraro, D. M. Monti, A. Amoresano, N. Pontillo, G. Petruk, F. Pane, M. A. Cinellu, A. Merlino, Gold-based drug encapsulation within a ferritin nanocage: X-ray structure and biological evaluation as a potential anticancer agent of the Auoxo3-loaded protein, *Chem. Commun.* **2016**, *52*, 9518–9521, DOI: 10.1039/c6cc02516a.

[122] D. M. Monti, G. Ferraro, G. Petruk, L. Maiore, F. Pane, A. Amoresano, M. A. Cinellu, A. Merlino, Ferritin nanocages loaded with gold ions induce oxidative stress and apoptosis in MCF-7 human breast cancer cells, *Dalt. Trans.* **2017**, *46*, 15354–15362, DOI: 10.1039/C7DT02370G.

[123] X. Liu, W. Wei, S. Huang, S.-S. Lin, X. Zhang, C. Zhang, Y. Du, G. Ma, M. Li, S. Mann, D. Ma, Bio-inspired protein-gold nanoconstruct with core-void-shell structure: Beyond a chemo drug carrier, *J. Mater. Chem. B* **2013**, *1*, 3136–3143, DOI: 10.1039/C3TB20081G.

[124] J. F. Hainfeld, Uranium-loaded apoferritin with antibodies attached: Molecular design for uranium neutron-capture therapy, *Proc. Natl. Acad. Sci. U. S. A.* **1992**, *89*, 11064–11068, DOI: 10.1073/pnas.89.22.11064.

[125] H. Wu, M. H. Engelhard, J. Wang, D. R. Fisher, Y. Lin, Synthesis of lutetium phosphate-apoferritin core-shell nanoparticles for potential applications in radioimmunoimaging and radioimmunotherapy of cancers, *J. Mater. Chem.* **2008**, *18*, 1779–1783, DOI: 10.1039/b717613a.

[126] L. Pandolfi, M. Bellini, R. Vanna, C. Morasso, A. Zago, S. Carcano, S. Avvakumova, J. A. Bertolini, M. A. Rizzuto, M. Colombo, D. Prosperi, H-ferritin enriches the curcumin uptake and improves the therapeutic efficacy in triple negative breast cancer cells, *Biomacromolecules* **2017**, *18*, 3318–3330, DOI: 10.1021/acs.biomac.7b00974.

[127] L. Chen, G. Bai, S. Yang, R. Yang, G. Zhao, C. Xu, W. Leung, Encapsulation of curcumin in recombinant human H-chain ferritin increases its water-solubility and stability, *Food Res. Int.* **2014**, *62*, 1147–1153, DOI: 10.1016/j.foodres.2014.05.054.

[128] J. C. Cutrin, S. G. Crich, D. Burghelea, W. Dastrù, S. Aime, Curcumin/Gd loaded apoferritin: A novel "theranostic" agent to prevent hepatocellular damage in toxic induced acute hepatitis, *Mol. Pharm.* **2013**, *10*, 2079–2085, DOI: 10.1021/mp3006177.

[129] L. Conti, S. Lanzardo, R. Ruiu, M. Cadenazzi, F. Cavallo, S. Aime, S. G. Crich, L-Ferritin targets breast cancer stem cells and delivers therapeutic and imaging agents, *Oncotarget* **2016**, *7*, 66713–66727, DOI: 10.18632/oncotarget.10920.

[130] V. De Turris, M. Cardoso Trabuco, G. Peruzzi, A. Boffi, C. Testi, B. Vallone, L. Celeste Montemiglio, A. Des Georges, L. Calisti, I. Benni, A. Bonamore, P. Baiocco, Humanized archaeal ferritin as a tool for cell targeted delivery, *Nanoscale* **2017**, *9*, 647–655, DOI: 10.1039/c6nr07129e.

[131] L. C. Montemiglio, C. Testi, P. Ceci, E. Falvo, M. Pitea, C. Savino, A. Arcovito, G. Peruzzi, P. Baiocco, F. Mancia, A. Boffi, A. des Georges, B. Vallone, Cryo-EM structure of the human ferritin–transferrin receptor 1 complex, *Nat. Commun.* **2019**, *10*, 1–8, DOI: 10.1038/s41467-019-09098-w.

[132] F. Palombarini, E. Di Fabio, A. Boffi, A. Macone, A. Bonamore, Ferritin nanocages for protein delivery to tumor cells, *Molecules* **2020**, *25*, DOI 10.3390/molecules25040825, DOI: 10.3390/molecules25040825.

[133] M. Lan, S. Zhao, W. Liu, C. S. Lee, W. Zhang, P. Wang, Photosensitizers for photodynamic therapy, *Adv. Healthc. Mater.* **2019**, *8*, 1–37, DOI: 10.1002/adhm.201900132.

[134] S. Kwiatkowski, B. Knap, D. Przystupski, J. Saczko, E. Kędzierska, K. Knap-Czop, J. Kotlińska, O. Michel, K. Kotowski, J. Kulbacka, Photodynamic therapy – mechanisms, photosensitizers and combinations, *Biomed. Pharmacother.* **2018**, *106*, 1098–1107, DOI: 10.1016/j.biopha.2018.07.049.

[135] H. S. Jung, P. Verwilst, A. Sharma, J. Shin, J. L. Sessler, J. S. Kim, Organic molecule-based photothermal agents: An expanding photothermal therapy universe, *Chem. Soc. Rev.* **2018**, *47*, 2280–2297, DOI: 10.1039/c7cs00522a.

[136] J. J. Hu, Y. J. Cheng, X. Z. Zhang, Recent advances in nanomaterials for enhanced photothermal therapy of tumors, *Nanoscale* **2018**, *10*, 22657–22672, DOI: 10.1039/c8nr07627h.

[137] Z. Zhen, W. Tang, W. Zhang, J. Xie, Folic acid conjugated ferritins as photosensitizer carriers for photodynamic therapy, *Nanoscale* **2015**, *7*, 10330–10333, DOI: 10.1039/c5nr01833a.

[138] Z. Zhen, W. Tang, Y. J. Chuang, T. Todd, W. Zhang, X. Lin, G. Niu, G. Liu, L. Wang, Z. Pan, X. Chen, J. Xie, Tumor vasculature targeted photodynamic therapy for enhanced delivery of nanoparticles, *ACS Nano* **2014**, *8*, 6004–6013, DOI: 10.1021/nn501134q.

[139] Z. Zhen, W. Tang, M. Wang, S. Zhou, H. Wang, Z. Wu, Z. Hao, Z. Li, L. Liu, J. Xie, Protein nanocage mediated fibroblast-activation protein targeted photoimmunotherapy to enhance cytotoxic T cell infiltration and tumor control, *Nano Lett.* **2017**, *17*, 862–869, DOI: 10.1021/acs.nanolett.6b04150.

[140] C. Huang, C. Chu, X. Wang, H. Lin, J. Wang, Y. Zeng, W. Zhu, Y. X. J. Wang, G. Liu, Ultra-high loading of sinoporphyrin sodium in ferritin for single-wave motivated photothermal and photodynamic co-therapy, *Biomater. Sci.* **2017**, *5*, 1512–1516, DOI: 10.1039/c7bm00302a.

[141] J. K. W. Lam, M. Y. T. Chow, Y. Zhang, S. W. S. Leung, siRNA versus miRNA as therapeutics for gene silencing, *Mol. Ther. - Nucleic Acids* **2015**, *4*, e252, DOI: 10.1038/mtna.2015.23.

[142] B. L. Davidson, P. B. McCray, Current prospects for RNA interference-based therapies, *Nat. Rev. Genet.* **2011**, *12*, 329–340, DOI: 10.1038/nrg2968.

[143] D. Castanotto, J. J. Rossi, The promises and pitfalls of RNA-interference-based therapeutics, *Nature* **2009**, *457*, 426–433, DOI: 10.1038/nature07758.

[144] L. Li, M. Muñoz-Culla, U. Carmona, M. P. Lopez, F. Yang, C. Trigueros, D. Otaegui, L. Zhang, M. Knez, Ferritin-mediated siRNA delivery and gene silencing in human tumor and primary cells, *Biomaterials* **2016**, *98*, 143–151, DOI: 10.1016/J.BIOMATERIALS.2016.05.006.

[145] E. J. Lee, S. J. Lee, Y. S. Kang, J. H. Ryu, K. C. Kwon, E. Jo, J. Y. Yhee, I. C. Kwon, K. Kim, J. Lee, Engineered proteinticles for targeted delivery of siRNA to cancer cells, *Adv. Funct. Mater.* **2015**, *25*, 1279–1286, DOI: 10.1002/adfm.201403680.

[146] R. Samanipour, T. Wang, M. Werb, H. Hassannezhad, J. M. L. Rangel, M. Hoorfar, A. Hasan, C. K. Lee, S. R. Shin, Ferritin nanocage conjugated hybrid hydrogel for tissue engineering and drug delivery applications, *ACS Biomater. Sci. Eng.* **2020**, *6*, 277–287, DOI: 10.1021/acsbiomaterials.9b01482.

[147] Y. Cai, T. Deng, Y. Pan, J. I. Zink, Use of ferritin capped mesoporous silica nanoparticles for redox and pH triggered drug release in vitro and in vivo, *Adv. Funct. Mater.* **2020**, *2002043*, 1–13, DOI: 10.1002/adfm.202002043.

[148] J. A. Han, Y. J. Kang, C. Shin, J. S. Ra, H. H. Shin, S. Y. Hong, Y. Do, S. Kang, Ferritin protein cage nanoparticles as versatile antigen delivery nanoplatforms for dendritic cell (DC)-based vaccine development, *Nanomedicine Nanotechnology, Biol. Med.* **2014**, *10*, 561–569, DOI: 10.1016/j.nano.2013.11.003.

[149] M. Kanekiyo, C. J. Wei, H. M. Yassine, P. M. McTamney, J. C. Boyington, J. R. R. Whittle, S. S. Rao, W. P. Kong, L. Wang, G. J. Nabel, Self-assembling influenza nanoparticle vaccines elicit broadly neutralizing H1N1 antibodies, *Nature* **2013**, *499*, 102–106, DOI: 10.1038/nature12202.

[150] S. H. Choi, K. Choi, I. Chan Kwon, H. J. Ahn, The incorporation of GALA peptide into a protein cage for an acid-inducible molecular switch, *Biomaterials* **2010**, *31*, 5191–5198, DOI: 10.1016/j.biomaterials.2010.03.016.

[151] Y. J. Kang, D. C. Park, H. H. Shin, J. Park, S. Kang, Incorporation of thrombin cleavage peptide into a protein cage for constructing a protease-responsive multifunctional delivery nanoplatform, *Biomacromolecules* **2012**, *13*, 4057–4064, DOI: 10.1021/bm301339s.

[152] Y. Cai, C. Cao, X. He, C. Yang, L. Tian, R. Zhu, Y. Pan, Enhanced magnetic resonance imaging and staining of cancer cells using ferrimagnetic H-ferritin nanoparticles with increasing core size, *Int. J. Nanomedicine* **2015**, *10*, 2619–2634, DOI: 10.2147/IJN.S80025.

[153] C. Cao, X. Wang, Y. Cai, L. Sun, L. Tian, H. Wu, X. He, H. Lei, W. Liu, G. Chen, R. Zhu, Y. Pan, Targeted in vivo imaging of microscopic tumors with ferritin-based nanoprobes across biological barriers, *Adv. Mater.* **2014**, *26*, 2566–2571, DOI: 10.1002/adma.201304544.

[154] S. Aime, L. Frullano, S. Geninatti Crich, Compartmentalization of a gadolinium complex in the apoferritin cavity: A route to obtain high relaxivity contrast agents for magnetic resonance imaging, *Angew. Chemie Int. Ed.* **2002**, *41*, 1017–1019, DOI: 10.1002/1521-3773(20020315)41:6<1017::AID-ANIE1017>3.0.CO;2-P.

[155] P. Sánchez, E. Valero, N. Gálvez, J. M. Domínguez-Vera, M. Marinone, G. Poletti, M. Corti, A. Lascialfari, MRI relaxation properties of water-soluble apoferritin-encapsulated gadolinium oxide-hydroxide nanoparticles, *J. Chem. Soc. Dalt. Trans.* **2008**, 800–804, DOI: 10.1039/b809645g.

[156] F. K. Kálmán, S. Geninatti-Crich, S. Aime, Reduction/dissolution of a β-MnOOH nanophase in the ferritin cavity to yield a highly sensitive, biologically compatible magnetic resonance imaging agent, *Angew. Chemie - Int. Ed.* **2010**, *49*, 612–615, DOI: 10.1002/anie.200904731.

[157] C. Chi, Y. Du, J. Ye, D. Kou, J. Qiu, J. Wang, J. Tian, X. Chen, Intraoperative imaging-guided cancer surgery: From current fluorescence molecular imaging methods to future multi-modality imaging technology, *Theranostics* **2014**, *4*, 1072–1084, DOI: 10.7150/thno.9899.

[158] Z. Zhen, W. Tang, H. Chen, X. Lin, T. Todd, G. Wang, T. Cowger, X. Chen, J. Xie, RGD-modified apoferritin nanoparticles for efficient drug delivery to tumors, *ACS Nano* **2013**, *7*, 4830–4837, DOI: 10.1021/nn305791q.

[159] X. Li, L. Qiu, P. Zhu, X. Tao, T. Imanaka, J. Zhao, Y. Huang, Y. Tu, X. Cao, Epidermal growth factor-ferritin H-chain protein nanoparticles for tumor active targeting, *Small* **2012**, *8*, 2505–2514, DOI: 10.1002/smll.201200066.

[160] K. Li, Z. P. Zhang, M. Luo, X. Yu, Y. Han, H. P. Wei, Z. Q. Cui, X. E. Zhang, Multifunctional ferritin cage nanostructures for fluorescence and MR imaging of tumor cells, *Nanoscale* **2012**, *4*, 188–193, DOI: 10.1039/c1nr11132a.

[161] R. I. Pakunlu, T. J. Cook, T. Minko, Simultaneous modulation of multidrug resistance and antiapoptotic cellular defense by MDR1 and BCL-2 targeted antisense oligonucleotides enhances the anticancer efficacy of doxorubicin, *Pharm. Res.* **2003**, *20*, 351–359, DOI: 10.1023/A:1022687617318.

[162] J. Robert, J. P. Armand, S. Huet, M. Klink-Alakl, G. Recondo, P. Hurteloup, Pharmacokinetics and metabolism of 4'-iodo-4'-deoxy-doxorubicin in humans, *J. Clin. Oncol.* **1992**, *10*, 1183–1190, DOI: 10.1200/JCO.1992.10.7.1183.

[163] N. R. Bachur, M. Gee, Daunorubicin metabolism by rat tissue preparations, *J. Pharmacol. Exp. Ther.* **1971**, *177*, 567–572.

[164] K. Fan, X. Yan, Bioengineered ferritin nanoprobes for cancer theranostics, *Handb. Nanomater. Cancer Theranostics* **2018**, 143–175, DOI: 10.1016/B978-0-12-813339-2.00006-2.

[165] G. J. Brewer, Copper toxicity in the general population, *Clin. Neurophysiol.* **2010**, *121*, 459–460, DOI: 10.1016/j.clinph.2009.12.015.

[166] Q. Wang, C. Zhang, L. Liu, Z. Li, F. Guo, X. Li, J. Luo, D. Zhao, Y. Liu, Z. Su, High hydrostatic pressure encapsulation of doxorubicin in ferritin nanocages with enhanced efficiency, *J. Biotechnol.* **2017**, *254*, 34–42, DOI: 10.1016/j.jbiotec.2017.05.025.

[167] R. Pelton, T. Hoare, Microgels and their synthesis: An introduction, *Microgels and Their Synthesis: An Introduction*, **2011**, DOI: 10.1002/9783527632992.ch1.

[168] A. P. H. Gelissen, A. Scotti, S. K. Turnhoff, C. Janssen, A. Radulescu, A. Pich, A. A. Rudov, I. I. Potemkin, W. Richtering, An anionic shell shields a cationic core allowing for uptake and release of polyelectrolytes within core–shell responsive microgels, *Soft Matter* **2018**, *14*, 4287–4299, DOI: 10.1039/C8SM00397A.

[169] Y. Zhang, Y. Guan, S. Zhou, Permeability control of glucose-sensitive nanoshells, *Biomacromolecules* **2007**, *8*, 3842–3847, DOI: 10.1021/bm700802p.

[170] A. J. Schmid, J. Dubbert, A. A. Rudov, J. S. Pedersen, P. Lindner, M. Karg, I. I. Potemkin, W. Richtering, Multi-shell hollow nanogels with responsive shell permeability, *Sci. Rep.* **2016**, *6*, 1–13, DOI: 10.1038/srep22736.

[171] H. Feil, Y. H. Bae, J. Feijen, S. W. Kim, Effect of comonomer hydrophilicity and ionization on the lower critical solution temperature of N-Isopropylacrylamide copolymers, *Macromolecules* **1993**, *26*, 2496–2500, DOI: 10.1021/ma00062a016.

[172] E. E. Makhaeva, H. Tenhu, A. R. Khokhlov, Conformational changes of poly(vinylcaprolactam) macromolecules and their complexes with ionic surfactants in aqueous solution, *Macromolecules* **1998**, *31*, 6112–6118, DOI: 10.1021/ma980158s.

[173] T. Hoare, D. McLean, Kinetic prediction of functional group distributions in thermosensitive microgels, *J. Phys. Chem. B* **2006**, *110*, 20327–20336, DOI: 10.1021/jp0643451.

[174] S. Çavuş, E. Çakal, Synthesis and characterization of novel poly(N-vinylcaprolactam-co-itaconic acid) gels and analysis of pH and temperature sensitivity, *Ind. Eng. Chem. Res.* **2012**, *51*, 1218–1226, DOI: 10.1021/ie2008746.

[175] L. V. Sigolaeva, D. V. Pergushov, M. Oelmann, S. Schwarz, M. Brugnoni, I. N. Kurochkin, F. A. Plamper, A. Fery, W. Richtering, Surface functionalization by stimuli-sensitive microgels for effective enzyme uptake and rational design of biosensor setups, *Polymers (Basel).* **2018**, *10*, DOI 10.3390/polym10070791, DOI: 10.3390/polym10070791.

[176] S. Thies, P. Simon, I. Zelenina, L. Mertens, A. Pich, In situ growth and size regulation of single gold nanoparticles in composite microgels, *Small* **2018**, *14*, 1–7, DOI: 10.1002/smll.201803589.

[177] H. Ni, H. Kawaguchi, T. Endo, Preparation of amphoteric microgels of poly(acrylamide/methacrylic acid/dimethylamino ethylene methacrylate) with a novel pH-volume transition, *Macromolecules* **2007**, *40*, 6370–6376, DOI: 10.1021/ma070358g.

[178] N. Häntzschel, F. Zhang, F. Eckert, A. Pich, M. A. Winnik, Poly(N-vinylcaprolactam-co-glycidyl methacrylate) aqueous microgels labeled with fluorescent LaF_3:Eu nanoparticles, *Langmuir* **2007**, *23*, 10793–10800, DOI: 10.1021/la701691g.

[179] N. Häntzschel, R. D. Hund, H. Hund, M. Schrinner, C. Lück, A. Pich, Hybrid microgels with antibacterial properties, *Macromol. Biosci.* **2009**, *9*, 444–449, DOI: 10.1002/mabi.200800219.

[180] A. Garcia, M. Marquez, T. Cai, R. Rosario, Z. Hu, D. Gust, M. Hayes, S. A. Vail, C. Do Park, Photo-, thermally-, and pH-responsive microgels, *Langmuir* **2007**, *23*, 224–229, DOI: 10.1021/la061632n.

[181] S. Schneider, F. Jung, O. Mergel, J. Lammertz, A. C. Nickel, T. Caumanns, A. Mhamdi, J. Mayer, A. Mitsos, F. A. Plamper, Model-based design and synthesis of ferrocene containing microgels, *Polym. Chem.* **2020**, *11*, 315–325, DOI: 10.1039/c9py00494g.

[182] S. Nayak, L. Andrew Lyon, Soft nanotechnology with soft nanoparticles, *Angew. Chemie - Int. Ed.* **2005**, *44*, 7686–7708, DOI: 10.1002/anie.200501321.

[183] T. Still, K. Chen, A. M. Alsayed, K. B. Aptowicz, A. G. Yodh, Synthesis of micrometer-size poly(N-isopropylacrylamide) microgel particles with homogeneous crosslinker density and diameter control, *J. Colloid Interface Sci.* **2013**, *405*, 96–102, DOI: 10.1016/j.jcis.2013.05.042.

[184] J. C. Gaulding, M. H. Smith, J. S. Hyatt, A. Fernandez-Nieves, L. A. Lyon, Reversible inter- and intra-microgel cross-linking using disulfides, *Macromolecules* **2012**, *45*, 39–45, DOI: 10.1021/ma202282p.

[185] X. Zhang, S. Malhotra, M. Molina, R. Haag, Micro- and nanogels with labile crosslinks – from synthesis to biomedical applications, *Chem. Soc. Rev.* **2015**, *44*, 1948–1973, DOI: 10.1039/C4CS00341A.

[186] L. Zhang, J. Bernard, T. P. Davis, C. Barner-Kowollik, M. H. Stenzel, Acid-degradable core-crosslinked micelles prepared from thermosensitive glycopolymers synthesized via RAFT polymerization, *Macromol. Rapid Commun.* **2008**, *29*, 123–129, DOI: 10.1002/marc.200700663.

[187] Y. Chen, N. Ballard, S. A. F. Bon, Waterborne polymer nanogels non-covalently crosslinked by multiple hydrogen bond arrays, *Polym. Chem.* **2013**, *4*, 387–392, DOI: 10.1039/c2py20615c.

[188] D. Schmitz, A. Pich, Responsive microgels with supramolecular crosslinks: Synthesis and triggered degradation in aqueous medium, *Polym. Chem.* **2016**, *7*, 5687–5697, DOI: 10.1039/c6py01039c.

[189] W. McPhee, K. C. Tam, R. Pelton, Poly(N-isopropylacrylamide) latices prepared with sodium dodecyl sulfate, *J. Colloid Interface Sci.* **1993**, *156*, 24–30, DOI: 10.1006/jcis.1993.1075.

[190] X. Hu, Z. Tong, L. A. Lyon, Control of poly(N-isopropylacrylamide) microgel network structure by precipitation polymerization near the lower critical solution temperature, *Langmuir* **2011**, *27*, 4142–4148, DOI: 10.1021/la200114s.

[191] H. Zhang, E. Tumarkin, R. M. A. Sullan, G. C. Walker, E. Kumacheva, Exploring microfluidic routes to microgels of biological polymers, *Macromol. Rapid Commun.* **2007**, *28*, 527–538, DOI: 10.1002/marc.200600776.

[192] J. W. Goodwin, R. H. Ottewill, R. Pelton, G. Vianello, D. E. Yates, Control of particle size in the formation of polymer latices, *Br. Polym. J.* **1978**, *10*, 173–180, DOI: 10.1002/pi.4980100304.

[193] J. W. Goodwin, J. Hearn, C. C. Ho, R. H. Ottewill, The preparation and characterisation of polymer latices formed in the absence of surface active agents, *Br. Polym. J.* **1973**, *5*, 347–362, DOI: 10.1002/pi.4980050503.

[194] H. Shimlzu, R. Wada, M. Okabe, Preparation and characterization of micrometer-sized poly(N-isopropylacrylamide) hydrogel particles, *Polym. J.* **2009**, *41*, 771–777, DOI: 10.1295/polymj.PJ2009039.

[195] F. Meunier, A. Elaissari, Poly(N-isopropylacrylamide)-based particles: Preparation and colloidal characterization, in *Colloid. Polym. Synth. Charact.* (Ed.: A. Elaissari), Marcel Dekker, Inc., New York, Basel, **2003**, 125–129.

[196] C. D. Jones, L. A. Lyon, Shell-restricted swelling and core compression in poly(N-isopropylacrylamide) core-shell microgels, *Macromolecules* **2003**, *36*, 1988–1993, DOI: 10.1021/ma021079q.

[197] J. Kleinen, A. Klee, W. Richtering, Influence of architecture on the interaction of negatively charged multisensitive poly(N-isopropylacrylamide)-co-methacrylic acid microgels with oppositely charged polyelectrolyte: Absorption vs adsorption, *Langmuir* **2010**, *26*, 11258–11265, DOI: 10.1021/la100579b.

[198] A. P. H. Gelissen, A. Oppermann, T. Caumanns, P. Hebbeker, S. K. Turnhoff, R. Tiwari, S. Eisold, U. Simon, Y. Lu, J. Mayer, W. Richtering, A. Walther, D. Wöll, 3D structures of responsive nanocompartmentalized microgels, *Nano Lett.* **2016**, *16*, 7295–7301, DOI: 10.1021/acs.nanolett.6b03940.

[199] N. C. Dubey, B. P. Tripathi, M. Stamm, L. Ionov, Smart core-shell microgel support for acetyl coenzyme A synthetase: A step toward efficient synthesis of polyketide-based drugs, *Biomacromolecules* **2014**, *15*, 2776–2783, DOI: 10.1021/bm5006382.

[200] C. D. Jones, L. A. Lyon, Synthesis and characterization of multiresponsive core-shell microgels, *Macromolecules* **2000**, *33*, 8301–8306, DOI: 10.1021/ma001398m.

[201] S. K. Wypysek, A. Scotti, M. O. Alziyadi, I. I. Potemkin, A. R. Denton, W. Richtering, Tailoring the cavity of hollow polyelectrolyte microgels, *Macromol. Rapid Commun.* **2020**, *41*, DOI 10.1002/marc.201900422, DOI: 10.1002/marc.201900422.

[202] Y. H. Yun, D. J. Goetz, P. Yellen, W. Chen, Hyaluronan microspheres for sustained gene delivery and site-specific targeting, *Biomaterials* **2004**, *25*, 147–157, DOI: 10.1016/S0142-9612(03)00467-8.

[203] S. L. Goh, N. Murthy, M. Xu, J. M. J. Fréchet, Cross-linked microparticles as carriers for the delivery of plasmid DNA for vaccine development, *Bioconjug. Chem.* **2004**, *15*, 467–474, DOI: 10.1021/bc034159n.

[204] L. P. B. Guerzoni, J. Bohl, A. Jans, J. C. Rose, J. Koehler, A. J. C. Kuehne, L. De Laporte, Microfluidic fabrication of polyethylene glycol microgel capsules with tailored properties for the delivery of biomolecules, *Biomater. Sci.* **2017**, *5*, 1549–1557, DOI: 10.1039/c7bm00322f.

[205] H. Z. An, H. B. Eral, L. Chen, M. B. Chen, P. S. Doyle, Synthesis of colloidal microgels using oxygen-controlled flow lithography, *Soft Matter* **2014**, *10*, 7595–7605, DOI: 10.1039/c4sm01400f.

[206] H. Peng, K. Rübsam, F. Jakob, P. Pazdzior, U. Schwaneberg, A. Pich, Reversible deactivation of enzymes by redox-responsive nanogel carriers, *Macromol. Rapid Commun.* **2016**, *37*, 1765–1771, DOI: 10.1002/marc.201600476.

[207] W. Chen, Y. Hou, Z. Tu, L. Gao, R. Haag, pH-degradable PVA-based nanogels via photo-crosslinking of thermo-preinduced nanoaggregates for controlled drug delivery, *J. Control. Release* **2017**, *259*, 160–167, DOI: 10.1016/j.jconrel.2016.10.032.

[208] G. Agrawal, R. Agrawal, A. Pich, Dual responsive Poly(N-vinylcaprolactam) based degradable microgels for drug delivery, *Part. Part. Syst. Charact.* **2017**, *34*, 1–9, DOI: 10.1002/ppsc.201700132.

[209] T. Hoare, R. Pelton, Impact of microgel morphology on functionalized microgel-drug interactions, *Langmuir* **2008**, *24*, 1005–1012, DOI: 10.1021/la7024507.

[210] L. Nuhn, M. Hirsch, B. Krieg, K. Koynov, K. Fischer, M. Schmidt, M. Helm, R. Zentel, Cationic nanohydrogel particles as potential siRNA carriers for cellular delivery, *ACS Nano* **2012**, *6*, 2198–2214, DOI: 10.1021/nn204116u.

[211] S. Deshpande, S. Patil, N. Singh, Enhancing gene-knockdown efficiency of Poly(N-isopropylacrylamide) nanogels, *ACS Omega* **2018**, *3*, 8042–8049, DOI: 10.1021/acsomega.8b00738.

[212] L. Nyström, A. A. Strömstedt, A. Schmidtchen, M. Malmsten, Peptide-loaded microgels as antimicrobial and anti-inflammatory surface coatings, *Biomacromolecules* **2018**, *19*, 3456–3466, DOI: 10.1021/acs.biomac.8b00776.

[213] R. Nordström, L. Nyström, O. C. J. Andrén, M. Malkoch, A. Umerska, M. Davoudi, A. Schmidtchen, M. Malmsten, Membrane interactions of microgels as carriers of antimicrobial peptides, *J. Colloid Interface Sci.* **2018**, *513*, 141–150, DOI: 10.1016/j.jcis.2017.11.014.

[214] G. A. Foster, D. M. Headen, C. González-García, M. Salmerón-Sánchez, H. Shirwan, A. J. García, Protease-degradable microgels for protein delivery for vascularization, *Biomaterials* **2017**, *113*, 170–175, DOI: 10.1016/j.biomaterials.2016.10.044.

[215] N. Welsch, A. L. Becker, J. Dzubiella, M. Ballauff, Core-shell microgels as “smart” carriers for enzymes, *Soft Matter* **2012**, *8*, 1428–1436, DOI: 10.1039/c1sm06894f.

[216] H. Peng, K. Rübsam, F. Jakob, U. Schwaneberg, A. Pich, Tunable enzymatic activity and enhanced stability of cellulase immobilized in biohybrid nanogels, *Biomacromolecules* **2016**, *17*, 3619–3631, DOI: 10.1021/acs.biomac.6b01119.

[217] S. Engel, H. Höck, M. Bocola, H. Keul, U. Schwaneberg, M. Möller, CaLB catalyzed conversion of ε -caprolactone in aqueous medium. Part 1 : Immobilization of CaLB to microgels, **2016**, 1–16, DOI: 10.3390/polym8100372.

[218] N. Murthy, M. Xu, S. Schuck, J. Kunisawa, N. Shastri, J. M. Frechet, J. M. J. Fréchet, A macromolecular delivery vehicle for protein-based vaccines: acid-degradable protein-loaded microgels, *Proc Natl Acad Sci U S A* **2003**, *100*, 4995–5000, DOI: 10.1073/pnas.0930644100\r0930644100 [pii].

[219] N. Murthy, Y. X. Thng, S. Schuck, M. C. Xu, J. M. J. Fréchet, A novel strategy for encapsulation and release of proteins: Hydrogels and microgels with acid-labile acetal cross-linkers, *J. Am. Chem. Soc.* **2002**, *124*, 12398–12399, DOI: 10.1021/ja026925r.

[220] K. S. Soni, S. S. Desale, T. K. Bronich, Nanogels: An overview of properties, biomedical applications and obstacles to clinical translation, *J. Control. Release* **2016**, *240*, 109–126, DOI: 10.1016/j.jconrel.2015.11.009.

[221] C. S. Pillay, E. Elliott, C. Dennison, Endolysosomal proteolysis and its regulation, *Biochem. J.* **2002**, *363*, 417–429, DOI: 10.1042/0264-6021:3630417.

[222] G. Agrawal, R. Agrawal, Functional microgels: Recent advances in their biomedical applications, *Small* **2018**, *14*, 1–18, DOI: 10.1002/smll.201801724.

[223] E. Mueller, R. J. Alsop, A. Scotti, M. Bleuel, M. C. Rheinstädter, W. Richtering, T. Hoare, Dynamically cross-linked self-assembled thermoresponsive microgels with homogeneous internal structures, *Langmuir* **2018**, *34*, 1601–1612, DOI: 10.1021/acs.langmuir.7b03664.

[224] G. Saito, J. A. Swanson, K. D. Lee, Drug delivery strategy utilizing conjugation via reversible disulfide linkages: Role and site of cellular reducing activities, *Adv. Drug Deliv. Rev.* **2003**, *55*, 199–215, DOI: 10.1016/S0169-409X(02)00179-5.

[225] J. M. Estrela, A. Ortega, E. Obrador, Glutathione in cancer biology and therapy, *Glutathione in Cancer Biology and Therapy*, **2006**, DOI: 10.1080/10408360500523878.

[226] A. Gupte, R. J. Mumper, Elevated copper and oxidative stress in cancer cells as a target for cancer treatment, *Cancer Treat. Rev.* **2009**, *35*, 32–46, DOI: 10.1016/j.ctrv.2008.07.004.

[227] A. Russo, W. DeGraff, N. Friedman, J. B. Mitchell, Selective modulation of glutathione levels in human normal versus tumor cells and subsequent differential response to chemotherapy drugs, *Cancer Res.* **1986**, *46*, 2845–2848.

[228] M. Mackiewicz, J. Romanski, E. Drozd, B. Gruber-Bzura, P. Fiedor, Z. Stojek, M. Karbarz, Nanohydrogel with N,N'-bis(acryloyl)cystine crosslinker for high drug loading, *Int. J. Pharm.* **2017**, *523*, 336–342, DOI: 10.1016/j.ijpharm.2017.03.031.

[229] W. Chen, M. Zheng, F. Meng, R. Cheng, C. Deng, J. Feijen, Z. Zhong, In situ forming reduction-sensitive degradable nanogels for facile loading and triggered intracellular release of proteins, *Biomacromolecules* **2013**, *14*, 1214–1222, DOI: 10.1021/bm400206m.

[230] J. H. Ryu, R. T. Chacko, S. Jiwpanich, S. Bickerton, R. P. Babu, S. Thayumanavan, Self-cross-linked polymer nanogels: A versatile nanoscopic drug delivery platform, *J. Am. Chem. Soc.* **2010**, *132*, 17227–17235, DOI: 10.1021/ja1069932.

[231] Z. Y. Qiao, R. Zhang, F. S. Du, D. H. Liang, Z. C. Li, Multi-responsive nanogels containing motifs of ortho ester, oligo(ethylene glycol) and disulfide linkage as carriers of hydrophobic anti-cancer drugs, *J. Control. Release* **2011**, *152*, 57–66, DOI: 10.1016/j.jconrel.2011.02.029.

[232] Q. Zhu, X. Chen, X. Xu, Y. Zhang, C. Zhang, R. Mo, Tumor-specific self-degradable nanogels as potential carriers for systemic delivery of anticancer proteins, *Adv. Funct. Mater.* **2018**, *28*, 1707371, DOI: 10.1002/adfm.201707371.

[233] M. Uchida, M. Terashima, C. H. Cunningham, Y. Suzuki, D. A. Willits, A. F. Willis, P. C. Yang, P. S. Tsao, M. V. McConnell, M. J. Young, T. Douglas, A human ferritin iron oxide nano-composite magnetic resonance contrast agent, *Magn. Reson. Med.* **2008**, *60*, 1073–1081, DOI: 10.1002/mrm.21761.

[234] E. Fantechi, C. Innocenti, M. Zanardelli, M. Fittipaldi, E. Falvo, M. Carbo, V. Shullani, L. Di Cesare Mannelli, C. Ghelardini, A. M. Ferretti, A. Ponti, C. Sangregorio, P. Ceci, A smart platform for hyperthermia application in cancer treatment: Cobalt-doped ferrite nanoparticles mineralized in human ferritin cages, *ACS Nano* **2014**, *8*, 4705–4719, DOI: 10.1021/nn500454n.

[235] B. Webb, J. Frame, Z. Zhao, M. L. Lee, G. D. Watt, Molecular entrapment of small molecules within the interior of horse spleen ferritin, *Arch. Biochem. Biophys.* **1994**, *309*, 178–183, DOI: 10.1006/abbi.1994.1100.

[236] L. Chen, G. Bai, R. Yang, J. Zang, T. Zhou, G. Zhao, Encapsulation of β-carotene within ferritin nanocages greatly increases its water-solubility and thermal stability, *Food Chem.* **2014**, *149*, 307–312, DOI: 10.1016/j.foodchem.2013.10.115.

[237] F. Yan, Y. Zhang, H. K. Yuan, M. K. Gregas, T. Vo-Dinh, Apoferritin protein cages: A novel drug nanocarrier for photodynamic therapy, *Chem. Commun.* **2008**, 4579–4581, DOI: 10.1039/b810949d.

[238] R. Fraczkiewicz, W. Braun, Exact and efficient analytical calculation of the accessible surface areas and their gradients for macromolecules, *J. Comput. Chem.* **1998**, *19*, 319–333, DOI: 10.1002/(SICI)1096-987X(199802)19:3<319::AID-JCC6>3.0.CO;2-W.

[239] R. E. Hansen, J. R. Winther, An introduction to methods for analyzing thiols and disulfides: Reactions, reagents, and practical considerations, *Anal. Biochem.* **2009**, *394*, 147–158, DOI: 10.1016/j.ab.2009.07.051.

[240] D. E. Shafer, J. K. Inman, A. Lees, Reaction of tris(2-carboxyethyl)phosphine (TCEP) with maleimide and α- haloacyl groups: Anomalous elution of TCEP by gel filtration, *Anal. Biochem.* **2000**, *282*, 161–164, DOI: 10.1006/abio.2000.4609.

[241] K. Tyagarajan, E. Pretzer, J. E. Wiktorowicz, Thiol-reactive dyes for fluorescence labeling of proteomic samples, *Electrophoresis* **2003**, *24*, 2348–2358, DOI: 10.1002/elps.200305478.

[242] M. Brugnoni, F. Fink, A. Scotti, W. Richtering, Synthesis and structure of temperature-sensitive nanocapsules, *Colloid Polym. Sci.* **2020**, *298*, 1179–1185, DOI: 10.1007/s00396-020-04686-5.

[243] J. Gao, B. J. Frisken, Cross-linker-free N-isopropylacrylamide gel nanospheres, *Langmuir* **2003**, *19*, 5212–5216, DOI: 10.1021/la0269762.

[244] M. Brugnoni, A. C. Nickel, L. C. Kröger, A. Scotti, A. Pich, K. Leonhard, W. Richtering, Synthesis and structure of deuterated ultra-low cross-linked poly(N-isopropylacrylamide) microgels, *Polym. Chem.* **2019**, *10*, 2397–2405, DOI: 10.1039/c8py01699b.

[245] V. K. Switacz, S. K. Wypysek, R. Degen, J. J. Crassous, M. Spehr, W. Richtering, Influence of size and cross-linking density of microgels on cellular uptake and uptake kinetics, *Biomacromolecules* **2020**, *21*, 4532–4544, DOI: 10.1021/acs.biomac.0c00478.

[246] A. Nel, E. Ruoslahti, H. Meng, New insights into “permeability” as in the enhanced permeability and retention effect of cancer nanotherapeutics, *ACS Nano* **2017**, *11*, 9567–9569, DOI: 10.1021/acsnano.7b07214.

[247] E. Blanco, H. Shen, M. Ferrari, Principles of nanoparticle design for overcoming biological barriers to drug delivery, *Nat. Biotechnol.* **2015**, *33*, 941–951, DOI: 10.1038/nbt.3330.

[248] X. Wu, R. H. Pelton, A. E. Hamielec, D. R. Woods, W. McPhee, The kinetics of poly(N-isopropylacrylamide) microgel latex formation, *Colloid Polym. Sci.* **1994**, *272*, 467–477, DOI: 10.1007/BF00659460.

[249] J. A. Reynolds, C. Tanford, Binding of dodecyl sulfate to proteins at high binding ratios. Possible implications for the state of proteins in biological membranes., *Proc. Natl. Acad. Sci. U. S. A.* **1970**, *66*, 1002–1007, DOI: 10.1073/pnas.66.3.1002.

[250] M. M. Burrell, *Enzymes of Molecular Biology*, Humana Press, Totowa, NJ, **1993**, DOI: 10.1385/0896032345.

[251] F. Kratz, A. Warnecke, K. Scheuermann, C. Stockmar, J. Schwab, P. Lazar, P. Drückes, N. Esser, J. Drevs, D. Rognan, C. Bissantz, C. Hinderling, G. Folkers, I. Fichtner, C. Unger, Probing the cysteine-34 position of endogenous serum albumin with thiol-binding doxorubicin derivatives. Improved efficacy of an acid-sensitive doxorubicin derivative with specific albumin-binding properties compared to that of the parent compound, *J. Med. Chem.* **2002**, *45*, 5523–5533, DOI: 10.1021/jm020276c.

[252] C. A. Butts, J. Swift, S. G. Kang, L. Di Costanzo, D. W. Christiansen, J. G. Saven, I. J. Dmochowski, Directing noble metal ion chemistry within a designed ferritin protein, *Biochemistry* **2008**, *47*, 12729–12739, DOI: 10.1021/bi8016735.

[253] N. Kamaly, B. Yameen, J. Wu, O. C. Farokhzad, Degradable controlled-release polymers and polymeric nanoparticles: Mechanisms of controlling drug release, *Chem. Rev.* **2016**, *116*, 2602–2663, DOI: 10.1021/acs.chemrev.5b00346.

[254] H. Huang, Matrix metalloproteinase-9 (MMP-9) as a cancer biomarker and MMP-9 biosensors: Recent advances, *Sensors* **2018**, *18*, 3249, DOI: 10.3390/s18103249.

[255] M. Lach, M. Künzle, T. Beck, Free-standing metal oxide nanoparticle superlattices constructed with engineered protein containers show in crystallo catalytic activity, *Chem. Eur. J.* **2017**, *23*, 17482–17486, DOI: 10.1002/chem.201705061.

[256] W. Wang, B. A. Malcolm, Two-stage PCR protocol allowing introduction of multiple mutations, deletions and insertions using QuikChange™ site-directed mutagenesis, *Biotechniques* **1999**, *26*, 680–682, DOI: 10.2144/99264st03.

[257] M. M. Bradford, A rapid and sensitive method for the quantitation microgram quantities of protein utilizing the principle of protein-dye binding, *Anal. Biochem.* **1976**, *72*, 248–254, DOI: 10.1006/abio.1976.9999.

12 Curriculum vitae

Personal information

Name : Made Budiarta

Date of birth : August 21, 1979

Place of birth : Mataram, Indonesia

Nationality : Indonesia

Education

Since 12/2017 Doctoral studies

Institute of Inorganic Chemistry

RWTH Aachen University, Germany

10/2013 – 05/2016 Master's studies in Advanced Materials

University of Ulm, Germany

Thesis: Multifunctional albumin-copolymer nanotransporter for theranostic applications

Degree: Master of Science (M.Sc.)

08/1997 – 03/2002 Bachelor's studies in Chemistry

Bandung Institute of Technology, Indonesia

Thesis: Modification of TiO_2 photocatalyst with Cu(II)-phthalocyanine to improve its activity to degrade organic pollutants.

Degree: Bachelor of Science (B.Sc.)

08/1994 – 07/1997 Senior high school

SMUK Frateran Surabaya, Indonesia

Declaration of Authorship

I, Made Budiarta, declare that this thesis and the work presented in it are my own and have been generated by me as the result of my own original research.

I do solemnly swear that:

1. This work was done wholly or mainly while in candidature for the doctoral degree at this faculty and university;
2. Where any part of this thesis has previously been submitted for a degree or any other qualification at this university or any other institution, this has been clearly stated;
3. Where I have consulted the published work of others or myself, this is always clearly attributed;
4. Where I have quoted from the work of others or myself, the source is always given. This thesis is entirely my own work, with the exception of such quotations;
5. I have acknowledged all major sources of assistance;
6. Where the thesis is based on work done by myself jointly with others, I have made clear exactly what was done by others and what I have contributed myself;
7. Parts of this work have been published or are in the process of being published:
    - Budiarta, M.; Xu, W.; Schubert, L.; Meledina, M.; Meledin, A.; Wöll, D.; Pich, A.; Beck, T. Protecting Redesigned Supercharged Ferritin Containers against Protease by Integration into Acid-cleavable Polyelectrolyte Microgels, *submitted*.
    - Budiarta, M.; Boesveld, S.; Strnad, P.; Beck, T. The application of ferritin-microgel systems for drug release and delivery, *in preparation*.

15th November 2020

Made Budiarta